studies in physical and theoretical chemistry
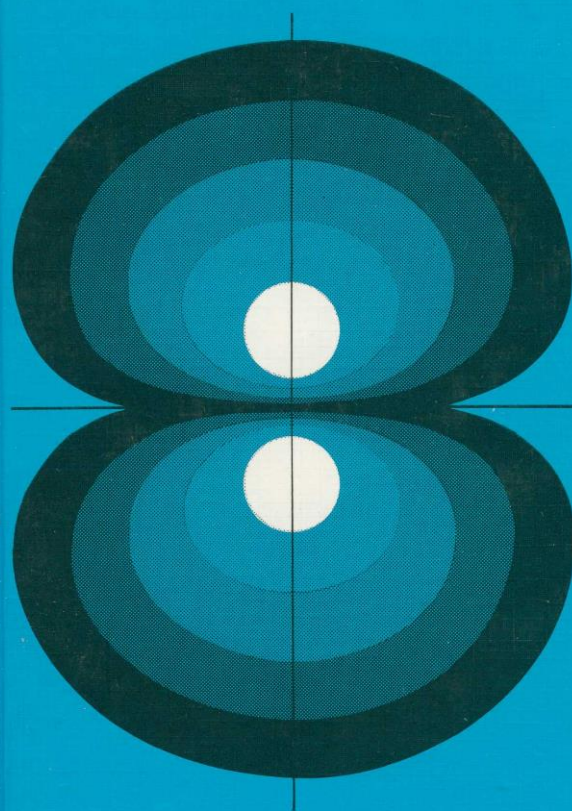
81

MÖSSBAUER STUDIES OF SURFACE LAYERS

G.N. Belozerski

elsevier

MOSSBAUER STUDIES OF SURFACE LAYERS

GUENNADI N. BELOZERSKI

Department of Chemistry St. Petersburg State University 199164 St. Petersburg Russia

Preface to the WEB edition.

The manuscript "MÖSSBAUER STUDIES OF SURFACE LAYERS" was published at 1993 by "ELSEVIER". It was prepared as copy ready manuscript in word processor CHIwriter.4.
At the beginning of 1998, "all rights was reverted to the original author(s)/editor(s)". After "ELSEVIER" copyright was finished my wife Ludmila and I converted the CHIwriter version in Word-97 version. On this way a lot of troubles appear connected first of all with formulas. Now all is in *.pdf format.
The title of the manuscript is slightly changed. Now it is "MÖSSBAUER EFFECT AND STUDIES OF SURFACE LAYERS". The change in the manuscript is minimal and connected with updating. The number of pages coincide practically with the number of pages of "MÖSSBAUER STUDIES OF SURFACE LAYERS" published at 1993 by "ELSEVIER".

I hope that the version will be valuable for those which would like strike up an acquaintance with Theory as well as Applications of Mössbauer spectroscopy. It will be useful also for those which are dealing with such matters as nanoparticles and monolayers research and also with the nanotechnology.

Gennady Belozerskiy

PREFACE

The study of solid surfaces is one of the most important problems in solid state science. One feature of such studies is the development of techniques which are able to examine solids over a wide range of compositions, gaseous pressures, different temperatures and under conditions of practical interest. The surface of such specimens of interest may be of any shape. It is also important to note that the different fields of science and technology have different notions of what constitutes a surface. For example, a physicist dealing with the interaction of absorbed atoms with the substrate surface means by the latter the actual geometric surface or a layer with the depth of less than 1 nm. A metallurgist's interest in a surface is generally that region of the solid which is tens and hundreds of μm deep. This is one of the reasons why some physics encyclopedia give no definition of a surface.

At this stage it is relevant to note that emission Mössbauer spectroscopy is capable of the examination of 10^{12} atoms implanted on a square centimetre which is equivalent to one hundredth of the number of atoms making up a monolayer on the area of one square centimeter. It is important to note that the technique can investigate the properties of layers which are tens of μm deep. Whilst nuclear physics has developed many novel methods of surface modification (e.g. implantation) and effective nuclear research methods, Mössbauer spectroscopy has developed as one of the few methods available for investigation of solids differing in depth by several orders of magnitude. Hence, it is only in recent times that the problems of surface investigation and the study of separate layers have been amenable to investigation.

Two factors may be identified which are responsible for the widespread use of Mössbauer spectroscopy in both fundamental and applied surface science research. Firstly, the absolute selectivity of Mössbauer spectroscopy which means that in each experiment a response is registered from only one isotope of the element. Furthermore, atoms of that element in non-equivalent positions give different responses with magnitude which is proportional to the populations of the positions. Secondly, Mössbauer spectroscopy has a high sensitivity which is determined by the minimum number of resonant atoms needed to get a detectable response. In the transmission Mössbauer spectroscopy for ^{57}Fe a response is given by a monolayer with the area of the order of 1 square centimetre. However, as has already been mentioned, higher sensitivities can be achieved in emission Mössbauer spectroscopy.

The parameters of the hyperfine interaction derived from the Mössbauer spectra provide valuable information on the chemical bond character and on magnetic properties of surface layers as well as on the change of the properties with the depth from the outermost surface layer. It is possible to carry out quantitative phase analysis and to use the technique to study different transformations in the solid which result from external effects under a wide range of temperatures and pressures. Certain problems are sometimes encountered which are caused by the limited activities of Mössbauer sources and by the rather low cross section of the radiation interaction with matter. However, such problems are compensated by the absence of any limitations on experimental conditions other than that the substance should be a solid. As a consequence, Mössbauer spectroscopy can be used in fundamental research and in various areas of applied science and technology including process monitoring. This book is one of the first attempts at a consistent presentation of theoretical and practical problems of the use of Mössbauer spectroscopy to study solid surfaces, its applications, and development.

The applications include: surface studies with hyperfine probes in the following fields: oxidation and corrosion of metals and alloys; passivating and protective coatings; physics of metals: annealing and quenching, mechanical and chemical treatment, ion implantation and laser treatment; texture of near-surface layers. The choice is based on scientific interests of the author and his practical experience in these fields. However, the limited space does not allow complete coverage of any of the topics mentioned above. It is also important to note some other fields - for example the unique capabilities of Mössbauer spectroscopy for fine particles studies: superparamagnetism, phase analysis and the magnetic structure of the surfaces of particles which may be smaller than 10 nm; the effect of the gas phase on the properties of small particles, the interaction of these particles with the substrate; and the importance of these studies in areas of industrial significance such as catalysis. It should also be noted that Mössbauer spectroscopy is one of the best methods for in situ characterization of solid/solid and solid/solution interfaces. This lends itself to in situ studies of surfaces under various coatings and processes, surface magnetism and the effect of the gas phase on the properties of the surface layers and the structure and magnetic properties of epitaxially grown monolayers on the surface of oriented single crystals .

TABLE OF CONTENTS

1. Physical Concepts of the Method

The Mössbauer effect is concerned with the scattering[1] and emission of γ–radiation by atomic nuclei in the condensed phase. It makes use of the probability that the state of a system will remain unchanged when γ–quanta are absorbed or emitted with an energy which is exactly equal to the nuclear transitions energy E_0. Hence the γ-spectrum $J(E)$ of a Mössbauer source may be represented by the sum of a line $J_R(E)$ which is displaced due to recoil effects and broadened by the Doppler effect, and a line $J_M(E)$ with its centre at the energy which is exactly equal to the transition energy, the half-width being close to the natural one - Γ_{nat}. The part of the spectrum $J_M(E)$ is of particular interest and reveals itself most strikingly when the source and the sample under study are in the solid state. There are many introductory books on Mössbauer spectroscopy which give further details of the fundamental principles of the theory and the technique [1.1-6].

The aim of this Chapter is to briefly familiarize the reader who is not an active practitioner of Mössbauer spectroscopy with the basic concepts of the method. It is intended that this information should be sufficient for the reader to understand the application of Mössbauer spectroscopy to the analysis of surface layers.

1.1. General Aspects of Mössbauer Spectroscopy

The emission probability f and the absorption probability f' of recoilless γ-quanta and the temperature dependence of f and f' are determined by the γ-quanta energy, the mass of the nucleus, lattice vibrations and other properties of the sample. The measurement of f enables the study of atomic vibrations or force constants.

In order to obtain information on chemical bonds of atoms in solids from experimental data, an explicit theoretical relation is needed to associate experimental f (or f') values with the phonon spectrum and the force constants of the crystal. Unfortunately this seemingly rather simple approach produces a number of problems which primarily result from the limited information which is available on the phonon spectra of solids of practical interest. Hence a more general concept of the Mössbauer effect probability may be best developed by use of the time-space correlation function.

The probability of γ–quantum resonant emission with a wave vector $\underline{k}$ when a nucleus undergoes a transition from an excited state e to the ground state g in a system going from a state ψ_n of eigenenergy $\mathcal{E}_n$ to the state ψ_{n0} of energy $\mathcal{E}_{n0}$, may be written:

---

[1] Only resonant scattering is considered here. If the process is assumed to be isotropic, then the probability of "forward" re-scattering may be neglected. In this sense, any scattering event results in the disappearance of the quantum from the incident well-collimated beam. The process is often referred to as "absorption". Thus, "physically" there is only scattering, still sometimes absorption is spoken of.

$$W(E,\psi_n) = \sum_n \frac{|<g\psi_{n_o} \mid H \mid e \,\psi_n \,\underline{k} >|^2}{|\; E - E_o - (\mathcal{E}_{n_o} - \mathcal{E}_n) + i\Gamma/2\,|^2} \; , \tag{1.1}$$

where H is the energy operator describing the interaction between the γ-ray and the nucleus in question; and E_0 and Γ are the energy and the full width at half maximum of the excited state, respectively.

Since the interactions of atoms in a solid are very weak as compared to nuclear interactions, the atomic interactions only effect the movement of the centre of mass of a nucleus or atom and do not effect the movement of nucleons in the nucleus. The matrix elements M of operator H may be now represented by the product of two factors

$$M = < \psi_{n_o} \mid \exp (i \,\underline{k}\, \underline{r})\mid \psi_n > < g \mid a \mid e > \, , \tag{1.2}$$

where $\underline{r}$ is the radius vector which is characteristic of the position of the nucleus.

The nuclear matrix element $< g \mid a \mid e >$ for any changes in the lattice is a common term which may be factorized. It determines the angular dependent properties of emitted or absorbed radiation and the relative intensity of the hyperfine components of the spectrum. The first term of (1.2) describes the momentum transfer of the quantum to the lattice and the resulting change of the phonon spectrum. The term determines the f or f' value and may have an angular dependence of its own. For a cubic crystal where interatomic forces may be assumed to be harmonic, we have

$$f = \exp\left\{ -k^2 \overline{x^2} \right\} \tag{1.3}$$

where $\overline{x^2}$ is the mean square displacement of the Mössbauer atom from its equilibrium position at temperature T.

The Debye model is most widely used and is assumed irrespective of the lattice symmetry and the number of atoms in the unit cell. Hence, from an observed f value the effective characteristic temperature may be evaluated and compared with the temperatures obtained for the substance by methods such as X-ray analysis or specificheat measurements.

According to the Debye model, the Mössbauer effect probability may be written:

$$f = \exp\left[-\frac{6E_R}{k\Theta} \left(\frac{T}{\Theta}\right)^2 \int_0^{\Theta/T} \left(\frac{1}{e^t - 1} + \frac{1}{2}\right) t\,dt \right] , \tag{1.4}$$

where $E_R = E_0^2/2Mc^2$ is the recoil energy imparted to an isolated nucleus of mass M; c is the velocity of light; Θ is the Debye temperature of the crystal, and k is the Boltzmann constant. For very low and high temperatures (as compared with Θ), expression (1.4) may be written:

$$f = \exp\left[-\frac{3E_R}{2k\Theta} \right] \quad \text{for } T << \Theta , \tag{1.5}$$

$$f = \exp\left[-\frac{6E_R T}{k\Theta^2}\right] \text{ for } T > \Theta ,\tag{1.6}$$

which enables one to further simplify the characteristic temperature determination.

The theoretical spectrum of the 129 keV γ-ray of ^{191}Ir emitted by atom in iridium metal is shown in Fig. 1.0. The Mössbauer spectrometer is sensitive only to the narrow, recoil-free line at zero energy shift, which contains 5,7% of total area under the curve at 4 K for ^{191}Ir, $E_0 = 129$ keV .
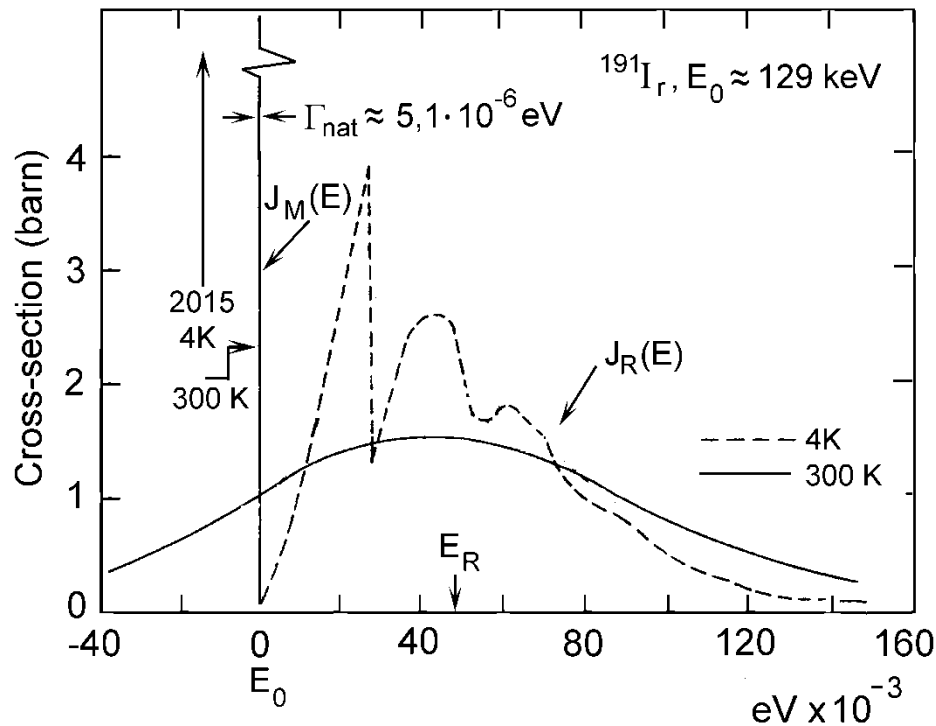
Fig. 1.0 Absorption cross-section for ^{129}Ir at 4 and 300 K. The Debye model was used to calculate the lattice vibration.

It is found that when there are several atoms in a unit cell, the Debye model is not adequate, and, apart from three acoustic phonon branches, optical branches also appear. The Mössbauer effect probability is higher if more optical branches determine the oscillation mode of the Mössbauer atom in the lattice. Light atoms, as a rule, vibrate in optical branches. The oscillation amplitude of a heavy atom in the optical branches is determined by the type of interaction of these atoms in the lattice and is significant only when the interaction between heavy atoms is strong.

Using resonance atoms as admixtures to various compounds extends the number of solids in which the Mössbauer effect is observable and this expands the resources of this method even further. Unfortunately the theoretical treatment is much more complicated than compared with the ordinary Mössbauer effect. In such situations it is the oscillations of the admixture atoms which are of the primary interest. At the same time these oscillations cause the translational symmetry to vanish and thus the theoretical treatment becomes rather complicated.

Atoms of the Mössbauer isotope present in a phase are characterized by their f or f' values. These are the important parameters needed for quantitative phase analysis. It has been proved experimentally that for some isotopes even at room temperature the f

values may exceed 0.5 which means that more than one half of the emitted γ-quanta are recoilless with energy equal to the energy of the nuclear transition. These quanta may resonantly interact in the sample under study.

It is unfortunate that there is at present no satisfactory compilation of f-values, although fairly comprehensive information is contained in the annual reference editions of "Mössbauer Effect Data Index" which contains reviews of relevant literature until 1976 and, more recently, in monthly issues of "Mössbauer Effect Data and Reference Journal". On using the results of quantitative phase analysis by Mössbauer spectroscopy, special attention should be paid to the validity of information on the f-values used in the analysis.

The consideration so far has not taken into account the dependence of phonon excitation on the direction of the recoil momentum of the nucleus with respect to the crystallographic axes. This must be considered especially when strong anisotropy is observed for laminar crystals. The anisotropy factor f' which is detected for some nontextured polycrystalline samples takes this into account in a phenomenon known as the Goldanskii-Karyagin effect. This enables the extraction of valuable information on solids such as the surface layer structure and texture.

The application of Mössbauer spectroscopy in diverse fields of qualitative and quantitative analysis is based on the ease with which hyperfine interactions can be observed. The information obtained from the Mössbauer spectra may be correlated to other methods by which hyperfine interactions can be examined such as NMR, EPR, ENDOR, PAC (perturbed angular correlations), nuclei orientation and neutron scattering. However, Mössbauer spectroscopy often proves to be experimentally simpler, more illustrative and an efficient method for studying applied problems. The Mössbauer nuclei are ideal "spies" supplying information on both the microscopic and macroscopic properties of solids. The spectrum of γ-rays emitted or scattered by such nuclei, is a source of information on the hyperfine interactions.

Until relatively recently one could measure the γ-rays energy with the inaccuracy $\Delta E \gg \Gamma_{nat}$. However, since the first work was reported on classic resonance scattering of γ-rays and since the modernization of crystal diffraction spectrometers, it has become possible to significantly increase the energy resolution R $\sim$ $\Delta E/E$ although it is still several orders of magnitude higher than Γ_{nat}/E. That is why γ-spectroscopy initially failed to give information on nuclear energy levels, similar to the information that could be obtained by optical spectroscopy on electronic structure. The direct study of hyperfine interactions by the accurate measurement of γ-rays energy was quite impossible since the energy of hyperfine interactions are of the same order as Γ_{nat}.

The discovery by R.L. Mössbauer made it possible to measure the hyperfine interaction directly. In this Chapter we shall outline the general concepts of Mössbauer spectroscopy in so much as it is necessary to describe the method and its various

applications. In Mössbauer spectroscopy the energy resolution is determined by the natural line width (for ^{57}Fe Γ_{nat} is equal to 4.8 10^{-9} eV). The experimental methods can measure the changes in line positions with an inaccuracy of less than 0.1 Γ_{nat}.

1.2. Hyperfine Interactions and Line Positions in Mössbauer Spectra

The energy of a nucleus, as well as of any system of charges and currents, changes upon interaction with an external electromagnetic field by an amount E'. Using classic electrodynamics, the energy may be described by the multipole moments series as:

$$E' = q\varphi_0 - \underline{p}\underline{E}_0 - \underline{\mu}\underline{H}_0 - \frac{1}{6}\sum_{i,k=1}^{3}\underline{Q}_{ik}(\partial^2\varphi/\partial x_i \partial x_k)_0 - ..., \qquad (1.7)$$

where $\underline{E}$ and $\underline{H}$ are the electric and magnetic field strength, respectively, φ is the electrostatic potential, $q = eZ$ is the nuclear charge, $\underline{p}$, $\underline{\mu}$ are vectors of electric and magnetic dipole moments, Q_{ik} is the tensor of the electric quadrupole moment. The subscript "o" means that the quantity is that in the centre of the nucleus. The moments of higher orders may be neglected. This is valid if: (i) the velocities of the nucleons are small as compared to the velocity of light; (ii) changes in the external field at nuclear distances are small (the hyperfine anomaly is neglected); (iii) the external field changes the distribution of charges and currents in the nucleus only to a negligible extent. Since nuclei do not have electric dipole moments, the second term of (1.7) is zero and the energy of a nucleus in an external electromagnetic field is determined by the product of the nuclear (q, $\underline{\mu}$, $\underline{Q}_{ik}$) and electron φ_0 , $\underline{H}_0$, $(\partial^2\varphi/\partial x_i \partial x_k))$ factors. In solid state physics and in the applied fields the first factors are supposed to be known.

The classical treatment is insufficient to obtain the positions of the nuclear levels, the relative intensities of the corresponding transitions, and the angular dependence of the emitted radiations and a quantum mechanical approach is needed. As seen from (1.7) the Hamiltonian H, describing the interaction of a nucleus with effective fields, may be represented as a sum of the two Hamiltonians: one for interactions of the nucleus with electron (H_Q) and the other for interactions with the magnetic field (H_M)

$$H = H_Q + H_M \quad . \tag{1.8}$$

The Hamiltonian of the electrostatic interaction is

$$H_Q = e \sum_{p=1}^{Z} \varphi(\underline{r}_p) \; , \tag{1.9}$$

where $\underline{r}_p$ is the radius vector of the p-th proton, $\varphi(\underline{r}_p)$ is the electric potential in the vicinity of the p-th proton, and the summation is over all protons p = 1,...Z. The coordinate system is chosen such that the origin is at the centre of the nucleus and the axes x^i (i = 1,2,3; $x^1 \equiv x$; $x^2 \equiv y$; $x^3 \equiv z$) are directed along the principal axis of the tensor of the electric field gradient (EFG) acting on the nucleus. Since the external electromagnetic field potential does not change appreciably within the nucleus, and by expansion of (1.9) over the multipoles, we can write

$$\mathcal{H}_Q = \sum_{p=1}^{Z} \varphi_p(0) + e \sum_{p=1}^{Z} \sum_{i=1}^{3} \left(\frac{\partial \varphi_p}{\partial x_p^i} \right)_0 x_p^i +$$

$$\frac{1}{2} e \sum_{p=1}^{Z} \sum_{i,k=1}^{3} \left(\frac{\partial^2 \varphi_p}{\partial x_p^i \, \partial x_p^k} \right)_0 x_p^i \, x_p^k + \ldots, \tag{1.10}$$

where $\varphi_p(0)$ is the electric potential at the centre of the nucleus due to the p-th proton. The first term in (1.10) displaces the energy of all nuclear levels equally and may be omitted. The second term describes the dipole electric interaction and equal zero (since in the state of a given parity the nucleus has no electric dipole moment).

It is the third term that determines the experimentally observed energy change of nuclear levels due to the interaction of the nucleus with external electric fields. For the analysis of experimental data a special method is usually used whereby the same term is added to and subtracted from the right-hand side of (1.10). The result is

$$\mathcal{H}_Q = \frac{e}{6} \sum_{p=1}^{Z} \sum_{i,k=1}^{3} r_p^2 \left(\frac{\partial^2 \varphi_p}{\partial x_p^i \, \partial x_p^k} \right)_0 \delta_{ik} +$$

$$\frac{e}{6} \sum_{p=1}^{Z} \sum_{i,k=1}^{3} (3x_p^i x_p^k - r_p^2 \delta_{ik}) \left(\frac{\partial^2 \varphi_p}{\partial x_p^i \partial x_p^k} \right)_0 \quad ,$$

where $r_p^2 = \sum_{i=1} (x_p^i)^2$. Using the fact that the electrostatic potential φ satisfies the Poisson equation $\nabla^2 \varphi = 4\pi\rho_e$, $\rho_e = -e |\psi(0)|^2$ is the charge density at the nucleus (r = 0) and introducing the tensor of nuclear quadrupole moment

$$Q_{ik} = \sum_{p=1}^{Z} \left(3x_p^i x_p^k - r_p^2 \delta_{ik} \right) \text{ and the EFG tensor,}$$

$\varphi_{ik} = (\partial^2 \varphi_p / \partial x_p^i \partial x_p^k)_0$, we can now rewrite (1.9) as

$$H_Q = H_\delta + H'_Q = -\frac{2\pi}{3} e^2 \sum_{p=1}^{Z} r_p^2 |\psi(0)|^2 + \frac{e}{6} \sum_{i,k=1}^{3} \varphi_{ik} Q \tag{1.11}$$

The nucleus is here considered to be a sphere with a mean-square radius $\overline{r^2} = \sum_{p=1}^{Z} \overline{r_p^2} / Z$

for the ground state - g and excited state - e. As a rule, $\overline{r_g^2} \neq \overline{r_e^2}$ and the nuclear charge is uniformly distributed inside the sphere. Thus the interaction of the nucleus with the electric fields may be expressed as a sum of two interactions corresponding to Hamiltonians H_δ and H_Q.
The external electric field acting on such a spherical nucleus does not split the levels but shifts them by the quantity

$$\delta E_{g,e} = \frac{2\pi}{3} e^2 Z r_{g,e}^2 |\psi(0)|^2 \quad . \tag{1.12}$$

The shift due to Coulomb interactions is of the order of 10^{-12} of the transition energy. The value of the shift for every nuclear level depends on the chemical state of the atom. This is characterized by the $|\psi(0)|_{a,s}^2$ parameter which is the electron density at the nucleus in the absorber (a) or in the source (s). In a Mössbauer spectrum this part of the full electrostatic interaction manifests itself as the chemical isomer shift δ [1.8] between the centre of gravity of the emission spectrum of the source and the centre of gravity of the absorption spectrum of the sample which is called the absorber (Fig. 1.1a and b).
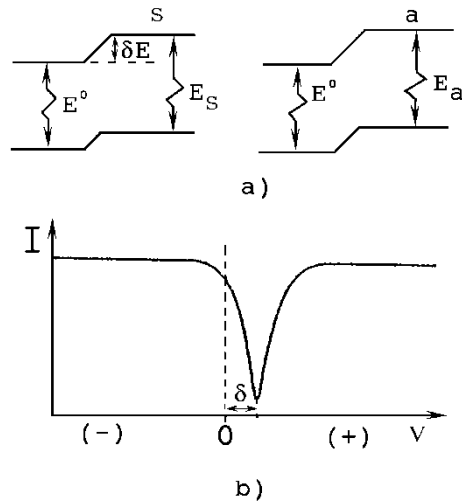
Fig. 1.1a, b Energy level shifts for a ^{57}Fe nucleus, resulting in the appearance of the isomer shift – δ (a); the corresponding Mössbauer spectrum (b).

Thus the transition energy in the source E_s is different from the energy E_a in the absorber, either of them being different from the transition energy E^0 for $\overline{r^2} = 0$. For a pair of the source and absorber nuclei we may write

$$\delta = \frac{2\pi}{3} Ze^2 (\overline{r_e^2} - \overline{r_g^2})(|\psi(0)|_a^2 - |\psi(0)|_s^2).$$

(1.13)

For the first excited level of ^{57}Fe $r_e^2 < r_g^2$.

It must be appreciated that in Mössbauer experiments it is not the absolute energy of the γ-quanta which is determined but the energy shift of the nuclear levels. The energy scanning is carried out by the use of the Doppler effect. Therefore the energy parameters (Γ, δ) are expressed in velocity units, v. If the source moves to the detector with velocity v, the energy of emitted radiation increases by S = Ev/c. For the 14.4 keV transition a change in the source velocity with respect to the absorber of 1 mm/s corresponds to the change in the γ-quantum energy of $4.8 \ 10^{-8}$ eV.

The charge density at the nucleus is mainly determined by s- and only partially by p-electrons. The main effect of the p- and d-electrons and any other electrons shells that do not contribute directly to the electron density $|\psi(0)|^2$, is to shield the s-electrons. For example, the addition of a sixth 3d- electron

in the $Fe^{+3} \rightarrow Fe^{+2}$ transition causes the shielding of the s-electrons to increase. In accordance with (1.13) ferrous compounds give larger positive isomer shifts in the Mössbauer spectra than ferric compounds.

The determination of the scale factor $\left(\overline{r_e^2} - \overline{r_g^2}\right)$ in (1.13) is called the isomer shift calibration. The interpretation of isomer shifts in Mössbauer spectra involves the correlation of a given $|\psi(0)|_a^2 - |\psi(0)|_s^2$ value with the known electronic structure of the Mössbauer atom or the change of the structure resulting from the examination of different samples. It should be noted that it is only one 10^{-20}-th of atomic electrons in a solid that directly participate in the isomer shift; the nuclear parameter $\left(\overline{r_e^2} - \overline{r_g^2}\right)$ is of the order of 10^{-29} cm^2. The isomer shift is four orders of magnitude smaller than the Lamb shift caused by quantization of the electromagnetic field. The measurements of isomer shifts are now carried out by Mössbauer Spectroscopy at the limits of experimental possibility i.e. (R ~ 10^{-13}).

The isomer shift value is often considered to be the main parameter which enables the oxidation state to be identified. However it is often difficult to identify the nature of the phase by the isomer shift alone. For example, approximately similar isomer shifts correspond to a variety of different ferric oxides. Compounds (both sources and absorbers) do exist with especially accurately known isomer shift values. Thus, for Mössbauer studies involving ^{57}Fe the sources are prepared by introducing ^{57}Co into chromium, rhodium, stainless steel(SS), palladium- or platinum-foils. Materials such as iron $(\alpha-Fe)$, sodium nitroprusside (SNP) and potassium ferrocyanide (PFC) are often used as standard absorbers. A diagram of isomer shifts for substances generally used in practice at 298 K is shown in Fig 1.2. The isomer shift is described relative to the centre of the α-Fe spectrum.

The diagram shows that the energy required for the transition of a ^{57}Fe nucleus in SS into the first excited state is less than it would be in platinum. In velocity units the difference is 0.3484 + 0.086 = 0.4344 mm/s. The Mössbauer γ–quanta emitted by a ^{57}Co(Pt) source would be too high in energy to be resonantly scattered in SS sample. The maximum resonant scattering would occur if the energy was lowered by application of the Doppler effect. In this case the source and the absorber have to be moved relative to each other. The negative velocity values correspond to the movement of the absorber away from source. Hence for the above example the maximum scattering will be observed at the velocity of - 0.4344 mm/s.

In ^{57}Fe Mössbauer spectroscopy the isomer shifts are
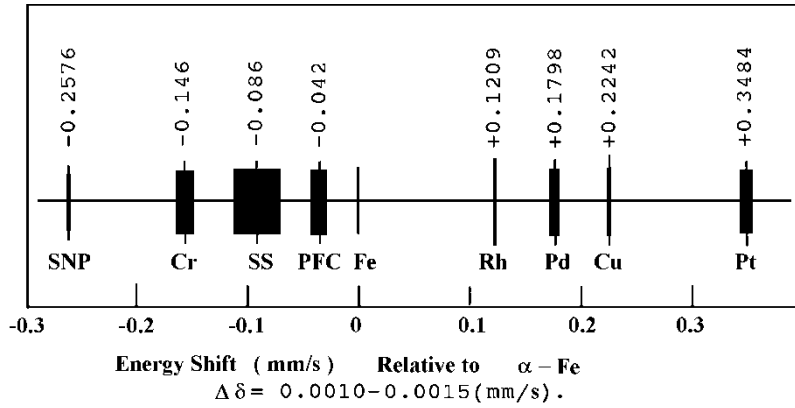
Fig. 1.2 Isomer shifts of sodium nitroprusside (SNP), potassium ferrocyanide (PFC) and stainless steel (SS) and ^{57}Co sources (chromium, palladium, copper and platinum matrices) relative to the center of the α-Fe spectrum.

usually quoted relative to α -Fe. Some works use the centroid of the SNP spectrum. Figure 1.2 enables the necessary conversions to be made. For example, if two spectra of PFC are obtained with the same spectrometer, one using a ^{57}Co(Cr) source and the other using a ^{57}Co(Pt) source, one spectrum will show a line in the positive velocity region whilst the other will show a line in the negative velocity region. The distance between them will be 0.4944 mm/s. Diagrams of the type shown for ^{57}Fe in Fig. 1.2 have also been formulated for other elements [1.9]. For every nuclide there is a compound used as a reference for the standardization of isomer shift data. For example, for tin it is SnTe and $BaSnO_3$, for iodine it is CsI, and for neptunium it is $NpAl_2$.
 Let us consider now the second of the above mentioned interactions known as the electric quadrupole interaction and described by the Hamiltonian H'$_Q$. By the Wigner-Ekart theorem, tensor components of the nuclear quadrupole moment are expressed through $\hat{I}_k$ operators of the nuclear spin projection I:

$$Q_{ik} = \frac{eQ}{2I(2I-1)}\left[\frac{3}{2}\left(\hat{I}_i\hat{I}_k + \hat{I}_k\hat{I}_i\right) - \hat{I}\left(\hat{I}+1\right)\delta_{ik}\right].$$

(1.14)

The value of Q_{zz} when the nucleus is in the state m = I is conventionally called the nuclear quadrupole moment
eQ = <I,I $\mid Q_{zz} \mid$ I,I>. The EFG tensor in the principal axes, taking into account LaPlace's equation is determined by the two independent parameters. Firstly, φ_{zz} , commonly called "the electric field gradient" or "the principal component of the electric field gradient tensor" and sometimes denoted as

φ_{zz} = eq; secondly, by η = $(\varphi_{xx}$ - $\varphi_{yy})/ \varphi_{zz}$,called the "asymmetry parameter", the axes being chosen such that $|\varphi_{zz}|$ > $|\varphi_{xx}|$ > $|\varphi_{yy}|$ with $0 \le \eta < 1$. The Hamiltonian of the electric quadrupole interaction for the nucleus (with quadrupole moment Q and spin I) may be written as

$$H'_Q = \frac{e\varphi_{zz}Q}{4I(2I-1)}\left[3\hat{I}_z^2 - \hat{I}(\hat{I}+1) + \frac{\eta}{2}\left(\hat{I}_+^2 + \hat{I}_-^2\right)\right],$$ (1.15)

where the shift operators $\hat{I}_\pm$ are introduced by usual relations $I_\pm = I_x \pm iI_y$.

In Mössbauer spectroscopy it is necessary to evaluate the eigen values of the H'_Q Hamiltonian, that is the energies E_Q^m for the ground state and for the excited state, the transition from which is followed by the emission of a Mössbauer γ–quantum (see Fig. 1.1c). The line positions in Mössbauer spectra are determined by the eigenvalues of the sum Hamiltonian H_Q for the nucleus in excited and ground states in the source and absorber, i.e. both δ-value and E_Q^m. The intensity of the lines which provide valuable information on the structure of the surface layers are determined by the eigenvectors of H_Q' Hamiltonian [1.10].

For the axially symmetric EFG tensor $(\eta = 0)$ the degeneracy of the nuclear energy levels is not completely split, and the energy depends only on the absolute value of the spin projection. The energy level displacement is given by the following expression:

$$E_Q^m = \frac{e\varphi_{zz}Q}{4I(2I-1)}\left[3m^2 - I(I+1)\right] ,$$ (1.16)

where m is the value of the spin projection onto the quantization axis. For $\eta \ne 0$, the E_Q^m values may be found by solving a secular equation which has no general analytical solution for I > 2. Hence line intensities and their positions can only be obtained by numerical methods.

For non-textured polycrystalline samples which do not show the Goldanskii-Karyagin effect or relaxation, the quadrupole interaction described by H'_Q does not shift the centre of gravity of the spectrum $\sum_{m=1}^{I} E_Q^m = 0$, that is, the quadrupole
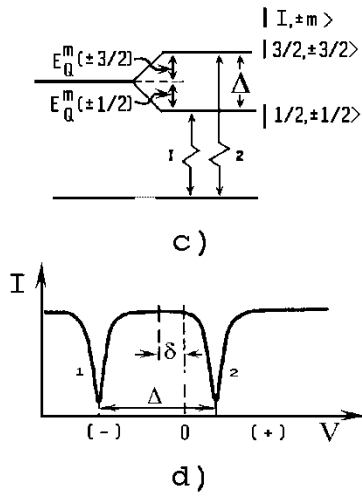
Fig. 1.1c, d The splitting of the excited level of a ^{57}Fe nucleus due to electric quadrupole interaction - (c) and the corresponding Mössbauer spectrum - (d).

interaction conserves energy. For the levels with I = 0 and I = 1/2, the quadrupole interaction energy is zero, since Q = 0. If the nuclear spin is half integral, the quadrupole interaction will cause the levels to be at least two-fold degenerate. If the spin values are integral the level degeneracy for $\eta \neq 0$ may be completely lifted.

Of special interest in Mössbauer spectroscopy are the transitions between states with spin quantum numbers I = 1/2 and I = 3/2. This is the case for ^{57}Fe, ^{119}Sn, ^{125}Te and many other nuclides. The spectra consist of two lines, the distance between them being equal to:

$$\Delta = \frac{|e\varphi_{zz}Q|}{2}\left[1+\eta^2/3\right]^{1/2} .$$

(1.17)

The EFG tensor parameters which are obtained depend on the point group for the nucleus in question rather than on the space group of the entire lattice. However, once the space group and the lattice positions are known, one can determine the point group for all sites by reference to the International Tables for X-ray Crystallography [1.11]. Following to Sternheimer, two primary sources of the EFG may be identified. Firstly, charges on ions surrounding the nucleus

(provided the symmetry of the surroundings is lower than cubic), and secondly, the unfilled valence shells (since filled shells possess a spherically symmetric charge distribution). For free atoms or ions electrons of the unfilled shells do not contribute to the EFG at the nucleus, since the corresponding electronic states are degenerate. If the atom is in a crystal lattice, a component of the EFG at the nucleus $(\varphi_{zz})_{lat}$ may also be evaluated which is caused by the surrounding ions. The actual EFG at the nucleus is determined by the extent to which the electronic structure of the Mössbauer atom is distorted by electrostatic interactions with external charges. This leads to the so-called "antishielding" effect, which is described by $1 - \gamma_\infty$. For iron compounds $\gamma_\infty \cong 10$. The EFG due to electrons in the unfilled shells $(\varphi_{zz})_{val}$ causes the polarization of the inner filled shells which leads to the appearance of an induced EFG of the opposite sign. This is known as shielding and the shielding effect is taken into account by using the R factor which is equal to 0.25 - 0.30 for iron compounds. The resulting EFG at the nucleus of an ion in a solid may be represented as

$$\varphi_{zz} = (1 - R) \ (\varphi_{zz})_{val} + (1 - \gamma_\infty) \ (\varphi_{zz})_{lat} \ . \tag{1.18}$$

Usually $(\varphi_{zz})_{val} \gg (\varphi_{zz})_{lat}$. At low values of the γ_∞ factor, the crystal field contribution to the EFG at the nucleus amounts to the electronic term splitting, which in its turn leads to the appearance of $(\varphi_{zz})_{val}$.

The Hamiltonian for the interaction of the magnetic dipole moment of a nucleus with the effective magnetic field $\underline{H}_{eff}$ acting on it may be written

$$H_M = -g_I \ \mu_n \ \underline{I} \ \underline{H}_{eff} \ , \tag{1.19}$$

where μ_n is the nuclear magneton, g_I is the gyromagnetic ratio, $\underline{I}$ is the nuclear spin operator (the quantization axis coincides here with the direction of $\underline{H}_{eff}$). The degeneracy of the nuclear levels is completely split. Figure 1.3 depicts the splitting of the nuclear energy levels and the corresponding Mössbauer spectrum. The shift of the levels is determined by the expression

$$E_M^m = -g_I \ \mu_n \ m \ H_{eff} \tag{1.20}$$

The number of lines in a spectrum is given by the selection rules for the given transition multipolarity. In ^{57}Fe, where the transition multipolarity of interest is M1, $m_e - m_g = 0, \pm 1$, and out of eight possible transitions in H_{eff} only six are present

(Fig. 1.3a).
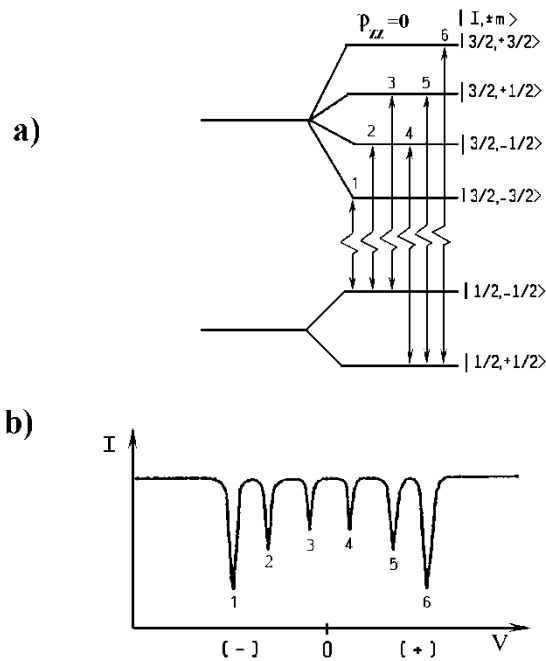
Fig. 1.3a, b Effect of the magnetic dipole interaction on energy level splitting in ^{57}Fe: a) energy level diagram in the field $H_{eff} \neq 0$, $\varphi_{zz} = 0$; b) corresponding Mössbauer spectrum.

The contributions to the effective magnetic field in, for example, iron alloys arise from:
    (i) The Fermi contact field:

$$\underline{H}_c = \frac{8}{3} \pi \mu_B \sum_s \left\{ \left| \psi_\uparrow^s(0) \right|^2 - \left| \psi_\downarrow^s(0) \right|^2 \right\} , \tag{1.21}$$

where μ_B is the Bohr magneton. The summation of the spin-up and spin-down densities at the nucleus is over all filled s- shells of the atom. The polarization of the filled s-shells of the atom caused by the exchange coupling of these s-electrons in magnetically ordered compounds of 3d-elements, results in the appearance of a magnetic field at the nucleus with the direction of the field being opposite to the atomic magnetic moment. In α-Fe such spin polarization of the ion core results in H_c = - (35.0 - 38.0) Tesla.
  (ii) The magnetic coupling between the nuclear spin I and

the orbital momentum L of electrons of the atom, when the LS- coupling occurs:

$$\underline{H}_L = -2\mu_B <1/r^3><\underline{L}> \; , \tag{1.22}$$

where the angular brackets denote averaging. For $\alpha-Fe$ the H_L contribution is (+5.0 ÷ +7.0) Tesla.

(iii) The direct contribution of the atom's magnetic moment $\underline{S}$ μ_B:

$$\underline{H}_D = -2\mu_B < \frac{3r(\underline{S}\,r)}{r^5} - \frac{S}{r^3} > \; , \tag{1.23}$$

which corresponds to the classical dipolar interaction with the nuclear magnetic moment. This contribution is zero for an ideal cubic lattice.

(iv) The externally applied magnetic field H_o which gives rise to Lorentz and demagnetizing fields, the total field upon saturation being in the order of 1.0 Tesla.

(v) The dipole field H_d produced by the resulting moment of 3d-electrons of neighbour atoms. H_d does not usually exceed 1.0 Tesla. In the cubic lattice of $\alpha-Fe$ H_d is zero since the fields of neighbouring atoms are quenched.

(vi) The field resulting from the contact interaction of the nuclear magnetic moment with the field of 4s-conduction which is also polarized by the total spin of 3d-electrons. The evaluation of the contribution of the 4s-conduction electrons is the most uncertain.

It is very often that all the three interactions i.e. the electric monopole-, magnetic dipole- and electric quadrupole- interaction occur simultaneously. In terms of the principal axis of the EFG tensor the Hamiltonian of the combined interaction may be written

$$H = \frac{eQ\varphi_{zz}}{4I(2I-1)}\left[3\hat{I}_z^2 - \hat{I}(\hat{I}+1) + \eta/2(\hat{I}_+^2 + \hat{I}_-^2)\right] -$$

$$g_I\mu_n H_{eff}\left[I_z\cos\theta + \frac{1}{2}(\hat{I}_+ + \hat{I}_-)\sin\theta\cos\theta + \frac{1}{2i}(\hat{I}_+ - \hat{I}_-)\sin\theta\sin\varphi\right] \tag{1.24}$$

where $\theta,$ φ are the polar and azimuthal angles specifying the magnetic field direction acting on the nucleus in the chosen axes system. If the quadrupole interaction is small as compared with the magnetic interaction ($E_Q^m << E_Q^m$), a correction to the interaction energy may be applied using the first-order perturbation theory for a nondegenerate spectrum. For the case of an axially symmetric EFG tensor ($\eta = 0$) the level positions are given by the following expression:

$$E_M^m = -g_I \mu_n m H_{eff} + \frac{eQ\varphi_{zz}}{4I(2I-1)}\left[3m^2 - I(I+1)\right]\frac{3\cos^2\theta - 1}{2} \tag{1.25}$$

The splitting of the energy levels and the corresponding Mössbauer spectrum are shown in Fig. 4 a and b. If the z-axis
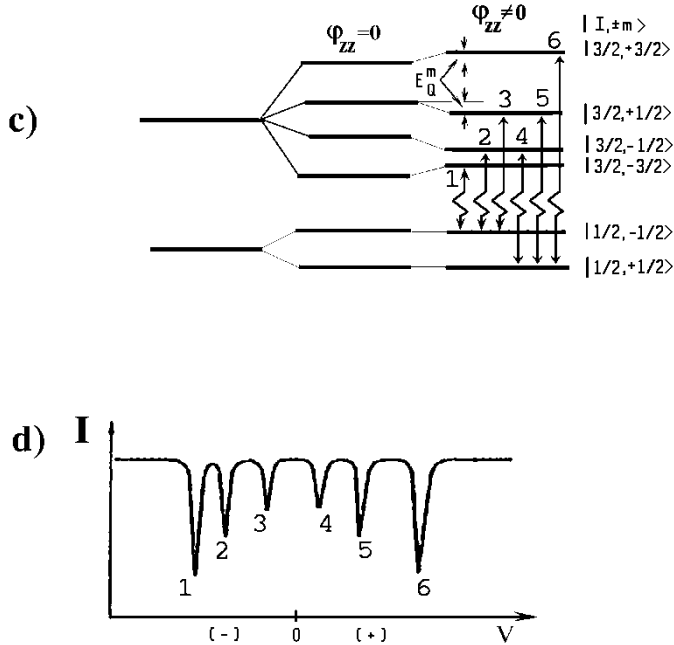
Fig. 1.3c, d. c) Energy level splitting diagram with combined hyperfine interactions (E_Q^m << E_M^m) for ^{57}Fe; d) corresponding Mössbauer spectrum.

of the axially symmetric EFG is parallel to the magnetic field ($\theta = 0$), the hyperfine structure is described by (1.25).

It follows from expression (1.25) that equidistant sublevels are shifted due to the quadrupole interaction. Provided φ_{zz} is positive the sublevels |3/2, ±3/2> shown in Fig. 1.3c are shifted by an amount $E_Q^m = \Delta/2$ to higher energies

and the sublevels |3/2, ±1/2> are shifted to lower energies. The sublevels are not equidistant. This results in an asymmetric magnetically split Mössbauer spectrum as depicted in Fig. 1.3d. For the more general case there is a dependence of the sublevels shift on the angle θ.

It is necessary to distinguish the proper constant of the quadrupole interaction $\Delta = eQ\varphi_{zz}/2$ for a nucleus in the state with the spin I = 3/2 from the constant $\Delta(\theta) = \Delta(3\cos^2\theta - 1)/2$ which is directly obtainable from the Mössbauer spectrum (see (1.25)). If $E_Q^m \sim E_M^m$, $\eta = 0$ and $\theta \neq 0$ then due to the operators $I_\pm$ and $I_\pm^2$ in the Hamiltonian (1.24) the wave-functions φ_m describing a nuclear state with a definite spin projection m into the z-axis are not the eigen-function of that Hamiltonian. The wave functions of the nuclear state with energies given by the roots of the secular equation

$$\text{Det} (H_{mm'} - \mathcal{E}\, \delta_{mm'}) = 0 \qquad\qquad (1.26)$$

will be a superposition of φ_m functions at different m ($H_{mm'}$ is the matrix element of the Hamiltonian H). The superposition will cause the relative line intensities of the Mössbauer spectrum to be different from these characterizing a pure magnetic interaction. This effect may also give rise to the appearance of additional lines in the Mössbauer spectrum.

1.3. Relative Intensities of Spectral Lines

The previous sections have presented a discussion of the hyperfine interaction parameters and the Mössbauer effect probabilities f (f') which enable the characterization of compounds and phases. These factors determine the line positions in the spectrum and the total area under the spectrum. In Mössbauer spectroscopy the line shape for atoms in definite positions and in the absence of relaxation phenomena is of Lorentzian form. The relative line intensities in the spectrum of a given phase and the radiation polarization also convey important information on the properties of the sample under examination. The correct interpretation of the experimentally observed intensity ratios gives information on the macroscopic structure of the sample, i.e. its spin texture. In the case of poorly resolved spectra recorded from textured samples, an incorrect account of line intensity ratios may lead to errors in the determination of hyperfine parameters and thereby to incorrect analysis of the data.

In the absence of relaxation effects and saturation arising from finite sample thickness, the intensity of a spectral component is determined by the nuclear transition characteristics (see Fig. 1.1d and 1.3). The most important of these are the spin and the parity of the excited and ground

states of the Mössbauer nuclei, the multipolarity of the transition, and the direction of the wave vector $\underline{k}$ of the γ-quanta emitted with respect to a chosen direction which is specified, for example, by the magnetic field or by the electric field gradient which causes the nuclear level degeneracy to be lifted.

This may be considered in terms of the expressions which determine the Mössbauer transition intensities for ^{57}Fe (the magnetic dipole transition M1). The probability P of the occurrence of a nuclear transition of multipolarity M1 from a state $|I_e m_e>$ to a state $|I_g m_g>$, equals

$$P(I_g m_g 1M, I_e m_e ; \theta, \phi) = |G(m_e, m_g)|^2 F_L^M (\theta, \phi) |<I_g||1||I_e>|^2, \tag{1.27}$$

where θ, ϕ are the polar and azimuthal angles determining the direction of emitted γ-quanta in the coordinate system defined by the magnetic field direction, $M = m_e - m_g$; $G(m_e, m_g) = <I_g m_g LM | I_e m_e>$, are the Clebsh-Gordan coefficients; $<I_g||1||I_e>$ is the reduced matrix element which does not depend
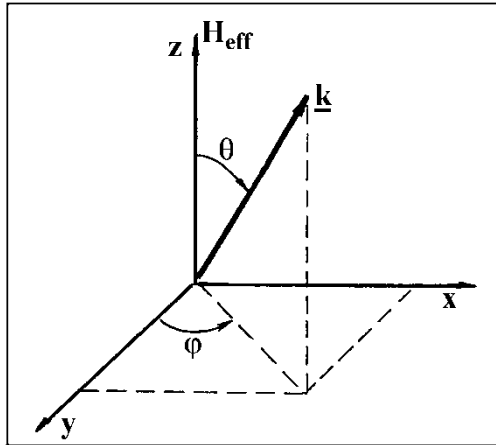
Fig. 1.4 Polar angles θ and ϕ, defining the wave vector $\underline{k}$ of the emitted γ-quantum. The quantization axis z is parallel to H_{eff}.

on the quantum numbers m_g, m_e. The angular function $F_L^M(\theta, \phi)$ is determined only by the transition multipolarity. The intensity

of the Mössbauer line is proportional to the product of the Clebsh-Gordan coefficients and the $F_L{}^M(\theta,\varphi)$ functions. The information for M1 (L = 1) and E2 (L = 2) transitions (which are of special interest in Mössbauer spectroscopy) and which occur between levels with I_e = 3/2 and I_g = 1/2 is given in [1.3].

Situations in which the purely magnetic hyperfine splitting of nuclear levels in the sample or the axially symmetric EFG tensor (η = O) correspond to radiation from an axially- symmetric oriented initial state. For an unpolarized axially symmetric source the angular distribution of I_i of the Mössbauer spectral components takes the following form:
(a) for the electric quadrupole interaction:

```
I₁(θ)  (±3/2 → ±1/2)  = 3/2 (1 + cos²θ)
I₂(θ)  (±1/2 → ±3/2)  = 1/2 (5 - 3 cos²θ)                    (1.28)
```

(b) for the magnetic dipole interaction:

```
I₁(θ) (+3/2 → +1/2)  = I₆(θ) (-3/2 → -1/2)  = 9/4(1 + cos²θ)
I₂(θ) (+1/2 → +1/2)  = I₅(θ) (-1/2 → -1/2)  = 3 sin²θ          (1.29)
I₃(θ) (-1/2 → +1/2)  = I₄(θ) (+1/2 → -1/2)  = 3/4(1 + cos²θ)
```

The corresponding plots of angular dependence of the intensities of the spectral components are given in Fig. 1.5. Equations (1.28) and (1.29) should be obeyed for nonpolarized source and a thin single crystal absorber if the isotropic factor f does not depend on θ. By these equations the direction of the magnetic field $\underline{H}_{eff}$ or of the EFG axes may be determined.

For an ideal thin single crystal the line intensity ratio for the electric quadrupole interaction (η = 0) is

$$R_g = \frac{I_1}{I_2} = \frac{1 + \cos^2\theta}{5/3 - \cos^2\theta} \cdot \qquad (1.30)$$

For the magnetic dipole interaction:

$$R_m = \frac{I_{2,5}}{I_{3,4}} = \frac{4(1 - \cos^2\theta)}{1 + \cos^2\theta}, \qquad (1.31)$$

The situation is more complicated if both the magnetic dipole-
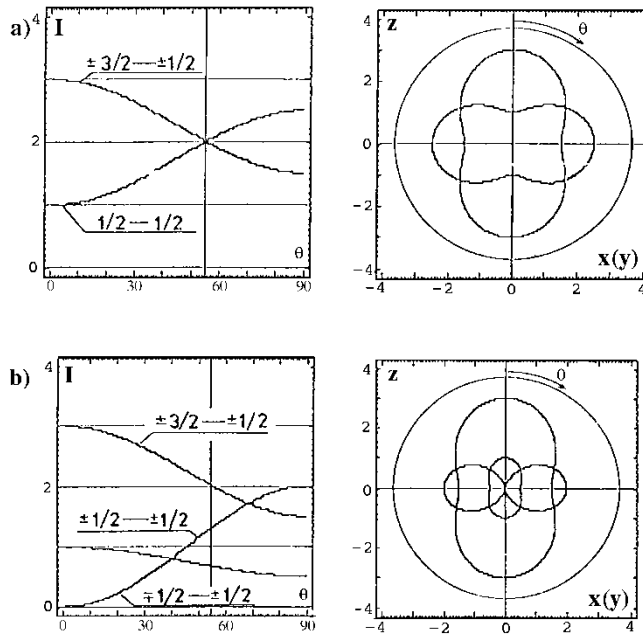
Fig. 1.5 Angular dependences of relative intensities of the hyperfine structure components for the I_e = 3/2, I_g = 1/2 transition in ^{57}Fe: a) for electric quadrupole interaction, η = 0, the quantization axis is the direction of the principal EFG axis, b) for magnetic dipole interaction, the quantization axis is the direction of H_{eff}, θ is the angle between the radiation direction and the quantization axis.

and electric quadrupole-interactions are present. For a polycrystalline absorber with a random orientation of crystallites with a cubic symmetry the intensity ratios are described by R_g = 1, R_m = 2, as a result of averaging over all directions.

The effect of anisotropy of atomic vibrations in solids causes not only the Mössbauer effect probability f to be anisotropic in single crystals, but may also lead to anisotropy in f for non-textured polycrystalline samples consisting of

randomly oriented crystallites. Such anisotropy in polycrystallites caused the values R_g and R_m to deviate from those described above. Similar deviations may be caused by texture, that is by a preferred orientation of crystals in a polycrystalline sample. To identify the origin of line asymmetry in a spectrum of polycrystallites as a result of either texture or the Goldanskii-Karyagin effect it is necessary to evaluate the effect of each of these phenomena on the Mössbauer spectra. Since the study of spin texture is described in detail in Sect. 5.3, only the Goldanskii-Karyagin effect is considered at this stage.

The expression for the Mössbauer effect probability (1.3) can be rewritten in the following form:

$$f = \exp(-<(\underline{k}\ \underline{u})^2>) , \tag{1.32}$$

where $\underline{k}$ is the wave factor of the incident γ-quanta; $\underline{u}$ is the displacement vector of an atom from its equilibrium position. Although the crystal here is anisotropic we assume, as before, that the Debye model is appropriate, and that there is a certain characteristic temperature Θ_D which is analogous to the Debye temperature. The exponent of (1.32) may be written as a function of polar angles θ and φ :

$$<(\underline{k},\underline{u})^2> = k^2 \left[(\overline{x^2}\cos^2\varphi + \overline{y^2}\sin^2\varphi)\sin^2\theta + \overline{z^2}\cos^2\theta \right] .$$

For the axially symmetric factor f, that is, if $x^2 = y^2$:

$$f(\theta) = \exp(-k^2\overline{x^2}) \exp(-a \cos^2\theta) , \tag{1.33}$$

where $a = k^2\left(\overline{z^2} - \overline{x^2}\right)$ is a certain real; $\overline{x^2}$ and $\overline{z^2}$ are the mean square amplitudes of the atomic vibrations which are parallel and normal to the principal EFG axis or to H_{eff} . When the electric quadrupole interaction $\eta = 0$ for a polycrystalline absorber with a random orientation of crystallites with an anisotropic factor f, $R_g \neq 1$ and is written

$$R_g = \frac{\displaystyle\int_0^\pi (1 + \cos^2\theta) \exp(-a \cos^2\theta) \sin\theta\, d\theta}{\displaystyle\int_0^\pi (5/3 - \cos^2\theta) \exp(-a \cos^2\theta) \sin\theta\, d\theta} , \tag{1.34}$$

when analyzing the experimental data it is often convenient to examine the dependence of R_g on the W_x- or W_z-parameters, which are characteristic of anisotropy of atomic vibrations in a lattice:

$$W_x = \frac{\overline{z^2}}{\overline{x^2}} = 1 + \frac{a}{k^2 \overline{x^2}} \quad , \quad W_z = \frac{\overline{x^2}}{\overline{z^2}} = 1 - \frac{a}{k^2 \overline{z^2}} \quad . \quad (1.35)$$

Suppose that a crystal whose $\Theta = 300$ K, is at room temperature. For ^{57}Fe (k = 7.28 Å) hence $\overline{x^2}$ = 8.76 10^{-3} Å^2 corresponds to the Debye temperature.

Following to [1.12] it is possible to consider a situation when the crystal is not axially isotropic $\left(\overline{x^2} = \overline{y^2} \neq \overline{z^2} \right)$. In this case $k^2 \overline{x^2} = 0.465$ and R_g values may be described by the parameter W_x. The requirement of $W_x > 0$ limits the allowed values of parameter "a" in expression (1.33) to a ≥ -0.465. Value of a < -0.465 may be realized only in terms of another model for the vibration spectrum, which is described by the parameter W_z. In this situation $k^2 \overline{z^2}$ = 0.465 and the experimentally observed R_g values are determined by the parameter W_z.

The R_g values found at room temperature and evaluated as functions of $W_x(W_z)$ for solids with characteristic temperatures of 200, 300 and 400 K are shown in Fig.1.6 a. Each curve in Fig. 1.6 corresponds to a family of crystal lattices of the same characteristic temperature but of different anisotropy. If $\overline{x^2} = 2\overline{z^2}$, then two cases are possible in which W_x= 0.5, or W_z = 2 each having its own a-value (1.33). For the characteristic temperature of 300 K R_g equals either 1.053 or 1.067 for the two cases. From Fig. 1.6 it follows that increasing the sample temperature (or decreasing Θ) causes an increase to be observed in the line asymmetry. In the case of the magnetic hyperfine splitting the anisotropy of the f factor may also manifest itself in a deviation of the line intensities ratio from R_m = 2. The room temperature dependence R_m on $W_x(W_z)$ for polycrystalline samples with characteristic temperature of 200, 300, and 400 K is shown in Fig. 1.6b.

Fig. 1.6 a. Dependences of the line intensity ratios (at room temperature) - R_g on the ratio of the mean square displacements W_x (W_z) or the parameter $a = k^2\left(\overline{r_z^2} - \overline{r_x^2}\right)$.
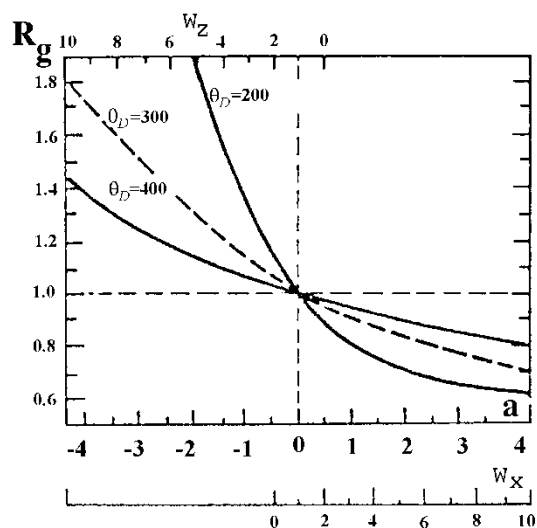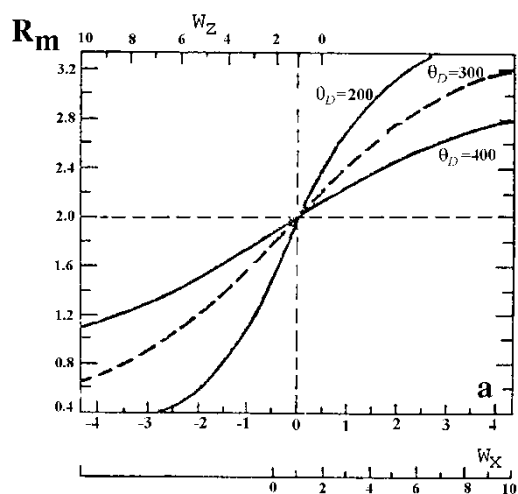

Fig. 1.6b Dependences of the line intensity ratios (at room temperature) - R_m on the ratio of the mean square displacements W_x (W_z) or the parameter a.

Hence, to observe the factor-f anisotropy a mechanically isotropic polycrystalline sample should be used. For such a sample the intensity ratios of the components in the Mössbauer spectra will not depend on the angle between the incident direction and the surface of the sample. The observation of such a dependence reflects texture effects. It should be noted that Mössbauer spectroscopy is sometimes the only experimental method suitable for the study of texture. A quantitative examination of spin texture requires the investigation of the effect of the anisotropy of the f-factor on the Mössbauer spectra.

1.4. Experimental

It is important to consider some problems which are associated with the Mössbauer experiment. To observe the Mössbauer effect and to obtain a spectrum the radiation from a Mössbauer source should be directed onto the sample under study. The Mössbauer spectrum is a measure of the dependence of the total intensity of radiation $I(v)$ registered by a detector in a definite energy region on the relative velocity v of the source.

A schematic diagram of a Mössbauer experiment and the spectrum is shown in Fig. 1.7 [1.3]. If both the source and the absorber are characterized by single lines of natural width Γ_{nat}, δ being zero the spectrum will show maximum absorption at $v = 0$. In this situation the resonant absorption of the γ-quanta is maximized, and the intensity ($I(0)$) registered by the detector is minimized (Fig. 1.7c). When the source moves at a certain velocity v, the emission line $J_M(E)$ is displaced relative to the absorption line $J^a(E)$. The overlap then decreases and the intensity registered by the detector increases. Finally, at a certain velocity, which may be considered to be infinitely large ($v = \infty$), the spectrum overlap becomes so small that any further increase in velocity will not result in a significant increase in relative intensity. This value of intensity may be described as $I(\infty)$. The fact that the line shapes of the source and absorber are described by Lorentzians causes the experimentally observed line for a thin absorber to be Lorentzian, and its half-height width is the sum of the line widths of the source and the absorber.

A typical device for accumulating the Mössbauer spectrum is the multichannel analyzer (MCA) where the count rate is a function of the channel number of MCA. Each channel corresponds to the energy of the γ-quanta with a definite (and often equal) dwell time for the accumulation of information. The count rate is normalized relative to the off-resonance count rate. Hence, for transmission mode Mössbauer spectroscopy relative intensities are always less than one (or 100%). In Mössbauer scattering experiments relative intensities always exceed 100% and can reach several hundred percent in the case of electron detection from
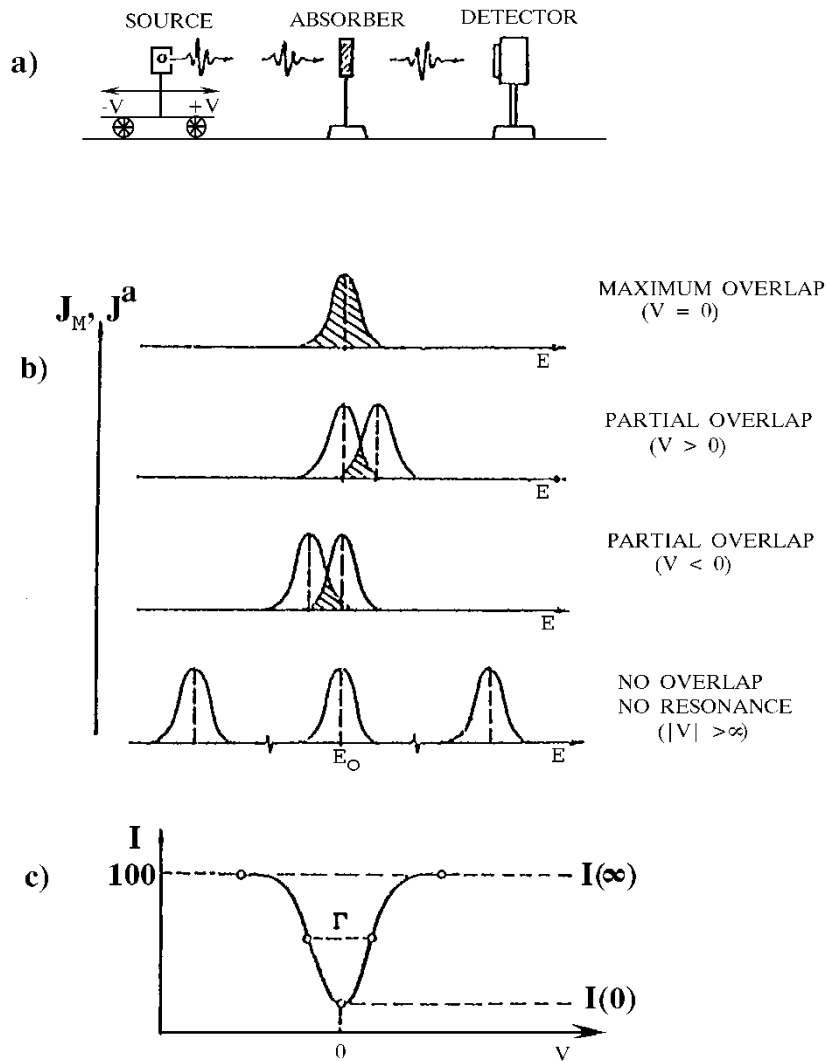
Fig. 1.7 Schematic illustration of the experimental arrangement (a), used to obtain a Mössbauer spectrum (c) for a single Lorentzian line both in the source and in the absorber (b).

samples with a high abundance of the resonant isotope. Each channel number corresponds to a definite value of the Doppler velocity. It is most often that the $-v_{max}$ value corresponds to the first channel and the $+v_{max}$ value to the last (N-th) channel. The velocity increment $\Delta v = 2v_{max}/N$ then corresponds to one channel.

The quality of a Mössbauer spectrometer is determined by how accurately the modulation of the γ-quanta energy follows

the chosen mode of movement e.g. sine or triangle. This modulation is primarily determined by the movement of a vibrating plunger which causes the source to move at a velocity v relative to the absorber. The v values should exactly correspond to the channel number of the accumulating device. Usually for the v(t) function one of the periodic laws of movement is used (Fig.1.8).
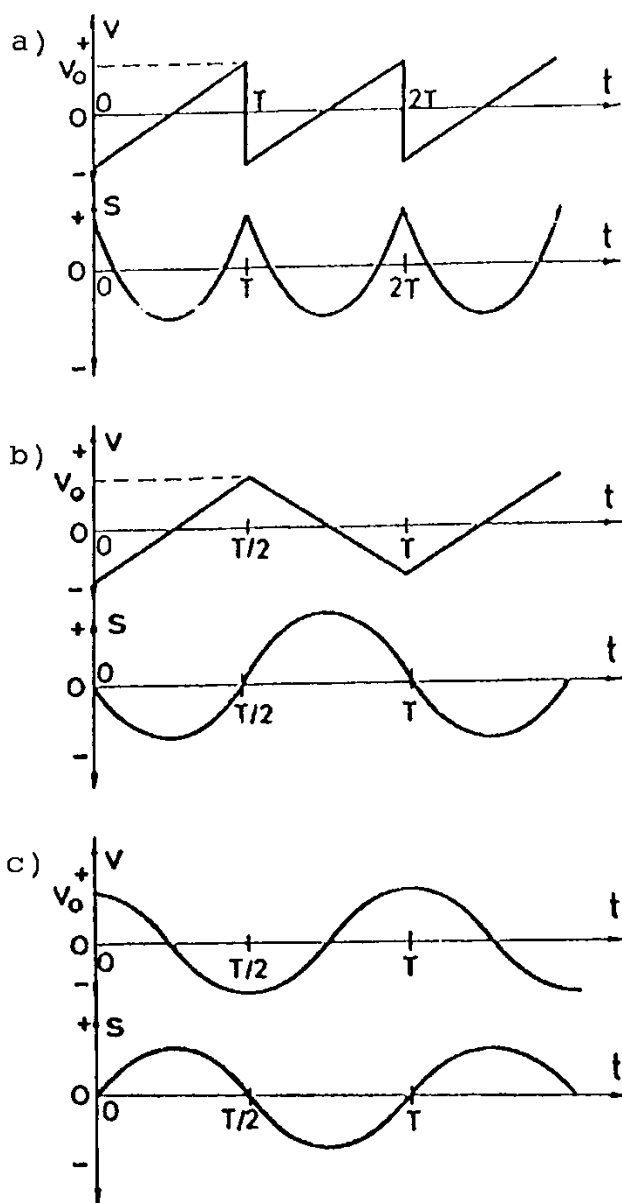
Fig.1.8 Velocity v and position s of the vibrating plunger of a Mössbauer spectrometer: a) parabolic movement, b) double parabolic movement, c) sine movement.

In parabolic movement the velocity change is with period T, following the saw tooth law. For practical reasons this law of movement is the most convenient although the vibrating plunger is hardly able to drive in such a fashion. Indeed, from the expansion of the velocity signal in the Fourier series

$$v(t) = \frac{2v_O}{\pi} \sum_{k=1}^{\infty} \frac{(-1)^{2k+1}}{k} \sin \frac{2k\pi t}{T}$$

where v_O - is the maximum velocity value, it is seen that a large number of harmonics are needed to be reproduced without distortion. Furthermore, the corrections are difficult to make for the various geometry effects that may lead to substantial distortions of the observed spectrum.

Double parabolic movement allows the avoidance of the geometry effects by permitting the convolution of the two resulting mirror spectra. It is then easier to achieve linearity here over the entire range of the velocities since the movement is represented by a smaller number of harmonics. If for the parabolic movement the amplitude ratio of the first harmonic to that of the third is 3, double parabolic movement gives a ratio of 25. This is very desirable since for a better generation of the reference signal a deep negative feedback can be used. Phase shifts accumulated within the system including the vibrator may lead to the feedback becoming positive for the higher harmonics and this is a potential cause of self-excitation. It is evident that in this mode of velocity change a deeper negative feedback can be used to generate a more accurate reference signal generation. In addition, the double parabolic mode gives no pulse forces.

The sine movement is also often used when the reference signal contains only one harmonic. An exceptionally high quality for the entire system can be reached when working at the resonant frequency of the vibrator which in turn raises the vibrator power. A disadvantage of this mode is the nonlinear velocity scale of the Mössbauer spectrum. For the linear conversion a computer or a microprocessor can be used. A classical Mössbauer spectrometer consists of four parts: (i) the drive which controls the vibrator movement; (ii) the detector; (iii) a multichannel analyzer for spectra storage and for the drive unit control; (iv) a computer for mathematical evaluation of the stored spectra, and a device to get the information in a required form. A new generation of spectrometers are now available. The main difference between the first- and second- generation spectrometers is the use of a microprocessor and large scale integrated circuits (LSIC's) in the new equipment. Such development offers the following benefits: i) the use of a function generator in the driving device which enhances the capabilities of the spectrometer; ii) the substitution of the multichannel analyzer by a dedicated unit; iii) the use of a microprocessor instead of the computer to evaluate the Mössbauer spectra. When the Mössbauer spectrum is being recorded the γ-quanta

from a source interact with the sample. The main types of interaction with matter of γ-quanta in the energy range of interest are the photoelectric effect, the Compton effect, Rayleigh scattering and resonant scattering. The Mössbauer experiment may be in transmission mode, where γ-quanta are detected or be a scattering experiment where any radiation which follows the resonant scattering is detected. The typical experimental arrangements are presented in Fig.1.9.

In both types of experiments the probability of the effect f' can be evaluated from the observed resonance effect magnitude $\varepsilon(v)$. For transmission geometry $\varepsilon(v)$ is determined by the following relation:

$$\varepsilon(v) = \frac{I(\infty) - I(v)}{I(\infty)} . \qquad (1.36)$$

Of utmost interest are $\varepsilon(v)$ value at v_i (i = O, 1, ...), corresponding to the maxima of resonant scattering. For unsplit lines in both the source and absorber the intensity on resonance is I(0).

Expression (1.36) is true in the absence of background radiation. To evaluate the possible magnitude of the effect one needs to know the energies and relative intensities of various γ-quanta groups per 100 disintegrations of the parent nucleus, all the relevant cross sections for the γ-quanta interaction with matter, and the value of the f' parameter characterizing the recoilless γ-quanta in the sample under study. Theoretical considerations of the f' factor in transmission spectroscopy, including the contribution of various experimental conditions, have been given in [1.13-18]. Scattering experiments permit the detection of conversion electrons in addition to γ-rays, X-rays, Auger electrons and even photons which follow resonant scattering. An important advantage of scattering experiments is that they enable an estimate of the thickness of the layer of the substance under examination.

Mössbauer scattering spectra obtained by detection of the γ-quanta or X-rays emitted out of the bulk of a material, convey information on the layer with a depth which is determined by the total linear absorption coefficient $\mu(E)$. The values of $\mu(E)$ for γ-rays and X-rays are generally different, therefore the Mössbauer spectra correspond to the layers which are different in depth from one to several μm. The interaction of electromagnetic radiations with matter gives no correlation between the γ-quanta or X-ray energy and the depth of the layer through which they have passed. By ignoring any resonant re- scattering the direction of the resonantly scattered quanta may be considered unchanged up to the moment of their interaction with matter.

Mössbauer scattering spectra obtained by detection of conversion electrons or Auger electrons, provide information on substantially thinner layers. This type of spectroscopy is called Conversion Electron Mössbauer Spectroscopy (CEMS). There are definite relations between the energy of detected electrons and the depth of the layer through which they have passed. If
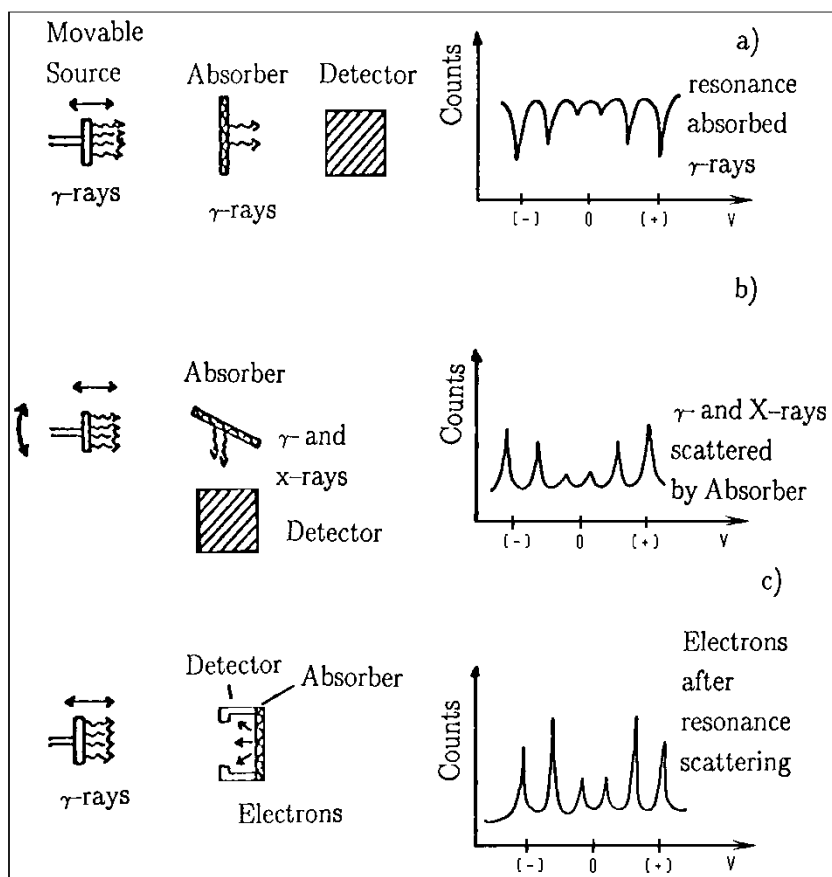
Fig.1.9 Experimental arrangements and Mössbauer spectra for a [57]Co (Cr) source and an absorber of α-Fe: a) transmission geometry, b) scattering geometry with the detection of γ- or X-rays, c) backscattering geometry with the detection of X-rays and electrons. 1. source at a velocity v , 2. sample, 3. detector.

these relations are used the depth selective analysis of the surface layers can be performed. The use of CEMS for quantitative measurements requires a good knowledge of the interaction of electrons with matter over an energy ranging from several hundred eV to several tens of keV. The problems encountered are extensively considered in [1.19-23], but so far there is no comprehensive theory of the interaction of such electrons with matter.

Although the Mössbauer effect is not observed for all elements (see Table 1.1) [1.24], for those which do have a Mössbauer active isotope such as iron, tin, dysprosium and many others, Mössbauer spectroscopy compares favorably as a versatile method by which important information can be obtained.

Table 1.1 Mössbauer periodic table.

References

1.1 G.K. Wertheim, Mössbauer Effect: Principles and Applications, Academic Press, New York, 1964.

1.2 V.I. Goldanskii, R. Herber (eds.), Chemical Applications of Mössbauer Spectroscopy, Academic Press, New York, 1968.

1.3 P. Gütlich, R. Link, A. Trautwein, Mössbauer Spectroscopy and Transition Metal Chemistry, Springer-Verlag, Berlin, 1978.

1.4 B.V. Thosar, I.K. Srivastava (eds.), Advances in Mössbauer Spectroscopy. Application to Physics, Chemistry..., Tata Institute of Fundam. Research, Bombay, India, 1983.

1.5 R.H. Herber (ed.), Chemical Mössbauer Spectroscopy, Plenum Press, New-York - London, 1982.

1.6 Gary J. Long (ed.), Mössbauer Spectroscopy Applied to Inorganic Chemistry, Plenum Press, New-York - London 1984, Vol.1; 1987, Vol.2 and 1989, Vol.3.

1.7 G.K. Horton, A.A. Maradudin (eds.), Dynamical Properties of Solids: Mössbauer Effect, Structural Phase Transitions, Vol. 5, Elsevier. Sci. Publ. B.V., Amsterdam.,1984.

1.8 G.K. Shenoy, F.E. Wagner (eds.), Mössbauer Isomer Shifts, North-Holl. Publ. Comp., 1978.

1.9 W.L. Gettys, J.G. Stevens, Mössbauer Isomer Shift, Mössbauer Effect Data Center, Asheville, 1979.

1.10 B.D. Dunlap, "An Introduction to Electric Quadrupole Interactions in Mössbauer Spectroscopy", in Mössbauer Effect Data Index, - Cover. the 1970 Literature, eds. J.G. Stevens, V.E. Stevens, IFI/Plenum, N.Y., 1972, pp.25-40.

1.11 International tables for X-ray Crystallography, eds. Henry N. F.M., Longsdale K., Kynoch Press, Birmingham, England, 1965.

1.12 H.D. Pfannes, U. Gonser, Appl. Physics 1 (1973) 93-102.

1.13 G.A. Bykov, Ph.Zuy Hien, Zh. Eksp. Teor. Fiz. 43 (1962) 909.

1.14 S.Margulies, P.Debrunner, H. Frauenfelder, Nucl. Instr. Meth., 21 (1963) 217-231.

1.15 R.M. Housley, N.E. Ericson, J.G. Dash, Nucl. Instr. Meth., 27 (1964) 29-37.

1.16 V.N. Belogurov, V.A. Bilinkin, Nucl. Instr. Meth., 175 (1980) 495-501.

1.17 G.J. Long, T.E. Cranshaw, G. Longworth, Mössb. Effect Ref. Data Journal., 6 (1983) 42-49.

1.18 P. Jernberg, Nucl. Instr. Meth. Phys. Res., B4 (1984) 412- 420.

1.19 R. Shimizu, Y.Kataoka, T. Matsukawa, T. Ikuta, K. Murata, H. Hashimoto, J. Phys. D: Appl. Phys., 8 (1975) 820-828.

1.20 D. Liljequist, J. Appl. Phys., 57 (1985) 657-665.

1.21 D. Liljequist, J. Phys. D: Appl. Phys., 16 (1983) 1567- 1582.

1.22 Yu.F. Babikova, O.M. Vakar, P.L. Gruzin, Yu.V. Petrikin, Izv. Vyssh. Uchebn. Zaved, Fiz., No 7 (1983) 10-14.

1.23 A.F. Akkerman, M.Ya. Grudskii, V.V. Smirnov, Secondary Electron Radiation from Solids Exposed to Photons, Energoatomizdat, Moscow, 1986.

1.24 J.G. Stevens, V.E. Stevens (eds.) Mössbauer Effect Data Index. Covering the 1976 Literature, IFI/Plenum, New York - Washington - London, 1978.

2. Mössbauer Spectroscopy Based on Detection of Electromagnetic Radiation

There are two types of Mössbauer spectroscopic experiments based on scattering and transmission techniques. Scattering Mössbauer experiments involve either the detection of resonantly scattered γ-quanta or other radiations which are emitted in the process of resonant scattering or immediately after it. The observed effect depends on the spectra of the scattered radiation, on the interaction of the radiation with matter and, to a greater extent than in transmission mode spectroscopy, it depends on the spectrometer design especially on the detector and its' position relative to the sample and the primary beam.

In transmission mode experiments the resonant scattering leads to the sharp attenuation of the radiation intensity registered by a detector, therefore it is sometimes referred to as resonant absorption. The resonant absorption cross section is the total cross section of resonant scattering; the probability of detecting the scattered radiation in transmission spectroscopy may be neglected when the geometrical arrangement is appropriate.

Classical transmission mode Mössbauer spectroscopy is sometimes used in studies of surface layers. Indeed, the analysis of Mössbauer spectra to date has been mainly based on the theory and techniques developed for transmission mode Mössbauer spectroscopy. These problems are dealt with in the first Section of this Chapter, thereafter a concept of scattering channels will be introduced and finally a classification will be given of low-energy γ-quanta scattering in solids. Resonance scattering channels are of prime interest in Mössbauer spectroscopy, hence it is necessary to introduce concepts of resonance fluorescence, coherence, interference and γ-γ correlations.

Based on all these, a theory can be developed of spectral shape and the energy distributions of incident and scattered radiation. Special attention will be paid to backscattering Mössbauer spectroscopy, which is the most promising technique for applied research and industrial applications. Problems of detector design, the evaluation of scattered intensities, and some experimental aspects are given in the last sections of the Chapter.

2.1. Radiation Transmission through Matter

Most surface studies by Mössbauer spectroscopy have been carried out with ^{57}Fe and ^{119}Sn nuclides. Most methodology problems for those isotopes have been successfully overcome, hence the information available for ^{57}Fe is frequently used in the considerations that follow.

 A diagram is given in Fig.2.1 of the nuclear transformations which produce ^{57}Fe. The ^{57}Mn nuclide decays by β^--emission with a half-life of 1.7 min. ^{57}Co nuclide also decays by electron capture (EC) with a half-life of 270 d to ^{57}Fe. The short half-life period of ^{57}Mn makes it practically impossible to use the nuclide in applied research. The Mössbauer 3/2 level with the probability $1/(1 + \alpha)$ decays by the 14.4 keV γ-quantum emission, where α is the total internal conversion coefficient. For the rest of the cases de-excitation of the nucleus is via the emission of conversion electrons followed by rearrangement of the excited atomic shell by X-ray emission and Auger processes. Considering that for approximately 88 cases out of 100, the ^{57}Co decay populates the 14.4 keV level a limiting value of 9.55 f Mössbauer quanta per 100 disintegrations of ^{57}Co can be obtained [1.24]. The number of the Mössbauer quanta cannot exceed 9.55f and is determined by the source material and the quality of its preparation. For further numerical evaluations ^{57}Co will be assumed to be in a rhodium matrix at room temperature and f = 0.77. The yields for γ-quanta of different energies for ^{57}Co , ^{57}Fe and ^{119}Sn nuclides are listed in Table 2.1. Table 2.2 gives the nuclear characteristics of interest for these Mössbauer nuclei.

$^{57}_{26}$Fe (14.4keV,136.5keV)
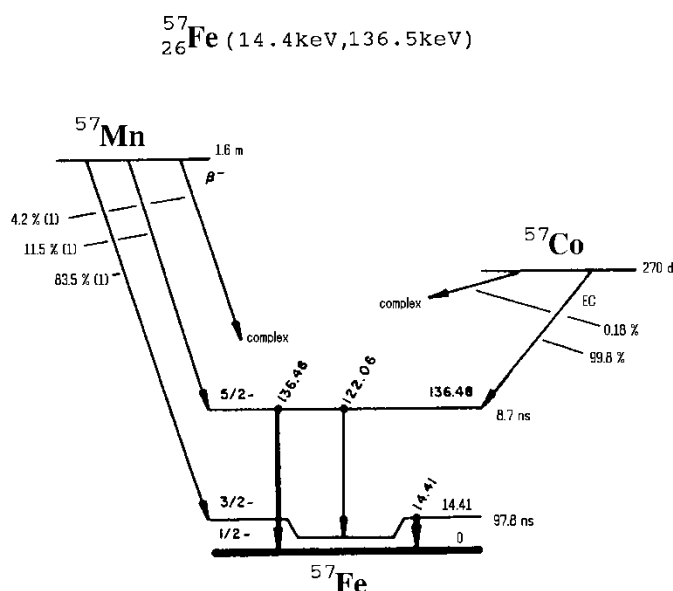
Fig.2.1 Decay scheme of ^{57}Fe and parent nuclei (from [1.24]).

Mössbauer sources are prepared by introducing the radioactive parent nuclei for the Mössbauer isotope into a substrate with a fairly perfect crystal structure. There are often several parent nuclides of the Mössbauer isotope, but one of them that is mostly used in practice.

Table 2.1   Energies and intensities of photons emitted after resonant excitation of the 14.4 keV state of ^{57}Fe, 23.8 keV state of ^{119}Sn and decay of ^{57}Co.

E KeV	Intensity* ^{57}Co	^{57}Fe	^{119}Sn
0.7 (L X-rays ^{57}Fe)		0.2	
3.6 (L X-rays ^{119}Sn)			5
6.47 (K X-rays ^{57}Fe)	54	26.3	
14.41	9.55	10.8	
23.87			16
122	85.6		
136	10.6		

* The intensities are given per 100 decays of the excited nuclear states.

Table 2.2   Nuclear data for the ground and first excited states of ^{57}Fe and ^{119}Sn.

	^{57}Fe Ground state	Excited state	^{119}Sn Ground state	Excited state
The γ-ray energies E (keV)	0	14.41	0	23.87
Half-life (10^{-6} sec)		0.098		0.178
Natural line width (neV) (mm×s^{-1})	0	4.66 (0.097)	0	25.8 (0.323)
Spin and parity	1/2-	3/2-	1/2+	3/2+
Quadrupole moment (10^{-24} cm^2)	0	+0.20	0	-0.064
Factor g	+0.181	-0.103	-2.09	+0.455
Total internal conversion coefficient		8.21		5.1
Natural isotopic abundance a (%)	2.14		8.58	

The observed effect is determined firstly by the interaction of Mössbauer quanta with matter. The γ-quanta interact not only with the sample under study, but also with the various construction materials used to make detection windows, cryostat windows, collimator and sample holders. The effect may be largely influenced by self-absorption in the source and the saturation absorption due to the finite thickness of the absorber. The correct evaluation of these effects is needed to select the optimum experimental conditions, such as sample and substrate thickness, source - absorber - detector distances and corresponding angles, and concentrations of Mössbauer isotopes in the source and absorber. The evaluation is necessary to carry out a phase analysis, and also to obtain a theoretical equation for the shape of the observed Mössbauer spectra. Some aspects of the passage of the Mössbauer radiation through matter and the dependence of spectrum shapes, line amplitudes and areas on the sample thickness and resonant isotope abundance are given below.

If the source is considered to be a cylinder of a unit cross section (see Fig.2.2), the number of parent radioactive
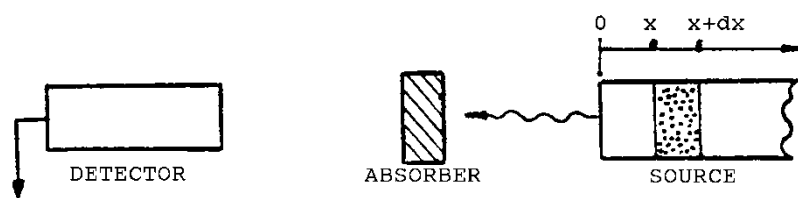
Fig.2.2 Self-absorption in a Mössbauer source.

nuclei for the Mössbauer isotope in a unit volume of the source n(x) is a function of x only. We can consider that the number of the Mössbauer nuclei in a unit volume of the source, n_s, is constant; f_s is the Mössbauer factor determining self-absorption in the source. If a volume element of a unit cross section with a coordinate x and the thickness dx is taken, the decay of n(x)dx radioactive nuclei produces a flux of γ-quanta dI(x) = Cn(x) dx in the direction close to normal to the source surface (C is a constant). The fraction (1 - f) of the disintegrations occurs with the energy transferred to the lattice, and the fraction f is recoilless. If the energy distribution of the corresponding radiations is $J_R(E)$ and $J_M(E)$, the following normalization conditions may be assumed:

$$\int_{-\infty}^{\infty} J_R(E)dE = 1-f \ ; \ \int_{-\infty}^{\infty} J_M(E)dE = f. \tag{2.1}$$

The particular dependence $J_R(E)$ is of no interest but it should be noted that the centre of gravity of this distribution is shifted by the amount of recoil energy E_R relative to the transition energy E_s in the source. The energy distribution of the Mössbauer γ-quanta $J_M(E)$ may be considered as Lorentzian $L(E)$ with the full half-width Γ such that $\Gamma = \Gamma_{nat}$. Due to the normalization conditions (2.1) $J_M(E)$ may be written as:

$$J_M(E) = \frac{f\Gamma_{nat}}{2} \frac{1}{(E - E_s)^2 + (\Gamma_{nat}/2)^2} = \frac{2f}{\pi\Gamma_{nat}} L(E) \qquad (2.2)$$

Radiation from the layer dx of the depth x of a Mössbauer source is described by the expression

$$dJ(E, x) = [J_R(E) + J_M(E)] e^{-\mu_s(E)x} dI(x), \qquad (2.3)$$

where

$$\mu_s(E) = \mu_s + \mu_{rs}(E) = \mu_s + n_s f_s \sigma_s'(E), \qquad (2.4)$$

and where $\mu_s(E)$ is the total linear extinction (absorption) coefficient for the source material, $\mu_{rs}(E)$ and $\sigma_s'(E)$ are the linear coefficient and cross section of γ-radiation resonant scattering in the source material, and μ_s is the nonresonant linear absorption coefficient. For a single-line source

$$\sigma_s(E) = \sigma_0 L_s(E), \quad \sigma_0 = 2\pi\lambda^2 \frac{2I_e + 1}{2I_g + 1} \frac{1}{1 + \alpha}, \qquad (2.5)$$

where σ_0 is the maximum cross section of the resonant interaction, λ is the wavelength of γ-radiation, and I_e, I_g are the nuclear spins for excited and ground states. In general, $L_s(E)$ differs from $L(E)$, however, for many sources such as ^{57}Co in Rh- or Cr-matrices they may be assumed to be equal. $L_s(E) = L(E)$. Then the energy distribution of γ-radiation from the source (2.3) needs to be integrated over x from 0 to ∞

$$J(E) = [J_R(E) + J_M(E)] C \int_0^\infty n(x) e^{-\mu_s(E)x} dx. \qquad (2.6)$$

If the source moves at a velocity v relative to the absorber, the energy distribution is determined by (2.2), where the L(E) Lorentzian is written as:

$$L(E,v) = \frac{\Gamma_{nat}^2/4}{(E - E_s - E_s v/c)^2 + \Gamma_{nat}^2/4} \quad,$$

$$L(E,S) = \frac{\Gamma_{nat}^2/4}{(E - E_s - S)^2 + \Gamma_{nat}^2/4} \quad,$$
(2.7)

$$L(E,\mathcal{E}) = \frac{\Gamma_{nat}^2/4}{(E - \mathcal{E})^2 + \Gamma_{nat}^2/4} \quad,$$

In the last expression the variable has been changed so that

$$\mathcal{E} = E_s + E_s v/c$$

Since it is always the relative velocity that is experimentally measured, v (the channel number) is usually given on the abscissa. In theoretical considerations the energy distributions of γ-quanta and intensities of detected radiations are often written as functions of energy E of incident γ-quanta and of parameter S. In theoretical aspects of scattering spectroscopy, especially for multilayer samples, the last of the three expressions (2.7) proves to be extremely useful. In this case the energy distribution of γ-quanta emitted by the moving source is treated as a function of the difference between the variable E, which takes on random values and has a Lorentzian distribution relative to the transition energy E_s and the energy parameter $\mathcal{E}$ which is determined by the spectrometer. To simplify the formulae the energies are usually taken in units of $\Gamma/2$. Since $\Delta E \gg \Gamma$, in usual transmission or scattering experiments, the detector is an effective integrator. Not only does it detect the Mössbauer recoil and recoilless quanta, it also detects the background radiation in the energy region which is incommensurably more than Γ_{nat}.

When the sample under study is placed between the source and the absorber of thickness d_a, the sample is characterized by the parameters E_a, $\sigma_a(E) = \sigma_r(E) + \sigma_a$, Γ_a, f', n_a, μ_a, the Lorentzian $L_a(E)$, where μ_a and σ_a are the linear absorption coefficient and the cross section for non-resonant interactions, respectively. The intensity of γ-quanta passed through the sample which gives the experimental Mössbauer spectrum is given by the following equation:

$$I(v,d_a) = \int\limits_{-\infty}^{\infty} J(E,v) \exp\left[-\mu_a d_a - L_a(E)t_a\right] dE \quad ; \qquad (2.8)$$

$$J(E,v) = C\left[J_R(E,v) + J_M(E,v)\right] \int\limits_{0}^{\infty} n(x) \exp\left[-\mu_s(E)x\right] dx \quad ;$$

$$t_a = \mu_r d_a = n_a f' \sigma_0 d_a \; .$$

where t_a is the effective thickness of the sample. It is used as frequently as the linear coefficient of resonant scattering or absorption $\mu_r(E)$ and its maximum value, μ_r without splitting, or μ_r^i at a velocity v_i for the split spectrum.

By use of (2.4), (2.8) and the effective thickness t_a an expression for $I(v,d_a)$ can be obtained:

$$I(v,d_a) = e^{-\mu_a d_a} C \left\{ \int\limits_{-\infty}^{\infty} J_R(E,v) e^{-L_a(E)t_a} dE \right.$$

$$\int\limits_{0}^{\infty} n(x) e^{-\mu_s x - L(E) t'(x)} dx + \int\limits_{-\infty}^{\infty} J_M(E,v) e^{-L_a(E)t_a} dE$$

$$\left. \int\limits_{0}^{\infty} n(x) e^{-\mu_s x - L(E) t'(x)} dx \right\} , \qquad (2.9)$$

where $t'(x) = n_s f_s \sigma_0 x$.

The evaluation of the integral in the first term of (2.9) over energy is based on the fact that the distance between the centres of gravity of the distribution $J_R(E,v)$, and of the resonant scattering cross section $\sigma_r(E)$, is equal to the recoil energy E_R. Since $E_R \gg \Gamma$, in the region where $\sigma_r \neq 0$, $J_R(E,v)$ is infinitesimal and the two exponents of the first term describing the resonant scattering are equal to unity. This means that the recoil radiation is virtually resonantly unscattered both in the source and the absorber. Using normalization conditions (2.1) and equation (2.2) and integrating over energy in the first term gives the expression (2.9) in the form:

$$I(v,d_a) = C\ e^{-\mu_a d}\left\{(1-f)\int_0^\infty n(x)\ e^{-\mu_s x}\ dx\right.$$

(2.10)

$$\left.+\frac{2\ f}{\pi\Gamma_{nat}}\int_{-\infty}^\infty e^{-L_a(E)t_a}\ L(E,v)\ dE\int_{-\infty}^\infty n(x)\ e^{-\mu_s x-L(E)t'(x)}\ dx\right\}.$$

This is the general expression for the intensity of γ-quanta emitted by the source and passed through a layer of thickness d_a. In transmission mode Mössbauer spectroscopy it is the $I(v,d_a)$ function that determines the line shape.

A source with a uniform distribution of radioactive nuclei: $n(x) = g_1$ if $0 \le x \le d_s$ and $n(x) = 0$ if $x > d_s$ must now be considered. Integrating (2.10) over x from 0 to d_s and dividing by Cg_1d_s gives the following expression

$$\frac{I(v,d_a)}{C\ g_1 d_s} = e^{-\mu_a d_a}\left\{(1-f)\frac{1-e^{-\mu_s d_s}}{\mu_s d_s}+\frac{2\ f}{\pi\Gamma_{nat}}\right.$$

(2.11)

$$\left.\int_{-\infty}^\infty \frac{e^{-L_a(E)t_a}\ L(E,v)}{\mu_s d_s + L(E)\ t'}\left[1-e^{-\mu_s d_s - L(E)\ t'}\right]dE\right\}.$$

If for the source of thickness d_s self-absorption is neglected, i.e. $n_s f'_s = 0$, then the intensity of radiation passing through a sample of thickness d_a may be written as:

$$\frac{I(v,d_a)}{C\ g_1 d_s} = \frac{e^{-\mu_a d_a}-e^{-(\mu_a d_a + \mu_s d_s)}}{\mu_s d_s}\left[(1-f)+\frac{f\Gamma_{nat}}{2\ \pi}\right.$$

$$\left.\int_{-\infty}^\infty \frac{e^{-L_a(E)t_a}\ dE}{(E-E_s-E_s v/c)^2+\Gamma_{nat}^2/4}\right].$$

(2.12)

This can be rewritten in the following form:

$$\frac{I(v,d_a)}{Cg_1d_s} = I_R(d_a) + I_M(v,d_a) \quad , \tag{2.13}$$

where $I_R(d_a)$ and $I_M(v,d_a)$ are the normalized intensities of recoil- and recoilless γ–quanta passed through the layer of thickness d_a. The $I_M(v,x)$ function is very important in scattering experiments. It determines the total intensity of γ-quanta which at a velocity v have reached a layer dx at a depth x. The resonant scattering of a part of this radiation in a layer dx results in emission of radiation from this layer. At $v \rightarrow \infty$, we can write

$$\lim_{v \rightarrow \infty} \frac{I(v,d_a)}{Cg_1d_s} = e^{-\mu_a d_a} \frac{1-e^{-\mu_s d_s}}{\mu_s d_s} \, . \tag{2.14}$$

It is evident from a comparison of (2.11) and (2.12) that instead of Lorentzian (2.7) and provided $\mu_s d_s \rightarrow 0$, self-absorption in the source allows the energy distribution of the emitted resonant γ-quanta to be described by the following

$$J_M^S(E,v) = \frac{f\Gamma_{nat}}{2\pi t'} \left[1 - e^{-L(E,v)t'} \right] \frac{L(E,v)}{L(E)} \, . \tag{2.15}$$

It is natural that for a thin source, i.e. when $t' \rightarrow 0$, the shape of the emission line should approach the Lorentzian. From now on it can be assumed that the source is thin, that the line is single and is a Lorentzian. Returning now to (1.36), by use of (2.12) and (2.14) we obtain:

$$\varepsilon(v) = \frac{f\,\Gamma_{nat}}{2\,\pi} \int_{-\infty}^{\infty} \frac{1}{(E - E_s - E_s\,v/c)^2 + \Gamma_{nat}^2/4}$$

$$\left[1 - e^{-L_a(E)t_a} \right] dE = \int_{-\infty}^{\infty} J_M(E,v) \left[1 - e^{-L_a(E)t_a} \right] dE \, . \tag{2.16}$$

If the resonant scattering cross section $\sigma_a(E)$, as well as $J_M(E,v)$, are characterized by a Lorentzian of natural width, $\Gamma = \Gamma_a = \Gamma_{nat}$, the maximum effect value (v = 0) is given by

$$\varepsilon(0) = f\left[1 - e^{-t_a/2} J_0(it_a/2)\right] = f\ p(t_a)\ , \qquad (2.17)$$

where J_0 is the Bessel function of zeroth order, $p(t_a)$ is the function which undergoes a fairly fast saturation on increasing t_a. Integral (2.16) cannot be given in an analytical form, however numerical calculations show that up to $t_a \sim 10$ it is closely approximated by a Lorentzian curve. Its width at half-height Γ_{exp} is a function of the absorber thickness:

$$\Gamma_{exp} = 2\ \Gamma_{nat}\ h(t_a)\ , \qquad (2.18)$$

where the function $h(t_a)$ may be written as:

$$h(t_a) = 1 + 0.135\ t_a \qquad\qquad \text{for } 0 \le t_a \le 4\ ,$$
$$\qquad\qquad (2.19)$$
$$h(t_a) = 1 + 0.145\ t_a - 0{,}0025\ t_a^2 \quad \text{for } 4 \le t_a \le 10.$$

Mössbauer nuclei in the absorber as well as in the source may be in slightly different conditions due to fluctuations of their local environment. This results in fluctuations of energy of the nuclear transition E_a in the absorber which causes the lines to broaden and change their shape. Nonetheless in many cases the lines may be described by Lorentzian curves whose widths are different from the natural ones:

$$J_M(E) = \frac{f\Gamma}{2\pi}\ \frac{1}{(E - E_s)^2 + \Gamma^2/4}\ , \qquad (2.20)$$

$$\sigma_a(E) = \sigma_0'\ \frac{\Gamma_a^2/4}{(E - E_a)^2 + \Gamma_a^2/4}\ , \qquad \Gamma \ne \Gamma_a > \Gamma_{nat}. \qquad (2.21)$$

A relation between σ_0' and σ_0 can be found since the area under the total absorption curve is the sum of individual absorption curves with natural widths. Since the area under a Lorentzian with the amplitude ε and the width Γ is $\pi\varepsilon\Gamma/2$, we may write $n\pi\sigma_0'\Gamma_a/2 = n\pi\sigma_0\Gamma_{nat}/2$, from which it follows that $\sigma_0' = \sigma_0\ \Gamma_{nat}/\Gamma_a$;

$$\sigma_a(E) = \sigma_0 \frac{\Gamma_{nat}}{\Gamma_a} \frac{\Gamma_a/4}{(E - E_a)^2 + \Gamma_a^2/4} = \sigma_0 \frac{\Gamma_{nat}}{\Gamma_a} L_a(E) \ . \qquad (2.22)$$

t_a is defined as

$$t_a = \sigma_0 f' n_a d_a \Gamma_{nat} / \Gamma_a \ . \qquad (2.23)$$

The quantity Γ_a depends on the sample structure. It is only for idealized samples that Γ_a approaches Γ_{nat} . If $\Gamma = \Gamma_a > \Gamma_{nat}$, expression (2.16) may be used as before, and (2.18) is replaced by $\Gamma_{exp} = 2\Gamma h(t_a)$, where t_a is given by (2.23). If $\Gamma \neq \Gamma_a$, the observed line width is given by

$$\Gamma_{exp} = \Gamma + \Gamma_a + 0.27 \ \sigma_0 f' n_a d_a \Gamma_{nat} \ , \qquad (2.24)$$

and (2.16) may be rewritten as

$$\varepsilon(v) = \int_{-\infty}^{\infty} J_M(E,v) \left[1 - \frac{\Gamma_a}{\Gamma} \exp\left[-t_a L_a(E) \right] \right] dE \ . \qquad (2.25)$$

For not very thick samples ($t_a < 10$) the line is still a Lorentzian, and (2.25) may be written as

$$\varepsilon(S) = f \left[1 - J_0(it_a/2) \exp(-t_a/2) \right] \Big/ \left[\left(\frac{2S}{\Gamma_{exp}} \right)^2 + 1 \right] \ . \quad (2.26)$$

In Mössbauer spectroscopy equations (2.17) and (2.18) are often used to determine parameters f and f' . For a very thin absorber we can write

$$\lim_{t_a \to 0} \varepsilon(0) = f \, t_a / 2 \ . \qquad (2.27)$$

However, time-consuming measurements have to be carried out to reach a satisfactory statistical accuracy.

In general σ_0 and Γ_{nat} are known and there are four unknown quantities: f, f' , Γ and Γ_a . The dependence of $\varepsilon(0)$ and Γ_{exp} on d_a can be measured providing $\Gamma_a = \Gamma$. Thereafter the dependence of Γ_{exp}/Γ on the easily measured parameter $\sigma_0 n_a d_a$ can be plotted. This should be a straight line with slope 0.27 f' and which gives f' immediately [1.14]. The intercept with the y-axis ($d_a = 0$) is $\Gamma + \Gamma_a$. The dependence of $\varepsilon(0)/f$ on t_a can then be plotted.

By the method of least squares the experimental data are approximated by (2.17) which yields f . However, since $J_0(it_a/2)$ is not a rapidly changing function of t_a , the accuracy of the procedure is low. Besides , if $\Gamma \neq \Gamma_a$, the method is more complicated. Similar consistent treatment can be carried out by assuming the lines in the source and absorber to be non-Lorentzian but Gaussian or combinations of the two.

A dependence of e(0) on t_a for the case f = 1 (Fig.2.3) can be obtained by numerical integration of equation (2.17). The dependence when $t_a \geq 0.15$ deviates substantially from linear.
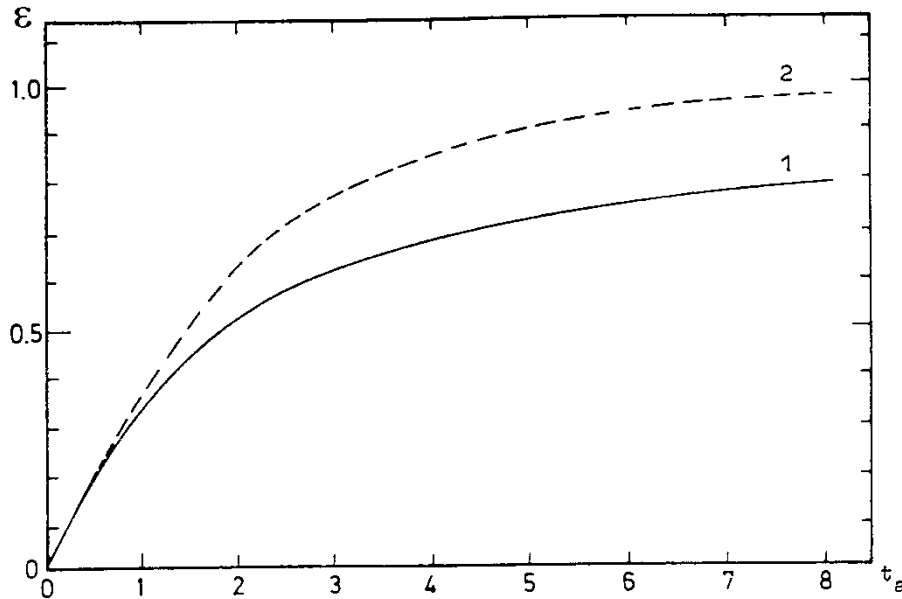
Fig.2.3 Dependences of $\varepsilon(0)$ (1) and spectral area (2) on t_a upon detecting the radiation caused by the Mössbauer transition and having passed through the sample of resonant atoms.

For large values of t_a the situation becomes more complicated. The intensity transmitted through a sample falls off rapidly with the sample thickness (2.12), therefore it becomes extremely difficult to observe the limiting $\varepsilon 0)$ value accurately at $t_a > 10$. Indeed, it can then only be derived after lengthy measurements. Furthermore, the limiting $\varepsilon(0)$ values (Fig.2.3) cannot be reached since equations (2.17) or (2.26) are derived from the sample consisting only of the resonant atoms. Even for monatomic samples having $a \neq 100$ % the photo-effect on non-resonant atoms causes the experimental dependence of $\varepsilon(0)$ on t_a to be non-monotonous and to have a maximum at a certain t_a and then to approach zero.

In Mössbauer spectroscopy the shape of the spectrum and its area are the "signals" conveying quantitative information on a phase.

There is a particular shape of the Mössbauer spectrum which corresponds to every given phase or state of resonant atoms. When the shape is known to be Lorentzian, for example, the amplitudes and the line positions are often used as parameters of the signal. The amplitudes of the lines are assumed to unambiguously determine the amount of a given phase in a sample. As can be seen from Fig.2.3, saturation effects can significantly complicate the phase analysis. Furthermore, some experimental features may greatly affects the line amplitudes. That is why it is a good practice to measure the areas under the spectral lines. A dependence is given on t_a of the spectral area obtained by numeric integration of expression (2.16) in Fig.2.3. By definition, the area under the spectrum is:

$$A(t_a) = \int_{-\infty}^{\infty} \varepsilon(v,t_a)dv = \int_{-\infty}^{\infty} \int_{-\infty}^{\infty} J_M(E,v)\left[1 - \exp(-t_a L_a(E))\right] dV\, dE.$$

(2.28)

Taking into account the normalization conditions, we have

$$A(t_a) = f \int_{-\infty}^{\infty} \left[1 - \exp\left[-t_a L_a(E)\right]\right] dE .$$

(2.29)

A significant deviation of this dependence from proportionality occurs at greater thicknesses. The area under the spectrum does not then depend on the line shape and self- absorption in the source, neither does it depend on the cross section of non-resonant interaction in the sample or on the geometry of the experiment or the instrumental line broadening.

The study by transmission Mössbauer spectroscopy of surface layers is of special interest when $t_a \ll 1$. Expression (2.29) is then considerably reduced and due to normalization (2.1) it can be written:

$$A = \pi f t_a \Gamma_a / 2 = \pi f f' n_a d_a \sigma_0 \Gamma_{nat} / 2 .$$

(2.30)

Thus the area under a given line of the spectrum is proportional to f' and the density of Mössbauer nuclei n_a in the phase.

The phase analysis from a fairly well resolved spectra requires no special treatment and (2.29) holds even when there is instrumental line broadening. Indeed, the addition of the noise velocity u_n to the average velocity of the source results in an additional energy change of γ-quanta $E u_n / c$. The distribution function for noise may itself depend on the average velocity v. If $p(u_n, v)$ is defined as the probability that at a given average velocity the actual velocity is between $v + u_n$ and $v + u_n + du_n$, the normalized function can be expressed

$$\varepsilon(v) = \int\limits_{-\infty}^{\infty} du_n \int\limits_{-\infty}^{\infty} p(u_n,v) \; J_M(E,v,u_n) \; [1 - \exp(-L_a(E)t_a)] \; dE$$

$$= \int\limits_{-\infty}^{\infty} J_M^*(E,v) \; [1 - \exp(-L_a(E) \; t_a)] \; dE \; ,$$

where

$$J_M^*(E,v) = \int\limits_{-\infty}^{\infty} p(u_n,v) \; J_M(E,v,u_n) \; du_n \; .$$

The area under the spectrum is given by an expression which is analogous to (2.29):

$$A = f^* \int\limits_{-\infty}^{\infty} [1 - e^{-L_a(E)t_a}] \; dE \; ,$$

where

$$f^* = \int\limits_{-\infty}^{\infty} dv \int\limits_{-\infty}^{\infty} p(u_n,v) \; J_M(E,v,u_n) \; du_n \; .$$

If the distribution function does not depend on v the equation is reduced, $f^* = f$, and the area under the spectrum is not affected by noise. If the noise distribution function does depend on v , the area depends on the line shape of the source. Hence it follows from (2.29) and (2.30) that for the simplest case of single lines the area under the spectrum depends only on f , f' , Γ_a and $n_a d_a$.

Up to now we have assumed implicitly the detector to register only the γ-rays of the Mössbauer transition. In practice this is not so because of the background noise. In transmission experiments there are three sources of the background: i) γ-and X-rays of higher energies which may be Compton-scattered before reaching the detector; Bremsstrahlung produced outside the detector may contribute to this, too; ii) High-energy γ-and X-rays having lost only a part of their energy in the detector; iii) X-rays that are not distinguished by the detector from the Mössbauer quanta.

The relative intensity of the background also increases sharply as the thickness of the absorber increases. The experimentally observed effect is given not by (1.36) but by the following

$$\varepsilon_{exp}(v) = \frac{I(\infty) - I(v)}{I(\infty)} \frac{I(\infty)}{I(\infty) + I_{back}} = p \ \varepsilon(v) \ . \qquad (2.31)$$

There is analogous relationship for the relative area under the spectrum

$$A_{exp} = pA \ . \qquad (2.32)$$

The background coefficient p is always less than unity. Usually the difficulties in determining p do not permit the absolute measurement of f by the above method. Furthermore, the measured f-value may also be lower since the Mössbauer quanta may lose a part of their energy as a result of the Compton effect. This effect is more significant with detectors of poor resolution.

With the exception of emission Mössbauer spectroscopy, work can be performed with standard sources with f-values which are provided with the details of this source. Otherwise f-values are determined using the "black" absorber which completely resonantly absorbs only the Mössbauer radiation [1.15,16].

Mössbauer spectroscopy requires a knowledge of the absolute values and ratios of the cross sections of both resonant and non-resonant processes. For ^{57}Fe in transmission experiments it is the 14.4 keV γ–quanta interaction which is of interest as it also is in scattering experiments together with the 6.46keV X- rays. In both theoretical and practical studies of the interaction of radiation with matter the appropriate absorption coefficients are expressed in different units. Thus, the atomic absorption cross sections σ_e are expressed in [cm^2] or barn [$10^{-24}cm^2$] per atom; the linear scattering (absorption) coefficients μ expressed in [cm^{-1}]; and the mass absorption coefficients μ^m in [cm^2g^{-1}]. For an element they are related by the following expression:

$$\mu = \mu^m\rho = \sigma_e\rho N/A \ , \qquad (2.33)$$

where ρ is the density, N is Avogadro number, and A is the mass number.

Theoretical aspects of Mössbauer spectroscopy use the interaction cross section per atom whilst for transmission experiments the mass absorption coefficients are preferred and, in scattering experiments, the linear scattering coefficient is used. A review of cross sections for the interaction of electromagnetic radiations in the energy range of interest can be found in [1.17,2.1]. For the Mössbauer 14.4 keV radiation and an iron absorber the following values apply: $\sigma_0 = 2.56 \ 10^6$ barn/atom,

σ_a = 5.9 10^3 barn/atom, μ_a = 0.0504 μm^{-1} and μ^m = 64 $cm^2 g^{-1}$. It is sometimes of convenience to use the quantities of the following type to quantify the non-resonant absorption length

$$1 = \mu_a^{-1} \ . \tag{2.34}$$

It shows, for instance, that a 18 mm thick iron foil will attenuate the 14.4 keV non-resonant γ-quanta by a factor e. Figures 2.4 and 2.5 depict the calculated dependence of the 14.4 keV γ-quanta and the 6.46 keV X-rays intensities on the filter thicknesses for some frequently used substances.
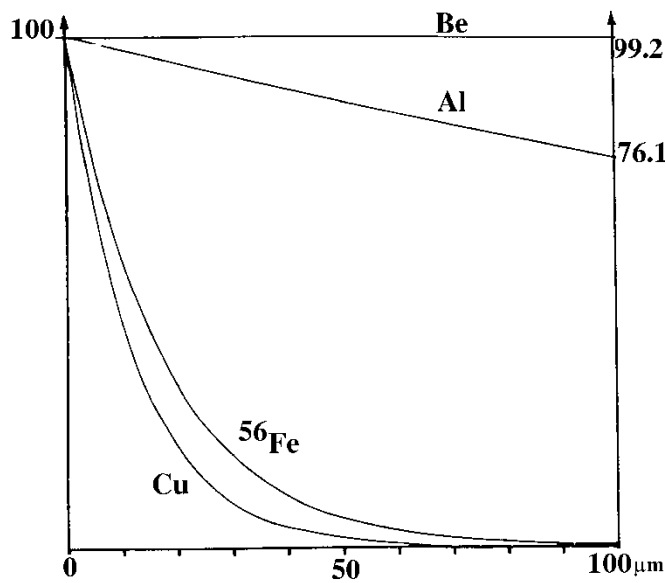
Fig.2.4 Intensity dependence of the 14.4 keV ^{57}Co γ-quanta on the filter thickness.

It is now possible to consider two iron absorbers with ^{57}Fe abundances of 2.14 % and 90 %, with f' = O.67 for iron [2.2] and H_{eff} = 33.0 Tesla. If v = v_0 ,v_1 ,v_2 ,v_3 be the relative velocities at which the source line $J_M(E,v)$ excites the centre of the spectrum and the first, second and third line in it, intensity ratios can be assumed to be 3:2:1:1:2:3. The maximum value of the linear resonant absorption coefficient for a line whose partial intensity is k_i may be written as:

$$\mu_r^i = n_a f' k_i \sigma_0 \ . \tag{2.35}$$
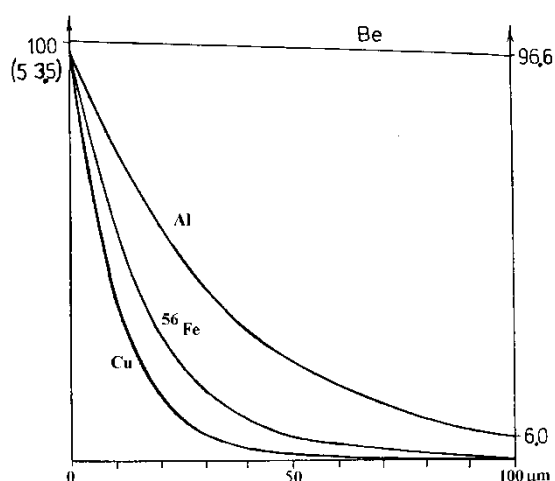
Fig.2.5 Intensity dependence of the 6.46 keV K-X-rays on the filter thickness.

In subsequent discussions of spectral simulations we shall use the hypothetical substance non-magnetic iron (H_{eff}= 0). The values of the linear resonant scattering coefficients for iron and the hypothetical substance are given in Table 2.3.

Table 2.3
Linear coefficients of resonant scattering $\mu_r(cm^{-1})$ at room temperature for α-iron and non-magnetic iron.

a, %	H_{eff} = 33. Tesla				H_{eff} = 0
	v_0	v_1	v_2	v_3	v_0
2.2	2	790	527	263	3160
90	83	32 800	21 900	10 900	131 000

Notes: 1. v_0, v_1, v_2 and v_3 for α-iron correspond to the spectrum centre and to line I, II, and III, respectively. 2. Linear coefficient of non-resonant absorption of the 14.4 keV γ-rays in α-iron are μ_{ph} = 497.5, μ_R = 5.75 and μ_C = 0.71 cm^{-1} for the photoeffect, Rayleigh scattering and the Compton effect, respectively.

The dependences of the γ-quanta intensity (E_0 = 14.4 keV, f = 0.77) on thicknesses of the "non-magnetic iron" absorber are shown in Fig.2.6 whilst Fig.2.7 shows similar dependences for α-Fe absorbers. Curves 1 and 4 are obtained for the source line at resonance with the first line of the sextet. The difference between the curves is caused by the different abundances of ^{57}Fe in the absorber.
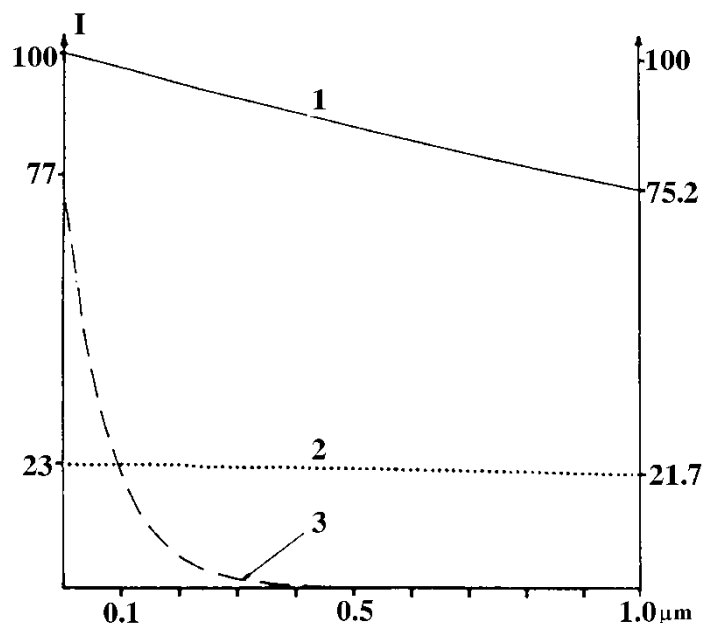
Fig.2.6 Intensity dependence of the 14.4 keV γ-quanta from a ^{57}Co(Rh) source (f = 0.77) on the thickness of a sample of non- magnetic iron (f' = 0.7, δ = 0) at room temperature: 1 - resonant and non-resonant interactions are accounted for, a = 2.14 %; 2 - beam of non-resonant γ-quanta; 3 - beam of resonant γ-quanta, a = 90 %.

An examination of the results presented in Figs.2.6 and 2.7 enable an evaluation of the amount of substance needed to obtain a required effect, and also the optimum thickness of the windows and substrates. In particular, from curves 2 and 3 in Fig.2.6 it follows that the maximum $\varepsilon(0)$ value in transmission experiments cannot exceed the value of f. Indeed, at a $\rightarrow$ 100 %, only the non-resonant γ-quanta will pass through an absorber whose thickness is ~ 0.4 μm and $\varepsilon(0)$ $\rightarrow$ f.
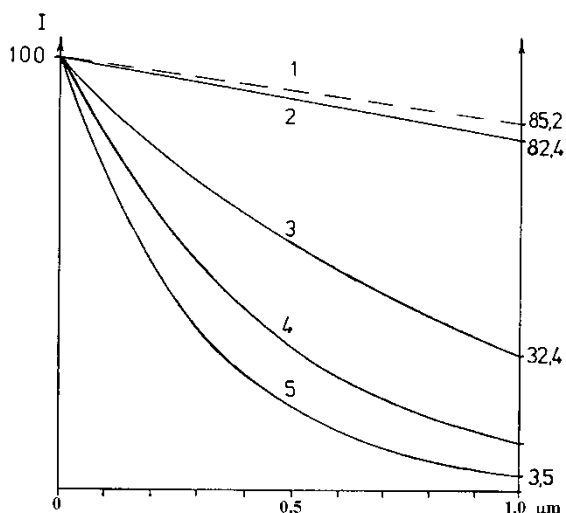
Fig.2.7 Intensity dependence of the 14.4 keV γ-quanta from a ^{57}Co (Rh) source on the thickness of a sample of metal iron at a constant velocity of the source. 1 and 5 are for v = v(1), 2 - for v = v(0), 3 - for v = v(3), 4 - for v = v(2); a = 2.14 % for 1, a = 90 % for 2 - 5.

2.2. Low-energy γ-quanta Scattering

There are various scattering channels of incident Mössbauer radiation, including the channels which give conversion electrons as opposed to γ-quanta. It is important in transmission Mössbauer spectroscopy, that if the secondary scattering is not taken into account every resonant scattering leads to the attenuation of the transmitted intensity, i.e. to absorption. Neither the type of the scattering channel nor the interaction of the scattered radiation with matter are of any significance here. Of primary interest in scattering experiments are the types of the scattering channels, their probabilities and the properties of the scattered radiation.

Let us divide all the scattering channels into two groups. The first group includes scattering channels yielding γ-quanta. Scattering channels of the second group correspond to all other possible interaction processes. As in transmission experiments, in a scattering geometry γ-quanta are detected but the background is caused by different processes. The main process competing with resonance interactions in the transmission mode experiments is the photoelectric effect (see Table 2.3). The Compton effect is to be taken into account when the source emits high-energy γ-rays in addition to the Mössbauer radiation.

In scattering Mössbauer spectroscopy the processes competing with Mössbauer scattering are the Compton effect, Rayleigh scattering and classical resonant scattering of γ -rays [2.3]. Non-resonant scattering of γ-rays occurs on free or bound electrons.

The maximum energy change is for the electrons which are assumed to be free, i.e. in Compton scattering. The minimum energy E' for the backscattered γ-quantum is given by $E'_b = E /(1 + 2\beta)$, where β is the ratio of the incident γ-quantum energy to the rest energy of the electron. For low-energy quanta the energy change is small. Thus, for ^{57}Fe E' = 13.6 keV. Ordinary detectors cannot discriminate the quanta backscattered due to resonance from the Rayleigh scattering and Compton scattering. Typical energy losses for the Compton effect are of the order of 10^2 - 10^4 eV. Compton scattering may or may not influence lattice vibrations, but the energy losses may be neglected since they are several orders of magnitude less than the energy transferred to the electron.

Rayleigh scattering is the scattering of γ-quanta from atomic shells and is completely analogous to X-rays scattering which leads to diffraction from the crystal lattice. Hence, there is no ionization or excitation of the atom. Rayleigh scattering occurs on atomic shells and the energy may or may not be transferred to the lattice. Hence, Rayleigh scattering is either elastic or inelastic. In scattering spectroscopy, as opposed to transmission mode experiments, Rayleigh scattering may play an important role. Interference between Rayleigh and resonant scattering results in series of interesting effects and allows a deeper insight into composition and structure of the substance. Phase analysis for even relatively simple samples may prove to be incorrect if the contribution of Rayleigh scattering is not taken into account. This is discussed in more detail in Chapt.4.

It is now necessary to examine the dependence of the Rayleigh scattering cross section on the γ-ray energy, the scattering angle and the atomic number Z of the scatterer. The Rayleigh scattering of high-energy γ-rays results in more than three-quarters of the scattered radiation within a cone of angle θ_0 [2.4]

$$\theta_0 = 2 \text{ arc sin } [2.6 \; 10^{-2} \; Z^{1/3} \; \beta^{-1}] \; . \tag{2.36}$$

The scattering cross section for this radiation at $\theta \rightarrow 0$ is approximately proportional to Z^2 and independent of E. Thus, inside the cone classical X-ray elastic scattering occurs, and the cross section can be found from tables, e.g. [2.1].

At scattering angles $\theta > \theta_0$ the cross section falls off rapidly and is given by [2.4]:

$$\sigma_R = 4.33 \; 10^{-33} \left[\frac{Z}{\beta}\right]^3 w'(\theta) \quad [\text{cm}^2/\text{sr}], \tag{2.37}$$

$$w'(\theta) = \frac{1 + \cos^2 \theta}{\sin^3 \theta/2} \quad .$$

For the 145 keV Mössbauer transition in ^{141}Pr $\theta_0 = 40°$, and the backscattering cross section can be evaluated from formula (2.37). If the γ-transition energy is less than 40 keV, the formula is inappropriate. Indeed, for E = 40 keV and Z = 26 (Fe), (2.36) gives $\theta_0 = 170°$. At these and lower energies, the photon wave length is of the order of an atomic radius and the angle dependence is determined not by (2.37) but by the atomic form factors. In backscattering Mössbauer experiments involving ^{57}Fe and ^{119}Sn the Rayleigh scattering mainly contributes to the background if there is no Compton scattering of higherenergy radiation. Indeed, from Table 2.3 it can be seen that for the 14.4 keV γ-quanta $\mu_R = 5.75$ cm^{-1} and the probability of Compton scattering is 8 times lower than for Rayleigh scattering.

The main processes of γ-rays scattering in solids for energies bellows 200 keV will be classified provided that scattering of γ-rays, whose energy is equal to the binding energy of atomic electrons, is not considered. Within this classification (Table 2.4) scattering processes are divided

Table 2.4
Classification of γ-ray scattering processes in solids.

Type of Scattering	Classification of γ-ray scattering processes			
	Fundamental classification			Empirical classification
Nuclear elastic and Rayleigh	resonant	coherent	recoilless	elastic or quasi-elastic
			Nonrecoilless	inelastic
	non-resonant	incoherent	recoilless	elastic or quasi-elastic
			nonrecoilless	inelastic
Compton	non-resonant	incoherent	recoilless	inelastic
			nonrecoilless	inelastic
Nuclear inelastic	resonant	incoherent	Recoilless	energy-shifted
			nonrecoilless	inelastic

primarily into resonant and non-resonant ones [2.5]. Resonant scattering occurs on nuclei if the energy of a γ-quantum is close to the γ-transition energy. Non-resonant scattering is the scattering by electrons. Both resonant and non-resonant scattering may be elastic or inelastic, coherent and incoherent. Elastic scattering is a process which results in no energy change of the scattered quantum.

A change of γ-quanta energy may occur in resonant scattering as a result of recoil. Typical energy changes are of the order of 10^{-2}eV. If resonant scattering is recoilless it may still be inelastic since, after scattering, the nuclear quantum state may change and the energy of the scattered γ-quantum will differ from the energy of the incident quantum by the value of the ground level splitting. Typical energy changes are about 10^{-8} eV. Only Mössbauer spectroscopy allows the observation of inelasticity in this type of scattering. Finally, different scattering channels may be coherent or incoherent. Coherence is the property of several stochastic processes characterizing their ability to strengthen or weaken each other. Even inelastic processes may be coherent.

In addition to the classification based on physical processes occurring in scattering, another classification is possible based on the energy resolution of the method used. An example of this classification is given in the right-hand column of the Tab. 2.4. In accordance with the classification, quasi-elastic scattering is the scattering where energy losses due to recoil are of the same order as Γ_{nat}. Energy shifted scattering is the scattering where the recoil energy is not transferred to the solid at the moment of scattering, but the energy of scattered γ-quantum differs from that of the incident quantum by a fixed amount which is determined by hyperfine interactions. We end this classification of scattering processes by noting that every scattering process has its own angular distribution.

The greatest advantage of scattering experiments as opposed to transmission mode experiments is that they may involve a significantly smaller background contribution. This has applications when observing the effect in relatively high-energy transitions [2.6]. A typical experimental arrangement is shown in Fig.2.8. The source is assumed to be a point source and a tungsten shield is used to shield the detector completely from direct γ-rays of the source. Such an axially symmetric backscattering arrangement ensures a higher efficiency and is convenient for low temperature measurements. Indeed, for a scatterer of $^{141}PrO_2$ at 20 K and a source of $^{141}CeO_2$ at 18 K (E_0 = 145 keV) the signal-to-background ratio is found to be 0.20, whereas for the equivalent transmission experiment the ratio would not exceed 0.01.

The gain in the observed effect is caused by the fact that in idealized scattering experiments only the radiation from the scatterer is detected; the direct radiation of the source is not registered by the detector neither is the radiation scattered by surroundings. If there are no γ-quanta with energies higher than

the Mössbauer transition energy the radiation from the scatterer consists of three components: Mössbauer, Rayleigh and Compton. The last one can be discriminated if the incident quanta energy is sufficiently high. If there is no hyperfine splitting in both the source and the scatterer then for a thin scatterer consisting of the resonant isotope only the observed effect will satisfy the relation:

$$\varepsilon \le \frac{1}{2} f\, f'(d\sigma_M/d\omega)(d\sigma_R/d\omega) \quad , \qquad (2.38)$$

where $d\sigma_M/d\omega$ is the differential cross section for Mössbauer scattering at resonant energy; and $d\sigma_R/d\omega$ is the differential cross section for Rayleigh scattering.
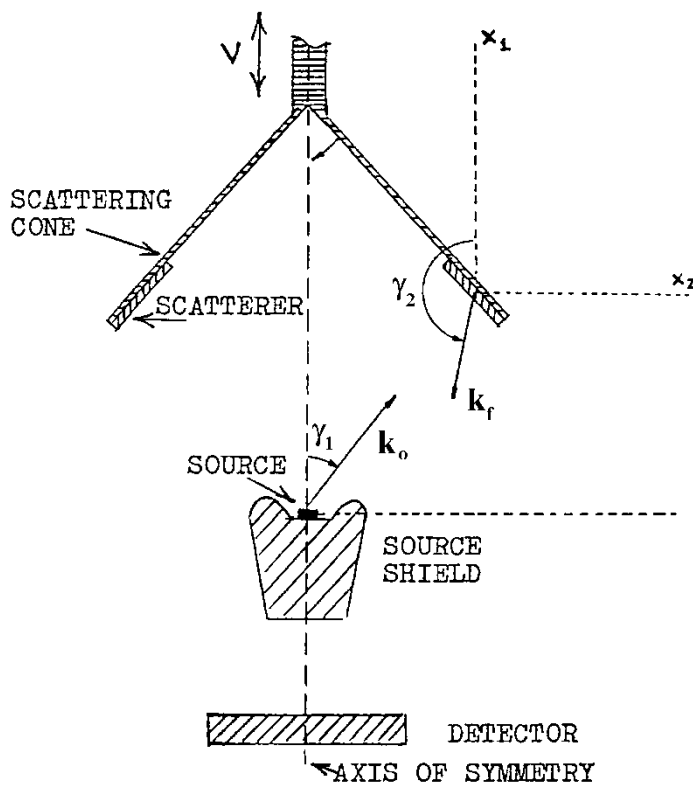

Fig.2.8 Scattering Mössbauer experiment in an axially symmetric geometry [2.6]. γ_1 and γ_2 are the angles of incidence and the scattering angle respectively; $\underline{k}_0$ and $\underline{k}_f$ are the wave vectors of γ-quanta.

For ^{141}Pr the ratio of the differential cross sections turns out to be 70400, and (2.38) takes the form

$$\epsilon \leq f\,(3.5\ 10^4\ f^{\,\prime})\ . \hspace{6cm} (2.39)$$

In transmission mode geometry ϵ is always less than or equal to f'. In scattering geometry the situation is different. For a hypothetical scatterer of ^{141}Pr with f' of only 0.01 %, the effect due to (2.39) may be 3.5 times larger than f' [2.6].

   The Rayleigh and Compton scattering cross sections taken per Mössbauer atom are usually many orders of magnitude less than the maximum cross section for resonant scattering by the atom. However, it should not be concluded that Mössbauer scattering makes the main contribution to the observed intensity of the scattered radiation. Indeed, Rayleigh or Compton scattering will arise from all atoms of all elements in the sample under study and will not depend on the isotopic composition. In contrast, the Mössbauer effect is observed on the isotope only. Even if the sample is monatomic, a factor a/100 must be introduced where "a" is the percent abundance of the resonant isotope. For natural iron this will lower the maximum value of the resonant scattering cross section by a factor of about 45. The hyperfine splitting, in its turn, lowers the maximum possible cross section value for Mössbauer scattering in the sample. It should be noted that if γ-quanta scattering from iron is observed which corresponds to the absorption maximum for the third or the fourth line, a factor f'/12 should be introduced in the expression for the scattered cross section. There are some other reasons for lowering the maximum value of the Mössbauer scattering cross section and these are outlined below.

In general, the classical resonance scattering should be accounted for. This arises from a partial overlap of emission and absorption γ-ray spectra which are significantly broadened by thermal motion of atoms in the source and the absorber. The centres of gravity of such spectra are shifted relatively to the transition energy E_0 in opposite directions by an amount equal to the recoil energy E_R. As a rule, classical resonance scattering does not change the shape and intensity of Mössbauer scattering spectra, since the process cross section is small and practically unchanged in the energy region used in Mössbauer spectroscopy.

2.3. Resonance Fluorescence and Interference Effects

The principles of resonance scattering of γ-rays have been detailed in the well known monograph of W. HEITLER [2.7]. The scattering of electromagnetic radiation of an energy very close to that E_0 of the scattering system was called resonance fluorescence. An important feature of the process is that the cross section on resonance is significantly larger than for any other scattering process and that the phase of the scattered radiation is definitely shifted. The shift is significant in the vicinity of resonance. On passing through the resonance the shift changes from $\pi/2$ to 0 at E $<<$ E_0 and to π at E $>>$ E_0 .

It was shown by W. Heitler that for an individual process of resonance fluorescence the energy E' of the emitted photon should not differ from energy E of the absorbed photon by more than the ground state width. For scattering Mössbauer spectroscopy involving stable ground states and no level splitting due to hyperfine interactions the energy of the scattered quantum is equal to that of the incident quantum within the ground-state width. If a beam of monochromatic γ-quanta of energy E which is close to the resonance energy E_0 is directed onto a resonant scatterer, the scattered radiation will be also monochromatic with energy E, as opposed to Lorentzian with linewidth Γ which is the case for an emission line.

Resonance fluorescence is a single coherent quantum process if there are no external perturbations. In a stationary case, it cannot be regarded as two subsequent unrelated processes of absorption and emission because the nucleus would not "remember" which γ-quantum had been absorbed and the relative probability to emit a γ-quantum of energy E would be given by a Lorentzian distribution of width Γ with a maximum at energy E_0 . For resonance fluorescence the scattered wave is coherent with the incident radiation. Its phase is shifted relative to the phase of the incident wave. Fundamental results for the development of resonance scattering theory for nuclear physics were obtained by LAMB [2.8] who developed a theory of resonance absorption of neutrons by nuclei bound in the crystal lattice. This theory was used by R. Mössbauer to explain his experiments on resonance γ-quanta scattering by nuclei in solids.

All Mössbauer scattering experiments show two types of dependence. The first type concerns the angular dependences of the scattered radiation. As a rule, the intensities are measured depending on either angles γ_1 and γ_2 for the incident and outgoing radiation or on the scattering angle θ. The experimental arrangement for the particular case of the scattering angle $\theta = \gamma_1 + \gamma_2 = 90°$ is shown in Fig.2.9. The angular dependence is determined by the parameters of the nuclear-excited and -ground levels as well as by other parameters of the sample such as the vibration spectrum, the crystal structure, texture, the resonant isotope abundance and hyperfine interactions. The intensity is considerably dependent on the collimation of the incident and scattered radiation, as well as on interference with Rayleigh scattering even at $\theta = 90°$ if the transition is not M1.

The second type of dependence is evident in various spectra. Most of the Mössbauer spectra are obtained by methods similar to those used in transmission experiments, i.e. by detection of all γ-quanta scattered by the sample at different Doppler velocities. Sometimes a more sophisticated experimental arrangement is used, allowing the energy spectrum of recoilless γ-rays at fixed Doppler velocity to be examined.

The analysis can be approached by considering the elastic scattering from an atom in a crystal where the divergences of incident and scattered radiation are small. It is initially necessary to consider the interference effects on the scattered
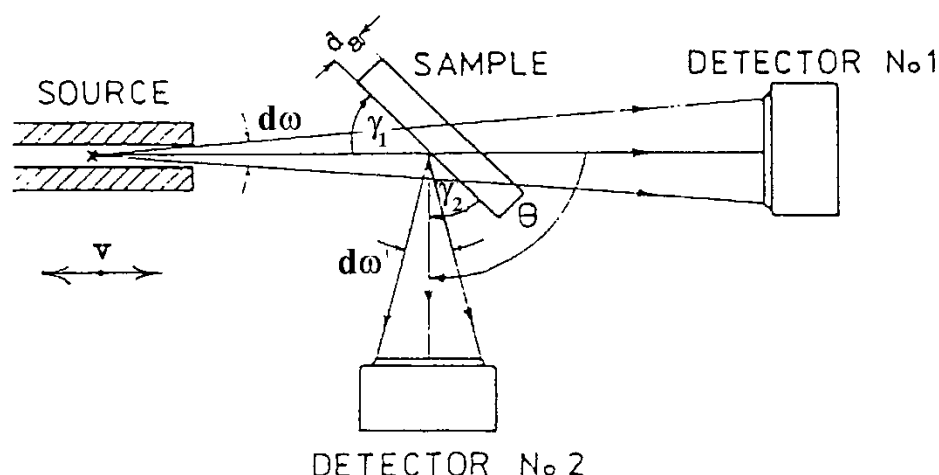
Fig.2.9 Experimental geometry for scattering $\theta = \gamma_1 + \gamma_2 = 90°$, allowing the simultaneous recording of the transmission spectra (detector 1) and scattering spectra (detector 2). γ-radiation is incident at an angle γ_1 within the solid angle $d\omega$ onto the sample under study of thickness d_a .

electromagnetic radiation with a wavelength of about 1 Å by a single atom. Rayleigh scattering by atomic electrons always produces interference, since the distance between electrons in an atom is also about 1 Å. The interference processes are accounted for by means of the atomic form factors. If this radiation is resonantly scattered by a nucleus, elastic Mössbauer scattering may occur and there will also be interference between incident and scattered radiation. Thereafter, the resonantly scattered radiation may interfere with the radiation scattered by electrons of the atom. Finally, Mössbauer scattering gives a specific interference which occurs if the hyperfine splitting is of the order of Γ_{nat}.

The problems related to Rayleigh scattering and atomic form factors are described in most textbooks on X-ray diffraction. We shall start with the interference effects taking place on resonant scattering. A theoretical problem is to derive an expression for the elastic resonant scattering amplitude $\mathcal{F}_r$, where all the experimental conditions are taken into consideration. For a given transition multipolarity, $\mathcal{F}_r$ will depend on the parameters of levels or sublevels of the initial and final nuclear states, on the direction of the quantization axis, on the energy of the incident γ-quantum, and on the wave-

vectors of the incident and scattered radiation and on the polarization vector. If these parameters are fixed, the scattering amplitude is the sum of partial amplitudes corresponding to all intermediate excited states. When the incident radiation is a mixture of multipoles, each of the partial amplitudes will contain contributions from each multipolarity.

The amplitude of the elastic nuclear resonance scattering for which the nuclear spin projection on the quantization axis changes as $m_g \rightarrow m_e \rightarrow m_g$, may be written [2.9,10] in the following form:

$$\mathcal{F}_r = aC \frac{\Gamma_\gamma}{2k_0} \sum_n \frac{\left(\psi_{n_0} \mid e^{-i\underline{k}_f\underline{r}} \mid \psi_n\right) \left(\psi_n \mid e^{i\underline{k}_0\underline{r}} \mid \psi_{n_0}\right)}{E - E_0 - (\mathcal{E}_n - \mathcal{E}_{n_0}) + i\Gamma/2} \quad . \tag{2.40}$$

where the values of ψ are the crystal wave functions, $\mathcal{E}$ describe their energy eigenvalues, C is a factor depending on polarization or multipolarity, E is the energy of an incident γ-quantum, $\underline{k}_0$ and $\underline{k}_f$ are the wave vectors of incident and scattered γ-quanta; $E_0 - i\Gamma/2$ is the resonance energy, Γ_γ is the partial width for de-excitation of the nuclear level by emission of a γ-quantum, $\Gamma_\gamma = \Gamma/(1 + \alpha)$. The nuclear matrix element, which depends on the multipolarity of the ã-transition and determines the nuclear part of the angular dependence for the scattered radiation, is factorized and included in C.

The terms "collision time" and "scattering length" are sometimes used in the theory of resonance scattering (see [2.9]). In Mössbauer spectroscopy the collision time, which is proportional to Γ^{-1}, is by several orders of magnitude longer than the lattice vibration periods. There is no correlation here between the initial $\underline{r}(0)$ and final $\underline{r}(t)$ positions of the atom and the process is considered in terms of slow collisions. Some times one speak about "slow scattering". Despite this the scattered wave remains coherent with the incident one. The quantity

$$\Gamma_\gamma / 2k_0[E - E_0 - (\mathcal{E}_n - \mathcal{E}_{n0}) + i\Gamma/2]$$

in the expression for the scattering amplitude (2.40) is the free-particle resonance scattering length [2.9]. In the centre- of-mass system the energy $E - (\mathcal{E}_n - \mathcal{E}_{n0})$ corresponds to this scattering length. Summation in (2.40) causes the main contribution to be made by the term with $n = n_0$. Therefore, for the elastic resonance scattering of γ -quanta we have

$$\mathcal{F}_r = C \ \frac{\Gamma_\gamma}{2k_0} \ \frac{\left(\psi_{n_0} \mid e^{-i\underline{k}_f \underline{r}} \mid \psi_{n_0}\right) \left(\psi_{n_0} \mid e^{i\underline{k}_0 \underline{r}} \mid \psi_{n_0}\right)}{E - E_0 + i\Gamma/2} \quad ,$$

which, for a cubic isotropic crystal, reduces to:

$$\mathcal{F}_r \simeq a \ \frac{\Gamma_\gamma}{2k_0} \ \frac{\exp(-k_0^2 \overline{x^2})}{E - E_0 + i\Gamma/2} . \qquad (2.41)$$

The nuclear transition energy in (2.40) in the presence of hyperfine splitting depends on the quantum numbers m_g and m_e. Let us assume that the initial and final nuclear states for a γ-transition are the eigen states of the angular momentum operators, and denote them by $\mid I_e m_e \rangle$ and $\mid I_g m_g \rangle$ respectively. The theory of angular momenta can be used to evaluate the matrix elements for the transition. To obtain an expression for the amplitude $\mathcal{F}_{coh}$ of the coherent resonance scattering of γ-quanta, it is necessary to sum the amplitudes $\mathcal{F}_r$ over all m_e values and to average the result over initial spin states m_g. The plane wave representation of the wave function is transformed into the spheric wave one. The amplitude $\mathcal{F}_{coh}^{\underline{k}_0 \sigma_1 \rightarrow \underline{k}_f \sigma_2}$ of the elastic resonant scattering of a γ-quantum with energy E and polarization σ_1, incident in the direction $\underline{k}_0$ on a nucleus whose spin projection to the quantization axis z is m_g, and scattered in the direction $\underline{k}_f$ with polarization $\sigma_2 = \pm 1$ for right- or left-hand circularly polarized waves and axially symmetric hyperfine interactions, is written [2.9, 11] as:

$$\mathcal{F}_{coh}^{\underline{k}_0 \sigma_1 \rightarrow \underline{k}_f \sigma_2}(E) = \frac{\Gamma_\gamma}{4k_0} \ \frac{2L + 1}{2I_g + 1} \ f_1 f_2 (\sigma_1 \sigma_2)^{\Delta(\pi)}$$

$$\sum_{m_g, m_e} \frac{D_{K\sigma_2}^{L\,*}(\hat{z} \rightarrow \hat{k}_f) \ D_{K\sigma_1}^{L}(\hat{z} \rightarrow \hat{k}_0) \ \mid G(m_e, m_g) \mid^2}{E - E_0(m_g, m_e) + i\Gamma/2} , \qquad (2.42)$$

where $K = m_e - m_g$. For an atom in an isotropic crystal the probability amplitudes of the Mössbauer effect are:

$$f_1 = \exp\left\{ - <(\underline{k}_0, \underline{u})^2> / 2\right\} \quad ; \quad f_2 = \exp\left\{ - <(\underline{k}_f, \underline{u})^2> / 2\right\}$$

where $\underline{u}$ is the displacement vector of an atom from equilibrium. The parity conservation for the system "nucleus - γ-quantum" leads to the following selection rule for the transitions between the two states of parities π_e and π_g: $\Delta(\pi) = (-1)^L$ and $(-1)^{L+1}$ for EL and ML transitions, respectively. For M1 transitions $\Delta(\pi) = 1$. The transformation of the angular momentum eigen-functions from the $\hat{z}$ coordinate system, where spins of the excited and ground nuclear states are quantized, into the $\hat{k}_0$ or $\hat{k}_f$ coordinate system connected with the propagation direction of the γ -quantum, is determined by special rotation functions - the D functions which are rotation matrices of the angular momentum eigenfunctions. The D-functions give the angular dependence of polarization and intensities of transmissions with energies $E_0(m_g, m_e)$.

If a scatterer is an isotropic substance then, for an M1 transition and in the absence of hyperfine splitting the expression for the coherent resonant scattering amplitude $\mathscr{F}_{coh}^{k_0\sigma_1 \to k_f\sigma_2}$ (E) is reduced to:

$$\mathscr{F}_{coh} = \frac{a}{4k_0} \frac{2I_e + 1}{2I_g + 1} f' D^1_{\sigma_2\sigma_1}(\hat{k}_f \longrightarrow \hat{k}_0)(\sigma_1\sigma_2)^{\Delta(\pi)} \frac{\Gamma_\gamma}{E - E_0 + i\Gamma/2}.$$

$$(2.43)$$

The approach presented here may be compared with other ways which have been used to derive the expression for the nuclear resonant scattering amplitude [2.12,13].

In parallel with the nuclear resonant scattering it is necessary to also consider Rayleigh scattering. If Rayleigh scattering is elastic the phase shift equals π. For the elastic scattering channel there will be two corresponding coherent (although phase-shifted) scattering processes, the Mössbauer and Rayleigh. The amplitude of the total elastic scattering of a γ-quantum of energy E turns out to be a sum of the Mössbauer amplitude $\mathscr{F}_r$ and the Rayleigh $\mathscr{F}_R$. The energy distribution J(E,S) of the scattered γ -radiation (at S = const) may differ substantially from that of the incident one.

Let γ -radiation with the energy distribution L(E) be incident on a sample. Let us measure energy in units of $\Gamma/2$. If there are no hyperfine splittings the energy distribution of γ -radiation after elastic scattering by an atom in an isotropic crystal may be written as [2.14-16]:

$$J(E,S) \sim \frac{1}{(E^2 + 1)} \left\{ \frac{c_2^2 \, f_1 f_2}{(E - S)^2 + 1} + c_3^2 \, f_R \right.$$

$$\left. \frac{2c_1 c_2 c_3 \, (E - S) \, \sqrt{f_R f_1 f_2}}{(E - S)^2 + 1} \right\} , \tag{2.44}$$

$$f_R = \exp \left\{ - < ((\underline{k}_0 - \underline{k}_f) \, \underline{u})^2 \right\} / 2 ,$$

where f_R is the Debye-Waller factor, C_1 is a constant that accounts for different scattering by nuclei and electrons of differently polarized quanta, C_2 is a constant, which is proportional to the resonant scattering length of a γ-quantum by a nucleus exactly in resonance, C_3 is a constant, which is proportional to the Rayleigh scattering length [2.15].

Each of the three terms in (2.44) has its own energy dependence. The energy distribution J(E) of the scattered radiation, corresponding to every term in (2.44) at S = 5, is given in Fig.2.10. For the calculations it may assumed that $C_3 \sqrt{f_R} = C_2 \sqrt{f_1 f_2} = 1$.

Two lines of equal widths are observed in the spectrum resulting only from resonant scattering (Fig.2.10a). Their amplitudes and areas are determined by convolution of the emission and scattering spectra. The large distance between the centres of the spectra means that the amplitudes of the lines are only 4 % of the scattering line amplitude in resonance, i.e. at S = 0. The Rayleigh scattering spectrum intensity in Fig.2.10c effectively coincides with the emission spectrum. As seen from Fig.2.10a and c at S = 5 it is the Rayleigh scattering that mainly contributes to the elastic scattering process. The interference term (Fig.2.10b) becomes zero for the γ-quanta energy corresponding to resonance in the scatterer. When the γ-quanta energies are greater than the resonant energy in the scatterer the interference term increases the total intensity of the elastically scattered radiation whereas for lower energies the total intensity is decreased.

The Mössbauer effect allows the observation of the energy distribution of the scattered γ-radiation when resonance detectors are used. However, such experiments are time consuming. In conventional Mössbauer spectroscopy the radiation detector usually serves as an energy integrator. It detects all γ-radiation of a given velocity which reaches the detector from a scatterer. It is now necessary in a way similar to that used

J

0.01

a)

0

0.2

b)

0

1.0

c)

0

-8   -4   0   4   E
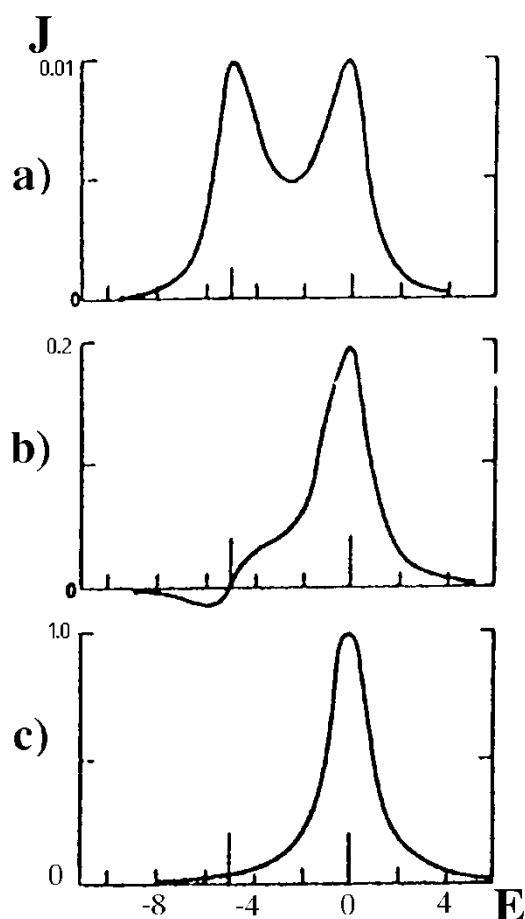
Fig.2.10 Contributions to the energy distributions of the radiation elastically scattered by a single atom of an isotropic crystal: a) - resonant scattering, b) - the interference term, c) - Rayleigh scattering. $S = 5$ $\Gamma_{nat}/2$. γ-Ray energy is in units of $\Gamma_{nat}/2$.

to analyze the separate spectral components (Fig.2.10), to analyze separately the radiation intensities resulting from the resonant scattering process, the Rayleigh scattering process, and the interference effects. As seen in Fig.2.11a the intensity of Rayleigh scattering is independent of S. Indeed, since it is not a resonant process, the energy change of the γ-quanta by an amount greater than, say a million natural widths, will not significantly change the cross section for scattering by electrons. The intensity of the resonantly scattered radiation (Fig.2.11b) follows the usual Lorentzian curve, whilst the contribution of the interference term (Fig.2.11c) to the total intensity of the scattered radiation takes the form of a dispersion curve. The maximum radiation intensity changes which arise from interference occur at $S = \pm \Gamma$.
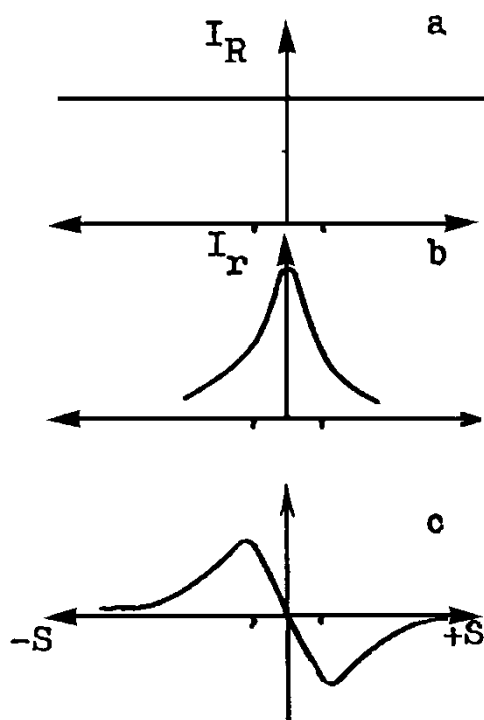
Fig.2.11 Partial contributions to the total radiation intensity as a function of the energy parameter S. a) - resonant scattering, b) - the interference term, c) - Rayleigh scattering.

The dependence of three terms in (2.44) on the scattering angle θ are determined in the first instances by the angular dependences of the scattering processes. The electric dipole interaction in Rayleigh scattering leads to an angular dependence of the form (1 + $\cos^2\theta$)/2. For the magnetic dipole transition, resonance scattering has an angular dependence of the same type, but the polarization of the magnetic and electric radiation components differ by 90° and the interference term in this case contains the angular factor $\cos\theta/(1 + \cos^2\theta)$. Thus, for a scattering angle of 90°, the interference term for M1- transitions vanishes. The Debye-Waller factor for Rayleigh scattering is anisotropic even for an isotropic crystal. It also causes the line shape I(S) to depend on θ . It is significant that all these dependences are smooth, and a change of the scattering angle, say by 1°, will not lead to an appreciable change of the line shape or the intensity of the scattered radiation.

Apart from the interference effects mentioned above, interference is possible as a result of scattering by sublevels of magnetic or electric hyperfine structures [2.17]. To an inci-

dent γ -quantum of any energy E there correspond different (and, in general, nonzero) amplitudes for scattering by all transitions of the hyperfine structure. Hence interference should occur which will manifest itself in an asymmetry of the energy distribution of the scattered radiation. If the scattering atom is in an ideal polycrystal the γ-radiation scattered into the solid angle dω' as a result of the Mössbauer effect can be written in the following form:

$$\frac{dI_r(v)}{d\omega'} \sim \sum_{k,m_g} P_k(\cos\theta) \left\{ \sum_{m_e} B_k(m_g,m_e,m_e') \frac{\Gamma_{nat}^2}{[v(m_g,m_e) - v]^2 + \Gamma_{nat}^2} \right.$$

$$+ \sum_{\substack{m_e,m_e' \\ m_e>m_e'}} \frac{B_k(m_g,m_e,m_e') [v(m_g,m_e) - v] [v(m_g,m_e') - v]}{\left\{[v(m_g,m_e) - v]^2 + \Gamma_{nat}^2\right\}\left\{[v(m_g,m_e') - v]^2 + \Gamma_{nat}^2\right\}}$$

$$\left. \frac{\left\{[v(m_g,m_e) - v(m_g,m_e')]^2 + 2\Gamma_{nat}^2\right\} \Gamma_{nat}^2 + 2\Gamma_{nat}^6}{[v(m_g,m_e) - v(m_g,m_e')]^2 + 2\Gamma_{nat}^2} \right\} \quad ,(2.45)$$

where I_e, I_g, m_e and m_g are the spins of the excited and ground nuclear states and their projections onto the quantization axis respectively. The coefficients $B_k(m_g,m_e,m_e')$ depend on quantum properties and the transition multipolarity. The Legendre polynomials $P_k(\cos\theta)$ describe the dependence of the separate spectral intensities on the scattering angle. The subscript k takes all even integral values from zero to the minimal 2L and $2I_e$ values, where L is the highest multipolarity of the transition. It should be recalled that k = 2 for the M1 transition. $v(m_g,m_e)$ is the Doppler velocity at which the line is observed corresponding to the γ-transition $E_o(m_g,m_e)$. The second term (in braces) in (2.45) takes into account the departure of the line shape from Lorentzian as a result of interference between scattering by different sublevels. The interference amplitudes $B_k(m_g,m_e,m_e')$ contribute to the intensity at resonance.

The relative contribution of the interference term to the total intensity of the scattered radiation is determined by the energy of hyperfine interactions. It has been calculated [2.18] that for Mössbauer scattering at an angle of 135° in the transition $I_g = 0$, $I_e = 1$ and in the presence of magnetic hyperfine interaction the relative contribution of the interference term in (2.45) does not exceed 1 % for $\mu \underline{H}_{eff}/\Gamma_{nat} = 5$ and rises to 5 % as this ratio decreases to 0.5.

Interference effects are observed on scattering from a real sample and not from an isolated atom. Interference effects were observed for the first time on scattering from a polycrystalline α-Fe foil (a = 65 %) using ^{57}Co in α-Fe γ-ray source [2.19]. Interference led to a slight asymmetry of the resonant scattering peak. The asymmetry agrees with a classical model of scattering by a damped resonator [2.20]. In this model resonant scattering is in phase with Rayleigh scattering when the incident radiation energy is above resonance but is in antiphase when below resonance and is in quadrature when on exact resonance. The use of Bragg reflections in single-crystal scatterer permits a substantial reduction in the contribution from incoherent scattering. The interference pattern in this case may be unambiguously connected with the crystallographic and electronic structure. It is therefore important that Mössbauer diffraction from single-crystal scatterers should be considered.

An analysis of interference effects on scattering by single crystals can be carried out in a similar manner to the above consideration of scattering from an isolated atom. The observed pattern is a sum of the three contributions: Rayleigh scattering, nuclear resonant scattering and interference between Rayleigh and nuclear scattering. The reader interested in Rayleigh scattering from single crystals is referred to textbooks and numerous monographs on X-ray diffraction. In addition, there are reviews, e.g. [2.5] and a monograph on coherent Rayleigh scattering of Mössbauer radiation [2.21]. We restrict ourselves here to a note on the fact that the scattering from crystals requires that the structure factors be used instead of the atomic form factors and that the absorption of the scattered radiation should be always taken into account. A correct estimation of the contribution by Rayleigh scattering to the total intensity of the scattered radiation is important when attempting to find the optimum geometry for the scattering of relatively hard radiations.

The detection of Rayleigh scattering of Mössbauer radiation enables samples which do not contain resonant nuclei to be studied. For this purpose a Mössbauer absorber must be placed between the scatterer and the detector. The absorber then serves as an analyser of the scattered radiation. The elastic Rayleigh scattering amplitude can be evaluated by measuring the difference between the intensities at a velocity corresponding to the isomer shift of the source relative to the analyzer, and the intensities at a very large velocity.

The measurement of a continuous velocity scanning experiment enables the Mössbauer spectrum to be obtained which provides more information about the sample. Detecting elastically and inelastically scattered γ-quanta with a resolution of ~ 10^{-7} - 10^{-9} eV allows the study of the effect of the low energy phonons on scattering. Experiments on thermal neutrons scattering require an energy resolution of better then 10^{-6} eV. The

technique is extremely convenient for studies of phase transitions, ordering phenomena, and dynamic effects, including diffusion. The angular dependence of the intensity of the elastically scattered radiation provides information on the static radial distribution function, and the inelastically scattered radiation gives information on diffusion and thermal motion.

Let us consider now coherent resonant scattering by single crystals [2.22,23]. The interaction of the scattered radiation with the sample material has a significant influence on the shape of the spectrum. The observed pattern will be a result of the competing resonant absorption and coherent scattering processes. The resonant absorption cross section in a monatomic scatterer is determined by the forward coherent elastic scattering amplitude, i.e. for $\underline{k}_0 = \underline{k}_f$

$$\sigma_a(E) = -\frac{4}{k_0} J_m \mathcal{F}_{coh} (\underline{k}_0 = \underline{k}_f) = a\sigma_0 f' L(E) . \qquad (2.46)$$

$\mathcal{F}_{coh}$ has been taken from equation (2.43) which was derived for an isolated scattering atom. This is fairly well justified for a polycrystalline scatterer. For a single-crystal scatterer, scattering by other atoms must be taken into account. Inserting the $\mathcal{F}_{coh}$ amplitude corresponding to the scattering by one atom into (2.46) when $\underline{k}_0$ is within a Bragg angle results in an underestimation of the total scattering cross section.

The coherent resonant scattering amplitude determines the scattering cross section. To obtain it, the squared $\mathcal{F}_{coh}$ modulus must be calculated, integrated over all angles and then summed over all polarizations

$$\sigma_{coh}(E) = a^2 \frac{\sigma_0}{3} \frac{1}{1+\alpha} \frac{2I_e+1}{2I_g+1} f'^2 L(E) = p\sigma_a(E) .$$

The p-factor, which determines the cross section ratio for the competing processes, is always less than unity. Thus, for example, for an α-^{57}Fe scatterer the coherent scattering cross section is less than 2 % of the total resonant scattering cross section.

Using the results obtained above, it is easy to find the total differential resonant (elastic and inelastic) scattering cross section of γ-rays. If there are no diffraction effects on scattering, then

$$\frac{d\sigma_r(E)}{d\omega} = \frac{\sigma_a(E)}{4\pi} \frac{1}{1+\alpha} .$$

Resonant absorption leads to the incident radiation reaching deeper layers of the scatterer to have a different spectral composition. To evaluate the radiation intensity which is elastically scattered by an isotropic sample of thickness d, one should use an expression of the following type:

$$I(S) = \int\limits_{-\infty}^{\infty} \int\limits_{0}^{d} J(E,S) \ F(E,S,x) \ dE \ dx \ , \ (2.47)$$

where a change of the spectral composition of the incident and scattered radiation is taken into account using a certain function $F(E,S,x)$. For $J(E,S)$ expression (2.44) may be used. On diffraction the expression for the spectral shape is significantly more complicated and in the case of interference between the resonant scattering and Rayleigh scattering the spectrum is generally a combination of peaks (intensity maxima) and dips (intensity minima).

The directions of Mössbauer diffraction, when the hyperfine splitting is absent, coincide generally with the θ_{hkl} directions of Rayleigh coherent scattering. However, the angular dependence of diffraction line intensities from nuclear scattering and Rayleigh scattering are different. Since the Debye-Waller factor decreases with the scattering angle it is necessary to use large scattering angles in order to increase the contribution of nuclear diffraction to the total spectrum. Sometimes, when there are several atoms in a unit cell, the Rayleigh scattering amplitudes from the atoms in the unit cell may compensate each other. This has made it possible to observe for the first time the pure Mössbauer diffraction from the (080) plane in a single crystal of potassium ferrocyanide $K_4{}^{57}Fe(CN)_6 \cdot 3H_2O$ [2.14]. Since the Rayleigh scattering amplitude from iron atoms is nearly exactly equal and opposite in the sign to the scattering amplitude from other atoms of the unit cell, a Bragg peak is observed at resonance whereas there is no peak at positions far from resonance.

When the hyperfine splitting is present the diffraction pattern caused by resonant scattering is substantially complicated. The line intensities of Mössbauer scattering then manifest an azimuthal dependence in contrast to Rayleigh scattering. The polarization of a scattered γ-ray is then determined not by scattering angle as in Rayleigh scattering, but by the mutual orientation of the axes system for the hyperfine interactions and $\underline{k}_f$. Thus the coherent resonant scattering by nuclei, whose hyperfine interaction axes' orientations are different, leads to a different polarization. The interference of the waves with these different polarizations within a unit cell gives spectra which contain information on structure, both the hyperfine interaction axes orientation, and the relative positions of nuclei in the unit cell. The azimuthal dependence leads to the necessity of using structure matrices [2.11] instead of the scalar scattering amplitudes (see (2.41, 43)) for the analysis of scattering by a unit cell in terms of polarization transformations.

The periodic repeat of lattices and numbers of resonant atoms which give rise to scattering and diffraction lines may give different effects in resonant and Rayleigh scattering. The scattering by a magnetic sublattice in a simple antiferromagnetic with the spins up means that the nuclei of another sublattice do not participate in the coherent scattering. When the nuclear level degeneracy is completely lifted as a result of a magnetic dipole interaction the purely nuclear maxima resulting from Mössbauer diffraction may be detected. This has been observed by SMIRNOV et al. [2.24] for an antiferromagnetic haematite crystal - α-$^{57}Fe_2O_3$ during investigations of diffraction in the [111] direction. Although the unit cells of the magnetic and crystallographic structure coincide for this case, the symmetry of the unit cell is such that the total Rayleigh scattering amplitude for the ((2n + 1)(2n + 1)(2n + 1)) reflections becomes zero. Magnetic fields at the iron atoms are not parallel. Only one of the spin subsystems participates in the coherent scattering of the quantum and there is no cancellation of the scattering amplitudes. This leads to the observation of pure nuclear diffraction maxima. Some works have reported a purely nuclear diffraction in scatterers when only quadrupole splitting is present. For example [2.25] studies of the diffraction of the ^{125}Te Mössbauer radiation by a Te single crystal have enabled the observation of pure nuclear reflections (001) and (002) which are caused by electric quadrupole interactions in the scatterer.

The Mössbauer lines are fairly symmetric when pure nuclear diffraction due to the absence of interference with Rayleigh scattering occurs. Nevertheless, thorough analysis of Mössbauer lines at the ((2n + 1)(2n + 1)(2n + 1)) reflections from an α-Fe_2O_3 single-crystal (a = 85 %, mosaicity ~ 30'') has shown that a dispersion term caused by interference of scattering from various components of the hyperfine structure can be separated [2.26]. For the (999) reflection, the line asymmetry of the central lines of the spectra (i.e. the ratio of the dispersion curve amplitude to the line amplitude) is approximately 5 %. The value of the interference term decreases rapidly with the distance between the resonances, which is about $30\Gamma_{nat}$ even for the central lines of haematite. However, the high sensitivity of the resonance line shape, measured under pure nuclear diffraction conditions, allows the detection of such a small interference effect.

The nuclear transition energies in spin sublattices of a crystal may happen to be close. This leads to a complex interference pattern. Thus, for example, in Fe_3BO_6 the γ -transition energies in ferric ions in 4c and 8d positions are close and, as a result, the first line of the spectrum obtained at the (1100) reflection is split [2.27].

The most complex spectral shapes are observed when the interference occurs between Rayleigh and nuclear scattering from single crystals at Bragg angles. The coherent elastic scattering amplitude from all atoms and resonant nuclei may be considered as a sum of the amplitudes of elastic scattering from each of them if the corresponding phase shifts are taken into account. An idea of the Mössbauer spectrum from a monatomic substance in the absence of both the hyperfine splitting and resonant absorption is given by the following expression which is obtained from Born's approximation [2.15]

$$I(S) \sim \left\{ \frac{2 \, N^2 a^2 f_1 f_2}{s^2 + 4} + A^2 f_R + \frac{2 \, a \, N \, C \, A \, S \, \sqrt{f_1 f_2 f_R}}{s^2 + 4} \right\}$$

$$\sum_n \sum_m \exp \left\{ i(\underline{k}_0 - \underline{k}_f)(\underline{r}_n - \underline{r}_m) \right\} , \qquad (2.48)$$

where $\underline{r}_n$, $\underline{r}_m$ are the atom positions in the lattice. The second factor of the right-hand part (cf.(2.44)) shows that the scatterer is a crystal. Bragg peaks are observed in the directions for which the condition $\underline{k}_0 - \underline{k}_f = \underline{\tau}$ holds $(\tau,$ the reciprocal lattice vector). In an idealized case of diffraction of Mössbauer radiation from a perfect crystal, the γ-quanta should be elastically scattered only in those directions; in all other directions the intensities will be quenched due to coherence of the processes involved. A change of the incident and scattering angles by several minutes may lead to a sharp change in intensity of the scattered radiation. Under these conditions the angular dependence of the first factor in (2.48) may be neglected.

The experimental investigation of the shape of Mössbauer spectra on diffraction requires that the $\mathcal{F}_r$ values be changed, as well as ratios of the elastic nuclear scattering amplitude to the elastic Rayleigh scattering amplitude $\xi = \mathcal{F}_r / \mathcal{F}_R$; and the resonant absorption cross section. The $\mathcal{F}_r$ value can be increased by lowering the temperature, but under such conditions the resonant absorption is also significantly changed. The elastic Rayleigh scattering amplitude can be decreased (and thereby the ξ parameter value increased), by using higher-order reflections. Thus, for example, the reflection of the 23.8 keV Mössbauer radiation from a source of $^{119m}SnO_2$ from the (020) plane of a tin single-crystal film (a = 88 %) gives rise to a typical diffraction peak (see Fig.2.12) [2.28], $\mathcal{F}_R = 1.15 \, 10^{-11}$cm. At room temperature $\xi = 0.45$, and the Mössbauer

spectrum obtained on diffraction at an angle of 5°7' is given in Fig.2.13. Lowering the temperature to 110 K results in the increase of the ξ value by a factor of ~ 7 due to the sharp increase of the f' factor. Further lowering of the temperature leads to an insignificant increase of the ξ parameter, but causes the resonant absorption to play a greater role. An increase in the contribution of the resonant channel without changing the resonant absorption cross section was achieved by using higher-order reflections from the (020) plane (see Fig.2.13).

 The appearance in the Mössbauer spectrum of a dip instead of a peak may in the first instance be associated with resonant absorption which leads to a sharp reduction of the penetration depth where Rayleigh scattering occurs. A smaller value of ξ also favours the appearance of dips in the Mössbauer spectrum. To observe peaks, the ξ parameter should be sufficiently large (i.e. more than 6, see [2.28]).

  Mössbauer spectra, corresponding to Bragg reflections, are significantly complicated if the hyperfine splitting is present. The interference of differently polarized waves may be weakened by polarization factors and this depends on the additional polarization phase shift [2.11]. These features of Mössbauer spectra were demonstrated by observation of the (2n 2n 2n) reflections from a haematite single crystal [2.29], but not the ((2n + 1)(2n + 1)(2n + 1)) reflections, where coherent Rayleigh scattering is absent [2.24]. The Mössbauer spectra were classified into three groups: asymmetric peaks at the (101010) and (888) reflections; asymmetric dips at the (444) reflection, and dispersion-like curves at the (666) and (222) reflections.

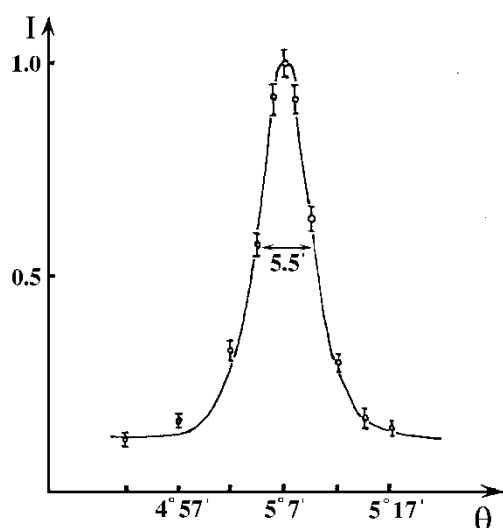Fig.2.12 Angular dependence of the 23.8 keV γ-radiation intensity scattered by a single crystal tin film 5 μm thick.

Dips were observed when Rayleigh scattering was dominant, peaks when the Mössbauer scattering dominated, and dispersion-like
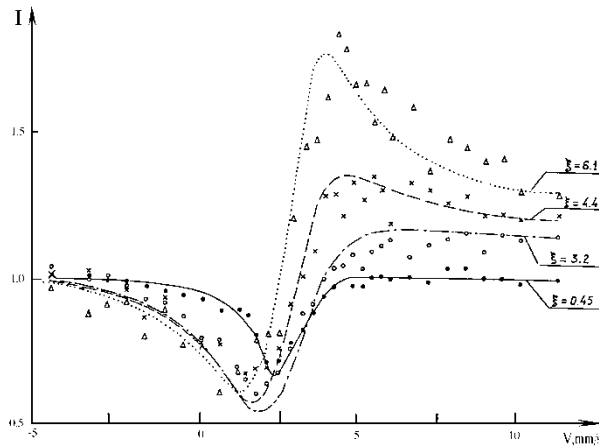
Fig.2.13 Mössbauer diffraction spectrum from a mosaic single crystal of tin (a = 88 %, d = 5 μm) [2.28] : solid circles - T = 293 K, the (020) reflection; open circles - T = 110 K, the (020) reflection; crosses - T = 110 K, the (040) reflection; triangles - T = 110 K, the (060) reflection. The curves have been calculated assuming a mosaic structure of the crystal and are normalized at v = - 6.7 mm/s.

curves were associated with interference when $\mathcal{F}_r \approx \mathcal{F}_R$. At certain scattering angles the phase relationships on scattering from the unit cell may be such that, unlike scattering by a single atom or by a polycrystalline foil [2.19], the interference between Rayleigh and nuclear resonant scattering is constructive for incident energies below resonance and destructive above resonance.

The interference of the elastically scattered radiation gives rise to a mirror reflected wave. The mirror scattered wave intensity becomes significant when the angle of incidence is less than the angle of total reflection - γ_{cr}. This is discussed later in Sec.2.5 where the total reflection of Mössbauer radiation applied for thin surface layer studies is considered.

The diffraction effects are observed when the incident beam of γ-quanta is strongly collimated such that the divergence angle is usually not more than 20". This considerably lowers the radiation intensity and requires long exposures to record statistically reliable spectra. No considerable decrease in the intensities of the scattered radiation is usually observed on departure from Bragg angles. There are many reasons

for that. Not all resonantly scattered radiation is coherent, even for scattering by a single atom. Indeed, if the ground-state spin is not zero the nucleus may, after scattering, be in some other spin state and coherence is lost despite there being no energy loss due to recoil (see Table 2.4). If it is also assumed that a magnetic field H_{eff} causes the levels with spins I_e , I_g to split, then the recoilless resonant scattering of γ-quanta, which is followed by a change of the spin state, is an inelastic (or energy-shifted) and an uncoherent process. The nuclear transition of multipolarity M1 from the ground state with $m_g = +1/2$, into an excited state with $m_e = - 1/2$, may be followed by the elastic transition into the initial state with $m_g = +1/2$, or by the inelastic one into the state with $m_g = - 1/2$ (see Fig.1.3).

The diffraction peaks are significantly influenced by the isotopic abundance and for scatterers with a low enrichment of the resonant isotope an isotopic incoherence results since $\sigma_{coh} \sim a^2$. For ordinary iron $a^2 \approx 5 \ 10^{-4}$. Spin incoherency also reduces the effects related to nuclear diffraction.

Each resonantly scattered γ-quanta may have a coherent counterpart in Rayleigh inelastic scattering which occurs with a probability $f(1 - f_R)$. For this coherence to be realized it is initially necessary that the lattice be in the same state after each of the processes. The total contribution of coherent inelastic scattering also depends on temperature. The contribution is small and may be considered as a second-order process relative to elastic scattering. A contribution to the intensity registered at a Bragg angle by the source recoil radiation arises if elastical scattering resulting from Rayleigh scattering occurs. Incoherent scattering (elastic and inelastic) does not cause any interference effects since it only appears in the background.

To summarize, two physical problems which have been studied in detail due to the progress in nuclear diffraction of Mössbauer radiation must be considered. Firstly, it is dynamical diffraction of Mössbauer radiation. The dynamical theory of Bragg reflection predicts that the reflectivity of a perfect crystal reaches nearly unity within a small angular region around the exact Bragg angle. The width and absolute position of this region is determined primarily by the real part of the scattering amplitude . The existence of the total reflection region near exact Bragg angle results in a broadeing of the effective energy width of the resonance. This occurs because, for a plane wave at the Bragg angle, the reflectivity is always high, even if the range of reflection is small. The energy broadening is significant and of the same order as the splitting of the multiplet [2.30].

At first dynamical diffraction of resonant radiation has been only studied in forward directions. Backward reflections are much weaker than forward reflections in the case of

electronic scattering, because the spatial extension of the atomic shell causes a loss of coherency at large scattering angles. Nuclear resonant scattering, by contrast, is not affected by such a spatial incoherence, and strong reflections are also expected here in backward scattering. Back-reflections in Bragg geometry offer in addition an essential practical advantage: the cross section off the beam accepted by the crystals is usually much larger in the back-reflection geometry than for the forward reflections. Characteristic features of resonant dynamical diffraction appeared in the Mössbauer spectrum of the reflection (3311) from $^{57}FeBO_3$ measured with a high angular resolution [2.31]. A considerable broadening of the resonance peaks and interference between the hyperfine transitions were observed.

Secondly, the suppression of inelastic scattering channels requires attention. The effect is the nuclear resonant analogue of the Borman effect and is realized when a thick perfect crystal containing Mössbauer nuclei is set up at a diffraction angle and the transmittance of the crystal increases when the source velocity is such that the system is brought into resonance. The problem is reviewed in [2.22, 23].

Considerable interest in pure nuclear back-reflections arises also from possible applications in γ -optical devices, such as the filtering of Mössbauer radiation from the white spectrum of synchrotron radiation [2.31 - 35]. The observation of nuclear resonant diffraction of synchrotron radiation has opened a new field of experiments with sub-ìeV beams of high brilliance. The use of pure nuclear back-reflections (with almost total reflectivity in an angular region of 10" - 20") as a pre-monochromator allows more Mössbauer radiation to be extracted from the synchrotron beam. Filtered X-ray beams with extremely narrow band width (10^{-6} - 10^{-8} eV) and small angular width (0.4 arc sec) have been obtained from the synchrotron radiation continuum. Progress in this technique has made it feasible to produce diffracted γ-quanta with intensities unattainable from conventional Mössbauer sources [2.32], thereby increasing interest in hyperfine spectroscopy.

Previously, the nuclear resonance of ^{57}Fe at 14.4 keV was used for pure nuclear Bragg reflection from highly enriched single crystals. Yttrium iron garnet and iron borate are well known examples. In 1990, it was shown that enriched epitaxial crystals provided an alternative to the use of large amounts of expensive bulk isotope for monochromating synchrotron X-ray beams to sub-μeV bandwidths. Later the measurement of coherent nuclear diffraction of synchrotron radiation from grazing- incidence antireflection films (GIAR films) containing ^{57}Fe showed that nuclear resonant filtering by the films was possible.

At present, resonant beams of a few hundreds of photon/sec have been obtained using synchrotron radiation. By optimizing the diffraction techniques and using more intense primary beams expected from undulators in future synchrotron light sources, it is anticipated that beams about 10^5 photons/sec will be obtained [2.33].

This new technique promises to become a powerful tool not only for hyperfine spectroscopy but also for γ-optical experiments. The standard experiment in the future will be the time-resolved observation of forward scattering from a polycrystalline target instead of the pure nuclear reflection from a single crystal which has been used to date. Using the time of excitation, which is known precisely and the spectrum of the delayed resonant quanta from the sample, the hyperfine interaction parameters may be determined within a few hours, even with resonant counting rates of only 1 Hz [2.34].

The use of synchrotron radiation may allow the Mössbauer effect to be observed in new isotopes. Such isotopes would need low-energy excited nuclear levels but need not have appropriate parent nuclei and hence they are not given in Table 1.1.

Additionally, this technique may be especially promising for magnetic field and EFG structure studies in crystals [2.35], and the measurement of the total external reflection of sub-μeV beams of high brilliance may be useful in the analysis of near surface layers (see subcec. 2.5 and 3.8).

2.4. Angular Dependences of the Scattered γ -radiation

The angular dependence of intensities is also important in conventional Mössbauer spectroscopy despite the fact that these dependences are not so sharp as in diffraction. It is of special importance in studies of surface layer where the Mössbauer spectra are the superposition of several partial spectra. For example, if $E_M{}^m(E_Q{}^m) \gg \Gamma_{nat}$ for each of the partial spectra then, since line intensities corresponding to the transition between different sublevels possess different angular dependences, spectra recorded at the scattering angles where these differences are maximized, are easier to interpret.

In another limiting case when $E_M{}^m(E_Q{}^m) \sim \Gamma_{nat}$, it is practically only the analysis of the angular dependence of the resonantly scattered radiation that permits the origin of line broadening in the Mössbauer spectrum to be understood.

Let us find what determines the intensity dependence on the scattering angle in the absence of interference. Suppose that a nucleus gives its excitation energy by a cascade of γ-quanta. The emission of a γ-quantum, followed by a change of the total nuclear momentum by L > 1, results in a definite orientation of the nuclear spin with respect to the direction of the emitted γ-spectrum. Let us assume that the emission of the subsequent γ-quantum occurs immediately after the emission of the preceding one. Radiation from such an oriented nucleus will be anisotropic. If the nuclear orientation is changed by perturba-

tions, the angular distribution of the subsequent γ-quanta will be also changed. The angular distribution of the direction of two successive γ-quanta is independent of whether the two quanta have been emitted or whether resonant scattering has occurred. This has made it possible to use the well developed theory of angular correlations [2.35] in resonant scattering of γ-quanta. In this theory, the directional correlation function W(θ) of resonantly scattered γ-quanta with respect to the direction of the primary beam should be the same as for the two successively emitted γ-quanta in transitions between levels with the same parameters as for the levels corresponding to resonant scattering. There are theoretical expression for the correlation functions W(θ) for all cases of interest [2.37,38]. It should be noted that Mössbauer scattering allows the observation only of the integral time dependence of the angular correlation function, since it is impossible to determine the exact moment of absorption of the incident γ-quantum.

The correlation function W(θ) is determined by the directional distribution of radiation for every γ-transition and by the Clebsh-Gordon coefficients. If the excited nucleus is not affected by any fields changing its orientation, the angular distribution of the γ-quanta for a given transition with respect to a chosen quantization axis is given by

$$F_L(\theta) \sim \sum_{m_e, m_g} P(m_e) \, G(m_e, m_g) \, F_L^M(\theta) \quad , \tag{2.49}$$

where $P(m_e)$ are relative populations of all sublevels m, $F_L^M(\theta)$ is the angular function of γ-rays for the transition between sublevels ($M = m_e - m_g$). Functions $F_L^M(\theta)$ depend only on the radiation multipolarity. For M1 transitions $F_L(\theta)$ is a sum of three terms with the angular dependences

$$F_1^0(\theta) = 3 \sin^2 \theta = 2 - 2P_2(\cos \theta) ,$$

$$F_1^{\pm 1}(\theta) = 3(1 + \cos^2 \theta) / 2 = 2 + P_2(\cos \theta) .$$

If the excited nuclei are randomly oriented, i.e. all the $P(m_e)$ are equal in any coordinate system, it follows from (2.49) that $F_L(\theta)$ is independent of θ and that radiation is isotropically emitted.

Generally, the directional correlation function is determined by the angular function for both the absorption process $(F_L^M(\theta))_a$ and the scattering process $(F_L^M(\theta))_s$. However, it is convenient to choose the direction of the quantization axis to coincide with the direction of the first quantum emitted in a cascade, since the function W(θ) is determined only by the function $(F_L(\theta))$.

For given transition multipolarity the directional correlation function is usually written in the form

$$W(\theta) = 1 + A_{22}P_2(\cos\theta) + ... + A_{k_m k_m} P_{k_m}(\cos\theta).$$ (2.50)

k_m is given by the selection rule $k_m = \min(2I_e, 2L)$. The coefficients A_{kk} can be explicitly calculated since they can be represented by two factors of the same form, each one being determined by the properties of one of the transitions in a cascade. If there are hyperfine fields, either static or fluctuating, a perturbation of angular correlations occurs. In a semiclassical approach, interactions of the nuclear magnetic dipole moment with the magnetic field H_{eff}, or the nuclear electric quadrupole moment with the electric field gradient EFG, result in the appearance of a rotation moment and the nucleus begins to precess about the symmetry axis (the quantization axis). Such changes in the nucleus orientation lead to a change in angular correlations. Coefficients A_{kk} in (2.50) are to be multiplied with the perturbation factors $G_{kk}(t)$, which are, in general, time dependent and depend also on the nature and energy of hyperfine interactions. Expression (2.50) now takes the form

$$W(\theta, t) = \sum_k A_{kk} G_{kk}(t) P_k(\cos\theta)$$

In this approach the random perturbation will not change the shape of the angular correlation function but will only diminish the coefficient at $P_k(\cos\theta)$.

The most important feature of the integrated perturbation factors for a randomly oriented static interaction (i.e. a scatterer of an ideal polycrystallite) is that they have finite lower limits G_{kk}. If the quantization axis is randomly oriented, the integrated angular correlation will not disappear even for very strong static hyperfine interactions in the solid. For axially symmetric fields :

$$G_{kk} = 1 / (2k + 1)$$

For M1 transition $G_{kk} = G_2 = 0.2$.

In a single crystal scatterer the angular distribution is completely determined by the crystal orientation with respect to the scattered radiation. If the direction of H_{eff} or EFG coincides with the direction of the incident radiation, then the relative populations $P(m_e)$ characterizing the nuclei orientation in the scatterer remain constant. At any energy of hyperfine interactions the correlations will be unperturbed. In other cases of static interactions the correlations are perturbed.

For time-dependent hyperfine interactions the angular correlations may vanish completely. Such a situation in the Mössbauer effect for ^{57}Fe is realized in paramagnetic substances. Indeed, the direction of H_{eff} changes stochastically at each nucleus. There are no quantization axes, whose populations could remain constant, hence all the sublevels are equally populated irrespective of the chosen quantization axes. Hence the directional correlation becomes isotropic. Therefore, the Mössbauer γ-quanta resonantly scattered from a scatterer whose Mössbauer spectrum is a single line of width Γ_{nat} will have an isotropic distribution.

Returning to the static hyperfine interactions let us now consider resonant scattering of the magnetic dipole radiation when the overlap of the spectrum components may be neglected. The angular distribution $W_1(\theta)$ of the components' intensities of the quadrupole doublet for the ($\pm 1/2 \rightleftarrows \pm 3/2$) transition, and $W_2(\theta)$ for the ($\pm 1/2 \rightleftarrows \pm 1/2$) transition, may be written as

$$W_1(\theta) = \frac{1}{16}(25 - 15\cos^2\beta_1 - 15\cos^2\beta_2 + 9\cos^2\beta_1\cos^2\beta_2) ,$$

$$W_2(\theta) = \frac{9}{16}(1 + \cos^2\beta_1 + \cos^2\beta_2 + \cos^2\beta_1\cos^2\beta_2) , \tag{2.51}$$

where θ is the angle between vectors k_0 and k_f, angles β_1 and β_2 specify the orientation of k_0 and k_f with respect to the quantization axis.

If the scatterer is an ideal polycrystallite the experimentally observed angular dependence (2.51) is to be averages over all orientations of the EFG tensor to give

$$W_1(\theta) = W_2(\theta) = 1 + 0.05\, P_2(\cos\theta) . \tag{2.52}$$

This means that even when the quadrupole interaction energy is very high, the angular correlations do not vanish completely. If $E_Q^m \approx \Gamma_{nat}$, i.e. on scattering of the γ-quantum with a given energy, the excited state of the scattering nucleus is not known, and the perturbation factor is written [2.39] as:

$$G_2 = 0.2\,[1 + 4\,/\,(1 + E_Q/\Gamma^2)] . \tag{2.53}$$

When $\Gamma_{nat} \leq 2\Gamma_{nat}$, the angular distribution of the resonantly scattered radiation will determined by the nature of line broadening. For example, if the broadening is due to the difference in the isomer shifts caused by nonequivalent positions of the resonant atoms then the angular distribution of the intensity of the scattered radiation will be isotropic. If the broadening is due to small quadrupole splitting the angular distribution is

$$W(\theta) = 1 + 0.25\ G_2\ P_2(\cos\theta)\ , \tag{2.54}$$

where G_2 is given by (2.53), and the anisotropy of the radiation intensity may be large. When the quadrupole interaction energy increases expression (2.54) in the limiting case transforms into (2.52).

The anisotropy of the resonantly scattered radiation also depends on the anisotropy of the factor f' . At $E_Q{}^m < \Gamma$ the factor f' has little effect on the angular dependence. Increasing E_Q requires that the anisotropy of the f' factor be taken into account. Now (2.52) may not be obtained from (2.51) as before since angular dependences of the Mössbauer effect probability in the scatterer should be introduced into the angular dependences of the resonantly scattered radiation (2.51) before averaging. The angular dependences of the scattered radiation intensity are strongly affected by the factor f' anisotropy. This provides an efficient method of experimentally investigating the factor f'.

If the scatterer is an ideal polycrystalline antiferromagnet, where the effective magnetic fields are strong and randomly oriented, the dependence of the intensities on the scattering angle for the first and the sixth lines of the spectra - $W_1(\theta)$, for the second and the fifth lines - $W_2(\theta)$, and for the third and the fourth lines $W_3(\theta)$, are given by the following expressions [2.11,37] :

$$W_1(\theta) = \left(\frac{3}{8}\right)^2 \frac{26 + 2\cos^2\theta}{15}\ ,$$

$$W_2(\theta) = \frac{1}{8}\ \frac{19 + 3\cos^2\theta}{15}\ , \tag{2.55}$$

$$W_3(\theta) = \left(\frac{1}{8}\right)^2 \frac{82 - 6\cos^2\theta}{15}\ .$$

To obtain the spectral line intensities, expressions (2.55) have to be averaged over θ, and for a thin sample the intensity ratios will be $3 : 2 : 1 : 1 : 2 : 3$.

2.5. Mössbauer γ-quanta Scattering as a Method of Surface Study

Let us analyse the line shape of scattering Mössbauer spectra when γ-quanta are detected, and the energy distributions of the resonant quanta. Similar problems for transmission have been considered in Sect. 2.1. Experiments in geometry (Fig. 2.9) are used in a variety of studies, e.g. diffraction, angular correlations, phase analysis. In studies of angular dependences this geometry allows the best angular resolution to be achieved when using large scatterers. We start the analysis with the spectra obtained in this geometry.

Let us make some simplifying assumptions. At first, let there be no splitting of the energy levels in either the source or the absorber. The recoilless part of the source γ-radiation of integral intensity I_0 may be written as

$$I_M(E,S) = \frac{2f}{\pi\Gamma} I_0 L(E,S) \ . \tag{2.56}$$

For this part of the beam it is always necessary to take into account the dependence of the interaction probability on the energy parameters E and S. Unless otherwise stated, the total beam I_0 is normalized to unity. If the energy distribution of the γ-quanta is of prime interest, the normalized beam $J_M(E,S)$ is called the energy distribution of the γ-quanta. This can be used to evaluate the spectral shape and the intensities of the detected radiation which can be obtained by integrating over all the γ-quanta energies. The beam or the intensity of radiation will be denoted by I(S).

The shape of the energy distribution of radiation changes as it penetrates the scatterer. At a certain depth x it is given by

$$J_M(E,S,x) = \frac{2f}{\pi\Gamma} L(E,S) \exp\left[-\mu_a(E) x \csc\gamma_1 \right] \ , \tag{2.57}$$

$$\mu_a(E) = \mu_r(E) + \mu_a \ , \qquad \mu_r(E) = \sigma_0 f' n_a \frac{(\Gamma_a/2)^2 \, W(\theta)}{(E - E_a)^2 + (\Gamma_a/2)^2} \ , \tag{2.58}$$

where $\theta = \gamma_1 + \gamma_2$.

If the energy distribution of the Mössbauer radiation at a depth x is known together with the differential cross sections for all the scattering processes contributing to the detected intensity and the thickness and composition of the scatterer, then the line shape of the Mössbauer spectrum and the energy distribution of the scattered radiation can be found. Both components of the recoilless and non-recoilless resonantly scattered radiation have different energy distributions. Resonant self-absorption of the scattered radiation in the sample may cause the partial contributions of the two components to the resulting Mössbauer spectrum to be quite different from the ratio f'/(1 - f').

Let us consider first the resonant scattering process without the loss of recoil energy and find the energy distribution $J_r(E',S,x)$ for γ-quanta scattered by a layer $dx/\sin\gamma_1$ at a depth x in the scatterer

$$\frac{dJ_r(E',S,x)}{dx / \sin \gamma_1} = n_a \int_{-\infty}^{\infty} J_M(E,S,x) \frac{d^2\sigma}{dE\ dE'}\ dE \ , \qquad (2.59)$$

where n_a is the number of resonant nuclei per unit volume.

For the general case the process cross section in (2.59) is a function of both the incident γ-quanta energy and the energy E' of the γ-quanta emitted as a result of scattering. For an isotropic crystal in the absence of diffraction effects the differential cross section of the process can be written in the form [2.40,41] :

$$\frac{d^3\sigma}{d\omega\ dE\ dE'} = \frac{\gamma}{2\pi}\ \frac{\Gamma_a^2}{4}\ \frac{\sigma_0}{1+\alpha}\ f'^2\ W(\theta)$$
$$\frac{1}{[(E'-E)^2 + \gamma^2/4]\ [(E'-E_0)^2 + \Gamma_a^2/4]} \ , \qquad (2.60)$$

where the function $W(\theta)$ is normalized to 4π , and γ is the ground state width due to the radiation field. The width γ is very small and by appropriate modification of (2.60) may be taken as zero. This is usually done in the following way. As the incident radiation is generally not monochromatic, we can assume it to have a Lorentzian distribution of width Γ. To describe the scattering of this radiation, γ in (2.60) can be replaced by Γ. If the centre of gravity of the energy distribution of the incident radiation $L(E,v)$ is shifted relative to the resonance energy in the scatterer (say, by $5\Gamma_{nat}/2$, as in Fig.2.10a), there will be two lines present in the scattering spectrum at energies E and E_0.

The total differential resonant scattering cross section without recoil energy loss, when the energy distribution $L(E,v)$ of the incident radiation is taken into account, is obtained by integration of (2.60) over the energy of scattered γ-quanta

$$\frac{d^2\sigma}{d\omega\ dE} = \frac{\sigma_0}{1+\alpha}\ \frac{\Gamma_a(\Gamma_a + \Gamma)}{4}\ \frac{f'W(\theta)}{(E-E_a)^2 + [(\Gamma + \Gamma_a)/2]^2} \ . \qquad (2.61)$$

In order to obtain the energy distribution of γ-quanta scattered recoillessly by a layer dx at a parameter S, (2.57) and (2.60) can be substituted in (2.59):

$$\frac{dJ_r(E',S,x)}{dx / \sin\gamma_1} = \frac{\sigma_0 f'^2 f \Gamma \Gamma_a^2 n_a}{8\pi(1+\alpha)}$$

$$\frac{\exp[-\mu_a(E')x \csc\gamma_1] \, d\omega}{[(E'-E_s-S)^2+\Gamma^2/4] \, [(E'-E_a)^2+\Gamma_a^2/4]} \, W(\theta) \,, \qquad (2.62)$$

where $d\omega$ is the solid angle within which the source radiation reaches the scatterer. The energy distribution of the γ-quanta which reaches the detector from the scatterer of thickness d_a, is obtained from (2.62) multiplied by the probability of the radiation leaving the scatterer at an angle γ_2 (Fig. 2.9), and integrated over x from 0 to d_a:

$$J_r(E',S) = \frac{D \, \sigma_0 f f'^2 n_a \Gamma \Gamma_a^2 \, W(\theta)}{8\pi \, \sin\gamma_1}$$

$$\frac{F_r'}{[(E'-E_s-S)^2+\Gamma^2/4] \, [(E'-E_a)^2+\Gamma_a^2/4]} \,, \qquad (2.63)$$

where

$$F_r' = \frac{1 - \exp[-\mu_a(E')d_a \, (\csc\gamma_1 + \csc\gamma_2)]}{\mu_a(E') \, (\csc\gamma_1 + \csc\gamma_2)} \,, \qquad (2.64)$$

$$D = d\omega \, d\omega'/ (1+\alpha) . \qquad (2.65)$$

$d\omega'$ is the solid angle within which the γ-quanta emitted by the scatterer reach the detector. It is to be noted that the factor D causes the substantial drop in the count rate of the γ-quanta in scattering experiments as compared to those performed in transmission mode. The shape of the energy distribution of the scattered γ-quanta substantially depends on the factor F_r' determined by the experimental geometry.

The calculated distribution for bulk scatterers when all backscattered radiation is detected are presented in Fig. 2.14.

The isomer shift δ and the ratio of linear coefficients for resonant and nonresonant interactions x = μ_r/μ_a are the tabulated parameters. The value of μ_r in this case is determined by the enrichment of the resonant isotope. Energies are given in units of $\Gamma_{nat}/2$. A comparison of the dependences shown in Figs. 2.10a and 2.14.2 shows that the interaction of γ-radiation with matter must be taken into account when a real sample, as opposed to the hypothetical case of a single atom scatterer, is considered.

A scatterer can be called thin if the following relation holds

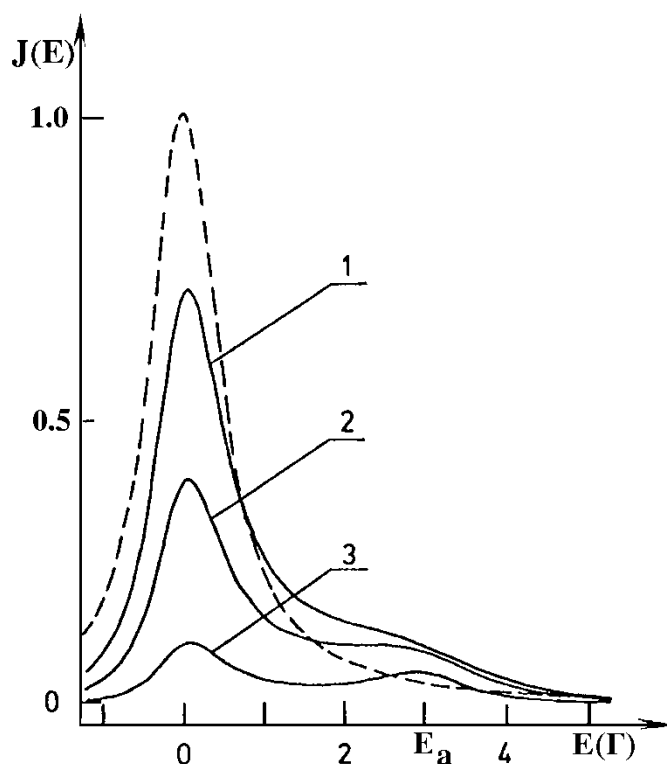$$t_s = (t_a + t_a^e) \csc\gamma_1 + b \csc\gamma_2 \ll 1 \ . \tag{2.66}$$

Fig.2.14 Energy distribution of γ-quanta scattered by a bulk sample of non-magnetic iron at different [57]Fe abundances. The dashed curve is calculated for x = 128, curve 1 - for x = 8, curve 2 - for x = 4, curve 3 - for x = 1. The zero energy corresponds to the centre of incident radiation spectrum. For convenience the intensities of curves 1 - 3 are enlarged by a factor of 3.

In Mössbauer scattering spectroscopy the effective Mössbauer sample thickness t_a (see (2.8) and (2.23)) used in

transmission spectroscopy together with two more analogous parameters: $t_a^e = \mu_a d_a$; and $b = \nu d_a$, where ν is the linear absorption coefficient for the detected radiation, must also be considered. The spectrum line shape from thin scatterer (2.64) can be described by the following expression:

$$I_r(S) = \frac{D t_a ff'^2 \Gamma \Gamma_a^2}{8\pi \sin\gamma_1} \int_{-\infty}^{\infty} \frac{W(\theta)\, dE'}{[(E' - E_s - S)^2 + \Gamma^2/4][(E' - E_a)^2 + \Gamma_a^2/4]} \quad . \tag{2.67}$$

Since in this case the lines in the source and the scatterer are Lorentzian, the integral in (2.67) has the value:

$$\int_{-\infty}^{\infty} \frac{dE'}{[(E' - E_s - S)^2 + \Gamma^2/4]\ [(E' - E_a)^2 + \Gamma_a^2/4]}$$

$$= \frac{8\pi}{\Gamma \Gamma_a (\Gamma + \Gamma_a)} \ \frac{1}{1 + \left[\dfrac{2(S - \delta)}{\Gamma + \Gamma_a}\right]^2} \quad . \tag{2.68}$$

If the scatterer is thin, the contribution of the recoillessly scattered γ-quanta into the Mössbauer spectrum is

$$I_r(S) = \frac{D\, t_a ff'\, W(\theta)}{\sin\gamma_1}\ \frac{\Gamma_a}{\Gamma + \Gamma_a}\ \frac{1}{1 + \left[\dfrac{2(S - \delta)}{\Gamma + \Gamma_a}\right]^2} \quad . \tag{2.69}$$

If the finite thickness of the scatterer is taken into account, the expression for the line shape becomes much more complicated. However, the expression for $I_r(S)$ can be written in the form:

$$I_r(S) = D\, t_a ff'\, W(\theta)\ \frac{F_r(2S/\Gamma_a, \beta_r, Q, \Gamma/\Gamma_a)}{1 + \sin\gamma_1\ \csc\gamma_2} \quad , \tag{2.70}$$

$$\beta_r^2 = 1 + t_a/\mu_a \quad ; \quad Q = \mu_a d_a(\csc\gamma_1 + \csc\gamma_2) \quad .$$

If the detector registers only nonrecoillessly scattered γ-quanta the beam of γ-quanta $I_{rn}(S)$ can be described by an expression analogous to (2.69) with the exception that f' must be replaced by (1 - f'). These quanta cannot be resonantly absorbed. For the thin absorber the intensities ratio is:

$$I_r(S)/I_{rn}(S) = f'/(1 - f') .$$
(2.71)

To obtain $I_{rn}(S)$ which is the contribution of the resonantly scattered nonrecoilless γ-quanta in the total spectrum, it is necessary to make the following substitutions: (1 - f') for f', $F_{rn}(S)$ for $F_r(S)$ and $\beta_{rn}^2 = 1 + t_a/\mu_a(1 + \sin\gamma_1 \csc\gamma_2)$ for β_2^2. The functions $F_r(S)$ and $F_{rn}(S)$ have been calculated for various absorbers and thicknesses and are tabulated elsewhere [2.29]. The tables and plots for $F_{rn}(S)$ can be used for any radiation where the attenuation in the scattering material follows the exponential law. This means that the formalism may also be used when scattered X-rays are detected.

It is now necessary to consider the situation when hyperfine interactions are present, the excited level splitting is such that the distance between the sublevels is much greater than Γ, and the interference effects on scattering from different sublevels are neglected. The resonant scattering occurs at energies $E_{ij} = E_j^e - E_i^g$ which are allowed by the selection rules (see Fig.1.3). The distance between the two ground-state sublevels is denoted by $\Delta_{ii'} = E_i^g - E_i^g$.

It is now possible to consider various contributions to the total spectrum recorded for the sample of α-iron and study the effects of the thickness of the scatterer and of the resonant isotope abundance on the line shape of the experimental spectra, the relative line intensities, and the effects on these of saturation phenomena. The most thorough methodology studies have been carried out by BALKO and HOY [2.41,43] and BARA et al [2.44,45]. The linear resonant scattering coefficient in the presence of hyperfine splitting is

$$\mu_r(E) = \frac{\Gamma_a^2 \, \sigma_0 f' n_a}{4} \sum_{i,j} \frac{W_{ij}(\theta_1, \varphi_1)}{(E - E_{ij})^2 + \Gamma_a^2/4} ,$$
(2.72)

where θ_1 and φ_1 are the polar and azimuthal angles of γ-rays incident upon the scatterer. The directional correlation function $W_{ij}(\theta_1, \varphi_1)$ for the transition of energy E_{ij} is determined by the corresponding $F_L^M(\theta)$ angular functions. The energy distribution of resonantly scattered recoilless γ-quanta

is determined as before (2.59). However, there is in this situation no unique relation between the energies of the incident and scattered γ-quanta. The scattered quantum may have the energy E' = E of the incident quantum, as well as the energy E' = E - $\Delta_{ii'}$. If θ_2, φ_2 are the polar and azimuthal angles for the scattered γ-rays, the differential resonant scattering cross section when the Lorentzian distribution of the incident radiation is taken into account can be written as

$$\frac{d^3\sigma}{dE\,dE'\,d\omega} = \frac{\sigma_0 f'^2 \Gamma \Gamma_a^2}{8\pi(1 + \alpha)}$$

$$\sum_{i,j,i'} \frac{W_{ij}(\theta_1\varphi_1)\,W_{ji'}(\theta_2,\varphi_2)}{[(E - E' + \Delta_{ii'})^2 + \Gamma^2/4][(E' - E_{ij} - \Delta_{ii'})^2 + \Gamma_a/4]} . \quad (2.73)$$

Let us assume that the correlation functions $W_{ij}(\theta,\varphi)$ are axially symmetric and normalized. The summation in (2.73) is over all the transitions allowed by the selection rules. If the allowed excitation of a sublevel takes place with energy E_j^e , corresponding to the transition $E_i^g \rightarrow E_j^e$ (see, for example transition 3 in Fig.1.3), the decay of the level is possible via the $E_j^e \rightarrow E_i^g$ and $E_j^e \rightarrow E_i^g$ transitions (solid arrows in Fig.1.3). Thus, for scatterers with hyperfine split levels, the energies E of incident- and E' of scattered - γ -quanta may be different. If the source radiation has Lorentzian line shape and the factor f is assumed to be anisotropic (2.59), integration over E gives expression in the form [2.41] :

$$\frac{dJ_r(E',S,x)}{dx\,/\,\sin\gamma_1} = \frac{\sigma_0 n_a f f'^2 \Gamma \Gamma_a^2}{8\pi(1 + \alpha)}$$

$$\sum_{i,j,i'} \frac{W_{iji'}(\theta)\,e^{-\mu_a(E' - \Delta_{ii'})\,\csc\gamma_1 x}\,d\omega}{[(E' - \Delta_{ii'} - E_s - S)^2 + \Gamma^2/4][(E' - E_{ij} - \Delta_{ii'})^2 + \Gamma_a^2/4]} , \quad (2.74)$$

where θ - is the angle between vectors $\underline{k}_0$ and $\underline{k}_f$. If splitting of the levels is such that interference of Mössbauer scattering from different sublevels may be neglected (see Sec. 2.3), the energy distribution of γ-quanta from a scatterer with thickness d_a is obtained by integration of (2.74) over x from 0 to d_a :

$$J_r(E',S) = \frac{D \ a_r \sigma_0 n_a f f'^2 \Gamma \ \Gamma_a^2}{8\pi}$$

<div align="right">(2.75)</div>

$$\sum_{i,j,i'} \frac{W_{iji'}(\theta) \ F_r'}{[(E' - \Delta_{ii'} - E_s - S)^2 + \Gamma^2/4][(E' - E_{ij} - \Delta_{ii'})^2 + \Gamma_a^2/4]},$$

where the function F_r' is determined by an expression analogous to (2.64)

$$F_r' = \frac{1 - \exp\left\{-d_a[\mu_a(E' - \Delta_{ii'}) \ csc\gamma_1 + \mu_a(E') \ csc\gamma_2]\right\}}{\mu_a(E' - \Delta_{ii'}) \ csc\gamma_1 + \mu_a(E') \ csc\gamma_2},$$

<div align="right">(2.76)</div>

where a_r is a constant determined by the particular experimental set-up [2.41].
The Mössbauer spectrum of the resonantly scattered recoilless γ-quanta is given by

$$I_r(S) = \int_{-\infty}^{+\infty} J_r(E',S) \, dE'$$

<div align="right">(2.77)</div>

The Mössbauer spectrum $I_{rn}(S)$ due to nonrecoillessly scattered γ-quanta may be obtained by replacing f'^2 by $f'(1 - f')$ and the function F_r' in (2.77) by the function F'_{rn} :

$$F'_{rn} = \frac{1 - \exp\left\{-d_a[\mu_a(E' - \Delta_{ii'}) \ csc\gamma_1 + \mu_a \ csc\gamma_2]\right\}}{\mu_a(E' - \Delta_{ii'}) \ csc\gamma_1 + \mu_a \ csc\gamma_2}.$$

<div align="right">(2.78)</div>

It is important to note that Rayleigh scattering of the resonant radiation also contributes to the Mössbauer spectrum. The contributions should be distinguished - the elastic Rayleigh scattering of Mössbauer quanta $I_R(S)$ and the inelastic Rayleigh scattering $I_{Rn}(S)$ (see Table 2.4):

$$I_R(S) = \frac{a_R f f_R n' \Gamma \ d\omega \ d\omega' \ W(\theta)}{2\pi(1 + \sin\gamma_1 \ csc\gamma_2)}$$

$$\int_{-\infty}^{\infty} \frac{1 - \exp\left[-\mu_a(E') \, d_a \, (\csc\gamma_1 + \csc\gamma_2)\right]}{\left[(E' - E_s - S)^2 + \Gamma^2/4\right] \mu_a(E')} \, dE' \, , \qquad (2.79)$$

$$I_{Rn}(S) = \frac{a_R f(1 - f_R) \, n' \, \Gamma \, d\omega \, d\omega' \, W(\theta)}{2\pi \, \sin\gamma_1}$$

$$\int_{-\infty}^{\infty} \frac{1 - \exp\left\{-\left[\mu_a(E') \csc\gamma_1 + \mu_a \csc\gamma_2\right)\right]d_a\right\}}{\left[(E' - E_s - S)^2 + \Gamma^2/4\right]\left[\mu_a(E')\csc\gamma_1 + \mu_a\csc\gamma_2\right]} \, dE' \, , \qquad (2.80)$$

where n' is the number of scattering atoms per unit volume.

Expressions (2.79) and (2.80) were initially used in [2.41] which considered scattering at 90° when $f_R = f'^2$ and the value of the angular term $W(\theta)$ was included in the constant a_R which is determined by the Rayleigh scattering cross section and the experimental set-up.

It is convenient to represent the experimental Mössbauer spectrum as the result of the combined action of four processes. If the fraction f is considered of γ -quanta recoillessly emitted from the source, then the total intensity of Mössbauer scattering at a velocity v may be written [2.41] in the form:

$$I(S) = I_r(S) + I_{rn}(S) + I_R(S) + I_{Rn}(S) \, . \qquad (2.81)$$

The contributions of the individual processes will be analysed in more details in Chapter 4. In backscattering geometry it is necessary to simply integrate over x. The spectra to be expected from (2.81) may be considered by examining an iron powder enriched in ^{57}Fe (a = 91 %) with parameters t_a= 153, f' = 0,7, μ_a = 205 cm^{-1}, and subjected to the calculations described in [2.41]. Difficulties in computation are at the last stage when it is not possible to integrate explicitly (2.75) over E' . The calculations may be substantially simplified by assuming that the radiation which is incident on the scatterer is monochromatic, i.e. Γ = 0. The results are presented in Fig.2.15 and 10^{-3} of the incident radiation intensity is taken as a unit of the scattered radiation intensity.

A characteristic feature of the spectra recorded from elastic resonant scattering as compared with spectra recorded in transmission experiments is the unusual effect of the

scatterer thickness on the line amplitudes. The amplitudes of all the lines approach different limiting values with that of the second line becoming the largest. The reason concerns the velocity v_2 which corresponds to the centre of the second spectral line. At this velocity the scattered radiation $J_r(E', v_2)$ consists of two components contributing to the intensities of the second and fourth lines of the spectra (Fig.1.3). The second component of the scattered radiation is less resonantly scattered than the first component (see Table 2.3). A nonresonant detector would register both components with equal probability. Hence, if attenuation of the scattered beam on the way to the detector is not taken into account the radiation penetration appears to increase and the amplitude of the second line increases as compared to scattering from a single atom. The opposite is true if scattering is at a velocity corresponding to the forth line and penetration of the elastically scattered radiation $J_r(E', v_4)$ appears to decrease in comparison with transmission experiments.

Nonrecoillessly scattered γ-quanta are not resonantly scattered on the way to the detector, and the amplitudes of all the lines of the spectrum $I_{rn}(S)$ are approximately equal.
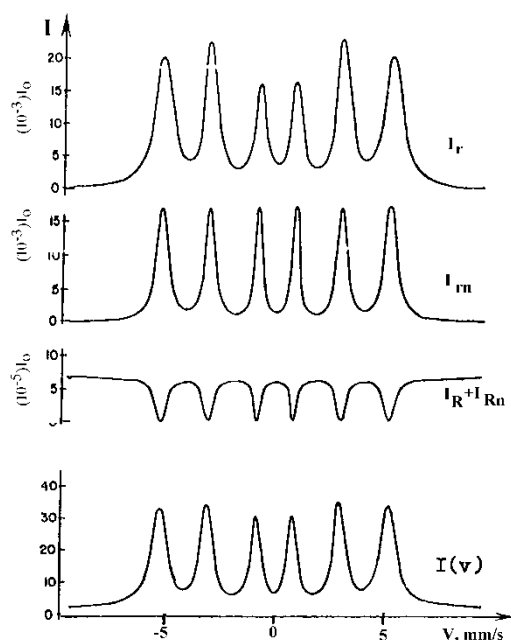

Fig.2.15 Calculated Mössbauer scattering spectrum I(v) and separate contributions to it [2.41].

At resonance velocities the count rate of γ-quanta scattered by electrons is at a minimum. This occurs because the Rayleigh scattering cross section is independent of energy in the energy region of interest: $E_0 \pm 1000\ \Gamma$. The incident γ-quanta passing through the scatterer are strongly attenuated at resonance energies, and the number of γ-quanta capable of Rayleigh scattering on resonance is therefore considerably less than at non-resonant conditions.

Although, we are considering here a thick scatterer enriched in ^{57}Fe, the total intensity of the scattered quanta even for such an ideal case will not exceed several percent of the incident intensity. For nonenriched scatterers the relative contribution of Rayleigh scattering into the total spectrum will be appreciably more than in the case being considered here.

The calculated spectra for thick scatterers of natural iron which correspond to the scattering of monochromatic radiation show neither significant line broadening nor saturation effects. However just the opposite is true for the enriched samples. This can be illustrated by considering the same scatterer but with a = 90 % ^{57}Fe. As the linear coefficient μ_a increases and at
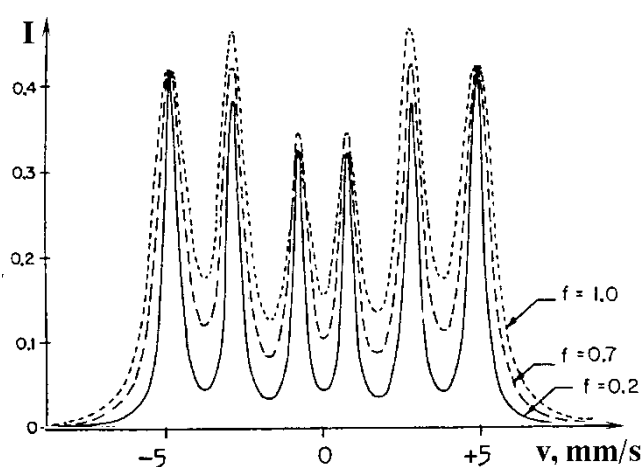

Fig.2.16 Calculated effect of the factor f' on the line shape of scattering Mössbauer spectra. The absorber is iron powder (a = 91 %; $\mu_a = 200$ cm^{-1}; $t_a = 175$). The spectra are normalized such that the intensities of the first lines are the same [2.41].

constant values of f' and t_a the lines of the Mössbauer spectrum become narrower because the contribution from deeper layers of the sample is less. As the f' factor increases and at constant values of μ_a and t_a the lines are significantly broader (Fig. 2.16) since the situation is equivalent to a higher enrichment of the resonant isotope in the scatterer.

Any attempt to observe the Mössbauer effect in scattering geometry, using only the principles of transmission experiments, would usually produce unsatisfactory results. Even with a scatterer of α-^{57}Fe (see Fig. 2.9) the magnitude of the effect would be in the order of 10 %. A successful experiment requires the proper collimation of the incident and scattered beams and correct distances between the source, the scatterer and the detector. Experience in Mössbauer scattering spectroscopy shows that the optimal geometry is realized in an experimental set-up where the removal of the sample under investigation results in only the γ-radiation caused by single scattering cannot reach the detector. In such a geometry the observed effect in α-^{57}Fe foils is between 150 % and 250 % .

The γ-spectra resulting from the scattering of radiation from a ^{57}Co (Cr) source by a 9 μm α-^{57}Fe foil are shown in Fig. 2.17. There are no filters between the source and the scatterer or between the scatterer and the detector. The solid circles show the amplitude spectrum obtained at a velocity near v_1. Open circles depict the spectrum at $v = 0$.
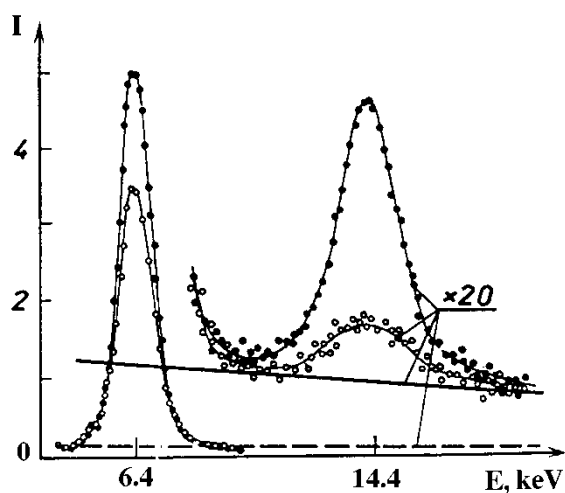

Fig. 2.17 Pulse-height spectra of the ^{57}Co radiation scattered from α-Fe.

The background measured in the absence of the scatterer is given by the solid line. The background detected in the absence of the source is represented by the dashed line. All the lines correspond to the same measuring time and are characteristics of the experimental conditions. The observed effect for the first line of the sextet is about 250 %.

By decreasing the diameter of the collimator and increasing the distance it is possible to exclude the γ-quanta resulting from multiple scattering. This gives an increase in the observed effect but with a decrease in intensity. Examples of this technique are given elsewhere [2.44, 45] where, using a geometry similar to that shown in Fig. 2.9 and with proper collimation, the dependence of the magnitude of the effect on the thickness of ^{57}Fe enriched and nonenriched iron and haematite scatterers have been studied.

Three Mössbauer spectra were recorded simultaneously using scintillation counters. These were the transmission spectrum and both γ- and X-rays scattering spectra. The authors succeeded in substantially lowering the background to obtain a large ε(0) value.

The dependence of the effect ε(0) and the intensities on the thickness of a haematite scatterer are shown in Fig. 2.18 [2.45]

$$\varepsilon(0) = [I(0) - I(\infty)]/ I(\infty) . \tag{2.82}$$

It can be seen that in Mössbauer scattering spectroscopy the maximum effect is observed for the thinnest sample. The largest effect can be observed when the resolution of the detector is high and when it is properly shielded from the hard radiation of the source and from the quanta scattered from surroundings such as the walls of the collimator.

The γ-quanta emitted nonrecoillessly from the source also contribute to the total intensity as a result of Rayleigh scattering and the Compton effect. The fraction of these quanta is (1 - f) and the contribution I_{R+C} is independent of the Doppler energy shift. Therefore, in [2.45] an expression is given for I(S) which contains five terms:

$$I(S) = I_r(S) + I_{rn}(S) + I_R(S) + I_{Rn+C}(S) + I_{R+C} . \tag{2.83}$$

In the authors' opinion (2.83) is more adequate than (2.81), since it more thoroughly accounts for the interaction of the scattered radiation with the sample. Resonant scattering has different effects on the first four contributions defined in (2.83) to the total Mössbauer spectrum. Thus, $I_r(S)$ depends on resonant scattering when radiation passes into the sample as well as on its way back to the detector. It could be important for selective excitation when the resonant interaction cross sections for the incident and scattered γ-quanta may not be the same.
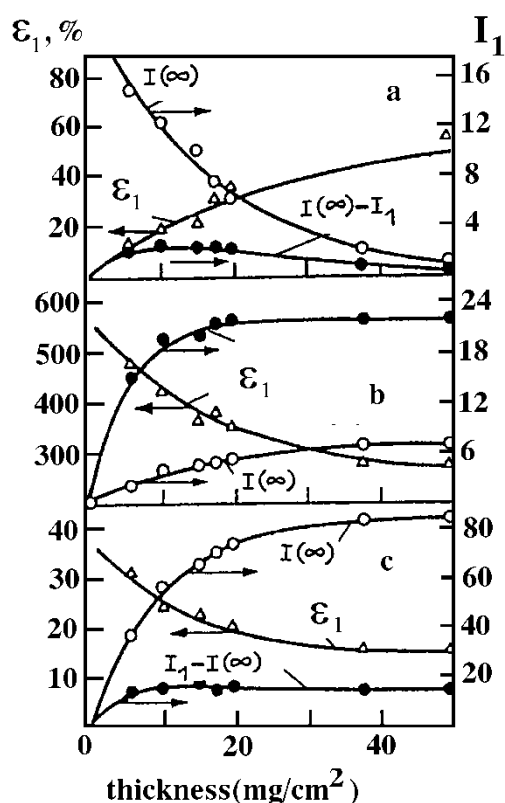
Fig. 2.18 Dependences of the effect value ε_1 and radiation intensities on the sample thickness for the Mössbauer spectrum of haematite (a = 80 %) [2.45]. a - transmission; b and c - scattering (b - γ-rays, c -X-rays).

The terms in (2.83) have their own angular dependences and, in addition, interference is possible between Mössbauer and Rayleigh scattering. However, on considering the angular distribution for I(S), all the interference effects in experiments of interest are usually neglected. There are two reasons for this. First, the contribution of interference to the total intensity is usually small. Second, the requirement to obtain a sufficient count rate leads to the use of large solid angles causing the interference effects to "smear out". It must also be remembered that there is no interference if the energy of the incident γ-quanta corresponds exactly to a resonant absorption peak.

The calculated [2.45] $\varepsilon(v_1)$ values are given in Fig. 2.19 for monochromatic source γ-radiation in transmission and scattering experiments as a function of the thickness of an iron sample for a = 2 % and 100 %, and for a series of hypothetical values of μ_a. The results show good agreement between the calculated results and the experimental data of Fig.2.18.

If relaxation processes or hyperfine interactions occur in the scatterer the interpretation of conventional scattering (or transmission) experiments is often complicated and the results are ambiguous. If the interpretation is possible the information on $\mu_a(E)$ ($\sigma_a(E)$) is usually obtained. The information on $\mu_a(E)$ alone does not help in detailed studies of hyperfine interactions in the samples mentioned above. Of much more help is any direct information on the differential cross sections (see e.g., (2.73) and (2.75)) which are a function of the incident and scattered γ-quanta energy. The incident γ-quanta energy should be fixed and the energy spectrum $J'(E', v_i)$ observed to show directly the energy change of γ-quanta on scattering. If there is no phonon spectrum excitation:
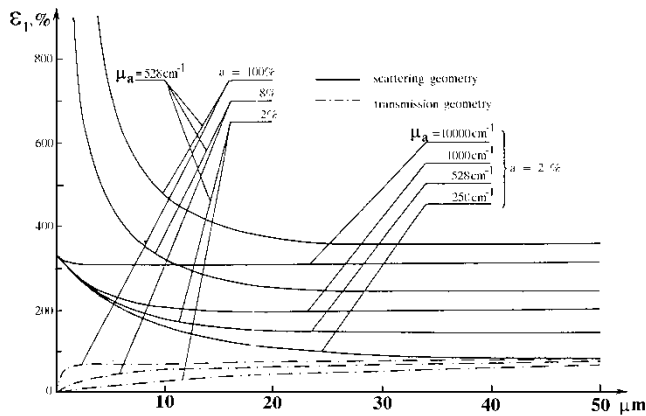
$$J'(E',v_i) = J_r(E',v_i) + J_R(E',v_i) . \tag{2.84}$$

Fig.2.19 Dependence of the effect value ε_1 of the Mössbauer spectrum of iron on the sample thickness d in scattering experiments (solid lines) and in transmission experiments (dashed lines). For samples of natural abundance, hypothetical cases of different μ_a have been considered.

The scattering angle $\theta = 90°$ should be taken for the minimum interference contribution. For a thin scatterer $J_R(E', v_i)$ is always Lorentzian (see Fig. 2.10c). The $J_r(E',v_i)$ distribution gives the necessary information and for a thin sample may be written as

$$I(v,v_i) = \int_{-\infty}^{+\infty} J'(E',v_i)[1-\mu'_a(E',v)d]\, dE' \,, \tag{2.85}$$

where $\mu'_a(E',v)$ is the total linear scattering coefficient in the "analyzer" moving at a velocity v, and d is the "analyzer's" thickness.

It is desirable that the $J'(E', v_i)$ distribution should not be different from the $J_r(E', v_i)$ distribution. For this purpose a constant velocity v_i is chosen so that the incident radiation is on resonance with one of the scatterer's lines. Rayleigh scattering contributes only to the amplitude of the elastic resonant scattering, does not change the line shape, and cannot result in misleading information.

To obtain the $I(v, v_i)$ dependence a γ-ray detector is needed with an energy resolution of approximately Γ_{nat}. For this purpose a resonant filter is placed in front of a conventional detector. This filter is a "single line" Mössbauer absorber and an enrichment in the resonant isotope is desirable. Driving the filter ("analyzer") in the constant acceleration mode and detecting the outgoing radiation allows the $I(v, v_i)$ spectrum to be produced (see Fig. 2.20). The observed effect is determined now by the two elastic resonant scattering processes (by four f factors). Two synchronized drive system are necessary to observe the two scattering processes. This is known as selective excitation double Mössbauer spectroscopy (SEDMS) [2.46 - 48].

The method is demonstrated by considering the SEDM spectrum recorded at $v_i = v_2$ from a 9 μm thick iron foil with a = 90 % ^{57}Fe (Fig. 2.21), that is for scattering at the energy corresponding to the -1/2 $\rightarrow$ -1/2 transition in the scatterer (Fig. 1.3). The Mössbauer spectrum $I(v,v_i)$ consists of the second and fourth lines of the usual spectrum of α-Fe, i.e. the lines corresponding to the -1/2 $\rightarrow$ -1/2 transition as well as to the -1/2 $\rightarrow$ +1/2 transition. The method has been applied to determine the f' factor for the first time in stainless steel [2.46]. Time-dependent effects have subsequently become the main field for SEDMS research [2.49, 50].

A SEDMS theory for time-independent hyperfine interactions has been given elsewhere [1.4, 2.43] and all the necessary energy distributions and SEDM spectral components have been
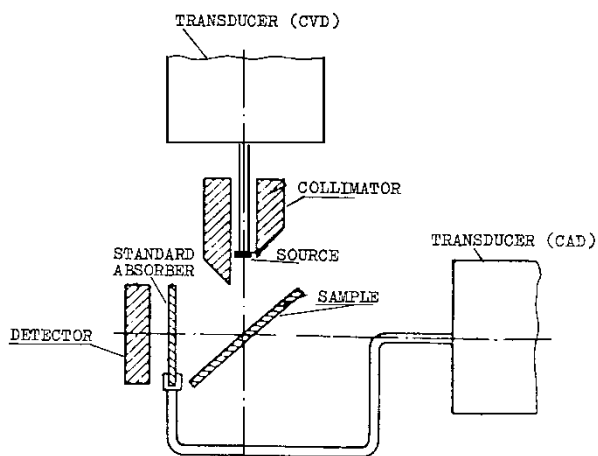
Fig.2.20 A schematic experimental arrangement used for Selective Excitation Double Mössbauer Spectroscopy.

considered. Three processes have been taken into account: resonant- and Rayleigh-scattering, and γ-rays absorption in the scatterer due to the photoeffect. The scattering angle has been selected as 90°. It has been shown that in the experimental spectra a line is always observed at an energy that is exactly equal to the energy of the incident γ-quanta. If this energy coincides with a transition energy in the scatterer, one more fairly intensive line may also appear in the spectrum.
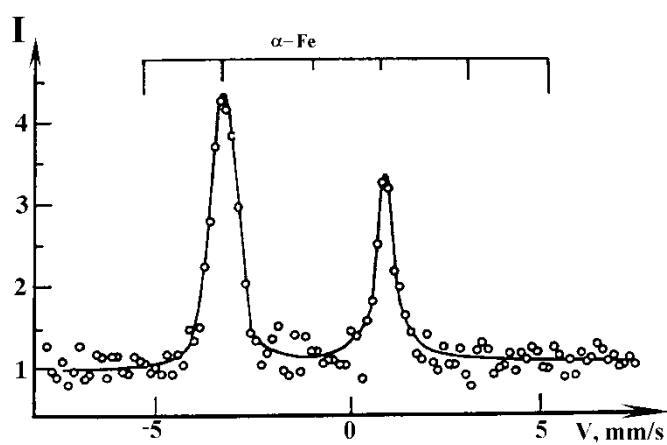

Fig.2.21 SEDM spectrum of α-Fe.

Energies of the incident γ-quanta which are much different from the transition energy in non-enriched scatterers result in the Rayleigh scattering contribution becoming so dominant that in the spectrum a line due to Rayleigh scattering occurs [2.51]. The Rayleigh scattering can be separated out and studied by SEDMS in a different manner. For example, if the velocity v_i is set to excite the -1/2 → -1/2 transition then the corresponding line in a SEDM spectrum will contain the Rayleigh scattering contribution although the line -1/2 → +1/2 that is observed in the same spectrum will not contain the contribution. By considering all the parameters affecting the line intensity ratio in the Mössbauer effect the Rayleigh scattering cross section can be obtained.

The main advantage of SEDMS is that the method offers a direct means by which the relaxation processes between sublevels of the excited nucleus can be observed. Indeed, the experimental spectrum $I(v,v_i)$ gives direct information on time- dependent hyperfine interactions which determine the nuclear level splitting. The relaxation times in the region of 10^{-7}- 10^{-10} sec are the most convenient to measure. The first studies in this field have been connected with the Morin transition in haematite. In the vicinity of the Morin temperature T_M there is a 90° change in the direction of spins of iron atoms [2.43]. Below T_M the spins of iron atoms are parallel to the [111] direction, above T_M they are in the (111) plane. Two different Mössbauer spectra correspond to these different orientations (see Fig.2.22). In the transmission spectrum taken at T = 298 K, i.e. above T_M, the sixth line is at v = 8.34 mm/sec (Fig. 2.22.a), and in the spectrum taken at 77 K (below T_M) this line is at v = 9.2 mm/sec (see Fig. 2.22.f). Near T_M (parts of the transmission spectrum, taken at 269.5 K; 265 K; 263.5 K and 261 K are given in Figs. 2.22.b - 2.22.e) the sixth line is significantly broadened and distorted. This may be due to either the existence near T_M of two ionic states with different orientations of the magnetic field direction with respect to the crystallographic axes, or to relaxation phenomena. SEDMS experiments allow these two possibilities to be examined. An experimental spectrum is given in Fig. 2.23 in which the calculated spectrum is shown in the absence of relaxation by the dashed line. The arrow shows the source velocity. The value of the relaxation time in haematite at 263.5 K is $(1.1 \pm 0.2) \cdot 10^{-7}$ sec.

A recent development in SEDMS line shape calculations is the superoperator approach [2.52]. This has made possible the analysis of the effects of various parameters and experimental conditions on the line shape. In studies of a classical paramagnetic tris-(pyrrolydine)dithiocarbamate Fe(III), (TPDC [Fe(III)]), which can be described by any of three possible relaxation models, one has been chosen [2.53]. The authors have shown the relaxation processes to depend on the sample temperature.
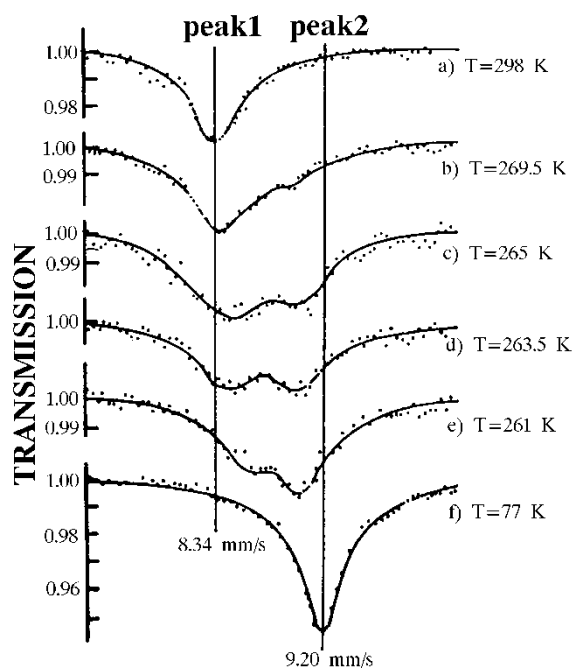
Fig.2.22 Transmission Mössbauer spectra from a thin sample of haematite (a = 90 %) in the vicinity of line VI (see text).
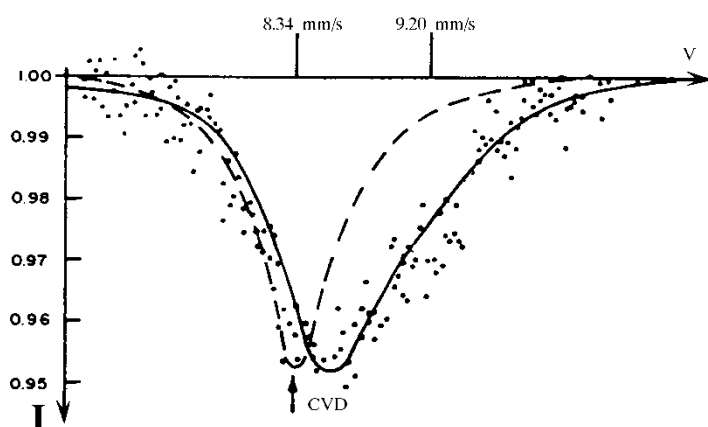

Fig.2.23 SEDM spectrum from a thin haematite sample at 263.5 K. The spectral line shape is given by the solid line calculated for a relaxation time of $1.1 \cdot 10^{-7}$ s.

Thus, at 5.4 K the relaxation is due to transitions between the sublevels of the Kramers doublet corresponding to the ground state. The relaxation rate was found to be in the order of $5 \cdot 10^9$ sec^{-1}. The use of ordinary Mössbauer transmission spectroscopy for similar systems does not permit the selection of the correct relaxation model from several possible ones.

To summarize, it should be noted that SEDMS has some substantial limitations connected with the insufficient strength of Mössbauer sources. The necessity to have two successive resonant interaction processes results in a very low detected intensity. Indeed, the second part of a SEDMS experiment is a transmission experiment with the scatterer being the Mössbauer source. If the levels are split, even for a scatterer enriched in the resonant isotope, the intensity of this source is not more than a percent of the intensity reaching the scatterer from the source. The observed effect in such a transmission experiment with an enriched analyzer is about 10 % (see Fig. 2.23). This means that studies of samples with only natural abundances of Mössbauer isotopes are very time-consuming.

Resonance detectors have been successfully used in Mössbauer emission spectroscopy. Since SEDMS experiments require the energy analysis of the Mössbauer radiation when the scatterer is the source, the use of a resonance detector as the "analyzer" allows a better signal-to-background ratio. A spectrum given in Fig. 2.21 is not typical for SEDMS experiments (cf. Fig. 2.23). It is taken using a resonance detector and the observed effect is several hundred percent. The effect with an ordinary Mössbauer source (without any scatterer) is about 1500 %. Most important in the use of resonance detectors in SEDMS is the low noise level. Thus, the use of a scintillation resonance detector, which is conveniently used in transmission experiments, is not efficient in SEDMS due to the high noise level of the detector. The use of gas-filled resonance detectors allows a shortening of the measuring time by a factor of 9 with the same statistic accuracy. Such resonance detectors can be made very light and the detector itself can be driven. Massive samples of any form may be studied, and SEDMS is a convenient technique in applied fields where the observed spectra are more complicated.

As noted in Sect. 2.3, one of the interference phenomena, the total reflection of γ-rays, may be used for studies of very thin surface layers. It is known that if electromagnetic radiation falls onto a mirror surface characterized by the complex index of refraction n = 1 - σ - iβ at a glancing angle $\gamma_1 \leq \gamma_{cr} \leq \sqrt{2\delta}$ the reflectivity R, i.e. the ratio of the reflected and incident intensities, becomes equal to unity [2.5, 11]. For real media there is always some absorption and the imaginary part of the index of refraction is not zero. However, if the R value rises sharply when γ_1 becomes less than γ_{cr} the situation is described as total external reflection (TER). The coherent amplification of the scattered wave under conditions of TER is analogous to diffraction on scattering   from   single

crystals. The index of refraction depends on the coherent scattering amplitude $\mathscr{F}_{coh}(\underline{k}_0 = \underline{k}_f)$ per scattering centre in the forward direction

$$\delta + i\beta = - \frac{2\pi \, n'}{k_0^2} \, \mathscr{F}_{coh}(\underline{k}_0 = \underline{k}_f) \, , \qquad\qquad (2.86)$$

where n' is the number of scattering centres per unit volume.

Where the scattering of Mössbauer radiation is concerned, $\mathscr{F}_{coh}(\underline{k}_0 = \underline{k}_f)$ is a complex scattering amplitude and consists of two contributions: $F_{coh}(\underline{k}_0 = \underline{k}_f)$ and $F_R(\underline{k}_0 = \underline{k}_f)$ [2.54]. As has been noted, near resonance the $F_{coh}(\underline{k}_0 = \underline{k}_f)$ values vary significantly with the incident γ-quanta energy whereas $F_R(\underline{k}_0 = \underline{k}_f)$ remains constant. Thus, the resulting value of $\mathscr{F}_{coh}(\underline{k}_0 = \underline{k}_f)$, and hence n and R, depend on γ-quanta energy and velocity v near the resonance. The index of refraction (2.86) depends only on the forward scattering amplitude and hence there is no phase shift between the waves scattered by various atoms and nuclei in the unit cell. Unlike the situation in diffraction, the structure factor of the basis need not be used for the unit cell.

Interference effects and, as a consequence, the dependence of R on the incident γ-quanta energy and the glancing angle γ_1 , have been observed by the Mössbauer effect [2.54-56]. At the same time it has been shown that in the presence of hyperfine splitting and of non-randomly oriented quantization axes in the scatterer, polarization effects should also be taken into consideration.

$\mathscr{F}_{coh}(\underline{k}_0 = \underline{k}_f)$ must then be replaced by a matrix of forward scattering amplitudes for various polarization components in the incident and scattered radiation. The medium becomes doubly refractive and a single refractive index is insufficient to describe the phenomena observed upon the action of Mössbauer radiation. Moreover, the effect can be sufficiently large to affect the line shape ($\sigma_r(E)$) in Mössbauer transmission spectroscopy.

An experimental set-up is given for studies of TER of Mössbauer quanta in Fig. 2.24 [2.57]. The design of the Mössbauer spectrometer for TER studies ensure: 1) simple and reliable setting and measurement the grazing angle γ_{cr}; 2) convenience in the adjustment of the angular beam divergence; 3) sample replacement without affecting the experimental geometry 4) reproducibility of all source-collimator-sample distances; 5) sample rotation in the range from 0° to 90°. The spectrometer consists of the analytical unit and electronic system for control, acquisition and processing of spectrometric data.
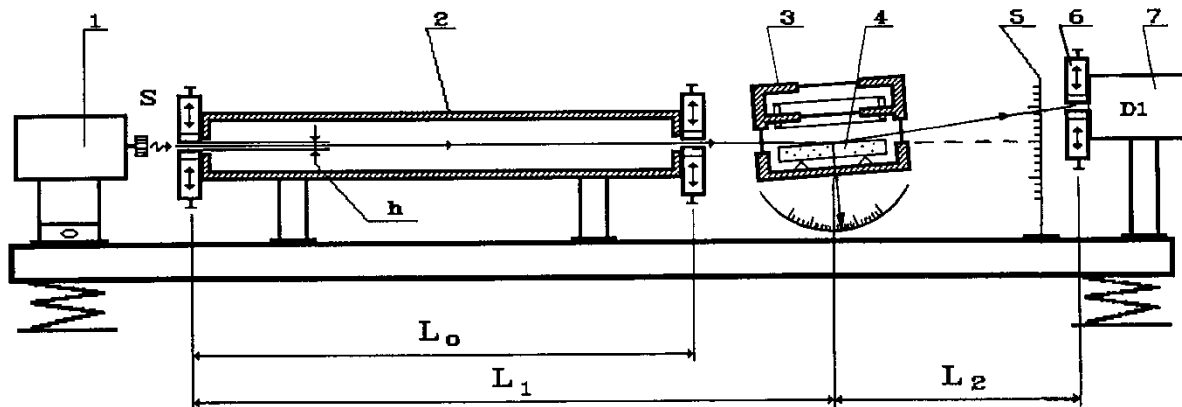
Fig. 2.24 An experimental set-up for studies of total external reflection of Mössbauer quanta. 1 - the Doppler modulator, S - source, 2 - slit collimator, 3 - the dual proportional counter, 4 - sample, 5 - screen, 6 - collimator, 7 - scintillation detector.

The analytical unit of the spectrometer comprises a vibration damping platform suspended on shock-absorbers. Mounted on the platform are guides of the "wedge slide" type which carry the Doppler modulator, shielding screens, collimator to form narrow directed plane-parallel radiation beams, proportional counter and scintillation detector. A narrow plane-parallel γ-rays beam from source S rigidly attached to Doppler modulator is formed by collimator 1 and through the entrance window of the dual detector - 3 falls on the sample 4. The γ-radiation reflected from the sample surface and passed through the exit window of the dual detector and slotted mask 5 is detected by scintillation detector D1.

 The geometric dimensions for the analytical part of the spectrometer were optimized based on the following requirements: the divergence value of the collimated γ-rays beam incident on the sample surface must ensure measurements for the angles $\gamma \leq \gamma_{cr}$ and the luminosity should be high enough at the reasonable analytical unit sizes. It is obvious, that near the grazing angle the divergence must be really less, then one half of mrad. As a starting point at the optimization of the geometric dimensions of the spectrometer the active part of the radioactive source were used. Solving the multiparameter optimization problem yielded the following values of basic dimensions and their adjustment intervals for the spectrometer : $\langle L_o \rangle \sim 600$ mm, $\langle L_1 \rangle \sim 700$ mm, $\langle L_2 \rangle \sim 400$ mm, maximum sizes of collimation slits "h" should be set below 1 mm and adjust with an accuracy better than 0,05 mm.

 The critical angle for the metal iron mirror is $\gamma_{cr} = 3.8 \cdot 10^{-3}$ sr [2.51]. On reflection at angles less than γ_{cr} the electromagnetic field intensity falls off rapidly. The penetration depth for the radiation (i.e. the thickness $\mathcal{L}$ of a

layer under study) is taken to be equal to the depth at which the intensity is less by times e. For β = 0 and $\gamma_1 < \gamma_{cr}$ the asymptotic $\mathcal{L}$ value is

$$\mathcal{L} = \frac{1}{2\sqrt{2}\,\gamma_{cr}\,k_0} \; . \tag{2.87}$$

If only the elastic scattering by electrons is considered, $\mathcal{L}$ is evaluated to be 1.3 nm for an iron mirror. In [2.54] the mirror was produced on an optically flat surface of a Pyrex plate by depositing an iron layer (91.2 % ^{57}Fe) 15 nm thick. It was shown that the metal surface, i.e. in the 2 nm thick layer, small amounts of wustite and nonmagnetic iron were present.

Although the analyzed layer is very thin, the technique has not been widely used. The reasons reflect the very low luminosity and difficulties in preparing the special surfaces for analysis. Of no less importance is the fact that interference effects complicate the interpretation of the experimental data. Substantial progress is achieved as shall be explained in Subsec. 3.9, by detecting not the scattered γ-quanta, but the electrons leaving the surface when Mössbauer radiation is incident at an angle which is less than critical. In this situation the intensity of the detected radiation increases and interference effects become less significant.

2.6. Scattering Experiments with Detection of Characteristic X-rays

It is known that Mössbauer transitions are usually highly converted and are followed by the emission of characteristic X-rays and Auger electrons. Typical parameters of characteristic X-rays for iron are given in Table 2.5. It can be seen that the weighted average energy of the K X-rays for Fe is 6.47 keV. The difference between the energies of the X- and γ-rays allows the X-rays to be filtered out of the Mössbauer radiation (see Figs. 2.4 and 2.5).

The detection of the characteristic X-rays instead of γ-rays was used in the first Mössbauer scattering experiments [2.58-60]. Such experiments involving ^{57}Fe were favoured by the fluorescence yield ω and the internal conversion coefficient α being overestimated. In fact the gain in intensity of the detected radiation is not as large as has been previously supposed [2.59] in studies aimed at showing that the scattered γ-radiation was more expedient to measure than the characteristic X-rays. The intensity gain for ^{57}Fe is less than 2.5. Of prime importance for the experimentalist is the quality of the spectrum. The maximum effect at a given intensity is a matter of experience.

Table 2.5
Energies of K-characteristic transitions   in iron and their relative intensities.

Transition Type	Transition Energy, eV	Relative Intensity of the Transition
$K_{\alpha 1}$	6403.9	100
$K_{\alpha 2}$	6390.9	51.1
$K_{\beta 1}$	7058.4	12
$K_{\beta 2}$	7058.4	6.1

 It is usually believed that in the scattering geometry depicted in Fig.2.9 a larger effect is observed on detection of the scattered γ-quanta, the spectrum quality (see Sect. 4.5) being higher (see Fig. 2.18). This is not generally true. Actually for such a gain it is necessary that the direct radiation does not reach the detector and is properly collimated. The sample must be relatively thin and the resonant isotope abundance must not be low. If any of this conditions is not fulfilled, and also if the parameter D (see (2.65)) is large as is necessary for applied research, the detection of X-rays may be preferable. Experiments involving the detection of different radiations are not competing, but may be considered as supplementing each other. The reason is that the difference in the penetration depth of the Mössbauer radiation and of the characteristic X-rays allows the acquisition of information from layers of different thickness by detecting γ-rays and X-rays in turn. There are exceptions to this however when, for example, the K- X-ray absorption in iron is such that μ_a values for the 14.4 and 6.46 keV rays are close.
Scattering experiments involving the detection of X-rays are easier to interpret because of the absence of resonant self- absorption of the radiation leaving the scatterer. In addition, except for the E1 Mössbauer transition, the detection of the backscattered characteristic X-rays means that interference effects may be neglected since they average out over all directions detected by the detector. This averaging causes the interference terms for the Mössbauer transitions of multipolarity M1 and E2 to cancel each other [2.61-63].
Based on numerical calculations, methods of surface layer analysis have been suggested for different experimental situations [2.64-67]. By assuming that the incident and the scattered radiation are well collimated, the dependence of the areas under the spectra and the intensities of K-X-rays, on the γ_1 and γ_2 angles have been investigated (see Fig. 2.9). The model calculations have been carried out for the two cases: $\gamma_1 = \gamma_2$ and $\gamma_1 + \gamma_2 = 90°$.

It was found that the thickness of the effective surface layer which contributes to the spectrum from iron atoms in any given state j depends on the experimental geometry, the total concentration of iron atoms in the sample and in the state j. The possibility of layer-by-layer analysis has been illustrated by the calculation of areas (A) (Fig. 2.25) in the spectra of a model sample consisting of four different layers which each give a well-resolved spectrum [2.67]. The upper spectrum corresponds to the first layer, the fourth (lowest) layer is the bulk consisting of non-magnetic iron with $n_{Fe}= 1.0$ (curve 4). The first, second and third layers were 3 μm thick with $n_{Fe} = 0.9$, 0.8 and 0.7, respectively (curves 1,2,3 in Fig. 2.25). The areas under the spectra are given for the two geometric arrangements in Fig. 2.25a for $\gamma_1 + \gamma_2 = 90°$ and in Fig. 2.25b for $\gamma_1 = \gamma_2$.
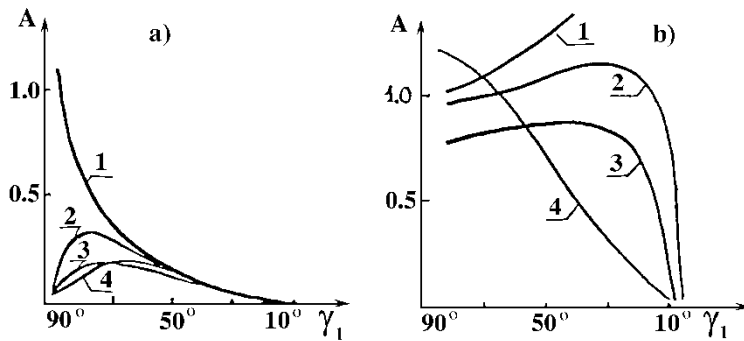

Fig. 2.25 Areas under the partial spectra from three layers (1,2 and 3) successively deposited onto a bulk sample, and the area of the spectrum from the bulk (4). a) $\gamma_1 + \gamma_2 = 90°$; b) $\gamma_1 = \gamma_2$.

The two dependences show that there may be two ways of layer-by- layer analysis. By the first one, in the geometry $\gamma_1 + \gamma_2 = 90°$, the succession of the layers and their composition are revealed on decreasing the angle of incidence from 90° to 45°. First, the spectrum from a layer of the minimum thickness is obtained, using the maximum angle of incidence γ_1 , and then by decreasing γ_1 the thickness of the analyzed layer is increased. By the method of successive approximations, adding and subtracting the spectra, it is possible to evaluate the thickness of the layers and their order. If the Mössbauer spectra corresponding to different layers overlap, the problem is too complicated and will be treated in a general form later in Chapter 4.

In the second method the angle of incidence is set equal to the scattering angle. The first spectrum is recorded at a minimum angle γ_1. The successive spectra are taken at larger γ_1 angles. The rest of the procedure is the same as for the first method. If collimation of the incident and scattered radiation is fairly good, it is possible to change the thickness of the analyzed layer from several micrometres to several tens of micrometres simply by changing the angle of the incident radiation. The effect and the line widths depend also on the solid angles $d\omega$ and $d\omega'$ (see Fig. 2.9). It is desirable that $d\omega$ and $d\omega'$ should be less than 5°, since larger radiation divergences diminish the contribution to the Mössbauer spectrum of the sample layers which are nearer to the surface. It should be noted that a better collimation of the radiation beam to increase the depth resolution necessitates longer measurements.

Other sources of the characteristic X-rays may substantially complicate the interpretation of the experimental data. In general the multiple scattering processes should be accounted for. Usually γ-quanta of higher energies are also emitted from the source and the photoeffect due to these quanta may contribute to the detected intensity. In the sample material there may be atoms whose characteristic X-rays are close in energy to the X-rays of interest and hence these are also detected. If the energy is higher, this relatively hard radiation may cause the subsequent emission of experimentally detectable characteristic X-rays. A limitation of the technique is that it is not possible to study a rough surface, for example, the surface of fractures.

The backscattering geometry of Fig. 1.9c makes it possible to work with intensities which are ten times as high as those given in Fig. 2.9. The backscattering geometry is not so flexible but it is simple, efficient, and suitable for any type of radiation. However, to detect γ-quanta a special detector is needed.

The principles of backscattering Mössbauer spectroscopy with detection of X-rays in the 2π solid angle have been given earlier in [2.68] devoted to forward scattering. The technique has also been used in studies of very thin films. The films were placed onto the detector window (Fig. 2.26). The X-rays of the source were filtered off and all X-rays leaving the scatterer were detected. In such experiments the only source of the background is the low photoeffect due to the 14.4 keV γ-quanta.

The scattered radiation may be at any angle θ ($0 < \theta < \pi/2$) with respect to the surface (see Fig. 2.26). The intensity of X- rays scattered as a result of the Mössbauer effect at an angle θ from the layer dx at a depth x is given by:

$$I_x(v,x,\theta) = \frac{C_x}{2} \int_\infty^\infty \mu_r(E)\, J_M(E,v,x)\, e^{-\nu_x(d_a-x)/\cos\theta} \sin\theta \; dE, \quad (2.88)$$

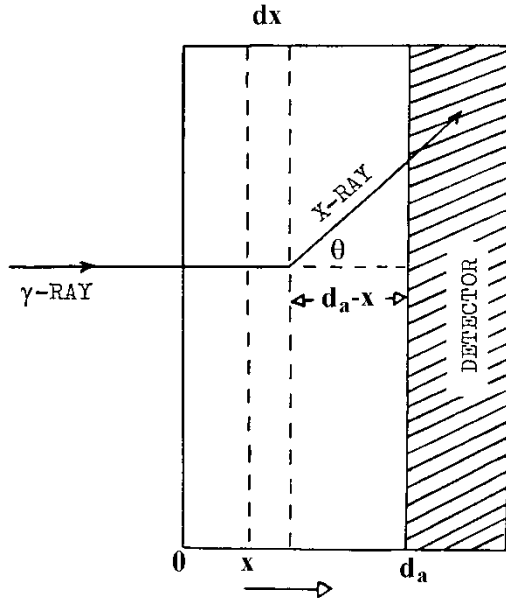Fig. 2.26 Schematic diagram for studies of thin films in a forward-scattering geometry.

$$C_x = \omega\,\alpha_K\,/\,(1 + \alpha)\,, \qquad\qquad\qquad\qquad (2.89)$$

where $J_M(E,v,x)$ is given by (2.57) for $\csc\gamma_1 = 1$, v_x is the total linear absorption coefficient for the X-rays.

The required integration over θ complicates the expression for the lineshape and the evaluation of the area under the spectrum. The area can be evaluated using the approximation method described elsewhere [2.67]. The area under the spectrum determined by (2.88) may be estimated in the following manner. Let the velocity change be linear from $-v_{max}$ to $+v_{max}$ with a period τ. In this case $dt = dv(\tau/2v_{max})$ and integration over v may be replaced by integration over t.

$$A = \frac{C_x f}{\pi\,\Gamma}\;\int_0^\tau\int_{-\infty}^\infty\int_0^{d_a}\int_0^{\pi/2} L(E,v)\;\mu_r(E)\;\exp(-G)\;\sin\theta\;d\theta\;dx\;dE\;dt\,,$$

where $G = [\mu_{ph} + \mu_r(E)]x + v_x(d_a - x)\,/\,\cos\theta$, $\mu_a \approx \mu_{ph}$. The integration over one cycle of the velocity change and also over scattering angles and γ-quanta energies yields the following:

$$A_\tau \simeq \frac{C_x \, f \, \tau \, \mu_r}{8 \, v_{max}} \int_0^d \exp\left[-(\mu_r/2 + \mu_a)x\right] J_0(i\mu_r x/2) \, H(v_x(d_a - x)) \, dx, \tag{2.90}$$

where

$$H(s) = \int_0^{\pi/2} e^{-s/\cos\theta} \sin\theta \, d\theta =$$

$$1 + s(\ln s - 0.42) - \sum_{n=2}^{\infty} (-1)^n s^n / \left[(n - 1) \, n!\right] .$$

By means of (2.90) and assuming that $\mu_a \ll \mu_r$, numerical calculations have been carried out [2.68] of areas under Mössbauer spectra and their dependence on the scatterer thickness.

To estimate the possibilities of studying thin films in the forward scattering geometry, the above mentioned dimensionless parameters $t_a = \mu_r d_a$, $t_a^e = \mu_a d_a$, $b = v_x d_a$
can be used. The film is thin if the following conditions are fulfilled simultaneously:

$$t_a \ll 1 \, , t_a^e \ll 1 \, , b \ll 1 \, . \tag{2.91}$$

The question as to whether transmission geometry or scattering geometry is a more efficient means to study these films can now be approached. The efficiency is the time required to record spectra of the same statistical accuracy. In general, this time depends on both the areas under the spectra and the signal-to-background ratio. For thin films the area may be evaluated by the expression:

$$A \simeq \frac{C_x f t_a}{8 \, v_{max}} \left[1 - \frac{t_a^e}{2} - \frac{t_a}{2} \frac{1}{2} - \frac{v_x}{\mu_r} \left(\ln\left(\frac{v_x}{\mu_r} t_a \right) - 1 \right) \right] . \tag{2.92}$$

Even for $v_x/\mu_r = 2$, the contribution of the last term is small.

The ratio of the area under the spectrum recorded from scattering experiments to that recorded from transmission experiments is $C_x / 2$. In the limiting case of $C_x \to 1$ the ratio may reach 0.5. For ^{57}Fe it is 0.15. The fact that the area in transmission experiments is larger does not mean that the transmission experiments are more informative.

Indeed, the background in scattering experiments is significantly lower than in the transmission ones, hence the signal-to-background ratio in scattering experiments may be better. The ratio of the maximum possible signal-to-background ratios in scattering and transmission experiments is $0.5 \, \alpha_k / \left[(1 + \alpha) \, t_a^e \right]$. For the iron film 10 nm thick the ratio is in the order of one thousand.

The ratio of τ_s - the time required to achieve the needed staistical accuracy (i.e.such that the effect equals to one standard deviation) in scattering experiments - to the corresponding time τ_a in transmission experiments is $\tau_s/\tau_a \approx 8(t_a^e) \, \omega \ll 1$ for $\alpha \gg 1$. Thus, thin film studies in the forward scattering geometry are more efficient than those performed in transmission mode.

2.7. A Theory of Backscattering Mössbauer Spectroscopy (X-ray Detection)

The source - scatterer - detector arrangement for Mössbauer backscattering experiments has been shown in Fig. 1.9c. In such an experiment one can detect any radiation in different scattering channels. In this section we shall be dealing with the theory of backscattering Mössbauer spectroscopy based on the exponential attenuation of radiation. Although straightforward for X-ray detection, in CEMS the line shape considerations are used with some restrictions. The geometry used in this analysis is shown in Fig. 2.27. The resonator is a uniformly dense semiinfinite slab.
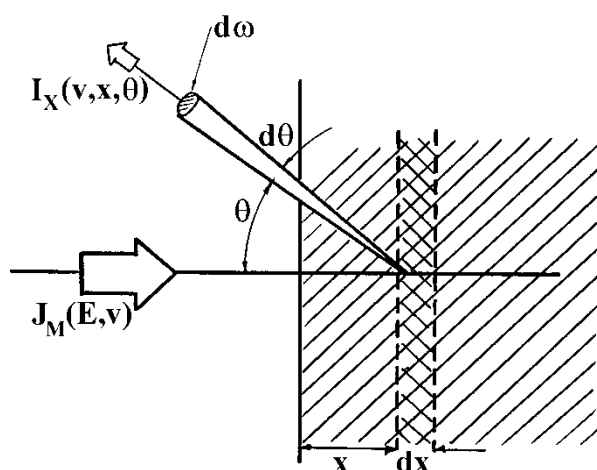

Fig. 2.27 Scattering from a bulk sample.

The energy distribution of the incident photons is given by $J_M(E,v)$. We are interested in calculating the intensity of X-rays escaping the resonator surface which have been produced by resonant scattering in dx about x and are emitted into the solid angle $d\omega$:

$$I_x(v,x,\theta)\,dx\,d\omega = \frac{C_x}{2} \int_{-\infty} J_M(E,v,x)\mu_r(E)\,e^{-v_x x/\cos\theta}\,\sin\theta\,dE\,dx\,d\omega$$

$$(2.93)$$

where C_x is given by (2.89). Sometimes the term "volumetric source strength" $S(v,x)$ for the layer of thickness dx is used in Mössbauer spectroscopy:

$$S(v,x) = \frac{2\,f}{\pi\Gamma} \int_{-\infty}^{\infty} L(E,v)\,\mu_r(E)\,e^{-\mu_a(E)x}\,dE\;.$$

$$(2.94)$$

This term is very convenient for some estimations. If the volumetric source strength of X-rays is of interest we can write:

$$S_x(v,x) = \frac{\omega\,\alpha_k}{1+\alpha}\,S(v,x)\;.$$

In this section we shall be concerned with the total backscattered intensity $I_x(v,x)$ which is due to the $S_x(v,x)$. Other contributions are neglected. Hence the intensity scattered by the layer dx and reaching the sample surface is given as

$$I_x(v,x)\,dx = \frac{1}{2}S_x(v,x)\,E_2(v_x x)\,dx\;,$$

where $E_2(x)$ - is a second order exponential Plachek function. All information about the radiation emergence from a layer dx at any angle to the surface is contained in the function

$$E_2(v_x x) = v_x x \int_{v_x x}^{\infty} \frac{e^{-\xi}}{\xi^2}\,d\xi\;.$$

After resonant scattering from a homogeneous sample of thickness d the intensity of radiation escaping the surface is:

$$I_x(v,d) = \frac{1}{2} \int_0^d S_x(v,x) \ E_2(\nu_x x) \ dx \ .$$

The integration of the equation over all x can be separated out and the result is presented by special functions $\hat{E}_2$. For the simplicity of further considerations and numerical evaluations Γ is set equal to $\Gamma_a = \Gamma_{nat}$, the energy is measured in $\Gamma_{nat}/2$ and the radiation flux is expressed as:

$$I_x(v,d) = fC_x w_x(v,b) \ . \ (2.95)$$

Thus, the spectral shape is determined by the probability $w_x(v,b)$ of resonant scattering occurring at a depth $x \le d$ and of the K-X-rays reaching the surface (the weight factor for this scattering channel is C_x):

$$w(v,d) = \frac{\beta}{2\pi} \int_{-\infty}^{\infty} \frac{L(E,v)}{(E - E_a)^2 + 1} \ \hat{E}_2(a(E),\nu d) \ dE \ , \qquad (2.96)$$

$$\hat{E}_2(a(E),b) = \int_0^b e^{-a(E)\xi} \ E_2(\xi) \ d\xi \ , \qquad (2.97)$$

where $b = \nu d$, $a(E)$ is the ratio of the total linear resonant scattering coefficient to the linear extinction coefficient for the detected radiation. In our case

$$a(E) = \frac{\beta}{(E - E_a)^2 + 1} + \gamma = \frac{\mu_a(E)}{\nu} \ , \qquad (2.98)$$

where $\beta = \mu_r/\nu$, $\gamma = \mu_a/\nu$. The $\hat{E}_2(a, b)$ function can be expressed by tabulated functions [2.69, 70]. In Mössbauer spectroscopy the a parameter is energy-dependent and in resonance $a(E)$ reaches the maximum value whereas the $\hat{E}_2(a(E), \infty)$ - is a minimum (see Fig.2.28). This Figure also depicts the $\hat{E}_2(a(E), \infty) / (1 + E^2)$ functions determining the line shape in experiments involving Mössbauer scattering with recoil.

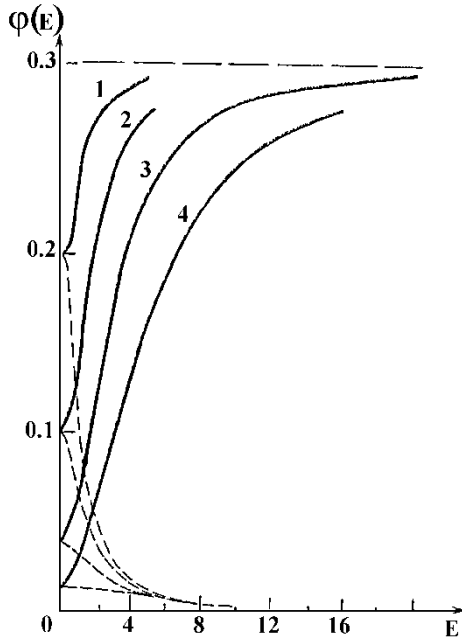The area A under the Mössbauer spectrum is the result of the integration of (2.95) over v:

Fig. 2.28 Plots of the φ(E) functions for a bulk scatterer of α-Fe at a source velocity v_1. Solid lines - φ(E) = $\hat{E}_2$(a(E), ∞). Dashed lines - $\hat{E}_2$(a(E), ∞)/(1 + E²). Energies are given in Γ/2 units. ^{57}Fe abundances: 1 - 2.14 %; 2 - 10 %; 3 - 30 %; 4 - 90 %

$$A = \frac{C_x \, f \, \beta}{\pi} \int_{-\infty}^{\infty} \frac{\hat{E}_2(a(E),b) \; dE}{(E - E_a)^2 + 1} \; . \tag{2.99}$$

A parameter c = γ cos θ [1 + (1 + (1 + cosθ)$^{-1}$] / 2 can now be introduced. On detection of the X-rays γ < 1 and on detection of electrons γ << 1, therefore c < 1. Taking this into account, equation (2.29) for a semiinfinite slab can be written in the form of series expansion in the power of the parameter γ. With the accuracy of terms proportional to c²

$$A = \frac{2 \, \pi^2 \mu_r}{\beta^2} \left\{ \frac{d^{3/2} - 1}{3} - \frac{d^{1/2} - 1}{1} - \frac{\gamma}{2\beta} \left[\frac{d^{5/2} - 1}{5} - \frac{d^{3/2} - 1}{3} - \frac{d^{1/2} - 1}{1} - \frac{1}{\sqrt{d}} - 1 \right] \right\},$$

where d = 1 + β.

An attempt to consider all the contributions to the registered intensity and also the experimental details results in a loss of generality of approach, especially in the role played by resonant scattering. Therefore it must be assumed that only resonant scattering determines the spectrum shape. This will be considered later in Chapter 4 when an insight into the effect of reemission and non-resonant scattering channels will be given.

Thus, equation (2.96) can be best used for numerical calculations. In addition to ordinary iron, samples of nonmagnetic iron (a = 2.14 % and 90 %) can also be considered. The thickness will be measured in μm or the parameter b ($v_x = 0.0685$ μm^{-1}), which characterizes the effective dimensionless thickness, will be used.

Calculated resonance probability values w(0,b) are given in Fig. 2.29 for X-rays and K-conversion electrons ($v_i = v_K = 17.5$ μm^{-1}) and different β values. It is now possible to demonstrate how these data can be used. For the enriched bulk sample, w(0,∞)

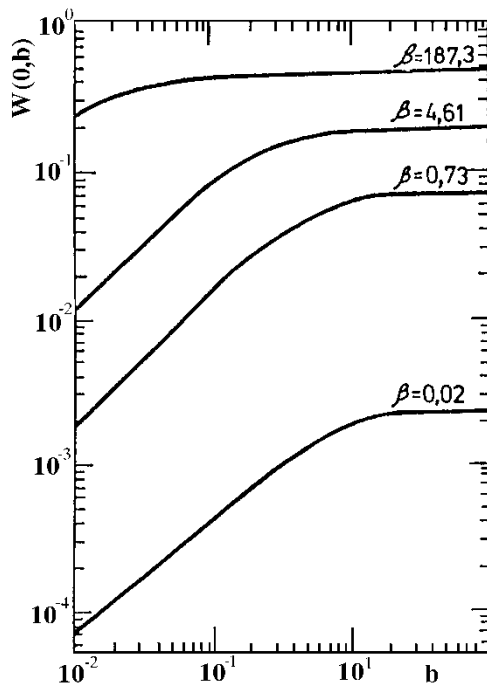Fig. 2.29 Dependence of the w(v, b) function on b at resonance for a scatterer of non-magnetic iron. β = 187.3 (a = 90 %) and β = 0.733 (a = 2.14 %) for X-rays; β = 4.61 (a = 90 %) and β = 0.018 (a = 2.14 %) for K-conversion electrons.

is equal to 0.4241 when X-rays are detected. The intensity on resonance is 0.4241 f C_x = 0.079 relative to the total γ-quanta intensity. For the same sample we have 0.0682 f C_K = 0.0375 for the detection of K-conversion electrons. The abscissa scale in Fig.2.29 allows a comparison of the results obtained by electron or X-ray detection. It must be remembered that a value of b = 0.01 corresponds to an iron layer thickness of only 0.6 nm for K-conversion electrons and of 146 nm for X- rays. Therefore, curves 1 and 3, 2 and 4 for b = 0.01 are spaced significantly apart. The distances between corresponding curves for enriched and non-enriched samples are approximately equal at b ~ 0.01. The backscattering electron intensity is well below the X-rays intensity for identical values of b .

The line widths, and especially their dependences on the sample thickness and its enrichment, are also important characteristics of the Mössbauer spectra. For scatterers of non-magnetic iron calculations by means of equation (2.96) have shown that the line broadening for natural iron does not exceed 0.065 mm/sec. Hence, the line broadening due to saturation effects cannot exceed this value for any real sample if it is non- enriched. The maximum possible line broadening due to saturation effects is 0.71 mm/sec for an abundance not exceeding 90 % .

The saturation effect on detecting X-rays or electrons can now be considered. The intensity of detected radiation (see (2.96)) is determined by an exponential function which is both energy- and depth-dependent. For an infinitely thin sample the exponential factor is proportional to $\mu_a(E)$ even at resonance.

A situation can now be considered in which both the scatterer and the source are characterized by Lorentzians with the width Γ. If two beams of monochromatic γ-quanta with energies E_0 and E_0 + Γ are alternately allowed to fall onto a sample the scattered radiation intensities will differ by a factor of 4. This is because the exponential factor values which determine the intensities for infinitely thin scatterers differ by the same factor of 4. The observed line is therefore a Lorentzian with width 2Γ.

When the thickness of the scatterer is increased the proportionality between the values $\mu_a(E)$ (the quantity of resonant atoms in the layer of unit thickness) and the exponential factor is broken. It first occurs on resonance when $\mu_a(E)$ is maximized. A change in the incident γ-quantum energy relative to the E_0 value by an amount ± Γ results now in the attenuation of the scattered radiation by less then fourfold. The experimentally observed line is then broadened and the line amplitude and area are then not proportional to the sample thickness and we speak of saturation. For the peak value to be proportional to the number of atoms in a given phase it is necessary that all the scattered radiation should reach the detector and be detected. None of this conditions can be fulfilled below a certain depth in the sample. In the first instance the condition which is determined by larger values of the linear extinction coefficients is violated.

In the literature on Mössbauer spectroscopy it is possible to find statements to the effect that the strong absorption of electrons means that a change in the energy distribution and the intensity of Mössbauer radiation in the scatterer, as well as various saturation effects, may be neglected. The calculated probability $w(0, \infty)$ is 0.00218 for a non-enriched bulk sample on detection of electrons. The same sample enriched in ^{57}Fe has a probability $w(0, \infty)$ of 0.0682, which is much lower than the value 0.0218 90 / 2.14 = 0.09 which can be expected in the absence of saturation effects. It is clear that the contribution of a thin surface layer to the spectrum is larger than that of the layer of the same thickness and composition which is beneath if the factor f' remains independent of depth.

Theoretically it is important to know the depth which can be reached by, say, 1 % of Mössbauer radiation. In applied aspects of the important depth is that from which the detection probability for the scattered radiation may be neglected. Thus, in Mössbauer methodology, it proves to be convenient to introduce such concepts as the reference layer and analyzed layer. The reference layer refers to the thickest layer in a sample of natural abundance from which the Mössbauer signal is still proportional to the number of resonant atoms (to the layer thickness). It is also supposed that all radiation back- scattered by this layer reaches the sample surface. For an enriched sample an intensity unit is the intensity from a reference layer multiplied by the ratio of the abundances. The thickness of the layer should be not more than 10 nm. The intensity of X-radiation back-scattered by this layer as a result of the Mössbauer effect is 0.03 % of the incident intensity. The dependence of the peak values at resonance and of the areas on the scatterer thickness as calculated by (2.106) and (2.109) are given in Fig. 2.30. The area under the spectrum originating from the reference layer can be described as $\pi I(0)\Gamma_{nat}$. As the scatterer thickness increases the line begins to broaden, towards the saturation value and its shape departs from a Lorentzian. Due to line broadening the dependence of the area under the spectrum on the sample thickness will show saturation effects which are not so strong as for the peak value. The difference in the saturation behaviour is illustrated in Fig. 2.30 where the calculated areas have been divided by $\pi\Gamma_{nat}$. All dependences for the same abundance are then normalized to one scale. At lower resonant interaction cross sections the departure from linearity is smaller. Hence, if there are two scatterers which differ only in that one gives a magnetically split spectrum and another does not (e.g. magnetic and nonmagnetic iron), the signal from the first scatterer will be larger than that from the second one at an equal thickness of the samples (see pairs of curves 1 and 2 in Fig. 2.30). Furthermore, if there is a Zeeman split spectrum, the saturation effects manifest themselves in a departure of the intensity ratios from
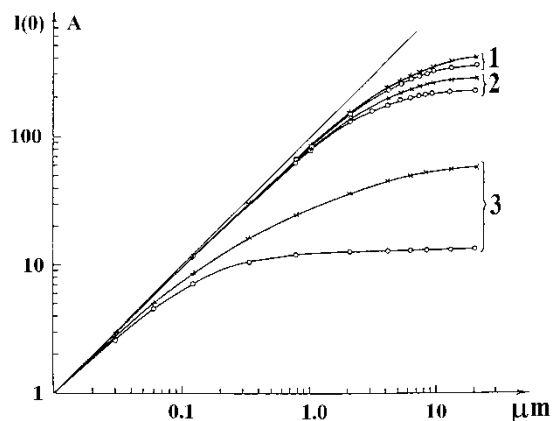
Fig. 2.30 Dependences of the K-X-ray intensities at resonance I(0) (circles), and areas A (crosses) on the scatterer thickness. The units of intensity and area correspond to the reference layer 10 nm thick. 1 - α-Fe, v_1, a = 2.14 %; 2 - non-magnetic iron, a = 2.14 %; 3 - non-magnetic iron, a = 90 %.

the theoretical ones. For an infinitely thin scatterer with no texture, the intensity ratios for the first three lines of the sextet, 3:2:1, are obtained by averaging (1.29) over the scattering angle. As shown by the calculations for a bulk iron scatterer (a = 2.14 %) there will then be appreciable departures of the line intensities from the ratio given above. If the enrichment is higher (a = 90 %) the saturation effects become so substantial that the line intensities are nearly equal (Fig. 2.31).

The analysis of sufficiently thick samples requires a knowledge of the thickness of the analyzed layer, i.e. the region wherein resonant scattering processes determine the intensity of radiation to be detected. Due to a stochastic character of the interaction of radiation with matter, there is always a finite (though low) probability for this radiation to reach and then leave a very large depth of the scatterer. This means that it is not possible to strictly determine the boundaries of the analyzed layer. The concept of the analyzed layer is based on the calculations considered above. For this purpose let us use the dependences of Fig. 2.30. The thicknesses at which the peak values (or areas under the lines) reach a specified fraction of their saturation values will be called the thicknesses of the analyzed layer. Let this fraction p be equal to 95 % of the saturation value. If the experiment is more statistically accurate the p value may be taken as 98 %.

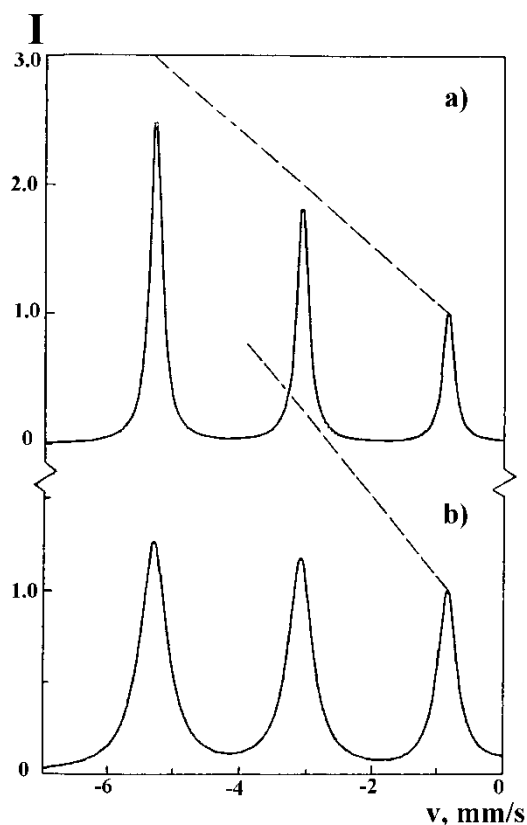Fig. 2.31 Calculated Mössbauer spectra for detection of characteristic K-X-rays scattered from samples of α-Fe 100 μm thick. a) a = 2.14 % ^{57}Fe; b) a = 90 % ^{57}Fe. The dashed lines correspond to the intensity ratio 3 : 2 : 1.

The thickness of the analyzed layer will depend on various factors, first of all on the sample composition (i.e. μ_a, μ_r and ν_i values) and also on the line shape and statistics.

Within the framework of the approach described above the thickness of the analyzed layer is firstly determined by the greatest linear coefficient (see (2.95) - (2.99)). In Table 2.6 the thicknesses of the analyzed layers of iron obtained from data on the dependences of the peak-values or areas under the spectra on the sample thickness. These values are denoted as d_I and d_A. Difference for the same sample is due to the above mentioned greater influence of saturation effects on the peak- values than on the areas. The detection of X-rays by non- enriched samples occurs with the μ_r , μ_a and ν_x values being approximately equal and the thickness of the analyzed layer is found to be about 15-20 μm. For enriched samples ($\mu_r \gg \mu_a$, ν_x) and the thickness of the analyzed layer is mainly determined by the μ_r value.

It can be seen from Table 2.6 that for a scatterer of non- magnetic iron (a = 90 %) d_I = 3.13 μm and d_A = 11 μm. At the

same such a scatterer is time μ_r for 12.7 μm^{-1} (see Table 2.3) and the probability for a γ-quantum of exactly the resonance energy passing through a layer 1 μm thick is $3 \cdot 10^{-6}$. This is not, as may appear, contradictory. Since Mössbauer radiation has a Lorentzian energy distribution, the quanta in the energy interval $E_0 \pm \Gamma$ are rapidly absorbed. Indeed, due to the tail in the Lorentzian distribution an appreciable fraction of the radiation emitted by the source in resonance with the scatterer will reach a depth of more than 10 μm and make an appreciable contribution to the Mössbauer spectrum. This can be seen in the data in Table 2.6.

Table 2.6
Thicknesses of the analyzed layers on detection of characteristic X-rays scattered from a sample of metal iron.

p,%	$H_{eff} = 0$				$H_{eff} = 33.0$ Tesla			
	a = 90%		a = 2.14%		a = 90%		a = 2.14%	
	d_I μm	d_A μm	d_I μm	d_A μm	d_I μm	d_A μm	d_I μm	d_A μm
95	1.63	10	8.5	14	3.1	12	14.8	17.6
98	3.13	11	12	19	5	13	19	21

Notes: d_I and d_A - the thicknesses of the analyzed layers of iron obtained from data on the dependences of the peak-values or areas under the spectra.

It should not be overlooked that various sublayers of the analyzed layer make different contributions to the observed signal. A greater part of the signal comes from the upper part of the analyzed layer whilst the lower third of the layer makes only a very small contribution to the observed signal (Fig. 2.32).

Real samples are often multilayered. However, the main aspects of backscattering Mössbauer spectroscopy may be elucidated by considering a two-layer model scatterer rather than an

N-layer one. It is convenient to use the E - $\mathcal{E}$ variable for analysis and to measure the energy in $\Gamma/2$ units. The line shape of the spectrum from the upper layer (see (2.95) and (2.96)) can be written as:

$$I_{x,1}(\mathcal{E}, d_1) = \frac{C_x f \beta_1}{2} \int_{-\infty}^{\infty} \frac{\hat{E}_2(a(E)_1, b_1) \, dE}{[(E - \mathcal{E})^2 + 1][(E - \delta_1)^2 + 1]} \, , \qquad (2.100)$$
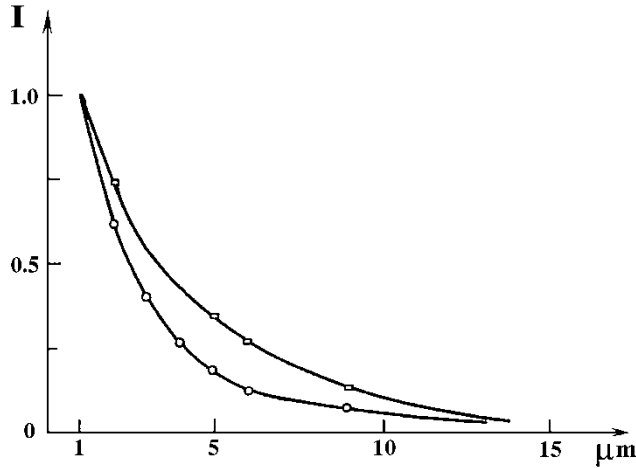
Fig. 2.32 Dependence of the Mössbauer line intensity from a 1 ?m thick layer on the position of this layer's lower boundary relative to the sample surface. Open circles - non-magnetic iron, open rectangles - ordinary iron, a = 2.14 %.

where δ - is the isomer shift of the source relative to the absorber. The index number 1 will be used when considering processes in the upper layer (e.g. $I_{x,1}$, μ_{a_1}, μ_{r_1} etc.), similarly index number 2 will be used when considering process in the lower layer.

Using (2.97) and (2.100), the line shape of the spectrum from the lower layer may be written as

$$
I_{x,1}(\mathcal{E},d_1,d_2) = \frac{C_x f\beta_2}{2} \int_{-\infty}^{\infty} \frac{\exp\left[-(t_s(E))_1\right]}{\left[(E - \mathcal{E})^2 + 1\right]\left[(E - \delta_2)^2 + 1\right]}
$$

$$
\int_{d_1}^{d_1+d_2} E_2\left[b_1 + \nu_2(x - d_1)\right] \exp\left[-(\mu_a(E))_2(x-d_1)\right] \, dE \, dx \quad .(2.101)
$$

For the purposes of computation the integration over the coordinate in (2.101) should be excluded. For this purpose all the coordinate-dependent terms are collected into a single factor $\mathcal{L}(E, \mathcal{E}, d_1 ,d_2)$ which is written explicitly in this form:

$$\mathcal{L}(E,\mathcal{E},d_1,d_2) = \int_{d_1}^{d_2} E_2(\nu_2 x + b') \; e^{-[(\mu_a(E))_2 x + \Delta]} \; dx \; , \qquad (2.102)$$

where the following substitutions have been introduced:

$$b' = (\nu_1 - \nu_2)d_1 \; , \; \Delta = [(\mu_a(E))_1 - (\mu_a(E))_2]d_1 \; .$$

After the change of variables: $y = \nu_2 x + b'$; $dy = \nu_2 dx$, (2.102) is reduced to:

$$\mathcal{L}(E,\mathcal{E},d_1,d_2) = \frac{1}{\nu_2} \; e^{-\Delta + \frac{(\mu_a(E))_2 b'}{\nu_2}} \int_{\nu_2 d_1 + b'}^{\nu_2(d_1+d_2)+b'} E_2(y) \; e^{-(a(E))_2 y} dy \; .$$

The integral in the right-hand part is expressed through the already known special functions $\hat{E}_2$ (a(E), b) (eq.(2.97)). Thus, the line shape of the spectrum from the second layer may be written as

$$I_{x,2}(\mathcal{E},d_1,d_2) = \frac{C_x f \; \beta_2}{2\pi} \int_{-\infty}^{\infty} \frac{\exp[-(t_s(E))_1] \; \exp\left[\frac{\nu_1}{\nu_2} (\mu_a(E))_2 d_1\right]}{[(E - \mathcal{E})^2 + 1][(E - \delta_2)^2 + 1]}$$

$$\left\{ \hat{E}_2[(a(E))_2 \; , \; (b_1 + b_2)] - \hat{E}_2[(a(E))_2, \; b_1]\right\} dE \; . \qquad (2.103)$$

The special functions used here may be expressed by simpler special functions ($E_1(x)$) which are tabulated and can be found elsewhere [2.70].

$$\hat{E}_2(a,b) = \hat{E}_2(a,\infty) - \frac{1}{a^2} \left\{ E_1(b(1 + a)) - e^{-ab} [(1 + ab)E_1(b)\right.$$

$$\left. - a \; e^{-b}]\right\} \; ,$$

where

$\hat{E}_2(a,\infty) = [a - \ln(1 + a)] / a^2$. (2.104)

These allow the line shape of the spectrum from a bulk sample covered with a layer of thickness d_1 to be written as

$$I_{x,2}(\mathcal{E},d_1,\infty) = \frac{C_x f\ \beta_2}{2\ \pi} \int_{-\infty}^{\infty} \frac{\exp\left[-(t_s(E))_1\right] \exp\left[\frac{\nu_1}{\nu_2}\ (\mu_a(E))_2 d_1\right]}{\left[(E - \mathcal{E})^2 + 1\right]\left[(E - \delta_2)^2 + 1\right]}$$

$$\left\{\ \hat{E}_2\left[(a(E))_2\ ,\infty\right] - \hat{E}_2\left[(a(E))_2,\ \nu_2 d_1\right]\right\} dE\ .$$ (2.105)

In the absence of the covering layer the line shape of the spectrum from a bulk sample of a uniform composition can be written in a fairly compact form:

$$I_x(\mathcal{E},\infty) = \frac{C_x\ f\ \beta}{2\ \pi} \int_{-\infty}^{\infty} \frac{a(E) - \ln\left[1 + a(E)\right]}{a^2(E)\left[(E - \mathcal{E})^2 + 1\right]\left[(E - \delta)^2 + 1\right]}\ E\ .$$ (2.106)

For quantitative analysis it is desirable to have a sufficiently simple expression for the area under the Mössbauer spectrum. It may be obtained by integrating (2.100), (2.103) or (2.106) over the variable E. Thus, the area under the spectrum from the upper layer of thickness d_1 can be written in a form analogous to (2.99), and that of from the bulk, covered with a layer of another phase of thickness d_1 can be written as

$$A_2(d_1,\infty) = \frac{C_x f\ \beta_2}{2\ \pi} \int_{-\infty}^{\infty} \frac{\exp\left[-(t_s(E))_1\right] \exp\left[\frac{\nu_1}{\nu_2}\ (\mu_a(E))_2 d_1\right]}{\left[(E - \delta_2)^2 + 1\right]}$$

$$\left\{\ \hat{E}_2\left[(a(E))_2\ ,\infty\right] - \hat{E}_2\left[(a(E))_2,\ \nu_2 d_1\right]\right\} dE\ .$$ (2.107)

The methods of spectral interpretation in transmission mode Mössbauer spectroscopy have been fairly well developed and are based on a restoration of the $\mu_r(E)$ function. The situation is somewhat different in scattering spectroscopy due to the necessity to account for non-resonant scattering channels, especially for multilayer samples.

Mössbauer radiation comes to the interface of the two layers with an energy distribution which is already non-Lorentzian. Thus, the source of resonant radiation for the second layer is the Mössbauer source radiation, having passed the first layer which is a resonant filter. The filtration depends on the source velocity. Under these conditions the Mössbauer spectra recorded from a substance will differ depending on whether the substance is covered or not covered with a layer of another material containing resonant atoms.

The validity of the initial assumption that the shape of the spectrum from a uniform sample is only determined by the resonant scattering process proves to be even more doubtful for spectra recorded from the lower layers than from a homogeneous sample. Indeed, if the upper layer is highly enriched in the resonant isotope, the non-resonant contributions to the Mössbauer spectrum from the lower layer may prove to be predominant. Generally speaking the concepts of classical Mössbauer spectroscopy without a knowledge of $(\mu_a(E))_1$ and d_1 , preclude an interpretation of spectra from a two-layer sample. The highest distortion of the spectra from the lower layer at a given upper layer thickness is to be expected when the line positions from these layers either coincide or when they are shifted relative to each other by not more than Γ.

The results calculated from two-layer samples can now be examined. If the upper layer thickness is allowed to vary and the thickness of the lower layer is 100 μm then the lower layer may be considered as the bulk. The resonant scattering spectrum of the lower layer will change as the thickness of the upper layer (i.e. the resonant filter) increases. If the two layers are of non-magnetic iron, normalization of the intensities from the two layers means that the line intensity from the upper layer may be assumed to equal unity. The growth of the upper layer thickness with a natural abundance of the ^{57}Fe isotope results in a line shape deformation from that of the lower layer such that at $d_1 > 3$ μm a dip appears in the centre of the spectrum (Fig. 2.33a) [2.71]. The enrichment of non-magnetic iron up to 90 % in ^{57}Fe leads to a change in the line shapes. Since the line from non-magnetic iron at a = 90 % is broadened considerably, splitting of the line from the lower layer begins at smaller d_1 values (see Fig. 2.33b).

The overlap of spectra which occurs when all the parameters of the Mössbauer spectrum are equal, is similar to that observed in studies of real multilayer samples. It occurs when some of the layers are identical or when the hyperfine splitting of the layers causes some Mössbauer lines to overlap. If the corrosion of iron gives rise to an initial layer of haematite covered by a magnetite layer then the Mössbauer spectra will show the coincidence of some of the lines.

For two layer samples where both layers are of ordinary iron, the lines from the lower layer may be broadened as the upper layer becomes thicker and the intensity ratios will change
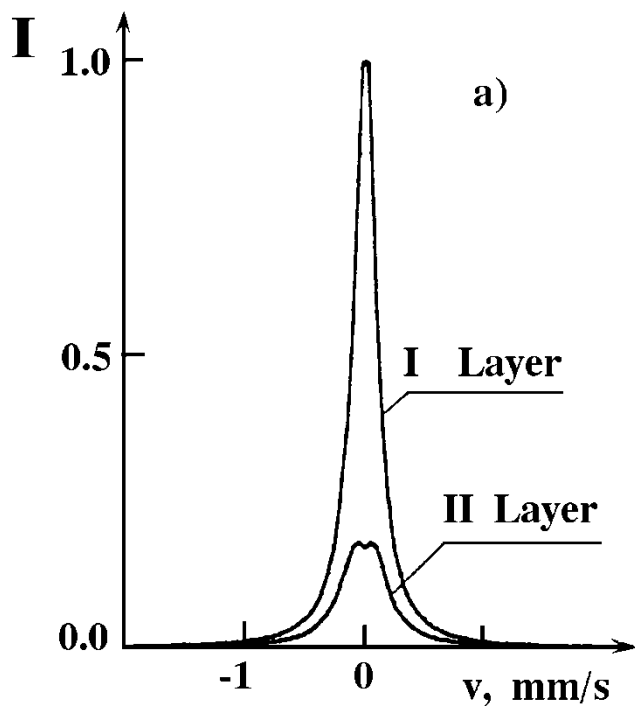
Fig. 2.33.a Calculated Mössbauer spectra from the upper layer (1) and the lower layer (100 μm thick) (2) from a non-magnetic iron scatterer; $d_1 = 5$ μm, $a = 2.14$ % ^{57}Fe.
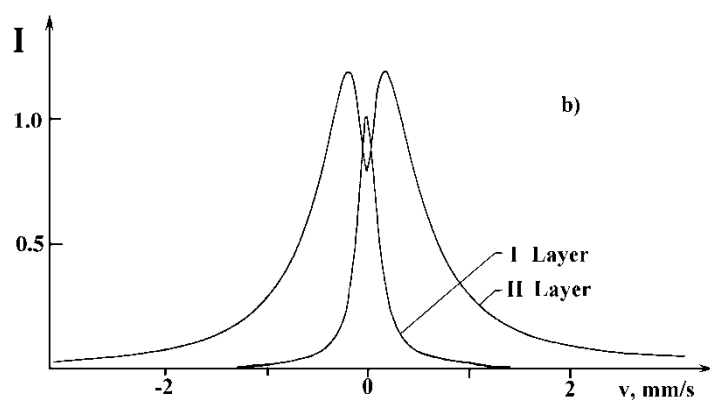

Fig. 2.33.b Calculated Mössbauer spectra from the upper layer (1) and the lower layer (100 μm thick) (2) from a non-magnetic iron scatterer; $d_1 = 0.13$ μm, $a = 90$ % ^{57}Fe.

from 2.48 : 1.81 : 1.0 at $d_1 \rightarrow 0$, to 1.24 : 1.26 : 1.0 at $d_1 = 20$ μm. At $a = 90$ % the line shape of the spectrum from the lower layer is strongly changed as the d_1 values increase, and

from $d_1 \sim 0.3\mu m$, line 1(6) of the spectrum from the lower layer will be split. Other lines of the spectrum will also split at larger d_1 values. Typical spectra are given in Fig.2.34. Spectra from both layers of the scatterer are normalized so that the intensity of line 1 becomes equal to unity.
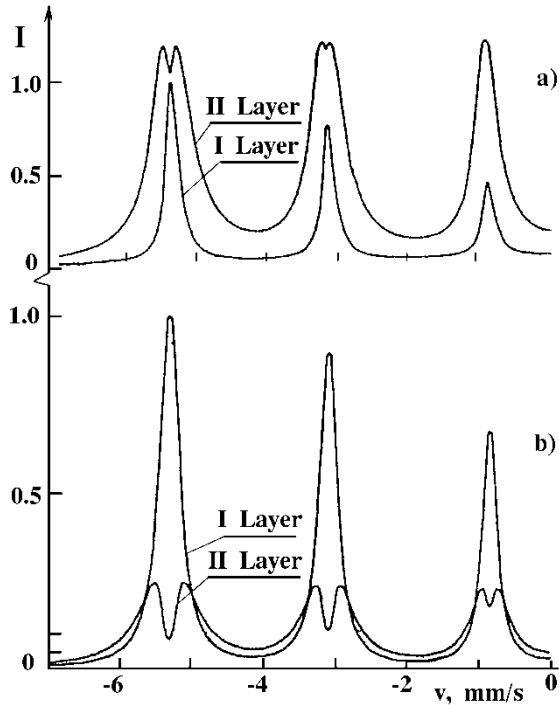

Fig. 2.34 Calculated Mössbauer spectra from the upper layer (1) and the lower layer (2) of a scatterer of α-^{57}Fe (a = 90%).
a) $d_1 = 0.33$ μm, b) $d_1 = 2$ μm.

In the analysis given above, the line shape of the spectrum corresponding to resonant scattering in the lower layer was deformed in such a way that the centre of gravity of the lines was not shifted. Suppose now that the lines from different layers are shifted relative one to another by an amount which is approximately equivalent to Γ. Let the sample, as before, be a two-layer one and be characterized by the same single lines as non-magnetic iron, but shifted relative to each other by $\Gamma/2$. For a = 2.14 % ^{57}Fe the observed line from the second layer at $d_1 > 7$ μm will be shifted by $\Gamma/4$ from its normal position and will appear asymmetric. For enriched samples (a = 90 % ^{57}Fe) shifts of the spectral lines from the lower layer(and also the line shape deformations) begin when the upper layer is

considerably smaller. For example, at $d_1 = 0.15$ μm and $\delta = \Gamma/2$, a splitting of the line from the second layer into two asymmetric lines is observed with the position of the most intense line being shifted by $\Gamma/2$ from the normal position (Fig. 2.35). As the line shift increases to $\delta = \Gamma$, the line shift from the second layer becomes smaller.
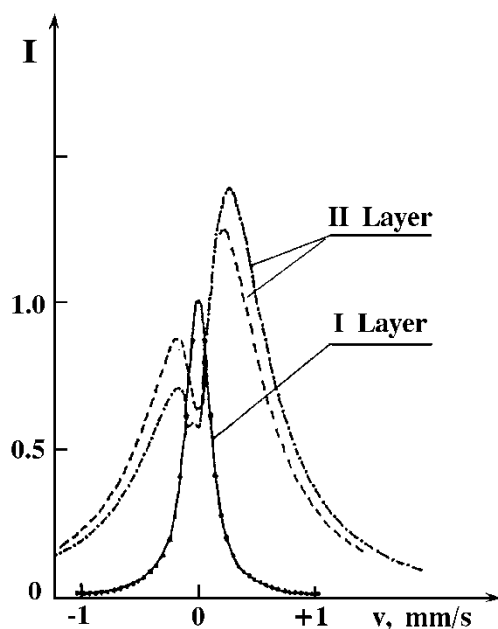

Fig. 2.35 Calculated Mössbauer spectra from the upper layer (1) and the lower layer (100 μm thick) (2) of a scatterer of non- magnetic iron (a = 90 % ^{57}Fe).

The experimental observation of the spectral line shape from the lower layer is best achieved by the detection of X-rays in scattering geometry as shown in Fig.2.9. The upper layer should be placed in front of the scatterer to serve as a resonant filter. An ordinary scattering spectrum recorded from an α-^{57}Fe foil (a = 90 %) 25 μm thick is shown in Fig. 2.36a whilst the spectra in Fig. 2.36b and c, were obtained after resonant filters made of 20 μm thick ordinary iron and 2 μm thick α-^{57}Fe (a = 90 %), had been included. A comparison of the experimentally obtained spectrum (Fig. 2.36c) with a calculated spectrum involving the same filter with only resonant scattering channels taken into account (Fig.2.34b) shows a distinct difference. The difference results from non-resonant scattering channels and, to account for these, it is necessary to subtract from the spectrum shown in Fig. 2.34b that depicted in Fig. 2.15 for $I_R + I_{Rn}$ caused by nonresonant scattering channels. Thus, the spectrum from the lower layer shows, when the velocities corresponding to resonant energies are approached, an initial increase in intensity followed by a dip.
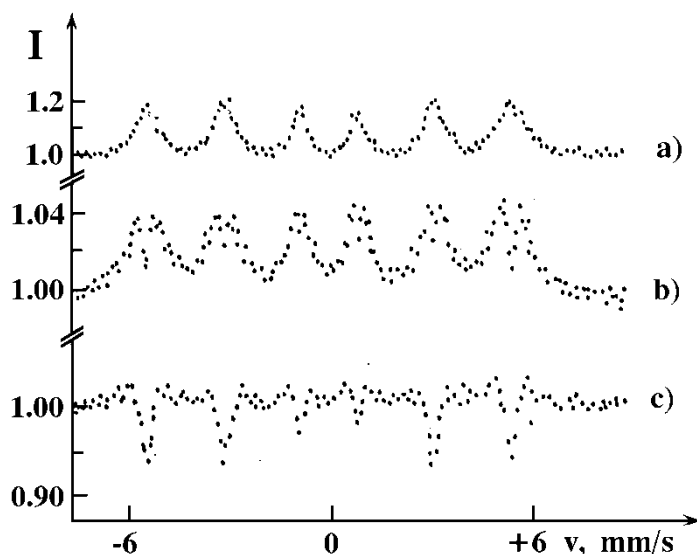
Fig. 2.36 Mössbauer spectra of α-^{57}Fe (a = 90 %), d = 25 μm. K- X-rays are detected. a) conventional CEM spectrum, b) with a filter of natural α-Fe, d = 15 μm, c) with a filter of α-^{57}Fe, d = 2 μm.

It should be noted that it is not possible to observe a spectrum from the lower layer in backscattering geometry, i.e. by placing a resonant filter (the upper layer) over the entrance window of the flat proportional counter with the scatterer inside. Forward-scattered X-rays from the sample simulating the upper layer can be removed by placing a filter which absorbs the X-rays from the resonant filter. However, there is an appreciable probability that due to the poor energy resolution of the detector it could detect not only the 6.46 keV radiation but also the 14.4 keV quanta. The intensity of the direct radiation (having passed the filter and reached the active counter volume) will be ten times greater than that of the scattered radiation. Therefore, despite a low detection efficiency for the 14.4 keV γ-quanta, the transmission spectrum from the upper layer will suppress the scattering spectrum from the lower layer.

2.8. Backscattering Mössbauer Spectroscopy by the Detection of X- and γ-radiation. Practical Aspects

Mössbauer spectra recorded by the detection of backscattered X-rays have been shown in [2.72]. The work involved an investigation of stainless steel foils which had

been covered with layers of iron of 5 and 12 μm thickness. A simple detector was used for the experiments (Fig. 2.37). The instrument is composed of a flat rectangular gas-flow proportional counter with an aluminium shell which acts as the cathode. The anodes are 20 - 80 μm diameter tungsten or stainless-steel wires supported on insulators inside the shell. The flow gas is usually an argon-methane mixture (about 10 % CH_4) with the flow-rate maintained at approximately 1 ml/s. A positive voltage as ca. 600 - 1600 V is needed for operation in the proportional region. The voltage applied in a particular experiment is determined by the anode wire diameter, by the distance between the wire and the entrance window, and by the gas flow-rate. Being simple to construct and highly efficient, the detector design has been extensively used in applied research. In Mössbauer spectroscopy similar detectors were firstused in [2.73, 74]. Since the authors were interested only in the detection of conversion electrons, the flow-gas used was a helium-methane mixture.
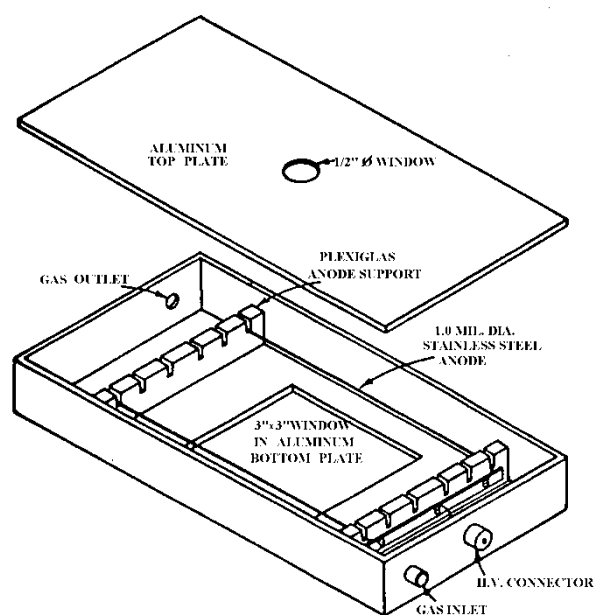

Fig. 2.37 Isometric view of proportional counter with top plate removed [2.72].

It has been shown by many experimentalists that the signal/noise ratio on the detection of γ-rays in the experimental geometry of Fig.1.9b is better than on detection of X-rays. By detecting γ-quanta, one can obtain a data acquisition rate which is superior to that obtained by the detection of X- rays of higher intensity [2.46, 75, 76]. At the same time the flat proportional counter has never been used to detect γ-quanta in the backscattering geometry of Fig. 1.9c. Indeed, the direct Mössbauer radiation of an intensity which is 100 times as high as the scattered intensity also passes through the detector such that the effect would be very small. The need to detect the resonantly scattered γ-quanta in a solid angle close to 2π stimulated the search for a detector capable of sensing scattered photons with an energy of 10 - 20 keV and which would be insensitive to the direct primary beam of γ-quanta.

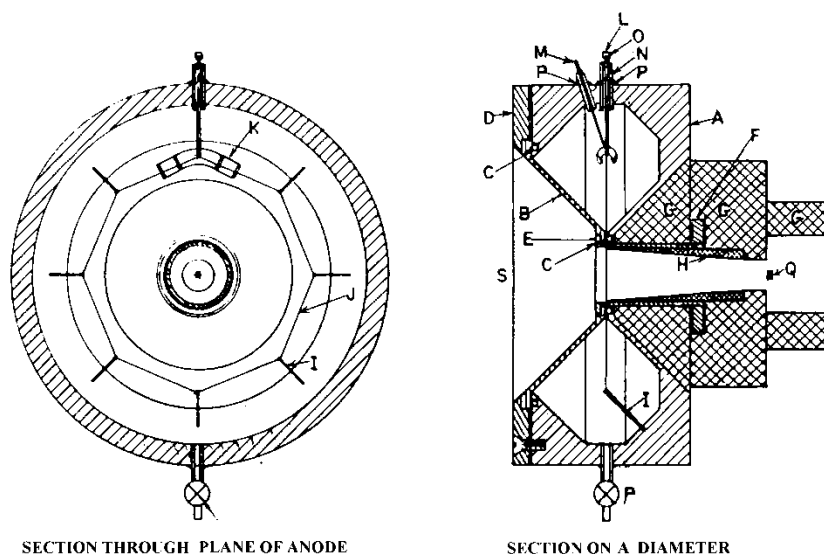SECTION THROUGH PLANE OF ANODE   SECTION ON A DIAMETER

Fig. 2.38 Sectional views of the toroidal counter. A: detector body (aluminium); B: nylon window (aluminized inner surface); C: O-rings; D: clamping plate (one of six bolts shown, aluminium); E: clamping sleeve (aluminium); F: clamping sleeve nut (brass); G: shielding (lead); H: collimator (lead); I: quartz support rod (one of seven, 0.5 mm diam.); J: anode wire; K: lead-in guard grid; L: anode lead (hypodermic needle tubing); M: guard lead (tungsten-Pyrex seal); N: Pyrex-Kovar seal; O: hypodermic needle tubing with soldered cap; P: Pyrex-epoxy- aluminium joints; Q: source position; R: high-vacuum valve; S: typical sample position.

The requirements have been met by the use of thoroidal detectors [2.77]. The main problem has involved the necessity to create the inner electric field with circular

equipotential lines around the anode. Unfortunately the electric field topography proved to be worse than in the flat proportional counter. One possible design is shown in Fig. 2.38 [2.78]. The main difficulty in the construction is the correct centering of the anode inside the toroid. Other problems involve the selection of the window material and window fabrication.

The anode wire shown in Fig. 2.38 which is supported by insulating rods is octagonal. After filling with a krypton-methane mixture the resolution for the 14.4 keV line for such a counter is approximately 15 %. Since the flow of krypton is expensive, a gas-filled counter was designed. However, a series of technical problems needed to be solved such as the prevention of oxygen contamination of the gas fill. With a scatterer of stainless steel (of effective area 5 cm^2) the effect $\varepsilon(0)$ of 176 % is achieved by detection of γ-quanta, and of 54 % by X-ray detection. Such a detector has been used for the examination of works of art containing iron-bearing pigments [2.79].

An improvement of the toroidal counter for Mössbauer studies [2.80, 81] involved the use of cylindrical grid wires surrounding the anode [2.82]. The grid is kept at a low potential with respect to the detector body. Electrons produced within the counter volume travel to the grid and through it to the anode wire. The gas multiplication factor is determined by the potential difference between the wire and the cylindrical grid. A section of a Mössbauer spectrometer using the counter is shown in Fig. 2.39.

Despite the toroidal nature of the counters described in [2.77-81], the shape of the cathode is always different from a true torus, and the anode is in the form of a square (see Fig.2. 39) or an octagon (see Fig. 2.38). Technical realization of the design is not simple, hence the next paper on the modernization of toroid detectors [2.83] appeared ten years after the initial work [2.80]. A substantial modernization was suggested with a special plastic being used as a window material. For the first time a counter with the cavity being a true torus was made with the symmetry of equipotential surfaces around the anode being close to that demanded by theory.

A new development of the original model of the toroidal counter [2.84] led to changes in certain details of construction. The body of the detector consists of only two parts which is aimed at lowering the leak rate. The anode lies not in the center of the toroid but is shifted about 10 % of the diameter towards the axis of the counter. The electric field gradient immediately around the anode wire is more uniform. The shielding has been changed to absorb more efficiently the direct radiation of the source. A mixture of argon, krypton and methane proved to be preferable for detecting the 14.4 keV γ-rays because of the reduction of the 1.8 keV escape peak of krypton. The gas-filling should be permanent because of the high price of krypton. Absorption for the 14.4 keV γ-rays was 73 %.

If X-rays are detected the absorption of the argon-methane mixture is as high as that of the more expensive counting gas. Because of the relatively low price of argon the counter can be operated with a continuous flow of the gas-mixture which is advantageous for the stable peak positions in the pulse-height spectrum and for the stable efficiency of the detector. It is shown that the toroidal proportional detector is easy to handle and can be usefully applied to surface studies with high efficiency.
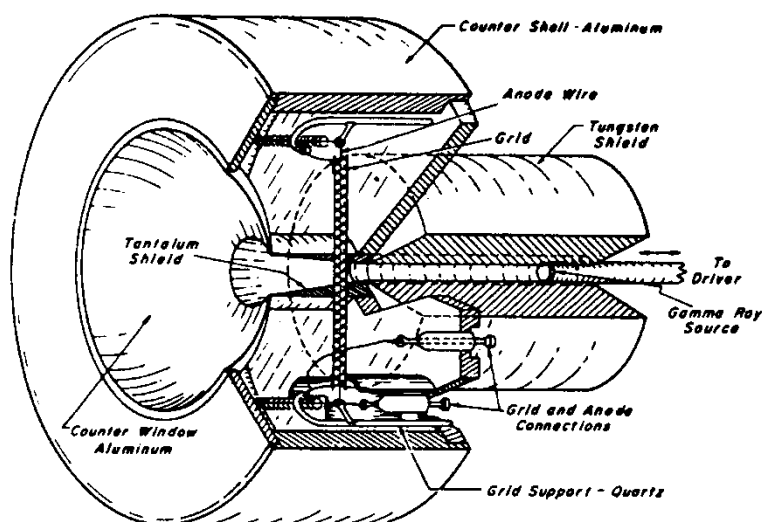
Fig. 2.39 Spectrometer based on the toroidal detector of Fig.2.38 (from [2.81]).

Apart from their complicated design there are some further disadvantages of the toroidal counters. For example, the instrument requires a sufficiently large sample area and the solid angle subtended by the detector must always be less than 2π. Nevertheless,the availability of these counters would have great benefits in many fields of research.

The simple design of the detector depicted in Fig. 2.37 is one of the reasons why the technique to date has been widely based on the use of flat proportional counters. In addition to the γ-quanta which is of main interest X-rays are also emitted which cause a decrease in the observed effect in the detector (see Table 2.1). To suppress the direct X-rays a filter composed of a low Z material is used. Aluminium is often used since it has a linear absorption coefficient for the 6.4 keV quanta of about 200 cm^{-1}, and for the 15 keV quanta - of approximately 21 cm^{-1}. Since non-enriched iron samples involve a X-ray scattering intensity of about 1 % of the incident γ-rays intensity whilst the X-ray intensity from the source is 7.5 times higher, the X- rays from the source are to be attenuated by a factor of approximately 750. Hence the direct X-ray beam reaching the detector is approximately equal to the beam of X-rays scattered due to the Mössbauer effect in the sample. This can be achieved by using an aluminium foil of 330 μm thick which absorbs about 48 % of Mössbauer radiation from the source. Many experimentalists use plexiglass filters. Our experience has shown that a 4 mm plexiglass filter is more efficient than aluminium filters. It provides the attenuation factor of 750 for the 6.4 keV quanta and of only 0.33 for the Mössbauer source radiation.

Once the filter material and its thickness have been selected it is necessary to determine the counter thickness (i.e. the thickness of the active detector volume). For the flat proportional counter this is determined by the doubled anode-cathode distance. Increasing the distance enhances the counter efficiency but at the same time, undesirable effects are observed, for example, sharp increases in the efficiency of the higher-energy radiation detection, increases of the source-scatterer distances, and an increased background due to the interaction of the incident radiation with the detector materials can occur. To observe the Mössbauer effect in ^{57}Fe the cathode-anode distance should be about 8 mm. Since the scattered quanta escape at any angle, their average range in the active counter volume is more than 16 mm. This results in an increase in efficiency of the scattered radiation detection.

When the anode-cathode distance is 8 mm and the anode tungsten wire diameter is 50 μm, the operation voltage must be near to 1200 V. Using a gas flow-rate of approximately 1 cm^3/min and an argon - 10 % methane gas mixture, the energy resolution at the 6.5 keV line is nearly 25 % which is quite satisfactory. Practice has shown that one central wire is sufficient and there is no reason to use several wires unless the multiwire proportional chamber is used.

Some possibilities of the technique are illustrated by the use of a two layer scatterer [2.85], the lower layer being the bulk substrate of 1 mm thick stainless steel and the upper layer of α-Fe with a thickness varying from 0.13 to 40 μm. The Mössbauer spectra obtained from various thicknesses of the iron coating are shown in Fig.2.40. Fig.2.41 shows the variation of the relative area η(d) under the spectrum from the stainless steel scatterer covered with an iron layer on the thickness (d) of the Fe-coating layer. The experimental dependence shown in Fig. 2.41 is a complex function of the thickness of the upper layer (see (2.107)). The range of thickness may be subdivided into three regions. In each of these the observed dependence can be presented by means of a certain effective linear extinction coefficient κ. For the coating thickness of up to 0.5 μm κ = 0.8 μm^{-1}, from 0.5 to 7.5 μm κ = 0.35 μm^{-1} and from 7.5 μm to 20 μm κ = 0.15 μm^{-1}. Such a formal approach is sometimes useful for the empirical interpretation and systematization of the experimental data.

It follows from the dependences shown above that the technique is capable of producing a Mössbauer spectrum from an iron layer 0.13 μm thick after a short counting time. The spectrum recorded from a stainless steel layer can be observed even if the iron coating is thicker than 20 μm. The highest differential sensitivity of the method is observed for the upper layer when it is less than 1 μm thick (see Fig.2.41).

The flat proportional counter provides a useful method by which the surface of real samples of quite different shapes can

be studied. For example, fractures of bars from 5 mm diameter and more and surface of wires. If a new phase is formed in the surface layer of a specimen under study as a result of a treatment, then simple models of the phase distribution using a calibration curve similar to the curve of Fig.2.41 can be constructed to evaluate quickly the properties (e.g. the surface fraction covered with a new phase and the average thickness).
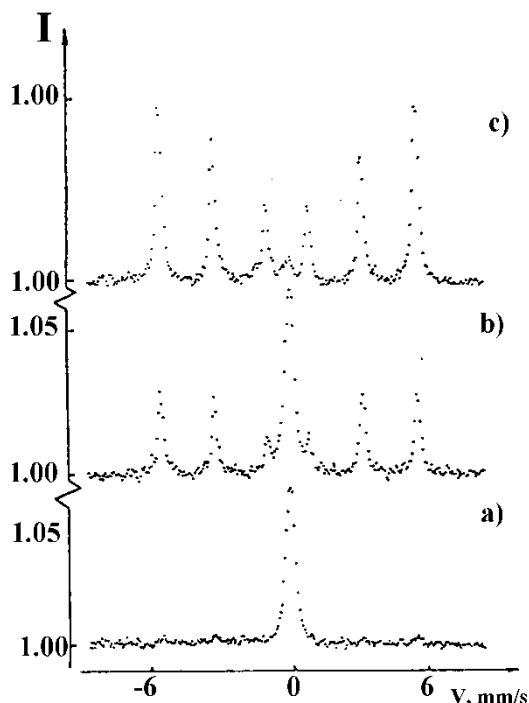

Fig.2.40 K-X-rays spectra of stainless steel (d_2 = 1 mm) coated with iron. a) thickness of the coating 0.13 μm; b) 1.9 μm; c) 20 μm .

If the new phase is growing with uniform distribution within a layer, the calibration data required are usually difficult to obtain. It is important to note that at a given factor f' value the area under a spectrum depends on the shape of the spectrum (i.e. on the nature of the hyperfine splitting). Indeed, hypothetical non-magnetic iron and ordinary iron have the same densities and f factor values. Hence, for thin scatterers the areas under corresponding spectra are equal. However, for ordinary iron the scattering probability at any resonance energy is essentially less than for the single resonance in the non-magneticiron. Hence saturation effects for ordinary iron are weaker and, from a given scatterer thickness, a significant distinction is seen in the magnitude of the signal (see dependences 1 and 2 in Fig.2.30).
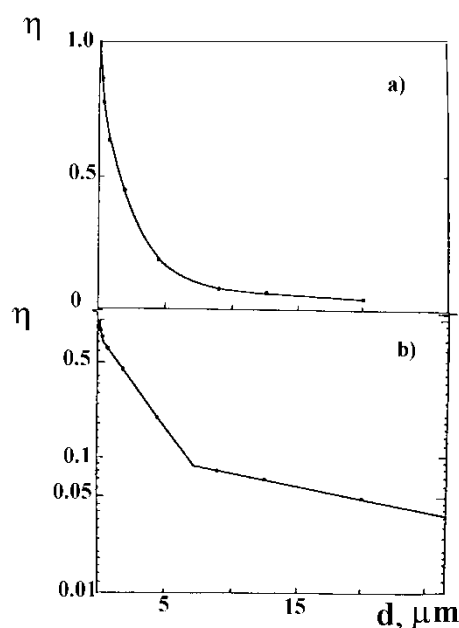
Fig.2.41 Fractional area under the K-X-rays spectrum of stainless steel, as a function of thickness of the α-Fe coating. a - linear plot; b - semilogarithmic plot.

For two bulk samples (a = 2.14 %), the ratio of the areas under the spectrum corresponding to the H_{eff} = 330 kOe and H_{eff} = 0, equals 1.43 and increases only up to 2.28 at a = 90 %. In other words a hypothetical bulk sample consisting of well mixed equal quantities of the magnetic and non-magnetic iron (a = 2.14 %) would give an area under the Mössbauer spectrum from the non-magnetic iron which would be less than 50 % of the total spectral area. This must be considered when phase analysis studies are being performed.

References

2.1 Nuclear Data Tables, sec. A. 7 (1970) 566-682.
2.2 G.P. Huffman, Nucl. Instr. Meth., 137 (1976) 267-290.
2.3 F. Metzger, Progr. Nucl. Phys., 7 (1959) 53-88.
2.4 P.B. Moon, Proc. Soc., 63A (1950) 1189-1196.
2.5 D.C. Champeney, Rep. Progr. Phys., 42 (1979) 1017-1054.
2.6 J.L. Croves, G. DePasquali, P.G. Debrunner, Phys. Rev., B7 (1973) 1974-1984.
2.7 W. Heitler, Quantum Theory of Radiation, Clarendon, Oxford, 1954.
2.8 W.E. Lamb Jr., Pnys.Rev., 55 (1939) 190-197.
2.9 G.T. Trammell, Phys. Rev., 126 (1962) 1045-1054.
2.10 J.P.Hannon, G.T.Trammell, Phys.Rev., 186 (1969) 306-325.

2.11 M.A. Andreeva, R.N. Kuz'min, Mössbauer γ-ray Optics, Izdat. Moscow Gosudarst. Universitet (MGU), Moscow, 1982.

2.12 Yu. Kagan, A.M. Afanas'ev, Z. Naturforsch., 28a (1973) 1351.

2.13 R.L. Mössbauer, F. Parak, W. Hoppe, in Mössbauer Spectroscopy II. The Exotic Side of the Method, ed. by U. Gonser, Springer, Berlin, 1981, pp. 5-30.

2.14 P.J. Black, I.P. Duerdoch, Proc.Phys.Soc., 84 (1964) 169- 171.

2.15 D.A. O'Connor, P.J. Black, Proc. Phys. Soc., 83 (1964) 941-948.

2.16 P.J. Black, D.E. Evans, O'Connor, Proc. Roy. Soc., 270 (1962) 168-185.

2.17 F.E. Wagner, J. Phys. (Paris) Colloq., 37, C6 (1976) 673- 689.

2.18 K. Gabathuler, H.J. Leisi, in Hyperfine Interactions in Excited Nuclei, ed. by G. Goldring and R. Kalish, Vol. 3, Gordon and Breach, New York, 1971, pp. 821-825.

2.19 P.J. Black, P.B. Moon, Nature, 188 (1960) 481-482.

2.20 P.B. Moon, Proc. R. Soc., 263 (1961) 307.

2.21 E.V. Zolotoyabko and E.M. Iolin, Coherent Rayleyigh Scattering of Mössbauer radiation, "Zinatne", Riga, 1986.

2.22 G.V. Smirnov, Hyper. Inter., 27 (1986) 203-218.

2.23 U. Van Bürck, Hyper. Inter., 27 (1986) 219-230.

2.24 G.V. Smirnov, V.V. Sklyapevskii, R.A. Voscanyan and A.N. Artem'ev, Pis. Zh. Eksp. Teor. Fiz., 9 (1969) 123 (Engl. trans. Sov. Phys. - JETP Lett., 9 (1969) 70).

2.25 V.S. Zasimov, R.N. Kuz'min, Phys. Stat. Sol. (b), 70 (1975) K55-57.

2.26 E.P. Stepanov, A.N. Artem'ev, I.P.Perstnev, V.V. Sklyarevskii, G.V. Smirnov, Zh. Eksp. Teor. Fiz., 66 (1974) 1150-1154.

2.27 P.P. Kovalenko, V.G. Labushkin, A.K. Ovsepyan, Pis. Zh. Eksp. Teor. Fiz. 39 (1984) 471.

2.28 V.K. Voitovetskii, I.L. Korsunskii, A.I. Novikov and Yu.F. Pashin, Zh. Eksp. Teor. Fiz., 54 (1968) 1361-1373 (Engl. Trans. Sov. Phys. - JETP 27, 729-735).

2.29 A.N. Artem'ev, I.P. Perstnev, V.V. Sklyarevskii, V.G. Smirnov and E.P. Stepanov, Zh. Eksp. Teor. Fiz., 64 (1973) 261-272 (Engl. trans. Sov. Phys.-JETP: 37, 136-141).

2.30 D.P. Siddons, J.B. Hastings, Gy. Faygel, J.R. Grover, P.E. Haustein, and L.E. Berman, Rev. Sci. Instrum., 60(7) (1989) 1649-54.

2.31 U. van Burck, G.V. Smirnov, and R.L. Mössbauer, J. Phys. C, 21(34) (1988) 5843-51.

2.32 E. Gerdau, R. Ruffer, H. Winkler, W. Tolksdorf, C.P. Klages, J.P. Hannon, Phys.Rev. Lett., 54 (1985) 835.

2.33 J.Z. Tischler, B.C. Larson, J. Appl. Pys., 70(12) (1991) 7532-36.

2.34 Ruffer R., Gerdau E., Grote M., Hollatz R.,Rohlsberger R., Ruter. H.D., Sturhahn. W., Nucl. Instr. Methods in Physics Research, Sec. A, A303, No 3 (1991) 495-502.

2.35 P.E. Haustein, L.E. Berman, G. Faigel, J.R. Grover, J.B. Hastings, D.P. Siddons, Hyperfine Interactions, 58 (1990) 2445-2450.

2.36 M.E.Rose, Multepole Fields, Chapman and Hall, London, 1955.

2.37 G.R. Hoy, S. Chandra, J. Chem. Phys., 47 (1974) 961-971.

2.38 N.N. Delyagin, B.A. Komissarova, L.N. Krukova, Hyperfine Interaction and Nuclear Radiations, Izdat. MGU, Moskwa, 1985.

2.39 B.A. Komissarova, A.A. Sorokin, V.S. Schpinel, Zh. Eksp. Teor. Fiz., 50 (1966) 1206-1217 (Engl. trans. Sov. Phys.- JEPT, 23).

2.40 A.J.F. Boyle, H.E. Hall, Rep. Progr. Phys., 25 (1962) 441- 524.

2.41 B. Balko, G.R. Hoy, Phys. Rev., B, 10, No.11 (1974) 4523- 4530.

2.42 P. Debrunner, R.J. Morrison, Rev. Sci. Instr., 36, No.2 (1965) 145-148.

2.43 B. Balko, G.R. Hoy, in Mössbauer Effect Methodology, ed. by I.L. Gruverman, Vol. 9, Plenum Press, New York, 1974, pp. 307-334.

2.44 J.J.Bara, B.F.Bogacz, phys. stat. sol., 44a (1977) K107- 109.

2.45 J.J. Bara, B.F. Bogacz, Mossb. Eff. Refer. Data J., 3 (1980) 217-222.

2.46 A.N.Artem'ev, G.V. Smirnov and E.P. Stepanov, Zh. Eksp. Teor. Fiz., 54 (1968) 1028-1030 (Engl.Trans. Sov. Phys.- JETP 27, 547-548).

2.47 W. Meisel, Monatsber. Deutschen Akad. Wiss. Berlin, 11 (1969) 335.

2.48 N.D. Heiman, J.C.Walker and L. Pfeiffer, Phys. Rev., 184 (1969) 281-284.

2.49 B. Balko, G.R. Hoy, Phys. Rev. B, 10 (1974) 36-49.

2.50 B. Balko, G.R. Hoy, J. Physique Colloq. C6, 37 (1976) 89.

2.51 B. Balko, G.R. Hoy, Phys. Rev.B, 13, No.7 (1976) 2729- 2734.

2.52 A.M. Afanas'ev, V.D. Gorobchenko, Zh. Eksp. Teor. Fiz., 67 (1974) 2246-2259 (Engl. trans. Sov. Phys. - JETP 40, 1114- 1120).

2.53 B. Balko, Phys. Rev. B, 33 (1986) 7421-7437.

2.54 S. Bernstein, E.C. Kampbell, Phys. Rev., 132, No.4 (1963) 1625-1633.

2.55 S. Bernstein, E.C. Campbell, C.W. Nestor, J. Phys. Chem. Solids, 26 (1965) 883-891.

2.56 F.E. Wagner, Z. Phys., b210 (1968) 361-379.

2.57 M.L. Alexandrov, G.N. Belozersk, Yu.V. Gladkov, O.V. Grishin, S.M. Irkaev, V.I. Nikolaev, V.G.Semenov, Hyperfine Interaction, 71, (1992), 1461-1464

2.58 H. Frauenfelder, D.R.F. Cochran, D.E. Nagle, Nuovo Cimento, 19 (1961) 183-185.

2.59 A.N. Artem'ev, V.V. Sklyarevskii, G.V. Smirnov, Zh. Eksp. Teor. Fiz., 52, No.5 (1967) 1157-1159.

2.60 J.H. Terrel, J.J. Spijkerman, Appl. Phys. Lett., 13, No.1 (1968) 11-13.

2.61 K.P. Mitrofanov, M.V. Plotnikova, N.I. Rokhlov, V.S. Shpinel, Pis. Zh. Eksp. Teor. Fiz., 12 (1970) 60-61 (Engl. trans. Sov. Phys. - JETP. Lett., 12, 60)

2.62 I.I. Lukashevich, V.D. Gorobchenko, V.V. Sklyarevskii, N.I. Filippov, Phys. Lett., 31A (1970) 112-114.

2.63 P. Steiner, G. Weyer Z. Phys., b248 (1971) 362-367.

2.64 Yu.F. Babikova, M.R. Gryaznov, L.M. Isakov, N.S. Kolpakov, M.N. Uspenskii, Prib. Tekh. Eksp., No.3 (1975) 152-155.

2.65 Yu.F. Babikova, N.S. Kolpakov, K.E. Nilov, Prikladnaya Yadarnaya Spektposkopiya, vip.11, Energoizdat, Moscow, 1982 pp.219-226.

2.66 N.S. Kolpakov and K.E. Nilov, Intern. Conf. on the Applic.of Mössbauer Effect, Alma-Ata, USSR, Programme and Abstracts, p.364.

2.67 Yu.F. Babikova,P.L. Gruzin, K.E. Nilov, Mossbauerovskaya Spectroskopiya s registraziey charakteristicheskogo rentgenovskogo izlucheniya, Moscowskii Injenerno- fizicheskii Instit., Moskwa, 1986.

2.68 N. Hershkowitz, C. Walker, Nucl. Instr. Meth., 53 (1967) 273-276.

2.69 H.Goldstein, Fundamentals of reactor shielding, Addison Wesley Publ. Co., Mass, 1959.

2.70 M.Abramowitz, I.A.Stegun (eds.), Handbook of mathematical functions, U.S. National Bureau of Standards, 1964.

2.71 G.N. Belozerskii, S.A. Chekasheva, Trudi I Vsesouznogo soveschaniya po izucheniu sverchtonkich vzaimodeystvii , (MGU), Moscow, 1985, p. 78-79.

2.72 K.P. Swanson, J.J. Spijkerman, J. Appl. Phys., 41 (1970) 3155-3158.

2.73 K.P. Mitrofanov, Prib. Tekh. Eksp., 3 (1965) 60-64.

2.74 J. Fenger, Nucl.Instr.Meth., 69 (1969) 268-270.

2.75 R.N. Ord, Appl.Phys.Letters, 15 (1969) 279-281.

2.76 R.N. Ord, C.L. Christensen, Nucl. Instr. Meth., 91 (1971) 293-294.

2.77 H.K. Chow, R.F. Weise, P.A. Flinn, Mössbauer spectrometry for analysis of iron compounds, U.S. Atom. Comm. Rep., No. NSEC-4023-1, 1969.

2.78 B. Keisch, Nucl. Instr. Meth., 104 (1972) 237-240.

2.79 B. Keisch, H.H. Miller,"Application of nuclear Technology to art identification problems - Final report", in U.S. Atomic Energy Comission Report, COO-3034-2, 1972,

2.80 R.A. Levy, P.A. Flinn, R.A. Hartzell Nucl. Instr. Meth., 131, No. 3 (1975) 559-562.

2.81 P.A. Flinn, in Mössbauer Effect Methodology, ed. by I.J. Gruverman, C.W. Seidel, D.K. Dieterly, Vol. 9 ,Plenum Press, New York, 1974, pp. 245-258.

2.82 R.J. Norman, Austr. J. Phys., 8 (1955) 419-427.

2.83 L. Blaues, H.G. Wagner, U. Gonser, Hyperfine Interactions, 29 (1986) 1571-1574.

2.84 P. Schaaf, L. Blaes, J. Welsch, H. Jacoby, F. Aubertin, U. Gonser, Hyperfine Interactions, 58 (1990) 2541-2546.

2.85 G.N. Belozerskii, S.A. Chekashova, V.N. Gittsovich in Application of the Mössbauer Effect, ed. by Yu.M. Kagan, I.S. Lyubutin, Vol. 3, Gordon and Breach Scie. Publl., Amsterdam, 1985, pp. 1073-1080.

3. Mössbauer Spectroscopy Based on the Detection of Electrons.

The principles of Mössbauer Spectroscopy were, in the preceding Chapter, considered in terms of the detection of electromagnetic radiation. Since Mössbauer γ-transitions are usually highly converted and the internal conversion process is followed with a high probability by the emission of Auger electrons, more than electron is produced per one resonant scattering event. Secondary electrons as well as the primary internal conversion electrons and Auger electrons may also be produced. The detection of electrons has proved in many cases to be the most efficient means of observing the Mössbauer effect.

The principal feature of Mössbauer spectroscopy based on the detection of electrons is that the average energy of an electron beam reaching the detector, and also the shape of the energy spectrum, depends on the depth x of a layer dx from which the beam has been generated. This provides interesting possibilities for layer-by-layer phase analysis. Various modifications of Mössbauer spectroscopy based on the detection of electrons have been developed including technique which allows the Mössbauer signal from a very thin surface layer (~ 3 nm) of a homogeneous bulk sample to be distinguished.

The techniques in this field of Mössbauer spectroscopy are classified as either integral or depth-selective. There are two approaches used to develop the theory of conventional conversion electron Mössbauer spectroscopy (integral techniques). The first one is based on the hypothesis of the exponential attenuation of the electron beam. This approach is adequate for phase analysis investigations. The second approach takes into account the elementary interactions of electrons with the medium and is therefore more accurate and is based on Monte Carlo calculations. This enables investigations of the effects related to angular- and energy- distributions.

Depth-selective Mössbauer spectroscopy requires the use of modern β-spectrometers of good energy resolution and high luminosity. However, even if these requirements are met, a quantitative interpretation of the results requires a well- developed theory. The progress which has been achieved in this field permits interesting studies on structure determination of the near surface layers. The requirement of enhanced selectivity for a given quality of the Mössbauer spectrum leads inevitably to a considerable increase in the measuring time. The need for depth selective analytical data has led to the use of detectors with a moderate energy resolution (~ 15 %) with a capacity to detect all the back-scattered electrons. The related theoretical and methodology problems are considered in Sect. 3.6 where other methods of electron detection are discussed.

3.1. The Interaction of Electrons with Matter Following Mössbauer Scattering

The interaction of photons with matter in the energy range of interest is well known and is determined by nuclear resonant scattering, the photoelectric- and Compton-effect, and by Rayleigh scattering. It is important that the photon should disappear in a single interaction. Thus the absorption of photons is approximated fairly closely by an exponential law even if the radiation is poorly collimated. It allows the line shape of Mössbauer spectra to be obtained and quantitatively analyzed. The first step: the analysis requires the number of single resonant interactions to be found in a layer dx of depth x, and then, knowing the attenuation law in the medium, i.e. the absorption coefficients and using the known values of α and ω, the number of quanta formed in the layer dx and reaching the surface can be computed.

It is generally not possible to do the same when detecting electrons since their interaction with matter differs from that of electromagnetic quanta. On the average, only a small part of the energy of an electron is lost as a result of its interaction with matter. Therefore, the number of resonant interactions in a layer dx at depth x cannot be used to count the number of electrons emerging from the surface, as simply as in the case of photon detection. Moreover, little can be said of the electron energy. To carry out a quantitative analysis a knowledge is needed of the electron interaction with solids in the energy region of less than 20 keV for ^{119}Sn and less than 15 keV for ^{57}Fe. At present there are no simple and convenient analytical models which describe the passage of electrons through a substance layer of a depth x, characterized by a function T(x), or their reflection from the sample, characterized by a function R(x) in the whole range of the layer thickness ($0 < x < \infty$), where T(x) and R(x) are the ratios of the transmitted and backscattered electrons to the incident ones.

It is often convenient for various numerical calculations to simplify the electron interactions with matter and to divide the elementary interaction events into two groups: elastic interactions, which result in only the trajectory change of the primary electron such that its energy loss can be neglected, and inelastic collisions where only the energy loss of the primary electron in the collision is considered and the direction of motion change of the incident electron is neglected. Electron- solid interactions, including low-energy electrons, are considered in several reviews [1. 23, 3.1-5]. Some original works relevant to Mössbauer spectroscopy [1. 20-22, 3. 6-11] are also important.

The main feature of the electron interaction with a solid may be discussed in terms of the following simplified model [3.9] which is illustrative and enables sufficiently accurate calculations for Mössbauer spectroscopy to be conducted. Simplified pictures of electron interactions with a solid in the

energy region of interest are shown in Fig. 3.1. The solid may be assumed to be an electron gas in which small heavy nuclei are sparsely distributed. The primary electron may come very close to one of the gas electrons, which results in mutual repulsion, the interaction with the rest of the solid may be neglected (Fig. 3.1a). Since both particles have equal mass the primary electron may lose a considerable fraction of its energy in the collision. Since the two electrons are indistinguishable, the electron having a greater energy is considered as a primary one after collision has occurred. One collision results in an energy loss of up to 50 % of the original energy. Such collision may only occur with weakly bound valence electrons with the probability depending on the binding energy of the atomic electrons.
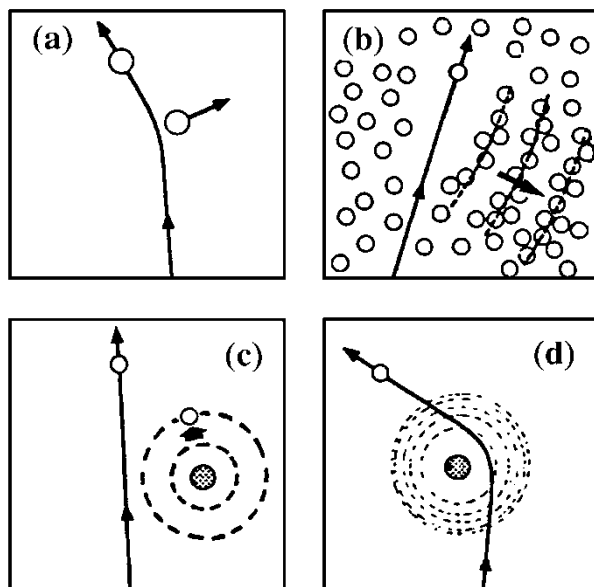

Fig. 3.1 Simplified picture of interactions of electrons with a solid (from [3. 9]). a - binary ("free") collision with an electron; b - energy loss by generation of a plasmon; c - resonancelike atomic excitation; d - elastic scattering by the nucleus.

The Coulomb interactions in the electron gas should also be taken into account. The electron gas is repulsed from the vicinity of the primary electron which is equivalent to the creation of a positive charge density around the trajectory. At a certain distance such screening effects disappear.

After the primary electron has passed, the electron gas (plasma) will try to restore its equilibrium state, which leads to the creation of a wave motion with a certain frequency. A part of the energy of the primary electron is lost during the creation of such quanta (plasmons) (Fig. 3.1b).

A primary electron passing by the atom may eject electrons from an atomic shell. This will be followed by characteristic X- rays or Auger electrons (Fig. 3.1c). The primary electrons may lose their energy in the nuclear Coulomb field and give rise to bremstrahlung.

The incident electron may also interact with an atom without changing its state. The incident electron may be deflected by the screened Coulomb field of the nucleus. Since the nuclear mass is much greater than that of the electron, the deflection may be very strong and will not lead to an appreciable energy loss of the primary electron. This collision is usually called elastic (Fig. 3.1d) and is the main cause of the change of direction "of the incident electrons" motion.

In reality the solid is different from the primitive model we have just considered. Thus, the regularity of atomic positions in the lattice lead to the appearance of energy bands and of characteristic energy losses within the band. The influence of the crystal structure of real solids also manifests itself in the energy distribution of the electrons transmitted through the sample or reflected from it. The influence of the crystal structure and the effect of sample treatment on the shape and intensity of the electron spectra in Mössbauer spectroscopy has been investigated by TS. BONCHEV et al. [3.10]. The authors observed both conversion electrons and photo electrons. The conversion electrons resulted from resonant scattering of γ-quanta in a SnO_2 layer of 40-50 nm thickness. Thin layers of metals were investigated after vacuum deposition onto the SnO_2 layers. The photoelectrons were produced by irradiation of quartz crystals with γ-rays from a source of $^{119m}SnO_2$. The photoelectric effect on silicon produced electrons with an energy of about 21 keV. The spectral shapes of electrons emerging from the three single crystal quartz wafers, cut perpendicular to the x, y and z axes, proved to be very similar. The small difference in intensities were attributed to the effect of crystal orientation and the difference between atomic densities in the planes of cutting.

Other effects of the lattice on electron interactions with matter include diffraction and channeling. However, in Mössbauer spectroscopy these effects may be neglected and the solid may be regarded as isotropic. This assumption allows two important conclusions to be drawn: first, that the probability P(s) for the primary electron to move a distance s in the sample without interacting with it is independent of direction; second, that the following relation is true:

$$P(s_1 + s_2) = P(s_1)P(s_2) . \tag{3.1}$$

The function for which (3.1) is fulfilled at P(0) = 1 is $P(s) = \exp(-s/\lambda)$,

where λ is the mean free path between the interaction events (collisions).

A description of electron movement through matter requires a knowledge of the energy dependence of λ and also the list of events (with their probabilities) which may happen in a collision. If all of these is known then by using theory or direct numerical calculations, the results of a large number of such collisions may be obtained.

Apart from the discrete approach there is also an approach based on the assumption that the electrons lose their energy continuously. The theory of electron stopping by matter was first developed by G. Bethe who regarded the energy loss of electrons as a continuous slowing-down process. Using the quantum theory the following formula was derived for the energy loss in a monatomic substance [3.12]:

$$\frac{dE}{ds} = \frac{2\pi \, e^4 nZ}{E} \ln \frac{1.16 \, E}{I} , \qquad (3.2)$$

where n is the number of atoms per unit volume, I is the mean excitation energy which is a weighted average (over all individual energy losses) per one interaction event. At not too low energies the I value is determined only by the atomic number Z.

The Bethe formula (3.2) allows the discrete process of energy loss to be described by the continuous average energy losses. If numerical values are inserted in (3.2) the stopping power can be obtained in MeV/cm:

$$\frac{dE}{ds} = 0.306 \, \frac{Z}{A} \, \rho \, \beta^{-2} \ln \frac{1.16 \, E}{I} , \qquad (3.3)$$

where $\beta = v_e/c$ (v_e, the electron velocity).

In practice, the following formula for the stopping power is used

$$S = -\frac{1}{\rho} \frac{dE}{ds} = 0.306 \, \frac{Z}{A} \, \beta^{-2} \ln \frac{1.16 \, E}{I} , \qquad (3.4)$$

which characterizes the energy loss per unit mass.

Equation (3.4) shows that the stopping power depends mainly on the electron energy and is only weakly dependent on Z. It should be noted that (3.4) only describes the energy loss along the path ds. It does not allow a determination of the energy loss of electrons generated with energy E at a depth x and which have escaped from the surface. Scattering effects cause the electron trajectory in a substance to be a complex matter and the stopping power of the substance increases continuously as the electrons continue to slow down. To a first approximation the energy losses of electrons in the medium are proportional to the density of the substance (see (3.3)), since changes the Z/A

ratio between light and heavy elements are small. Hence on studying the passage of electrons through matter the layer thickness is often expressed not in linear units centimetre) but rather mass units with the dimension of mass/area [g·cm^{-2}]. Since the energy losses are mainly dependent on the number of electrons $N = n\,Z\,x$ in the layer through which the electron has travelled (see formula (3.2)), some authors suggest to measure the absorber thickness in units of [electrons·cm^{-2}]. These units are to be used only when the incident energy is much higher than the binding energy of atomic electrons. However, this method of measuring the thickness has not found application in Mössbauer spectroscopy.

Let us suppose now that conversion or Auger electrons of energy E_0 emerge at a depth x and move back to the surface. Due to scattering their trajectories will be changed. If energy losses were only a function of the path length, then the spread of the energy loss would be determined by the path length only, that is, only by scattering. However, even for the electrons travelled a certain path length, there will be a distribution of the energy losses, which is known as straggling. It is partly due to the following reasons. First, there are statistical fluctuations in the number of inelastic collisions on that path length. Second, there are fluctuations of energy losses in each collision. Hence, if the electrons reach the surface, their energy distribution will be determined by both scattering and straggling. Sometimes straggling may be neglected and the energy losses, which are the function of the path length, can be calculated using formulae of type (3.4). This approach is called the continuous slowing-down approximation with an important parameter r_B, which is the Bethe range defined as the hypothetical total path length of the electron travelled in the solid until the energy is at some lower limit, usually I. The electron is then incapable of further ionization and is regarded as "absorbed". The above approximation means that all electrons of a given initial energy will be "absorbed" when they have travelled the path length r_B.

Both scattering and straggling effects may be accounted for or used analytically by transport theory or in numerical calculations. The most direct methods involve calculations by the Monte Carlo method which allow the simulation of the electron trajectory in a step-by-step manner. The use of this method has drastically changed the studies of electron penetration in solids. Thus, there is now no need to solve complicated theoretical problems of transport theory and it is possible to concentrate on the elementary interactions in the solid which are of primary interest.

Calculations of penetration and scattering of electrons in the energy region of interest for Mössbauer spectroscopy are well documented, e.g. in [1. 20-23, 3.13-19]. Fig. 3.2 shows how scattering is accounted for in the Monte Carlo method when an electron trajectory is computed. The scattering angle θ can be chosen from a screened Rutherford distribution. The azimuthal scattering angle ψ is chosen at random from the interval $0 - 2\pi$.

The electron trajectory is tracked along one axis in space which is the perpendicular to the foil surface. The polar angle is measured between the axis and direction of motion. Scattering events occur at points joined by free-path segments (Fig. 3.2). It is assumed that the electron loses its energy continuously, the energy loss being given by equation (3.3).
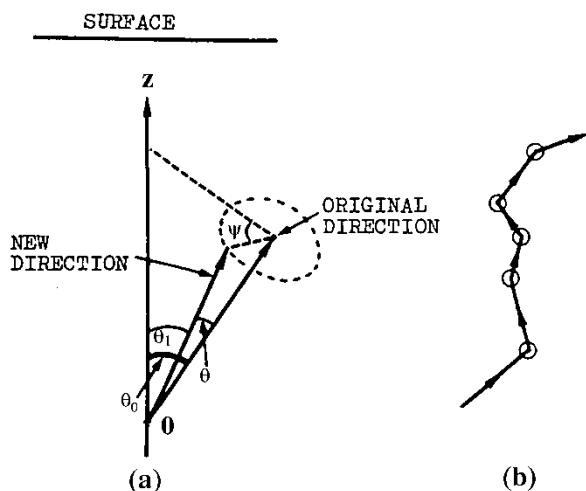

Fig. 3.2 Illustration of Monte Carlo calculations of electron trajectories (from [3. 9]).a - an electron moving at an angle θ to the z-axis has changed the direction of motion into a new one, at angle θ_1 to the z-axis; b - picture of a computed collision sequence.

Fig. 3.2 is an illustration of the calculation method but it does not explain the behaviour of the electron in the substance. Such an explanation would require the examination of a large number of trajectories. The trajectories computed by the Monte Carlo method allow the variation of the electron energy with the sample material to be assessed. It has been shown that light substances (low Z) are "soft", i.e. the penetration of electrons is easy, and backscattering is small. Heavy substances (high Z) are "hard" for electrons, and the main process is then backscattering. For a given Z an increase of energy E causes only the penetration depth to increase without any change in backscattering.

The experimentalist is primarily interested in the probabilities of electron penetration through foils and of their backscattering; in the dependences of T(x) and R(x) on the foil thickness; in energy distributions of backscattered and transmitted electrons; and in the angular distributions. Some of these dependences can be simulated by the Monte Carlo method and presented in Fig. 3.3. The Figure describes the situation when a

beam of electrons with initial energy E_0 is incident onto a plane foil of thickness d (Fig. 3.3a). The shape of the T(d) and R(d) curves, and also that of the energy distribution of backscattered electrons together with some other features of the curves, are correlated in Fig. 3.3. The dependences shown in Fig. 3.3 allow the introduction of important parameters such as the extrapolated range R_e and maximum range R_m. If measured in units of mass/area, they depend mainly on the incident energy.
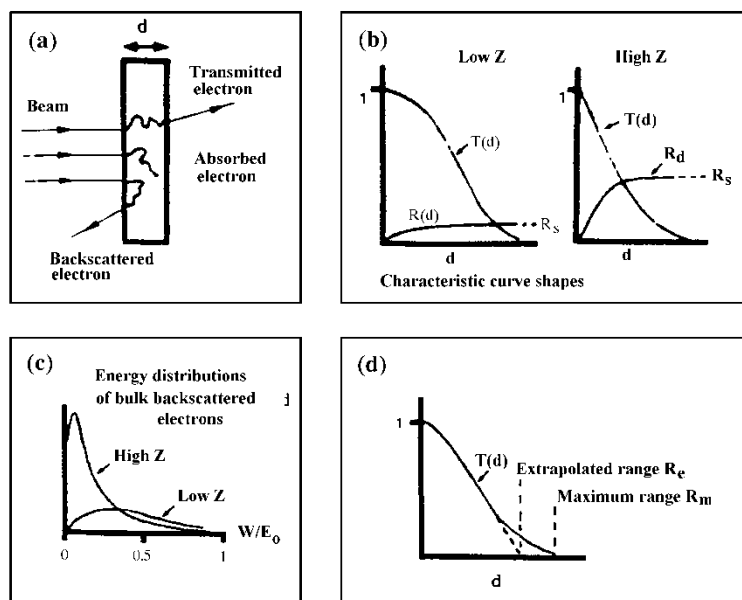
Fig. 3.3 Schematic picture and main features of electron-solid interactions. a - electron paths; b - transmission curves T(d) and backscattering curves R(d); R_s is the maximum fraction of the back-scattered electrons; c - energy distribution of the back-scattered electrons; d - determination of the extrapolated (R_e) and maximum (R_m) ranges (from [3. 9]).

In one of the first theoretical papers on studies of the interaction of electrons with matter, W. Bothe predicted an exponential attenuation of the electron beam [3.20]

$$T(d) \sim \exp(-vd) . \qquad (3.5)$$

However, G. Bethe has shown that the function T(d) is better approximated by the expression [3.9, 21]

$$T(d) \sim \frac{1.724}{1.438 + d / \lambda_{tr}}, \qquad (3.6)$$

where λ_{tr} is the transport mean free path

$$\lambda_{tr} = \frac{\lambda_e}{1 - (\cos\theta)_{av}}, \qquad (3.7)$$

where λ_e is the mean free path between collisions, and $(\cos\theta)_{av}$ is the average value of the cosine of the scattering angle θ in an elastic collision.

A detailed comparison of theories with the experimental data has been carried out by COSSLETT and THOMAS [3.6, 7.22], who showed that if the entire T(d) curve is considered then no theory gives satisfactory results. For electrons of moderate energy all experimental parameters are more weakly dependent on E_0 and Z than for high-energy electrons. The dependences are further weakened at energies of ca 5 keV. There is no universal theory which can be applied to such low-energy electrons. The experimental dependences for the transmission function T(x) for monoenergetic electrons through Cu and Au foils are shown in Fig. 3.4. Three regions are easily seen. At first each curve is bent, then it is nearly linear and finally it becomes exponential. In the authors' opinion, different types of scattering correspond to the three regions. In the first region plural scattering is dominant, in the second multiple scattering is most important and the third region corresponds to diffusion processes. The dashed line MS of Fig. 3.4b separates the first and second regions, and the line DD shows at what depth the scattering may be regarded as diffusion, and the attenuation of the electron beam - as exponential.

The two most important experimental results to be singled out are these: the transmission curves for the same initial electron energies are nearly independent of Z if the foil thickness is measured in units of mass/area [g·cm^{-2}]; and for the energy interval of interest the exponential attenuation is only at the end of the range. For higher Z the exponential dependence is observed at relatively smaller foil thicknesses. In contrast, for light elements, e.g. Al, the T(d) dependence becomes exponential only after 80 % of the incident electrons have been absorbed. On penetration into the medium the relative contribution of inelastic processes increases and, in the opinion of some authors (e.g. [3.9, 13]) the exponential dependence should be attributed not only to diffusion, but to an increase in energy losses.
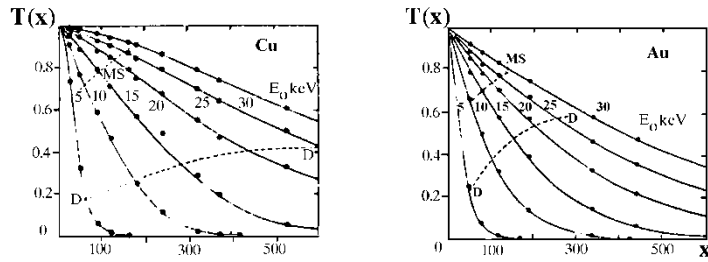
Fig. 3.4 Transmission functions T(x) for monoenergetic electrons with the initial energy E_o from 5 keV to 30 keV, through a: copper foils, b: gold foils (From [3. 6]).

Despite the fact that it is only a part of the transmission curve T(x) which can be sufficiently well extrapolated by the exponent for an initially monoenergetic beam of electrons, COSSLETT and THOMAS [3.6, 7] have introduced some absorption coefficients ν. The ν values have proved to be nearly independent of Z in the case of 5 - 15 keV electrons. The coefficients can be calculated by the formula

$$\nu = 1.4 \cdot 10^{10} \rho \, E_0^{-3/2} \, . \tag{3.8}$$

For higher-energy electrons the dependence of ν on the incident energy assumes a different character and is dependent on Z. Thus, for E_0 values of 15 - 25 keV the absorption coefficient is

$$\nu = 1.9 \cdot 10^{11} \, \rho \, E_0^{-2} \, Z^{1/2} \, . \tag{3.9}$$

The incident energy E_o in expressions (3.8) and (3.9) is given in eV's. The experimentally determined absorption coefficients are smaller than those theoretically predicted by W. Bothe [3.20].

An important parameter which is required when preparing for experimental studies is the electron range. In spite of the similarity in shape of transmission curves for different Z, the layer thickness expressed in mass/area gives rise to quantitative distinctions. Thus, as it has been shown by Cosslett and Thomas, for the 20 keV electrons the energy loss per mass-thickness unit in Al is 50 % higher than in Au, and hence the range in these units is more in gold than in aluminium. If the extrapolated electron range is measured in units of length then, for the 5 - 15 keV electrons, a good approximation is given by the formula

$$R_e = k \, E_0^{3/2} \, , \qquad\qquad\qquad (3.10)$$

where E_0 is in keV, R_e in Å, and the constant k equals 147, 103, 82 and 45 for Al, Cu, Ag and Au, respectively. On using the units of mass/area the difference in the R_e values diminishes. The R value is obtained by extrapolation of the linear part of the dependence of ln(T(d)) on d onto the abscissa. A foil of thickness R_e transmits approximately 2 % of the incident intensity. The above discussion concerns monoenergetic collimated electron beams. In Mössbauer spectroscopy the situation is more complicated since on scattering a successive emission of electrons having various energies may occur. The angular distribution of the electrons is usually assumed to be isotropic.

The electron beam absorption of various incident energies have been studied for β-emitters. It is known from nuclear physics that the exponential attenuation is obeyed approximately in the case of simple β-spectra. The lower the maximum energy of the β-spectrum and the higher the atomic number Z, the better this law is obeyed [3.23]. However, there are no strict quantitative criteria.

Experimental studies by a number of authors (e.g. Cosslett and Thomas) have made it possible to develop and widely use the Monte Carlo method for various calculations in solid state physics. One of the problem is the evaluation of parameters of Mössbauer spectra [1.20, 21; 3.9, 13, 14, 17, 18] and the Monte Carlo method has been used in Mössbauer spectroscopy to calculate the energy spectra of electrons produced by resonant scattering [3.8].

To analyse the Mössbauer spectra, angular distributions of the scattered electrons are required [3.5,19]. Let us consider three groups of electrons produced by irradiation of an α-Fe target by a [57]Co Mössbauer source. The groups are: LMM Auger electrons ($E_0 = 0.65$ keV), K-conversion electrons ($E_0 = 7.3$ keV) and Compton electrons ($E_0 \approx 122$ keV). Assume the O.65 keV and 7.3 keV electrons to be emitted isotropically, and the angular distribution of the 122 keV electrons to be described by the relativistic angular distribution formula for photoelectrons. The angular distributions calculated by the Monte Carlo method for the three groups and for different depths of origin, are presented in Fig. 3.5. It can be seen that as the depth of electron generation increases, the angular distributions of back-scattered electrons are no longer dependent on the initial angular distributions, and are determined by the cosine of the scattering angle.

Computational methods have been used to evaluate the weight functions T(E,x) [1.20, 21; 3.9, 14]. This function serves to replace the exponent in the expression for the spectral shape (see (2.100), (2.101)) describing the attenuation of the beam of photons emerging from a layer dx in the scatterer following
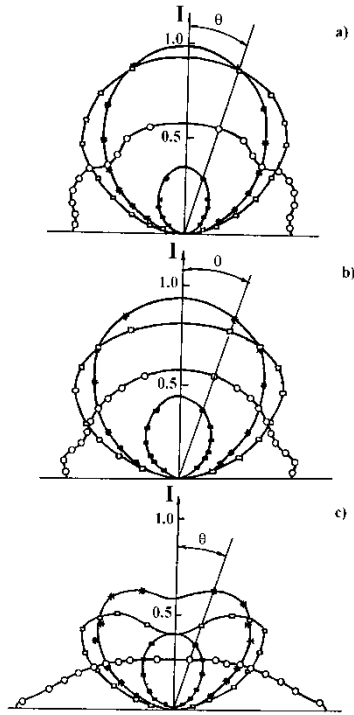
Fig.3.5 Polar plots of theoretical angular distributions of back-scattered electrons (from [3.19]).
a - initial energy = 0.65 keV, final energy = 0 to 0.65 keV. Depth of origin: open circles = 0.0 nm (surface); open squares = 0.2 nm; stars = 0.5 nm; solid squares = 2.0 nm.
b - initial energy = 7.3 keV, final energy = 0 to 7.3. keV. Depth of origin: Open circles = 0.0 nm (surface); open squares = 8.0 nm; stars - 20 nm; solid squares = 80 nm.
c - initial energy = 122 keV, final energy = 0 to 122 keV. Depth of origin: open circles = 0.0 nm (surface); open squares = 1000 nm; stars = 2000 nm; solid squares = 10000 nm.

resonant scattering. Upon computation of the weight functions and analyzing other dependences one is always faced with a problem of what physical parameters are the best to characterize exactly the processes and to describe the dependences required. Of course, it is important that the number of the parameters should be minimal. In the above mentioned studies, it has been demonstrated that the evaluation of the energy losses requires consideration of the stopping power S

$$S = \frac{\mathcal{E}_{av}}{\lambda_i} = \frac{1}{\lambda_i} \int E \, F(E) \, dE \, , \qquad (3.11)$$

where λ_i - is the total inelastic mean free path related to inelastic collisions; E_{av} is the average energy loss in a collision; $F(E)$ is the normalized probability of losing energy E in an inelastic collision.

The main energy dependent parameter for the scattering process is the transport mean free path λ_{tr} (see (3.7)).

Let us imagine a set of electrons incident on a sample in a definite direction. The center of mass of this set will move with an exponentially decreasing speed through the scattering medium and will stop at a distance λ_{tr} from the surface. In some cases the elastic scattering processes or energy losses in the continuous slowing down approximation can be described by using only the $\lambda_{tr}(s)$ function (s, the electron path length). To describe such quantities as the energy distribution of transmitted electrons or their angular distribution requires a knowledge of the total differential scattering cross section. It was shown in [3.9] that λ_{tr} decreases linearly with the path length, and that it is the main feature of the electron transport in solids in the energy range of interest. The scattering and slowing down processes can be characterized by a dimensionless parameter $\alpha = r_B / \lambda_{tr}$ which determines the role played by elastic collisions in the slowing down process.

One of the extreme cases is $\alpha = \infty$, which corresponds to elastic collisions. The absence of scattering (the continuous slowing down) gives $\alpha = 0$. In a general case the center of mass of a set of electrons will stop at a distance r_0 from the surface:

$$r_0^{-1} = \lambda_{tr}(0)^{-1} + r_B^{-1} \ . \quad (3.12)$$

The computation of energy distributions is more complicated since it requires that straggling processes be taken into account. If straggling is not accounted for in the continuous slowing down approximation all electrons will be absorbed at the end of the path length ($\sim r_B$). Straggling, if accounted for, results in the calculated total path length $s = 1.5 \ r_B$ being traversed by approximately 15 % of the incident electrons. The Monte Carlo method squared average energy for the non-absorbed electrons, the relative number of remaining electrons, and also absorption per unit path length as functions of the path length in solids in units of the Bethe range are given in Fig. 3.6 [3.9]. Straggling has been taken into account using the model of binary (free) collisions. The minimal energy transferred in a collision is taken to be 0.001 E_0. It should be recalled that in simple models used for calculations of electron interaction with matter, the stopping power is assumed to be proportional to E^{-1}. As a result, the dependence of the square of the average electron energy on their path length is linear (the dashed line in Fig. 3.6). Due to straggling the dependence departs from the linear one (curve 1 in Fig. 3.6).

It is evident from the above that there is currently no full and consistent theory to describe the low-energy electron interaction with matter. There are two experimental approaches which can be used to treat the interaction of electrons with matter. The first approach is based on empirical dependences and approximations. An example is the hypothesis of the exponential

decrease of the electron beam intensity, when it is assumed that this attenuation is caused by many stochastic effects. The hypothesis is quite satisfactory to explain the CEMS data. Indeed, of prime interest is the probability that electrons originating from a layer dx at a depth x with energy E_0 leave in a random direction from the surface with any energy and at any angle and will be registered by a detector. This approach is not applicable if the electron energy is required.
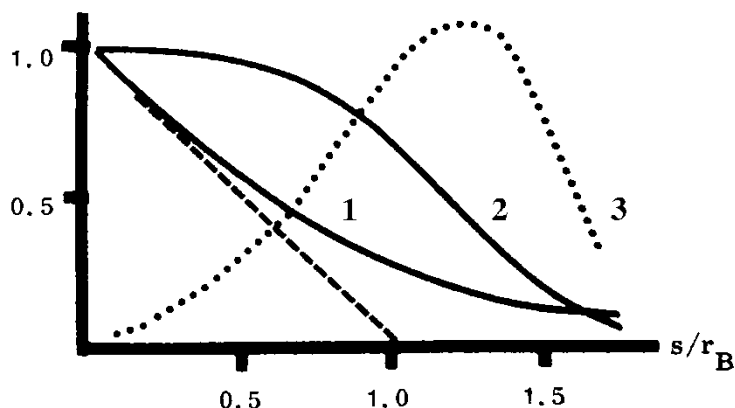
Fig. 3.6 Absorption and average energy as functions of path length, obtained by Monte Carlo simulations (E_o = 7.3 keV) (from [3.9]). 1 - squared average energy for the non-absorbed electrons, 2 - relative number of remaining electrons, 3 - absorption probability (arbitrary units).

The second approach is based on the Monte Carlo calculations of parameters determined by the stochastic character of interactions. Thus, in depth selective conversion electron Mössbauer spectroscopy (DCEMS) we are interested in the group of electrons with a fixed energy leaving the surface at a certain angle within a small solid angle $d\omega$. To describe the experiments in this case, used are not the empirical dependences but the Monte Carlo numerical calculations. The first approach gives a lower accuracy in calculations than the second one, but it is simple and allows some general conclusions to be drawn. The results of approach to CEMS will be discussed in the next section.

3.2. Conversion Electron Mössbauer Spectroscopy Theory Based on the Exponential Attenuation of the Electron Beam

The observation of the Mössbauer effect by the detection of conversion electrons was reported by MITROFANOV and SPINEL [3.24] and KANKELEIT [3.25]. Using magnetic β-spectrometers of rather low luminosity the authors detected the conversion

electrons following the de-excitation of the Mössbauer level in ^{119}Sn and ^{182}W. These studies have demonstrated the possibility of observing the Mössbauer effect in highly converted transitions. This was followed by the development of two Mössbauer techniques for the detection of electrons from surface layers.

The first technique was developed after the paper of BONCHEV et al. [3.26], where it was shown that the energy resolution of modern β-spectrometers allows the conversion electron energy to be related to the depth of the layer from which they emerge. This lead to the appearance of DCEMS which will be discussed in Sec.3.4. The realization of DCEMS in its classic form requires a fairly good energy resolution of the spectrometer. The experiment is carried out within the energy and the angle interval where the contribution of the detected electron beam is practically due to the group of electrons which is generated from resonant scattering. The weight functions T(x,E), corresponding to a β-spectrometer setting for the detection of these electron groups should be appreciably different. The depth resolution is hindered by the contribution of conversion or Auger electrons having other energies and by the photoelectric effect.

The idea of the second technique was described by MITROFANOV [2.70]. The technique is based on the detection over a wide energy range of electrons emitted by the sample surface with an energy which is equal to, or less than, the Mössbauer transition energy. The technique has been developed and become widely used, as described by SPIJKERMAN et al. [2.69, 3.27, 28], where a flat proportional gas-filled counter was used for various applications (see Fig. 2.37). A flat parallel-plate avalanche counter for Mössbauer spectroscopy has been developed by WEYER [3.29]. As compared to the counters shown in Fig. 2.37, the avalanche counter is more fast and efficient for low energy electrons and allows the study of samples with larger areas. A disadvantage is the need to use grids in front of the rough surface of samples.

CEMS is based on the internal conversion process and involves the detection of electrons. The technique might have been named Mössbauer spectroscopy based on the detection of almost all electrons, following the Mössbauer scattering process. The electrons may be divided into several groups: conversion electrons, Auger electrons, low-energy electrons resulting from shake-off events and secondary electrons resulting from the re-emitted Mössbauer quanta and the characteristic X-rays. The energies and relative intensities of the first two groups of electrons for ^{57}Fe and ^{119}Sn are given in Table 3.1. CEMS is, in principle, an integral technique, although appropriate depth selection methods may also be used. Apart from the problems connected with the need to describe the passage of monoenergetic electrons through matter, CEMS also requires that the contribution by the different groups of electrons be considered.

Table 3.1 Main radiation characteristics for the ^{57}Fe and ^{119}Sn de-exitation.

Type	^{57}Fe		^{119}Sn	
	Energy, keV	Probability per de-excitation c_i	Energy keV	Probability per de-excitation c_i
K-conversion	7.3	0.796		
L-conversion	13.6	0.09	19.6	0.83
M-conversion	14.3	0.01	23.0	0.13
KLL Auger	5.4	0.543		
LMM Auger			2.8	0.74

Some problems of CEMS have been considered by KRAKOWSKI and MILLER [3.30]. Because there had been no analytical expression describing the passage of a beam of electrons of interest through matter, the exponential law was taken as the first approximation. It followed many techniques which are well known in Mössbauer spectroscopy, e.g. in the Mössbauer effect with the detection of X-rays (see Sec. 2.6) to be used. The linear absorption coefficients for electrons were taken from the well- known works of COSSLETT and THOMAS [3.7, 22]. A comparison of the calculated results obtained by the diffusion theory and by the exponential law showed that there was no significant disagreement [3.30].

The applicability of the exponential attenuation law in CEMS is an urgent problem and is worthy of detailed consideration. To solve the problem the passage of electrons produced by the Mössbauer effect through layers covering the surface of a resonant scatterer must be examined. Suppose that the area under a Mössbauer spectrum is A + A', where A is given by (2.29) and A' is due to all processes of the non-resonant interaction of Mössbauer radiation with the sample. With a good accuracy, A may be assumed to be proportional to the number of electrons produced by the Mössbauer effect, and A' - to the number of non-resonant electrons, i.e. those produced by the photoelectric effect and Compton effect.

The passage of electrons, produced in films of α-^{57}Fe 0.02 - 0.2 µm thick evaporated onto a bulk sample of α-^{56}Fe, through layers of Al, ^{56}Fe, Sn and Au has been investigated in [1.22, 3.5] (see Fig. 3.7). On the ordinate the ratio is given by $\tilde{\gamma} = (A/A')_x/(A/A')_0$. The 0 and x indices correspond to the Mössbauer spectra before and after depositing the layer of thickness x. Despite the layer thickness being expressed as mass/area, the dependences of Fig.3.7 for the coating layers are different for different values of Z for the coatings. This apparent contradiction with the data of Fig. 3.4 is caused by the fact

that on plotting the dependences of Fig. 3.7, the dependence on Z has not taken into account the photoelectric absorption cross section. This means that $\tilde{\gamma}$ is also dependent on Z of the absorbing coatig. Cumbersome calculations are needed to account for all of these in detail. BABIKOVA et al. [3.5] have taken all the main processes into account and have shown that the curves in Fig. 3.7 coincide after accounting for the Z-dependence of A1. The role played by re-scattering processes should be considered only at a thickness of the coating layer $x \geq R_e/2$, (see (3.10)).
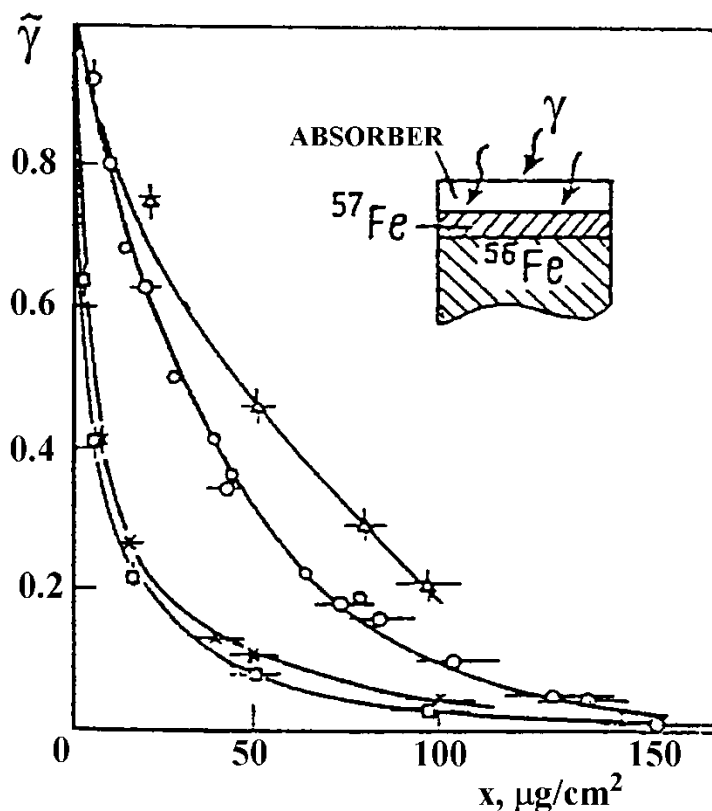
Fig. 3.7 Transmission of electrons due to resonant scattering in an α-^{57}Fe layer (a = 92 %, d ~ 65 $\mu g/cm^2$) through layers of aluminium (open triangles), iron (^{56}Fe, open circleses), tin (crosses) and gold (open squares) (from [1.22]).

Thus, the attenuation law for electrons resulting from resonant scattering, as well as for β-particles, may be assumed to be exponential with $v = (18.0 \pm 1.0)$ μm^{-1} for a scatterer of α-Fe. In accordance with the authors' evaluation, 90 % of electrons contributing to A for a scatterer of α-Fe emerge from a layer ~ 130 nm thick. The dependences obtained in [1.22, 3.5] allow a determination of the thickness of coatings made from non-resonant atoms. The validity of the exponential attenuation law for the 5 keV electrons is justified by analysis of a large amount of experimental data and also by the Monte Carlo calculations [3.31]. When the exponential law is valid, the equations used for phase analysis and dealt with in Chapter 2 are simplified in CEMS.
The expression for the area under the spectrum from a bulk sample (see (2.99)) may be substantially reduced, since the

ratio of the linear non-resonant absorption coefficient for electrons is always significantly less than unity. For example, for a scatterer of iron metal and K-conversion electrons $\gamma = 0.003$. At $\gamma \ll 1$, the area under the spectrum from a bulk sample can be described as

$$A = \frac{2\,\pi^2\mu_r}{3\,\beta} \; \frac{\beta\sqrt{1+\beta} - 2(\sqrt{1+\beta}-1)}{\beta^2} \; . \qquad (3.13)$$

If $\beta \ll 1$, further reduction of the expression giving the area under the spectrum from a bulk sample is possible.

$$A = \pi^2\beta \left[\frac{1}{2} - \frac{\beta}{6} - \frac{\beta^2}{8} \right] . \qquad (3.14)$$

Usually both γ and $\beta \ll 1$. Thus, for a scatterer of α-Fe in the limiting case (a = 90 %), the β parameter is 0.18 and (3.14) may be simplified as:

$$A = 0.474\,\pi^2\,\beta \; . \qquad (3.15)$$

As has been shown in Sect.2.7, the angular dependence in the exponent $\exp(-x/\cos\theta)$ of (2.93) substantially complicates the calculations and leads to the appearance of complex special functions. This is why HUFFMAN [2.2, 3.32] has suggested a description of the attenuation of the electron beam by the function $\exp(-vx)$. According to this description $\exp(-vx)$ should be used as soon as conversion electrons can be considered to participate in the diffusion process. This simplifies the calculation and gives a more advanced theory of CEMS as compared to that described by R. Krakowski and R. Miller. However, it must be noted that such results cannot be used in backscattering experiments where γ-quanta or X-rays are detected. Huffman's model is important because all electrons on the sample's surface are considered as opposed to the electron beam due to K-conversion electrons. It allows the theory to be applied to the quantitative interpretation of CEMS experiments. For example, a multilayer sample was considered and a relation obtained which connected the parameters of the Mössbauer spectrum with the depth of the layers. This is explained by letting $P_j(v, x)$ be the fraction of the Mössbauer quanta beam absorbed on the way to the layer dx. The expression for the volumetric source strength of this layer due to the K-conversion electrons may be written in the form

$$S_{K,j}(v,x) = f \frac{\alpha_K}{1 + \alpha_{j-1}} e^{-B_{j-1}} e^{-\mu_{aj} x} \frac{dP_j(v,x)}{dx} dx , \qquad (3.16)$$

$$\text{where} \quad B_{j-1} = \sum_{i=1}^{j-1} \mu_{ai} d_i .$$

Following Huffman, the effect is due to both the conversion and Auger electrons. The beam of Auger electrons from the layer under consideration $S_{A,j}(v, x)$ for ^{57}Fe is

$$S_{A,j}(v, x) = 0.7 \, S_{K,j}(v, x) . \qquad (3.17)$$

The beam of conversion electrons from a j-layer on the sample surface at a velocity v is

$$I_{K,j}(v) = \frac{1}{2} \int_0^{d_j} S_{K,j}(v,x) \, e^{-(\nu_{Kj} x + D_{j-1})} \, dx$$

$$\qquad (3.18)$$

$$= \frac{f\alpha_K}{2(1 + \alpha)} e^{-(B_{j-1} + D_{j-1})} \int_0^{d_j} e^{-(\mu_{aj}+\nu_{Kj})x} \frac{dP_j(v,x)}{dx} dx ,$$

$$\text{where} \quad D_{j-1} = \sum_{i=1}^{j-1} \nu_{Ki} d_i .$$

The beam of Auger electrons is

$$I_{A,j} = \frac{0.7 \, f\alpha_K}{2(1 + \alpha)} e^{-(B_{j-1} + G_{j-1})} \int_0^{d_j} e^{-(\mu_{aj}+\nu_{Kj})x} \frac{dP_j(v,x)}{dx} dx ,$$

$$\qquad (3.19)$$

where ν_{Aj} is the linear absorption coefficient for the Auger electrons in a layer j,

$$G_{j-1} = \sum_{i=1}^{j-1} \nu_{Ai} d_i .$$

The total beam of electrons on the sample surface will also contain contributions from photoelectrons due to the photoelectric effect in the layer dx - $S_{ph,j}(x)$ and the subsequent Auger electrons - $S_{phA,j}(x)$

$$S_{ph,j}(x) \sim (n_{Fe})_j \, \sigma_{ph} \, e^{-B_{j-1}} \, e^{-\mu_{aj}x} \, dx \quad ,$$

(3.20)

$$S_{phA,j}(x) = 0.7 \, S_{ph,j}(x) \ .$$

The energy of the photo- and Auger-electrons equals the energy of K-conversion and Auger electrons which are generated on resonant scattering. The two contributions to the total beam (3.20) may be assumed to be independent of the velocity. The generated electrons are not isotropic, however the angular dependence for the low-energy photoelectrons in which we are interested is not very strong [3.4, 5]. These electrons contribute only to the background which is composed of other components which are difficult to be quantified. Hence Huffman suggested a fairly good approximation to assume the isotropic emission. The contribution into the background from the photoelectrons of the j layer under these assumptions may be written as:

$$I_{ph,j} = \int_0^{d_j} S_{ph,j}(x) \, \frac{e^{-\nu_{Kj}x} \, e^{-D_{j-1}}}{2} \, dx$$

(3.21)

$$= \frac{\sigma_{ph}(n_{Fe})_j}{2} \, \frac{e^{-(B_{j-1} + D_{j-1})}}{\mu_{aj} + \nu_{Kj}} \left[1 - e^{-(\mu_{aj} + \nu_{Kj})d_j} \right] \ .$$

The total normalized beam of background electrons on the sample surface, which at the same time is the beam at $v \to \infty$, can be written in the following form

$$I'(\infty) = I' + \sum_j (I_{ph,j} + I_{phA,j})$$

(3.22)

$$I_{phA,j} = \frac{0.7\sigma_{ph}(n_{Fe})_j e^{-(B_{j-1} + G_{j-1})}}{2 \qquad \mu_{aj} + \nu_{Aj}} \left[1 - e^{-(\mu_{aj} + \nu_{Aj})d_j} \right] \ .$$

I' describes the detected electron beam due to all electrons except the photoelectrons and the related Auger electrons.

Although the intensity is difficult to calculate, it can be determined experimentally. Thus, following Huffman, the total beam of electrons from a scatterer at a Doppler velocity v, may be represented as:

$$I(v) = I'(\infty) + \sum_j (I_{K,,j}(v) + I_{A,,j}(v)) .$$ (3.23)

The area A under the Mössbauer spectra is the sum of contributions $A_{K,j}$ from K-conversion electrons and $A_{A,j}$ from Auger electrons

$$A = \int_{-\infty}^{\infty} \frac{I(v) - I'(\infty)}{I'(\infty)} \, dv = \sum_j (A_{K,j} + A_{A,j}) ,$$ (3.24)

$$A_{K,j} = \frac{1}{I'(\infty)} \int_{-\infty}^{\infty} I_{K,j}(v) \, dv .$$

For the area under the spectrum from the outermost layer, the analytical expression derived by Huffman is:

$$A_{K,1} + A_{A,1} = \frac{\pi \, f \, \alpha_K}{I'(\infty)(1 + \alpha)} \left\{ H(\kappa, t_a/2) + 0.7 \, H(\eta, t_a/2) \right\} .$$ (3.25)

The H function and the results of its graphic evaluation as a function of the effective layer thickness t_a are given in [2.2]. The κ and η parameters are determined by the linear absorption coefficients for γ-quanta and conversion electrons or Auger electrons:

$$\kappa = \frac{2(\mu_a + \nu_K)}{\mu_r} + 1 ; \qquad \eta = \frac{2(\mu_a + \nu_A)}{\mu_r} + 1 .$$ (3.26)

For a bulk sample the area under the spectrum may be written as:

$$A_{K,1} + A_{A,1} = \text{const} \left[\frac{1}{(\kappa^2 - 1)^{1/2}} + \frac{0.7}{(\eta^2 - 1)^{1/2}} \right] .$$ (3.27)

It is more difficult to derive simple and exact expressions for the spectral shape. Since the spectral shape from conversion electrons is similar to that from Auger electrons, it is reasonable to consider only the former. On resonance, at a Doppler velocity v_i, the intensity of K-conversion electrons

from the first layer may be written as:

$$I_{K,j}(v_i) = \frac{f \; \alpha_K}{2(1 + \alpha)} \; \mathcal{L}(\kappa, t_a/2) \; . \qquad\qquad (3.28)$$

The $\mathcal{L}(\kappa, t_a/2)$ function and the results of numerical calculations are given in [2.2]. The theory does not neglect the angular dependence in $\exp(-vx/\cos\theta)$ (see Sect. 2.7), and it is expedient to use this theory and formalism of $\hat{E}_2$ functions.

The main questions to be answered by any theory used for CEMS are: (i) how the depth phase analysis can be performed when no model is assumed? and (ii) when can the model be assumed and only its characteristic parameters be obtained? In the first case, based on experimental data only, the sample structure must be elucidated. In other words, the questions are whether and how it is possible to make the depth selection and determine the integrity of the coating. These are the most complicated problems and an entire subsection will be devoted to them.

The phase analysis of surface layers of oxidized or specially treated samples of iron and tin has been considered by Huffman who determined, for example, the layer thickness of haematite and magnetite formed on the α-Fe surface. Either of the hypotheses discussed above for the exponential attenuation of the electron beam assuming the sample surface to be ideally smooth results in approximately the same weight functions as are produced in Monte Carlo simulations (see Sect. 3.3). The effect of the surface roughness has been recently investigated and the calculations are reported in [3.18, 33].

In most evaluations of the surface thickness the exponential attenuation hypothesis is quite adequate. However, one should not overestimate the accuracy of the surface thickness determination, which for a scatterer of iron of less than ~ 60 nm thick is in the order of ± 10 nm and for thicker layers is about ± 20 nm.

To analyze the influence of saturation effects and resonant scattering in upper layers on the parameters and line shape in CEMS, and also on the thickness of the analyzed layer, the theory developed in Sect. 2.7 can be used. The linear extinction coefficients for the electrons of interest calculated by (3.8) are: $v_K = 17.5$ μm^{-1} for K-conversion electrons, $v_L = 6.88$ μm^{-1} for Auger electrons. Let us assume that the model samples and their parameters are the same as in Sect. 2.7, where it has been shown (see Fig. 2.29) that saturation effects are appreciable even for monophasic samples. These effects influence the dependence of the line intensities on the effective thickness of the scattering layer. The line broadening, even for a bulk scatterer (a = 90 % ^{57}Fe), is negligible.

The concept of the "reference unit layer" introduced in Sect. 2.7 can now be used. For the K-conversion electrons and an absorber of α-Fe this layer should be ~ 1 nm thick and is determined by the v_K value.

 The departure from the linear dependence of the Mössbauer signal (see (2.30)) on increasing the thickness of the absorber of non-magnetic iron is illustrated by Fig. 3.8 where the intensity from the reference unit layer is taken as unity. This is one of the most obvious illustrations of saturation effects. The deviation of the calculated values from the straight line at a = 2.14 % is caused entirely by the electron absorption. The coincidence of the calculated intensities and areas (the $\pi\Gamma$ coefficient is to be included) confirms the validity of the conclusion. The difference in the dependences of intensities and line areas for a = 90 % on the thickness and their values are determined by saturation effects and by the fact that the scattered intensity from the reference unit layer is 41.5 times as high as from the same layer at a = 2.14 %.
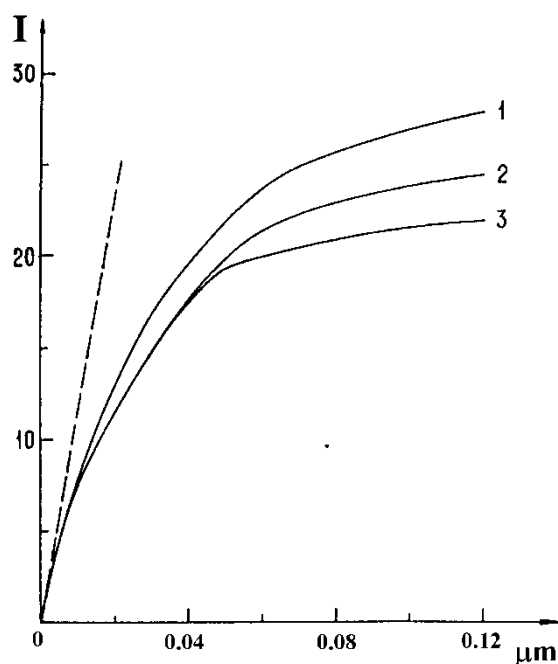
Fig. 3.8 Dependences of intensities and areas under the Mössbauer spectrum on the thickness of the scatterer of non- magnetic iron (detection of K-conversion electrons). 1 - the dependences coincide at a = 2.14 %; 2 - areas and 3 - intensities for a = 90 %.

The saturation effects may be observed also for two-layer samples. The effects do not influence the line shape of the spectra from samples of non-magnetic iron (a = 2.14 %). But, for the enriched samples (a = 90 %), saturation effects are evident and at d ~ 0.15 µm the spectrum from the lower layer is split. The peak-value is approximately one percent of the line intensity in the spectrum from the upper layer.
In CEMS, electrons of different energies provide information on layers of different thickness, which is illustrated by Table 3.2. In practice it is necessary to know the thickness of the analyzed layer which corresponds to the

detection of all electrons and this requires a knowledge of all contributions to the spectrum. The contributions of Auger, K-, and L+M-conversion electrons to the observed Mössbauer signal from the second layer ($d_2 = 100$ μm) of the sample are shown in Fig. 3.9. Both layers correspond to the hypothetical non-magnetic iron (a = 2.14 %). The contribution of a given group of electrons to the area under the spectrum from a homogeneous bulk sample ($d_1 = 0$) is taken as unity. The calculated area under the spectrum from K-conversion electrons is 0.0138, that from L- conversion electrons is 0.0346, and from Auger electrons is 0.0087. If these values are divided into $\pi\Gamma$ then the intensities at resonance are obtained. Furthermore, if the probabilities of generating the K-, L+M - conversion and Auger electrons are taken into account, the probabilities for the emergence of the corresponding electrons can be evaluated. At resonance, K-conversion electrons may be expected to emerge from the sample surface with a probability of about 0.0012. For L- conversion electrons the probability is 0.0004, for Auger electrons it is 0.0005.
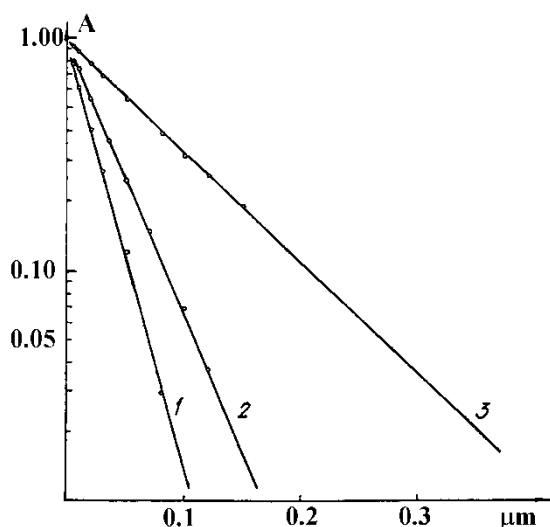
Fig. 3.9 Area under the Mössbauer spectrum from the bulk as a function of the thickness of the upper layer. The spectra correspond to the detection of: 1 - Auger electrons; 2 - K- conversion electrons; and 3 - L-conversion electrons.

Apart from the sample consisting of thin layers on a bulk substrate, two-layer films are also of practical interest. On studying the films to evaluate the thickness of each it is necessary to know the redistribution of Mössbauer signals (i.e. the areas under spectra) as a function of thickness of one of the films. The dependences of the areas under the spectra, from the inner layer thickness of α-^{57}Fe at two values of the second

layer thickness is shown in Fig.10.

 As has been shown in Sect. 2.7, a small difference in line positions (S ~ Γ) for the two layers may be lead to a distortion of the spectrum (see Fig. 2.35). Similar calculations in CEMS have shown that only at S ~ Γ/2 is there a small distortion in the line shape from the inner layer.

3.3. Theory of CEMS Based on Elementary Electron Interactions

 The Monte Carlo method using fast computers for the direct simulation of electron interactions in the energy interval of interest has enabled much progress over the last fifteen years for the development of CEMS theory and in the interpretation of the results. It has been found feasible to evaluate some of the important parameters for the processes related to the detection of conversion electrons. It is therefore appropriate that the weight functions should be considered in greater detail.

Table 3.2
Thicknesses of the analyzed layers on separate detection of conversion and auger electrons scattered from a sample of metal iron.

| p, % | $H_{eff} = 0$ | | | | $H_{eff} = 33.0$ Tesla | | | |
| | a = 90 % | | a = 2.14 % | | a = 90 % | | a = 2.14 | |
	d_I μm	d_A μm	d_I μm	d_A μm	d_I μm	d_A μm	d_I μm	d_A μm
	K-conversion electrons							
95	0.085	0.10	0.11	0.12	0.11	0.12	0.12	0.12
98	0.105	0.12	0.13	0.14	0.13	0.135	–	–
	Auger electrons							
95	0.065	0.07	0.07	0.085	–	–	–	–
98	0.07	0.08	–	–	–	–	–	–
	L+M – conversion electrons							
98	0.17	0.3	0.3	0.3	–	–	–	–

 Notes: d_I and d_A – the thicknesses of the analyzed layers of iron obtained from data on the dependences of the peak-values or areas under the spectra.

Notes: d_I and d_A - the thicknesses of the analyzed layers of iron obtained from data on the dependences of the peak-values or areas under the spectra.
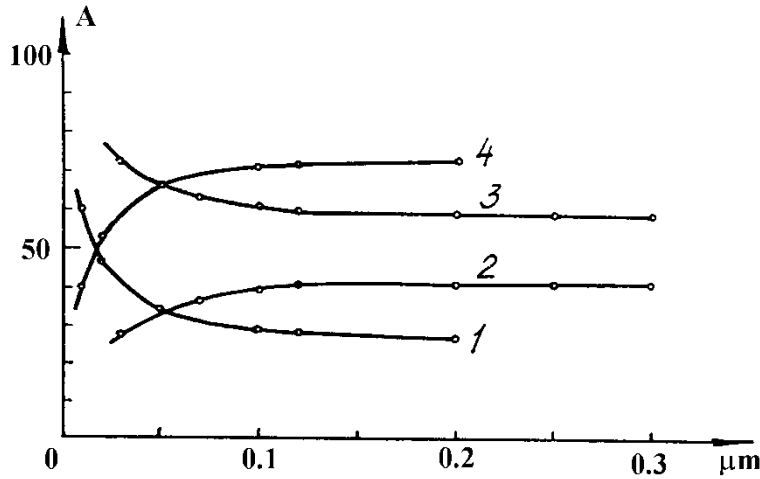
Fig. 3.10 Area dependences of the spectra from the upper layer (1 and 3) and lower layer (2 and 4) for a two-layer sample of ordinary iron (a = 90 %), on the thickness of the lower layer. 1,4 - d_1 =0.01µm; 2,3 - d_1 = 0.03µm

The weight functions were introduced and computed by the Monte Carlo method in [3.9,15, 33-35]. These functions are, in the first instance, functions of distance from the surface, i.e. of the depth x. The weight functions are needed to evaluate the average number of electrons which are detected for each resonant scattering event occurring at the depth x. This requires a knowledge of the weight functions and the parameters of the arrangements used for selecting and detecting the electrons. Let us assume that an electron to be detected is generated at a depth x and leaves the surface with an energy E at an angle θ. The weight function for a plane surface will depend on the x, E and θ parameters. At this stage the contributions from separate groups of electrons into the weight functions are not singled out and the function is denoted by the superscript "tot".

The function $T^{tot}(E, x, \cos\theta)dE\ d\cos\theta$ gives the probability for an electron travelling in a random direction at a depth x to leave the absorber in a direction in the interval between $\cos\theta$ and $\cos\theta$ + $d\cos\theta$ with an energy from E to E + dE. The discussion will be illustrated by numerical evaluations for [57]Fe. The corresponding electron spectrum recorded by a retarding field electron spectrometer is presented in Fig. 3.11 [3.36]. The energy resolution R is 1.5 % at 7.3 keV.

When variables in the weight function are fixed they are described as subscripts. If the integration is performed over all their possible values, the subscripts will be replaced by subscripts t. The type of electrons will be indicated by a superscript.

For each scatterer there is function, $T_{t,t}^{tot}(x)$ which may be represented as the sum of two functions:

$$T_{t,t}^{tot}(x) = T^e(x) + \hat{T}(x). \tag{3.29}$$

$T^e(x)$ is the part due to electrons directly emitted as a result of resonant scattering and $\hat{T}(x)$ is the contribution of electrons produced photoelectrically by X-rays and γ-rays from the scattering process in the sample. In this notation the possible correlation (the so-called pairing effect [3.37]) between the K- conversion electrons and photoelectrons produced by X-rays is neglected.
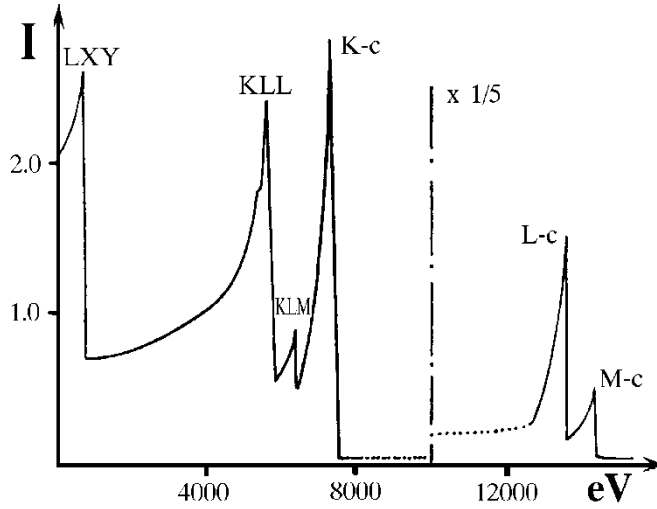

Fig. 3.11 Electron spectrum of a ^{57}Co Mössbauer source (18 mCi), recorded with the retarding grid electron spectrometer (from [3.36]). K-c, L-c and M-c are the K-, L- and M-conversion electrons; KLM, KLL and LXY - are the Auger electrons.

Detectors used in CEMS, e.g. gas-flow counters of the type in Fig. 2.37, are characterized by an efficiency function $\in(E, \cos\theta)$ for detecting electrons. This function is the probability of an electron with energy E emerging at an angle θ to the surface normal being detected. For our purposes the efficiency may be assumed to be independent of both E and cosθ and to be the same for all the groups of electrons.

The weight function $T^e(x)$ contains the contributions from K-, L- and M-conversion electrons and Auger electrons

$$T^e(x) = \in \left\{ C_K T_{t,t}^K(x) + C_A T_{t,t}^A(x) \left[1 - \in T_{t,t}^K(x) \right] + C_L T_{t,t}^L(x) \right\} 2 \ , \tag{3.30}$$

where all the Auger electrons are taken together as well as L- and M-conversion electrons; the C_i values are given in Table 3.1.

The factor $[1 - \in T_{t,t}^K(x)]$ has been introduced in [3.37]. This accounts for the Auger electrons following the K-conversion electrons. A detector of the type presented in Fig. 2.37 would register the simultaneous emergence of the two electrons as one event and generate only one electric pulse.

It is evident from Fig.3. 11 and Table 3.1, that the 6.3 - 7.3 keV energy interval is of most interest. The K-conversion electrons are dominant, since the contribution from "harder" electrons is small and practically independent of energy in this energy interval. The beam of electrons with an energy less than 6.3 keV is determined by groups of electrons with different initial energy. Electrons whose energy is originally less than 1 keV are not taken into consideration. One of the reasons is that the thickness of a layer from which the electrons are able to emerge is such that the resonant scattering probability is negligible.

Let us introduce the following functions: $T_{E,\cos\theta}^K(x)$, which is the probability for a K-conversion electron coming from a depth x, leaving the scatterer with an energy E and at an angle θ; and $T_{x,\cos\theta}^K(E)$, which is the energy distribution of K-conversion electrons originating from a depth x and leaving the scatterer at an angle θ. $T_{E,x}^K(\cos\theta)$ is the angular distribution of these electrons. Let the electrons detected be emitted from the scatterer in solid angle from θ_1 to θ_2 and in an energy interval $E_1 \leq E \leq E_2$. The weight function is written in the following form:

$$T_{E,\cos\theta}(x) = \int_{\cos\theta_1}^{\cos\theta_2} \int_{E_1}^{E_2} T(E,x,\cos\theta)\ dE\ d\cos\theta \ . \tag{3.31}$$

If all the electrons are detected irrespective of their energy and angle, the weight function takes the form

$$T_{t,t}(x) \int_0^1 \int_0^\infty T(E,x,\cos\theta)\ dE\ d\cos\theta \ . \tag{3.32}$$

The beam of K-conversion electrons detected at a Doppler velocity v (i.e. the Mössbauer spectrum), is

$$I_K(v) = \int_0^\infty T_{t,t}^K(x)\ S_K(v,x)\ dx \ . \tag{3.33}$$

The calculated weight functions for K-conversion electrons and scatterers of iron, aluminium and haematite are shown in Fig. 3.12. Since the weight function $T_{t,t}(x)$ for K-conversion electrons is both angle- and energy-independent, the calculations are substantially simplified and can be performed according to the continuous slowing down model (cf. Sect. 3.1). It is more difficult to calculate the $T_{E,\cos\theta}(x)$ functions since there is an energy dependence and straggling should also be considered. It has been found convenient in CEMS to express the depth in units of mass/area, equivalent to the mass thickness of a monoatomic substance layer 1 Å thick. For example, the mass thickness of any substance equal to 7.86 $\mu g \cdot cm^{-2}$ is described as
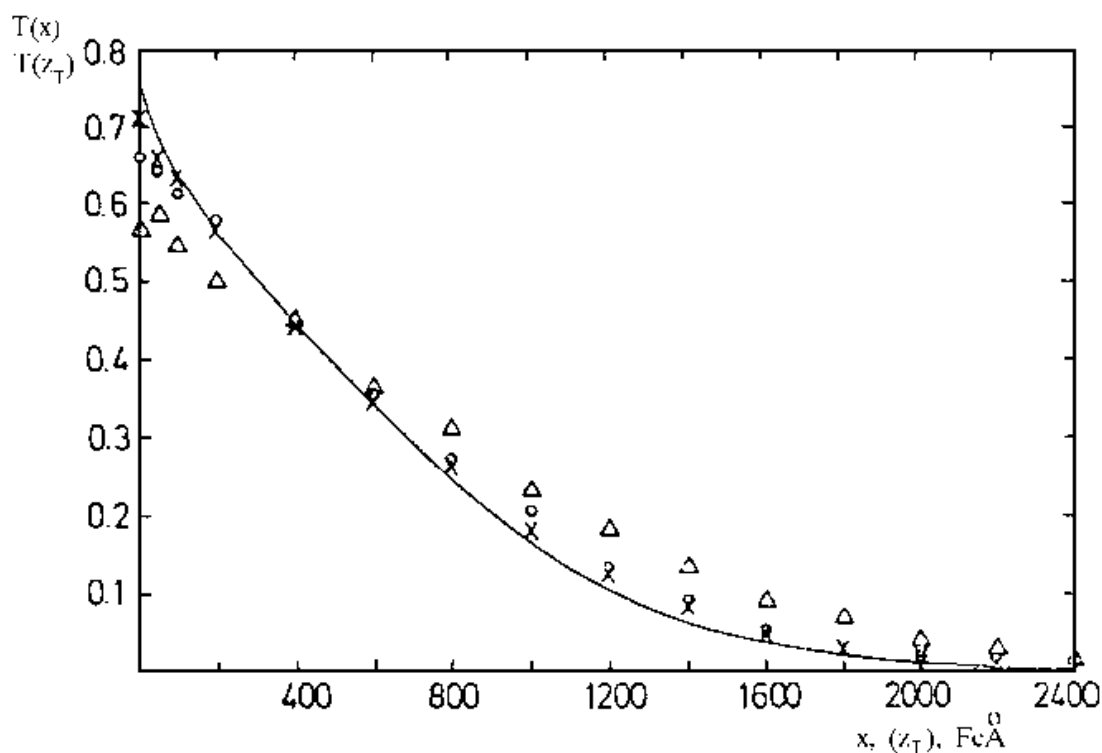
Fig. 3.12 Calculated weight-functions for a plane surface. Solid line - Monte-Carlo calculated results for iron, haematite and aluminium. The calculated topographic weight functions are given for the wavy surfaces which are characterized by the amplitude A and the wavelength W: crosses - A = 1000, W = 10000; open circles - A = 500, W = 2000; open triangles - A = 1000, W = 2000 (from [3.18]).

100 FeÅ. The calculated results for iron, haematite and aluminium are very similar (Fig. 3.12) and may be approximated by the simple formula

$$T_{t,t}^{K}(x) = 0.74 - 2.7(x/r_{B}^{K}) + 2.5(x/r_{B}^{K})^{2} \; ; \qquad 0 \le x \le 0.55 \; r_{B}^{K} \; ,$$

$$(3.34)$$

$$T^K_{t,t}(x) = 0 \; ; \qquad\qquad\qquad x > 0.55 \; r^K_B \; .$$

The Bethe range r_B^K of the K-conversion electrons corresponding to a scatterer of iron is taken to be 3200 FeÅ.

A more accurate calculation and a more detailed treatment of the electron interaction with matter has only a negligible effect on the calculated function $T_{t,t}^K(x)$. For a substance X of density ρ_X

$$[T(E_o,x)]_X = [T(E_o,x\rho_X / \rho_{Fe})]_{Fe} \; .$$

If proper r_B values are used, formula (3.34) is applicable not only to various phases, but also to electrons of various energies. This is due to the shape of the transmission curves (T(d) in Fig. 3.4) being practically independent of r_B. The initial value of the function $T_{t,t}^i(0) \approx 0.75$ is determined by the fact that 50 % of electrons created on the sample surface will leave immediately. The rest of the electrons will move inwards, but half of them may be reflected and leave the surface, too.

To calculate the total electron beam from the surface it is sometimes convenient to use function U(x) which are defined as the primitive functions of the corresponding weight functions T(x)

$$U(x) = \int_0^x T(x') \; dx' \; . \qquad\qquad\qquad (3.35)$$

Since T(x) functions are dimensionless, the U(x) function has the dimension of length (e.g. in FeÅ).

For non-enriched samples the function $S_K(v,x)$ may be assumed independent of x. Indeed, even in the limiting case of "nonmagnetic" iron, the intensity $I_M(E, v, x)$ in the layer whose thickness is $0 < x < 0.2$ μm, is constant within 3 %. Therefore, on irradiation by a Mössbauer source of real non-enriched samples, the surface layer may be considered as a source of K- conversion electrons, whose $S_K(v)$ function is independent of depth. Thus, the intensity of K-conversion electrons, generated in the layer of depth x and escaping from the surface in any direction with any energy, is

$$I_K(v,x) = S_K(v) \; U^K_{t,t}(x) \; .$$

The $U_{t,t}^i(\infty)$ function is a measure of the yield of electrons of the i-th group from the surface of a bulk sample. Monte Carlo calculations give:

$$U_{t,t}^K(\infty) \simeq C_K \; 0.149 \; r_B = 477 \; C_K \; Fe\overset{\circ}{A} \; . \qquad\qquad (3.36)$$

Sometimes it is convenient to introduce the so-called effective range r_{eff} which is analogous to the depth of the analyzed layer; r_{eff} is the depth from which the electrons have an appreciable (say, more than 1 %) chance of escaping. The calculations give $T_{t,t}^K(2000 \; Fe\overset{\circ}{A} = 0.012 \pm 0.001$ (see Fig.3.12); $r_{eff} \approx 0.60 \; r_B^K \approx 2000 \; Fe\overset{\circ}{A}$. Note, that if the exponential attenuation law is obeyed, electrons whose probability of escaping the surface is higher than 10%, will have $r_{eff} \approx 1300 \; Fe\overset{\circ}{A}$ (see Sect. 3.2), which is in a good agreement with the value above.

The calculated dependences [3.17] which are important for understanding the physical concepts and for progress in CEMS are shown in Fig. 3.13. The average energy and average path length of K-conversion electrons which are detected above the surface are given in Fig. 3.13 as functions of the depth of their origin. It is interesting that the average energy of the beam is not strongly changed even after the electrons have passed through the layer $r_{eff}((E_{av}/E_0)_{r_{eff}} \approx 0.49)$, but the beam intensity decreases by a factor of about 100.
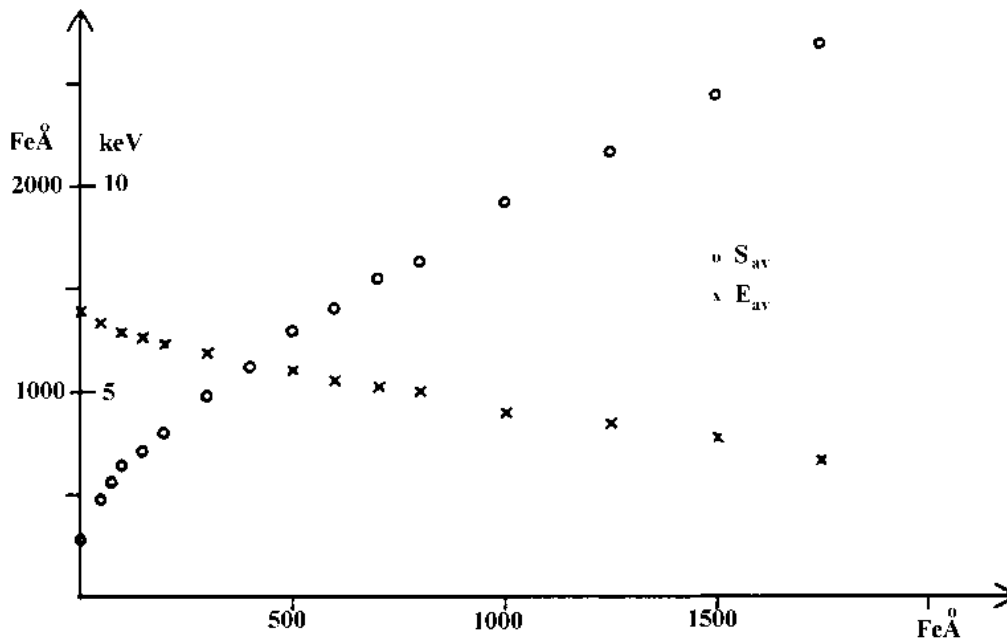
Fig. 3.13 Average energy E_{av} and the average path length S_{av} of K-conversion electrons emerging at all angles and energies (from [3.15]).

The angular distribution of electrons generated at different depths is presented in Fig. 3.14. It demonstrates the possibility of depth selection in CEMS by the use of an appropriate angle of detection. Indeed, if the electrons starting from the surface are isotropic, for a layer of only 2 nm thick the number of electrons coming out in "glancing" angles decreases sharply. For electrons from the 10 nm layer the $\cos\theta$ distribution is valid. For larger depths of origin the distribution is proportional to $\cos^2\theta$.
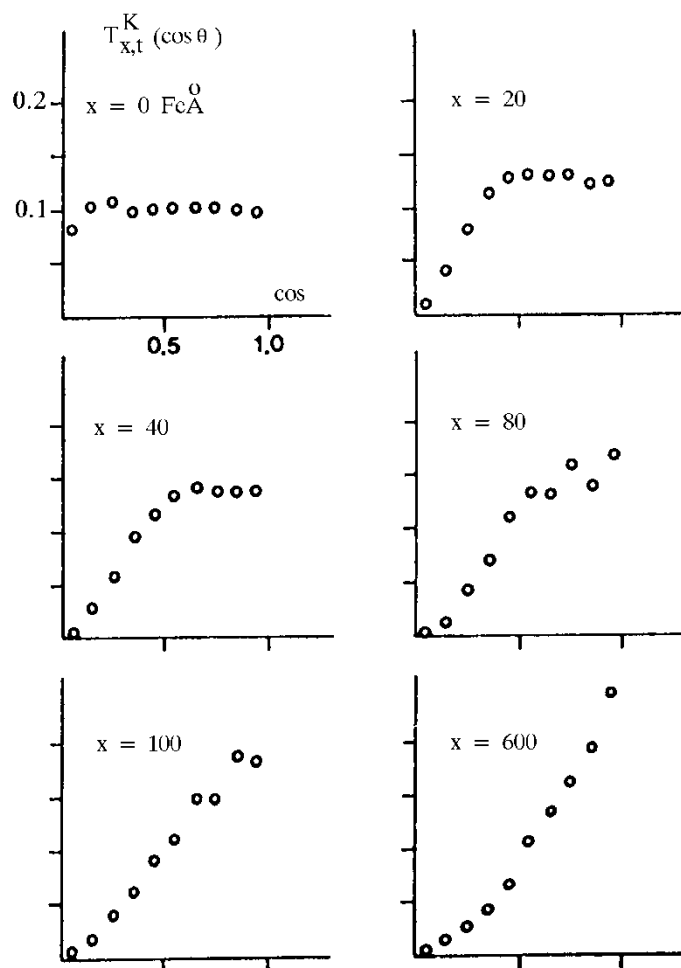
Fig. 3.14 Weight-functions $T^K(\cos\theta)$ (from [3.15]), x is the depth of origin.

In addition to Fig. 3.13 some energy characteristics of the beam of K-conversion electrons are illustrated by Fig. 3.15. The energy distributions of K-conversion electrons leaving the scatterer at any angle are given as functions of the depth of origin x in a scatterer of α-Fe.

The dependences illustrate a possibility of the depth selectivity if a detector is used with a fairly good energy resolution.

Thus, for example, the probability for electrons with $E = 7.3$ keV escaping from the layers deeper than 300 FeÅ may be neglected. The dependences $T_{x,t}^{K}(E)$ (Fig. 3.15) which are important for the depth selective analysis are considered in the energy interval which is restricted by the peaks of K-conversion and KLM-Auger electrons (see Fig. 3.11). This 6.3 - 7.3 keV energy interval is known as the APK (Almost Pure K-conversion) interval.
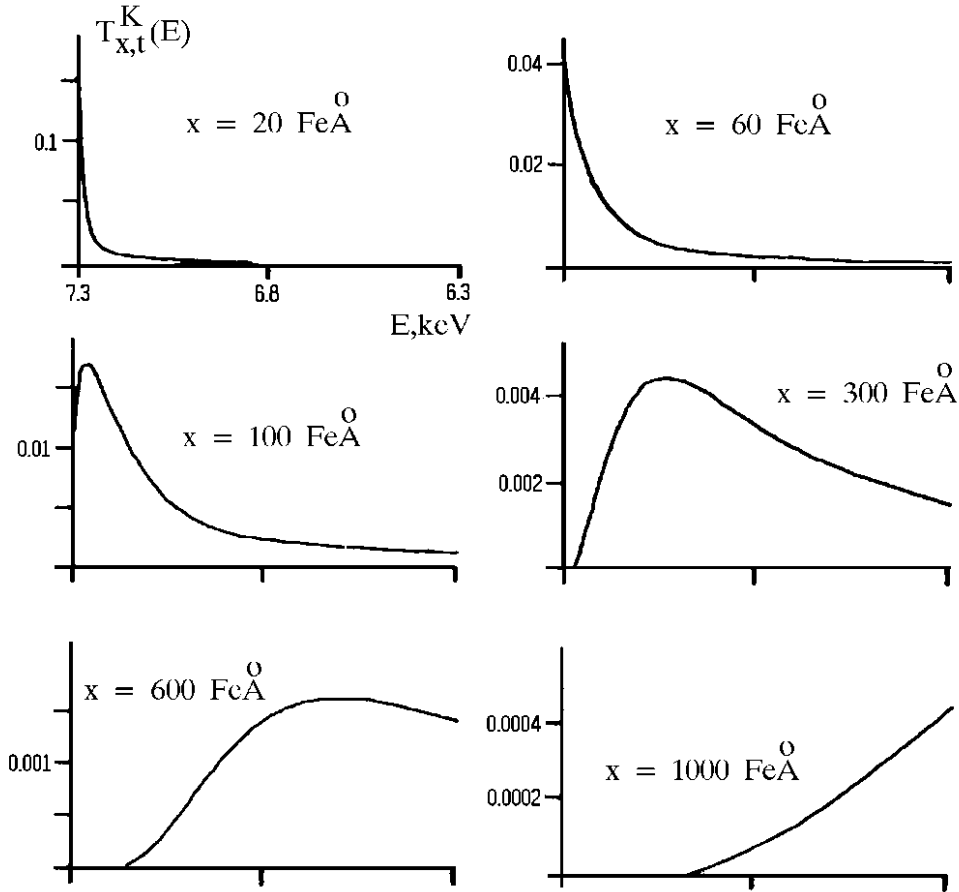
Fig. 3.15 Weight functions $T_{x,t}^{K}(E)$. K-conversion electrons detected at all angles (from [3.15]).

In order to develop a general theory of CEMS the weight functions for electrons with the initial energy E_0 can be written:

$$T(E_0, x) = \ell \left(\frac{x}{r_B} \right) ,$$

where f is a continuous positive function which decreases sufficiently rapidly as a x grows. It turns out that the function f may be represented by the finite series [3.39]

$$T(E_0, x) = \sum_i f_i \exp \left\{ -q_i \frac{x}{r_B(E_0)} \right\} , \qquad (q_i > 0) \qquad (3.38)$$

This is a general procedure which allows the analytical solution of integral appearing in the theory. It transpires that the application of equation (3.38) to a scatterer of α-Fe gives the following f_i and q_i values

$$
\begin{aligned}
f_1 &= 0.203851 , & q_1 &= 31.4112 , \\
f_2 &= 147.585 , & q_2 &= 5.34677 , \\
f_3 &= -42.1327 , & q_3 &= 6.02607 , & (3.39) \\
f_4 &= -106.307 , & q_4 &= 5.08245 , \\
f_5 &= 1.41436 , & q_5 &= 3.12760 .
\end{aligned}
$$

The calculations by equation (3.38) using the values of (3.39) for a scatterer of α-Fe give the same results (within the accuracy of the calculations) as direct calculations by the Monte Carlo method [3.38].

For an N-layer sample the probability of an electron of energy E_0 at depth x in the N-th layer escaping the surface is given by expression [3.39]:

$$\left\{ T(E_0, x) \right\}_N = \sum_i f_i \exp \left\{ -q_i \left[\sum_{\ell=1}^{N-1} \eta^\ell(E_0) d_\ell + \eta^N(E_0) x \right] \right\} , \quad (3.40)$$

where

$$\eta^l(E_0) \equiv \rho_l / (\rho_{Fe} \, r_B(E_0)) .$$

The calculations of line shapes and parameters of Mössbauer spectra are also given in [3.39]. The background and pairing effects are considered together with the influence of the latter upon the intensity and line shape of the spectra. Alternative approaches are possible for approximating the weight functions. It has been shown that, at least for iron, the most accurate approximations of the weight functions by a power series is attained using (2.34) with slightly changed numerical coefficients. The calculations of the weight functions for multilayer samples are also given in [3.40].

Before analyzing contributions of electrons from other groups attention should be given to the following situations. All evaluations and calculations thus far have assumed that the scattering surface was flat. The surface of real samples is always rough. Surface roughness is expected to influence the dependences described above. A rigorous analysis of the effect of surface roughness on electron scattering and energy loss is very difficult. However, for a specified surface shape it is possible to perform the calculations by a Monte Carlo simulation of the electron trajectories. Such calculations have been made for scattering of the K-conversion electrons of ^{57}Fe in α-Fe by LILJEQUIST and ISMAIL [3.18, 33].

The solid is regarded as an electron-scattering continuum separated from a vacuum by a boundary which has a shape of a rough surface. The electron trajectories depend on the electron location relative to the surface. A surface model is presented in Fig. 3.16. The surface shape is described by the function
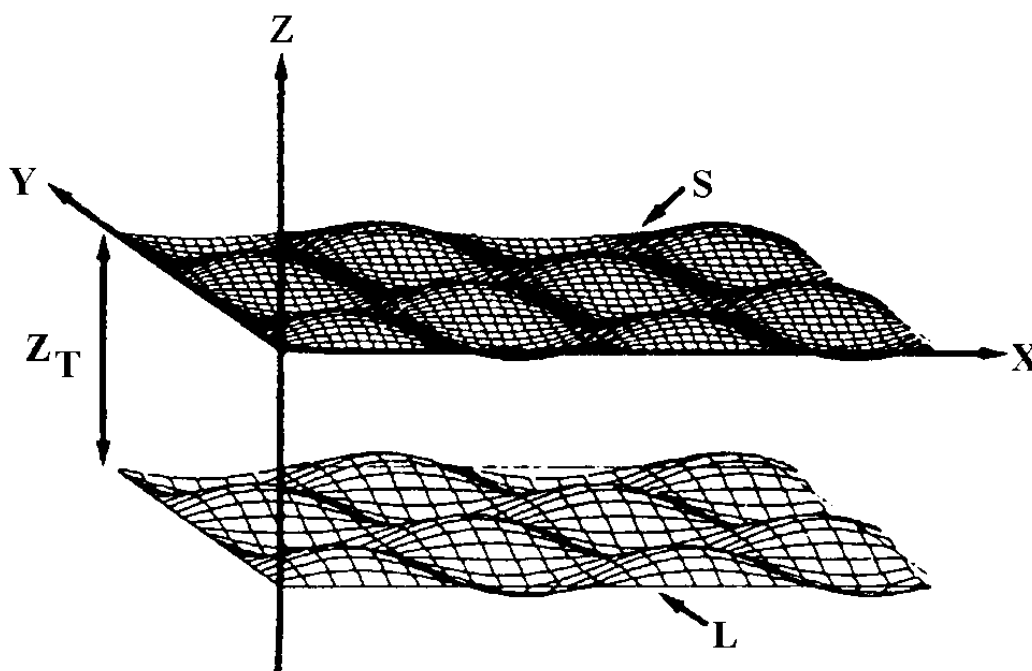
Fig. 3.16 Surface model. S - surface, L - topographic layer ($dz_T = 0$) at topographic depth z_T (from [3.18]).

$$z_{surf} = A \sin(2\pi x/W) \sin(2\pi y/W),\qquad(3.41)$$

i.e. the surface is wavy and is characterized by the amplitude A and the wavelength W. Trajectories of the 7.3 keV electrons, whose effective range in iron is about $2 \cdot 10^3$ Å, may be affected by surface roughness which is equivalent, within the context of this model, to A values from 5 to 10^3 Å and to W values from 10^2 to 10^4 Å.

Surface roughness effects are expected to be larger for higher values of amplitude A and larger A/W ratios. If the effect of surface roughness is small for a given surface roughness (A, W), than it is expected to be small for a (A', W') surface where A' < A and W' < W.

Instead of the weight function T(E,x,cosθ), a topographic weight function T(E, z_T, cosθ) may be introduced for the surface model. The function gives the probability for an electron starting in a random direction from a topographic layer of thickness dz_T at the topographic depth z_T, to escape into a vacuum in the direction cosθ ± dcosθ with energy E ± dE. The topographic layer is defined as

$$z_{surf}(x,y) - z_T - dz_T/2 < z < z_{surf}(x,y) - z_T + dz_T/2 \ .$$

If the simulated topographic weight functions T(z_T) are compared with the weight functions T(x) (Fig. 3.12), the main difference is in a certain decrease of the total transmission from surface layers and in a slight increase of the total transmission from deeper layers. Thus, surface roughness does not seriously affect the shape of the T(x) weight function if A < 10^3 Å and A/W ≤ 0.1.

The effect of surface roughness on the angular distributions of electrons, presented in Fig. 3.14, is very small with a deviation from the nearly isotropic distribution being only observed for electrons emitted from very near surface (x = 0). For a sample of thickness d ≥ r_{eff} no difference in the angular distributions is observed for a plane and a rough surface. The energy loss dependence on the surface shape may be also neglected in CEMS, hence all the evaluations made in CEMS assuming the surface to be plane may be applied to real surfaces.

Let us consider now the Auger electron contribution. Assuming that all these electrons have an initial energy of 5.6 keV, their range in iron r_B^A is about 2100 Å. The values of $T_{t,t}^A(x)$ and $U_{t,t}^A(x)$ may be easily obtained from (3.34) and (3.36), if a scale factor $r_B^A / r_B^K \approx 0.66$ is introduced. Thus, for the Auger electrons in iron

$$r_{eff}^A \approx 1300 \ \text{Å} \ ; \qquad U_{t,t}^A(\infty) = C_A \ 313 \ \text{Å}.$$

As a good approximation, L- and M-conversion electrons may be taken as one group; $r_B^L =$ 9100 Å.

$$r_{eff}^{L} \approx 5700 \text{ Å} ; \qquad U_{t,t}^{L}(\infty) = C_{L} \ 1356 \text{ Å}.$$

These electrons contribute to the K-conversion electron beam since their initial energy is higher.

Assume that only electrons with the energy in APK interval are detected. The weight function $T_{APK,t}^{K}(x)$ is given in Fig. 3.17 a. On comparison with Fig.3.12 it is seen that the depth of the layer analyzed with K conversion electrons is substantially diminished L+M conversion electrons, being detected in the APK interval, convey information on depths of iron down to 5000 Å (Fig. 3.17b). However, their contribution into the total signal is small (note the scales on the ordinate in Fig. 3.17a and b).
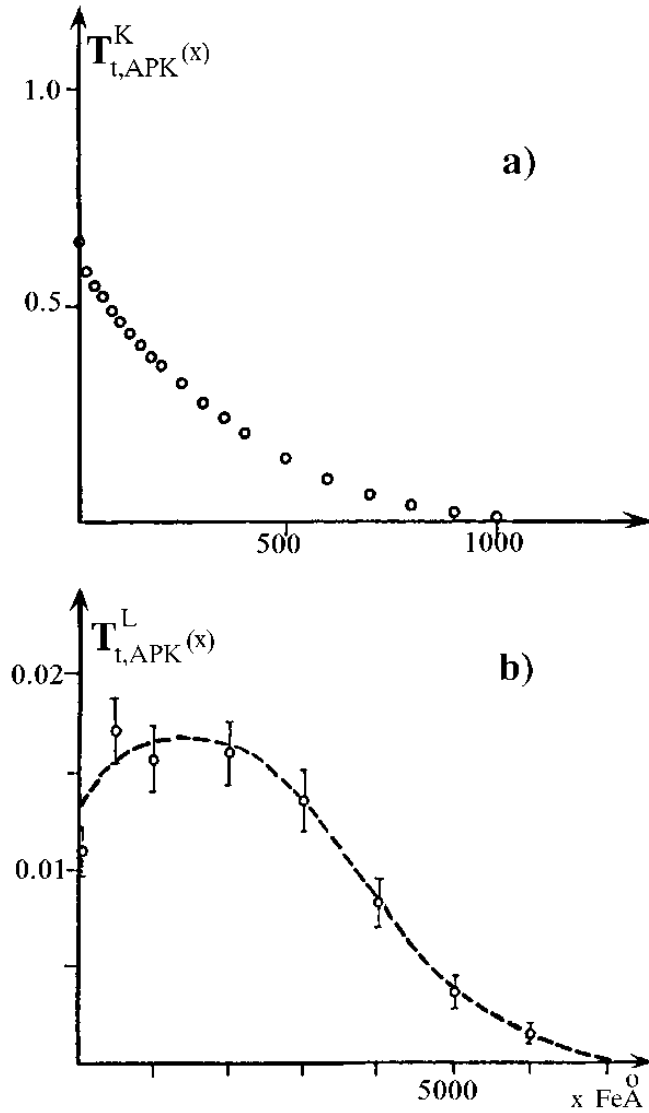
Fig.3. 17 Transmission at all angles of K- and L-conversion electrons into the APK interval (from [3.15]).

To evaluate the contribution of electrons generated by the resonant scattering processes in a layer of depth r_{eff}^{i}, the $U^{e}(x)$ function may be evaluated, using (3.31) and (3.36)

$$U^e(x) = \varepsilon \int\limits_0^x \left\{ C_K \, T_{t,t}^K(x') + C_A \, T_{t,t}^A(x') \left[1 - \varepsilon \, T_{t,t}^K(x') \right] \right.$$

$$\left. + C_L \, T_{t,t}^L(x') \right\} dx' \; . \tag{3.42}$$

The number of pairs of electrons (K-conversion and Auger electrons) simultaneously escaping the surface of a bulk sample for $\varepsilon = 1$ can be evaluated

$$C_A \int\limits_0^{r_{eff}^A} T_{t,t}^A(x) \, T_{t,t}^K(x) \, dx = 151 \, C_A \, \text{Fe\AA} \; . \tag{3.43}$$

Hence, for an iron scatterer we have

$$U^e(\infty) \approx (0.8 \cdot 477 + 0.53 \cdot 313 - 0.53 \cdot 151 + 0.1 \cdot 1356) \, \text{Fe\AA} = 603 \, \text{Fe\AA}. \tag{3.44}$$

The γ-quanta scattered at a depth of more than r_{eff}^i may also generate detectable electrons. Indeed, γ-quanta resonantly scattered in a layer whose thickness is μ^{-1} or μ_r^{-1} will produce a γ-quantum ($C_\gamma = 0.1$) and an X-ray ($C_x = 0.27$). 50 % of the γ-quanta produced will be backscattered. Due to the photoelectric absorption of the quanta in a layer r_{eff}^i photoelectrons and Auger-electrons are generated. The $T_{t,t}{}^A(x)$ weight function corresponds to the γ-ray-produced ones. Each of the weight functions has its own weight factor C_i. Furthermore, a part of γ-quanta, fC_γ, may be resonantly absorbed and also contribute to the beam of electrons. These electrons are taken into account by the $T^e(x)$ function with a different C_i coefficient. The sum of these three functions gives the $\hat{T}(x)$ function which is the second contribution into $T_{t,t}{}^{tot}(x)$.

Calculations within the approach of [3.34, 38] make it possible to evaluate the contribution of different layers to the Mössbauer spectrum recorded from a bulk sample. Let all the electrons leaving the surface of a bulk scatterer of non- enriched iron be detected and consider only the electrons produced by the resonant scattering of γ-quanta. According to evaluations of LILJEQUIST [3.38], 93,3 % of the Mössbauer

spectrum from a scatterer of α-Fe will result from electrons generated after the resonant scattering process in a layer with a thickness $r_{eff}^L \approx 5700$ Å. As already noted, $S(v,x)$ within this layer is constant. However, since most of the electrons produced by scattering are K-conversion and Auger electrons, which are rapidly absorbed, the surface layer down to $r_{eff}^A = 1300$ Å will produce ≈ 75.5 % of the total beam of electrons. The next layer 700 Å to $r_{eff}^A = 2000$ Å will produce about 7 % more. Not more than 11 % of the total beam (or this percentage of the Mössbauer spectrum area) corresponds to the remaining 3700 Å thick layer. The results of Monte Carlo computation are in a good agreement with evaluations based on an exponential attenuation of the beam of electrons (see Fig. 3.9).

It follows, that resonant scattering of γ-quanta in the bulk of a sample, and the subsequent production of γ- or X- rays may make a contribution of less than 7 % to the total spectrum area. In other words, if a sample is covered with a film of iron 5700 Å thick which contains no Mössbauer isotope, then the detection of electrons leaving the sample surface gives a Mössbauer spectrum originating from the bulk of the sample under the coating.

Direct calculations of the functions $T^e(x)$, $\hat{T}(x)$, $U^e(x)$, $U^{tot}(x)$ have been made by LILJEQUIST et al. [3.15, 38] and simple approximate expressions were obtained for the $T^e(x)$ and $U^e(x)$ functions (see, for example, (3.34) and (3.36)). The functions depend only on the r_B parameter and this is easily calculated for any substance [3.15]. Programs for calculating the above functions for a duplex sample are given in [3.38].

A simple example gives an idea of the approach. Let the scatterer be a uniform bulk sample (phase B), covered with a layer of another phase (phase S) whose thickness is $d < r_{eff}^i$. The Mössbauer spectrum from this sample is described by the expression

$$I(v) = \int_0^\infty T^e(x) \, S(v,x) \, dx + \int_0^\infty \hat{T}(x) \, S(v,x) \, dx \ . \qquad (3.45)$$

The area under the Mössbauer spectrum from each phase is obtained by integrating (3.45) over v:

$$A_S = \int_0^\infty I(v) \, dv = C_S \, n_{eff}^S \int_0^d T^e(x) \, dx = C_S \, n_{eff}^S \, U^e(d) \ , \qquad (3.46)$$

$$A_B = C_B \, n_{eff}^B \, [\, U^e(\infty) - U^e(d)] + \int_d^\infty \hat{T}(x) \, s^B(x) \, dx \, , \qquad (3.47)$$

where C_i is a certain constant proportional to μ_r, n_{eff}^i is the effective density of Mössbauer atoms in a given phase equal to the product of the atom concentration and f' factor ($n_a f'$); i = S,B. The function $U^e(\infty)$ can be calculated. The second term of (3.47) is more difficult to calculate, but a program is given in [3.38]. Thus, one required parameter - the surface layer thickness d can be obtained from the two equations (3.46) and (3.47). By a similar algorithm the layer thickness of multilayer films can be evaluated if the layer structure is known.

As has been noted in Sect. 2.8 it is convenient in backscattering ^{57}Fe Mössbauer spectroscopy to calibrate (see Figs. 2.40 and 2.39) using bulk scatterers (substrates) of stainless steel covered with layers of iron of a varying thickness. Scatterers of this type are widely used in CEMS. The use of these scatterers enables the calibration to be performed and the results may be compared to other data in the literature. It is also enables different theoretical models describing the spectral shape (or parameters of the spectra) from mono- and multilayer samples as a function of thickness of separate layers to be tested.

A frequently used procedure involves the calculation of the dependence of the relative area under the spectrum from a stainless steel scatterer covered with iron on the layer thickness d (the $\eta(d)$ function). The $\eta(d)$ values may be taken from theliterature e.g. [2.69, 81]. Experimental data are given together with the results of Monte Carlo computations [3.34] in Fig. 3.18. It is seen that the detector efficiency $\in$ has negligible effect on $\eta(d)$. Moreover, writing the weight function in the form (3.34) allows the same dependence $\eta(d)$ to be obtained.

3.4. Depth Selective Conversion Electron Mössbauer Spectroscopy

BONCHEV et al. [3.26] have shown that the high energy resolution of β-spectrometers allows the depth of origin of emitted electrons to be determined. The authors have made use of expression (3.2) to calculate the energy loss of electrons in a solid and then calculate the escape depth x_1 for electrons with an energy E_1 on the surface

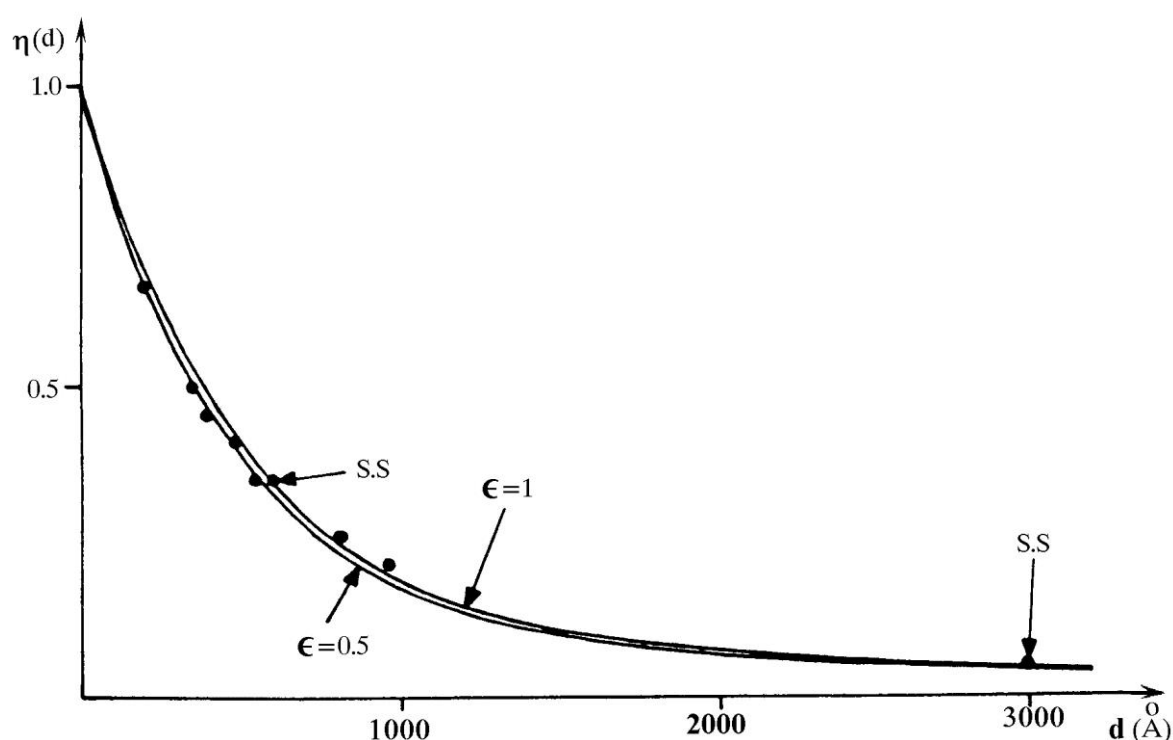$$x_1 = \int_{E_0}^{E_1} dE \, / \, \frac{dE}{ds} \, . \qquad (3.48)$$

Fig.3.18 Relative area under the CEM spectrum from a stainless steel substrate as a function of the thickness of an iron layer (from [3.34]). Solid curves are calculated by Monte Carlo simulations. Dots marked SS are the experimental results of SPIJKERMAN [2.72].

The detection of electrons with energy E by a β-spectrometer gave the Mössbauer spectrum corresponding to the phase at a depth x_1 in the scatterer. The quantitative advantages and disadvantages of the technique have also been evaluated.

The use of the technique has been demonstrated by a study of the interaction of bromine vapours with a β-Sn plate (Fig.3.19). Curve 1 was obtained from electrons having lost most of their energy, and corresponds to the Mössbauer spectrum of a bulk β-Sn sample. At a β-spectrometer setting E_L (curve 3) the authors, in addition to the main surface phase $SnBr_2$, detected two more phases on the surface: $SnBr_4$ and SnO_2. The technique has also been used for studies of thin surface layers obtained by diffusion of tin into copper.

A few years later DCEMS was developed in several laboratories. In Sweden by BOEVERSTAM et al. [3.41-43], in Japan by TORIYAMA et al. [3.44], in the USSR by GRUZIN et al. [3.45] and in France by SCHUNK et al. [3.46]. A schematic picture of a DCEM spectrometer is given [3.46] in Fig. 3.20. It is based on the magnetic β-spectrometer, which is a typical (though not optimal) instrument for uses in Mössbauer spectroscopy and similar to the spectrometers used in [3.26,44,45]. In these devices both the energy resolution (R = 5 %) and transmission (T = 6 %) are rather modest. Spectrometers of this type have been used in β-spectrometry and were designed for operation with point β-sources. Despite the disadvantages, the spectrometers

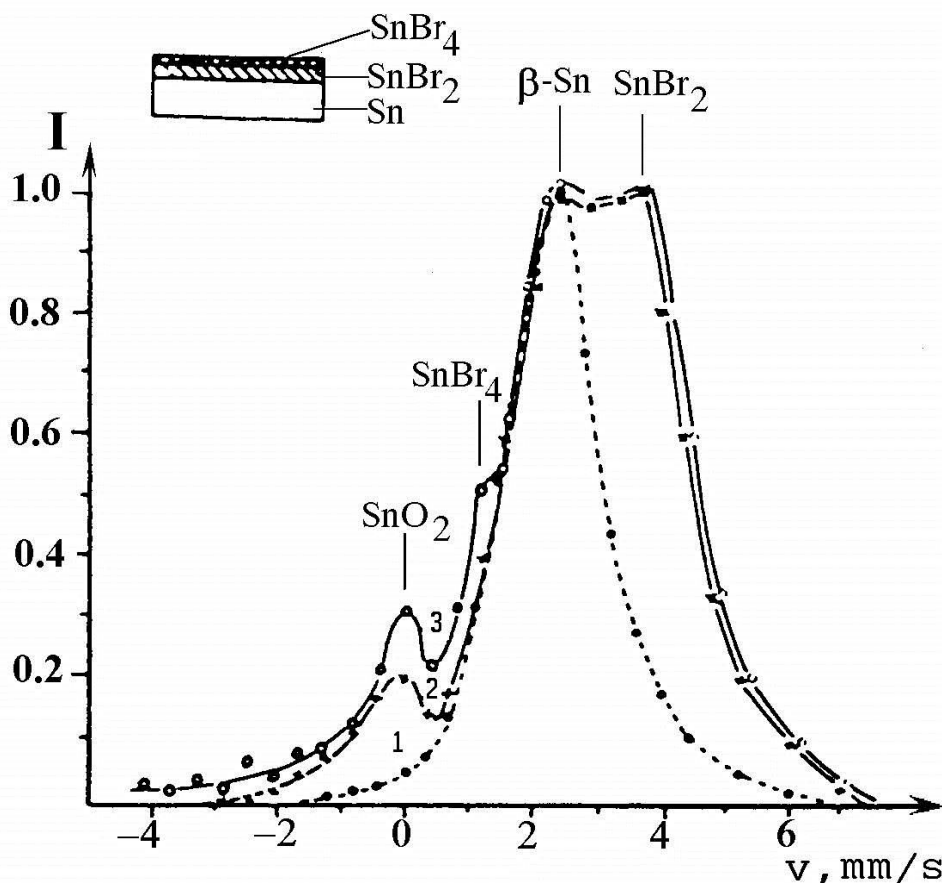Fig.3.19 DCEMS spectra of the surface of a β-Sn plate exposed to bromine vapours (from [3.26]) The β-spectrometer (R _ 5 %) was tuned to detect electrons with the following energies: 1 - 13.9 keV; 2 - 17.5 keV; 3- 19.1 keV. A model of the near surface layer is shown in the insert.

are commonly used in Mössbauer spectroscopy since a DCEMS apparatus can easily be based on the β-spectrometer.

DCEMS development and its use in applied fields has been much slower than that of CEMS. This is mainly due to the absence of a DCEMS theory, the complexity of the technique and the low intensities of electron beams, i.e. the problem of statistical accuracy. In CEMS the Mössbauer spectrum shape is given by (3.42) and is derived on the assumption that the detector efficiency $\in(E, cos\theta)$ is independent of both the electron energy and its trajectory in the active volume of the counter, and is equal to unity. In other words, there is no energy resolution. In contrast, the $\in(E,cos\theta)$ function is widely used in DCEMS.

In DCEMS the S'(V,E) function is often used instead of the $\in(E,cos\theta)$ function and is called the spectrometer profile. V = cE is a variable parameter value (current or voltage) of the spectrometer setting, at which it is tuned to detect an electron beam of energy E; c is a constant for the spectrometer. The S'(V,E) function is the probability of detecting by the
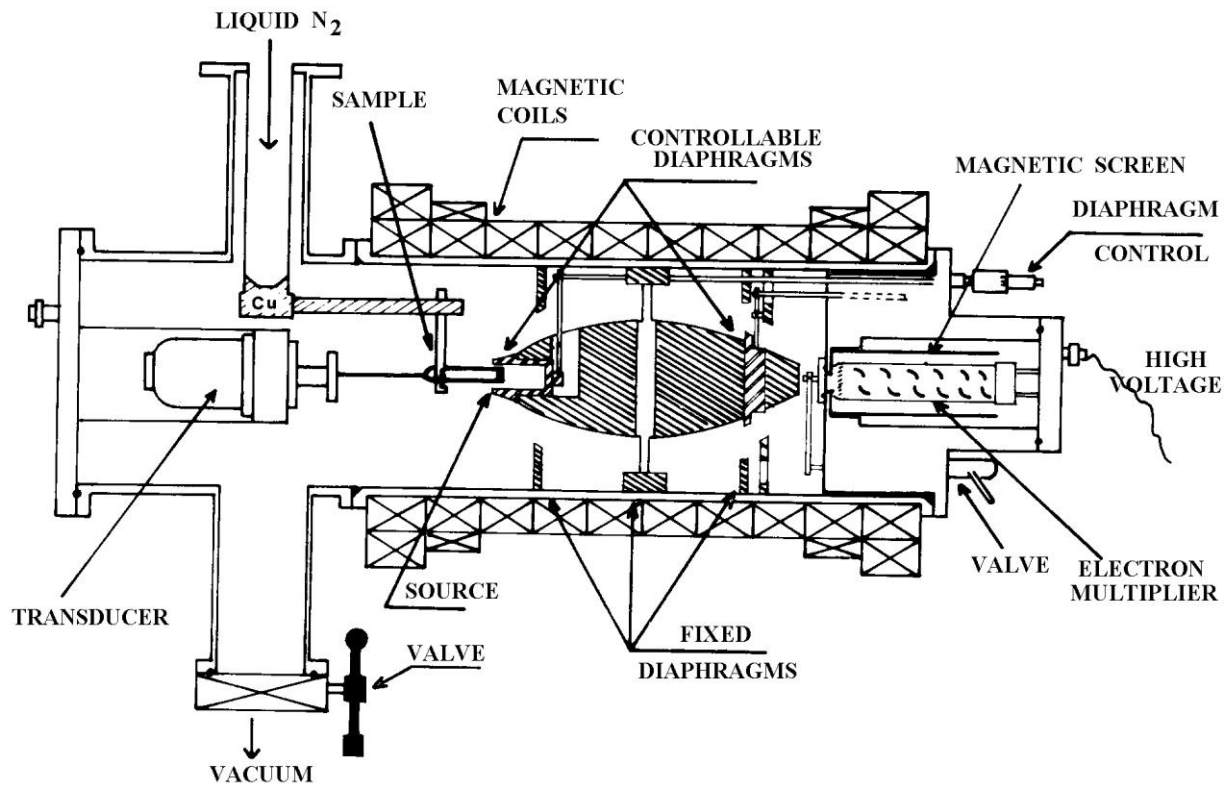
Fig.3.20 DCEMS spectrometer based on the magnetic β-spectrometer; θ _ 60°, R~5 % (from [3.46]).

spectrometer at a setting V electrons with an energy E emerging from the sample surface. By this definition of the S'(V,E) function two parameters are included that are usually unchanged during the spectrometer operation: θ, the average angle at which electrons enter the input slit of the spectrometer; and dω the solid angle. Usually the shape of the spectrometer profile is approximately Gaussian or triangular, but sometimes is more irregular.

   In DCEMS the S'(V,E) function should be included in the definition of the weight function. The weight function T_V(x) at a spectrometer setting V is introduced by means of (3.21)

$$T_V(x) = 3 \quad 4S^{'}(V,E) \ T(E,x,cosθ) \ dE \ dcosθ \ . \qquad (3.49)$$

The Mössbauer spectrum at a setting V may be written as:

$$I_V(v) = c \int T_V(x) \, S(v,x) \, dx \; . \qquad\qquad (3.50)$$

where c is a constant.

An important methodology problem in DCEMS is the statistical accuracy required (measuring time). Examples will be   given for ^{57}Fe and the statistical problems compared to those encountered in CEMS. The contribution to the electron spectrum of only one group of electrons led to the idea of DCEMS. For ^{57}Fe it is the APK interval where the contribution to the intensity is due only to the K-conversion electrons. The latter results in an electron beam attenuation by a factor of 2 ($C_1 \approx$ 0.5) in DCEMS. Detecting a part of the beam at an energy resolution R = 1.5 - 3 % causes a further attenuation ($C_2 \approx$ 0.05) of the beam. Of all electrons with a given energy the β- spectrometer detects the ones within a certain angle dω, hence the third factor $C_3 \approx$ 0.1 appears. The thickness of the analyzed layer in DCEMS is significantly less than in CEMS, and is determined by the weight function shape; that is where the fourth factor originates ($C_4 \approx$ 0.3). Thus, the intensity of the electron beam detected in DCEM experiments should change by a factor of C_5 as compared with the intensity in CEMS:

$$C_5 = C_1 \, C_2 \, C_3 \, C_4 \approx 10^{-3} \; .$$

To compensate for the intensity loss, Mössbauer spectra corresponding to electrons of various energies may be recorded simultaneously. The idea has been realized in [3.47] where a   special β-spectrometer was designed for DCEMS (Fig.3.21). The focusing magnetic field produced by a direct current through an array of 36 copper wires was placed equidistantly around the symmetry axis. The wires are bent near the source so as to form the lateral surface of a conical frustum. The best focusing was achieved at a bending angle of near 50°. At this angle electrons emitted between 30° - 60° are focused into a narrow ring with a circumference containing scintillator detectors. A current of   40 A is supplied. This allows the K-conversion electrons to be focused into a ring with the internal radius of about 18 cm and 0.5 cm wide, R = 3 %. The use of several ring scintillators and collimators allows several Mössbauer spectra to be simultaneously recorded.

A DCEMS spectrometer based on the retarding field analyzer [3.48] possesses a high luminosity allowing samples which are non-enriched in the resonance isotope to be examined. The β-spectrometer has a transmission of 10 % of 2 and allows the detection of electrons with an energy up to 25 keV at an energy resolution from 0.1 % to 6 %. For a typical DCEM spectrum the energy resolution is 6 %. The temperature of the sample may be varied in the range of 25 to 1000 K, and its orientation relative to the spectrometer axis may be changed from 6° to 30°.
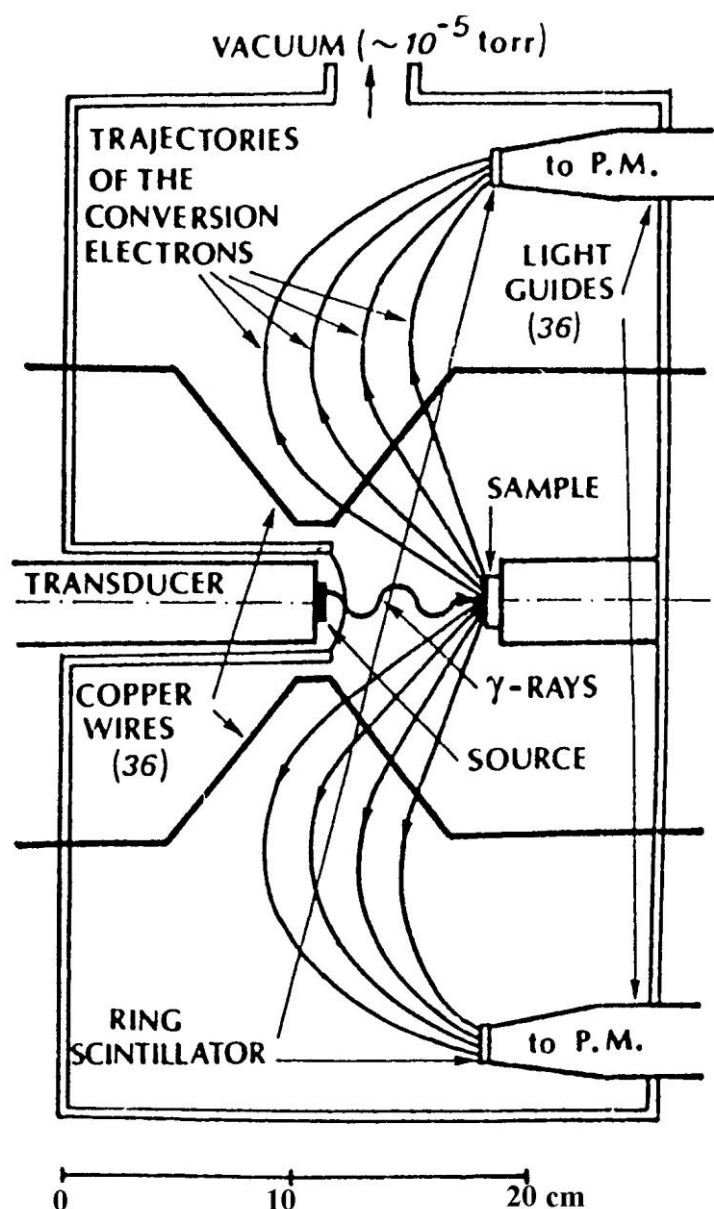
Fig.3.21 Schematic picture of a DCEM spectrometer; $\theta = 45°$, R = 3% (from [3.47]).

For the electronic spectrometers, especially those where grids are used, the geometric transmission (luminosity) which is determined by the slit width and by the size of the source of electrons is quite different from the real transmission determining the measuring time for a spectrum. The real transmission depends on the grid on the slit, on the electric field distribution in the vicinity of the grids, as well as other factors.

One factor, not included in the above consideration is of principal importance and requires attention. The beam of electrons is also determined by the area of the scatterer S (the area of the electron source in a β-spectrometer). The spectrometers described above were developed for β-spectroscopy and designed to operate with small area sources, often of a specific shape. The low intensity of the source of electrons (scatterer) means in DCEMS experiments that spectrometers should be used which allow the examination of a comparable sample area to that used in CEMS. The problem is a compromise between the energy resolution of the spectrometer and the transmission since enhanced energy resolution usually causes the transmission to fall.

The problem of an optimum relation between R and transmission has been treated by the Stockholm group [3.49,50] where it was shown that at low resolution the poor depth selectivity could not be compensated by improved intensity. A resolution better than 1 % is not reasonable, since the depth selectivity is determined by the width of the weight function and the accuracy of its calculation or determination. In the authors' opinion, the optimum R value is 2 - 3 %.

Analysis of energy resolution, transmission and luminosity of the DCEM spectrometer based on the cylindrical mirror analyzer (having the same resolution as above) as a function of the size and positions of the source and detector and also of the slit width is given elsewhere [3.51]. A parameter of more importance in DCEMS than the transmission is the luminosity L, which is the product of the spectrometer transmission and the area of the source of electrons

$$L \approx (\cos\theta_1 - \cos\theta_2) \, S/2 \, ,$$

where $\cos\theta_1 - \cos\theta_2 = \Delta\cos\theta$ is the angular interval which is dependent on the spectrometer design.

Further discussions of the optimum R value have been given in [3.52,53]. The resolution enhancement from 3 % to 1 % is significant for experiments involving the investigation of surface layers 0 - 5 nm thick. To investigate a thinner layer (0 - 2.5 nm thick), the β-spectrometer should detect separate groups of electrons in the 7.2 - 7.3 keV interval, and it is desirable to have $R \approx 0.5$ % and $\theta \approx 90°$. On detecting electrons with an energy less than 7.2 keV there is no advantage at R = 0.5 % over R = 1 %. The maximum possible selectivity can probably be attained with electrostatic β-spectrometers whose accuracy of energy determination is about 1 eV and the half- width is - 10 eV on the 7.3 keV line [3.54,55].

In addition to magnetic β-spectrometers, electrostatic electron spectrometers are widely used in DCEMS allowing a better R and T values to be obtained than with magnetic spectrometers which detect electrons with energies less than 50 keV, and using large-area sources of electrons. These spectrometers are easier and less expensive to build than magnetic ones with the same parameters. The first electrostatic spectrometers for DCEMS were constructed in Sweden [3.56], USA [3.57,58] and Japan [3.36]. An electrostatic cylindrical mirror analyzer and spherical-grid retarding-field electrostatic spectrometer has also been tested [3.56]. The properties were simulated and the optimum conditions of operation were calculated. After preliminary tests the differential spherical grid spectrometer proved to have a high noise level, and the cylindrical mirror analyzer was built despite a higher luminosity of the spherical grid spectrometer.

A DCEM spectrometer, based on the mirror analyzer is depicted in Fig.3.22. Electrons, starting from inside the inner cylinder at angles close to 45° to the sample

surface (1 cm^2), move out through slits in the inner grounded cylinder 108 mm diameter into a strong field region (the outer cylinder is at -5000 V to -6000 V). The field bends the trajectories of electrons back towards the inner cylinder. The group of electrons of interest with energy E = V/c passes through another   slit to be collected on the spectrometer axis in the spot which depends on second-order focusing conditions. A detector is placed at this position. The slits are covered with stainless- steel grids to provide a uniform electric field. A diaphragm is used in front of the detector because of aberrations which attenuate the electron beam reaching the detector. The spectrometer is connected to a vacuum chamber (below the sample position) where the sample may be heat-treated without exposing   it to the atmosphere. The spectrometer has the following parameters: R ≈ 2.5 %, transmission ≈ 12 % of 4π and luminosity ≈ 5 mm^2. With a source of 100 mCi ^{57}Co(Rh), a scatterer of α-Fe (a = 90 %) and with the source - sample distance of 2 cm, a spectrum with good statistics can be accumulated within a day or even within six hours.

The modernization of DCEM spectrometers based on the mirror analyzer has been carried out [3.59,51]. These spectrometers operate at a vacuum of ≈ 10^{-9} mbar and allow very clean surfaces   to be studied. Furthermore, the luminosity of the spectrometer described in [3.51] is such that non-enriched samples including spin glasses were examined.

The measuring time for such DCEM spectrometers may be shortened if use is made of electrons focused on the spectrometer axis (see Fig.3.22). If a position-sensitive detector is placed on the axis, a series of Mőssbauer spectra corresponding to different electron energies can be recorded simultaneously. The idea has been implemented in experiments on spin densities at ^{57}Fe nuclei in magnetic materials using an electrostatic cylinder mirror analyzer [3.60]. A schematic description of the instrument is given in Fig.3.23. Using three slits enables the simultaneous recording of K-, L- and M-conversion electron   spectra. Although the energy resolution is good the spectrometer has not found applications in DCEMS because of its low luminosity.

A spherical electrostatic spectrometer designed specially for DCEMS has proved an effective tool for detecting electrons [3.58]. A schematic description of the spectrometer is shown in Fig.3.24a and the instrument itself without the outer cover of the vacuum system is reproduced in Fig.3.24b. The electric field between the two spheres is used to focus electrons. The outer sphere consists of a cage of 42 bent aluminium rods of 0.3 cm

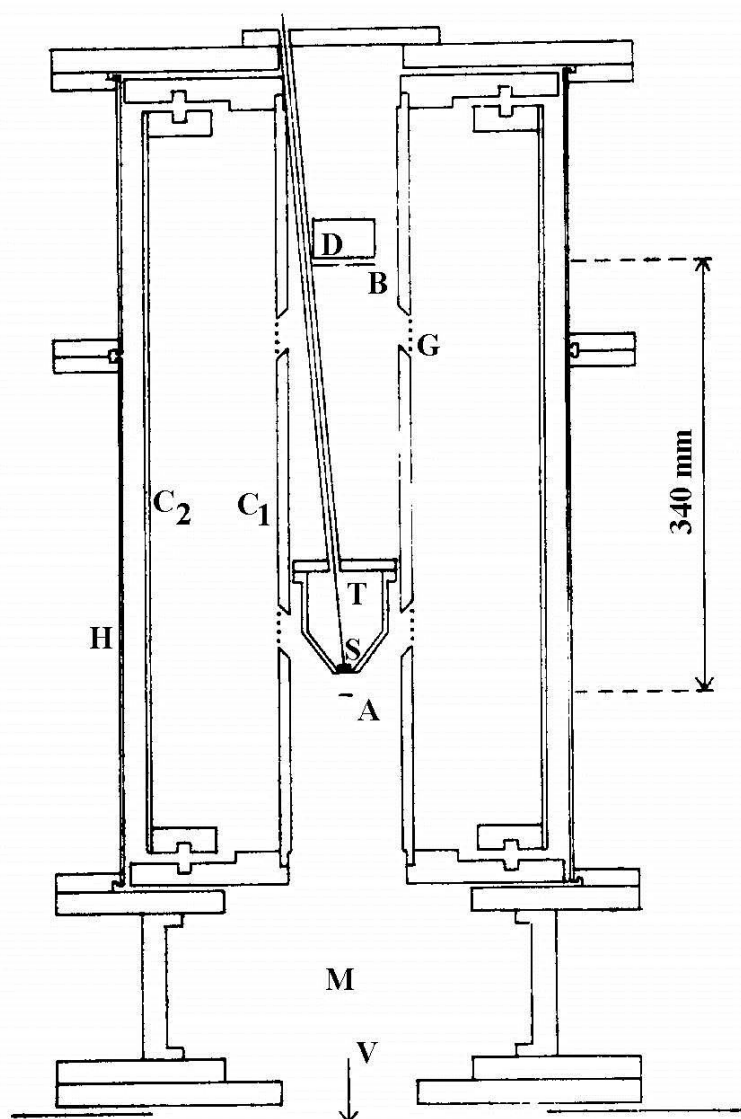Fig.3.22 Schematic picture of a DCEM spectrometer ($\theta = 45°$, R = 2.8 %) designed and built on the base of the electrostatic cylindrical electron mirror analyzer (from [3.56]); C_1 - inner cylinder (radius = 54 mm), C_2 - outer cylinder (radius = 158 mm), G - thin grids (slit width = 34 mm), A - absorber (i.e. electron source), B - detector baffle, D - detector, T - transducer rod, S - Mőssbauer source, H - vacuum tank, M - absorber treatment chamber, V - outlet to vacuum system.

diameter to reduce electron scattering. The electrons are forced
to travel along elliptical paths between the spheres and are returned to the symmetry axis of the spectrometer. The sample (absorber) is on the inner sphere (Fig.3.24a) and is irradiated with Mőssbauer γ-quanta. An adjustable slit is located in the focal plane. A field-free region where a detector of electrons is located is positioned beyond the slit.

The focal plane and the adjustable slit position (i.e. the exit angle χ) are the key elements determining the spectrometer parameters. For the energy resolution and transmission of the spectrometer the following relations are satisfied (for a point source):
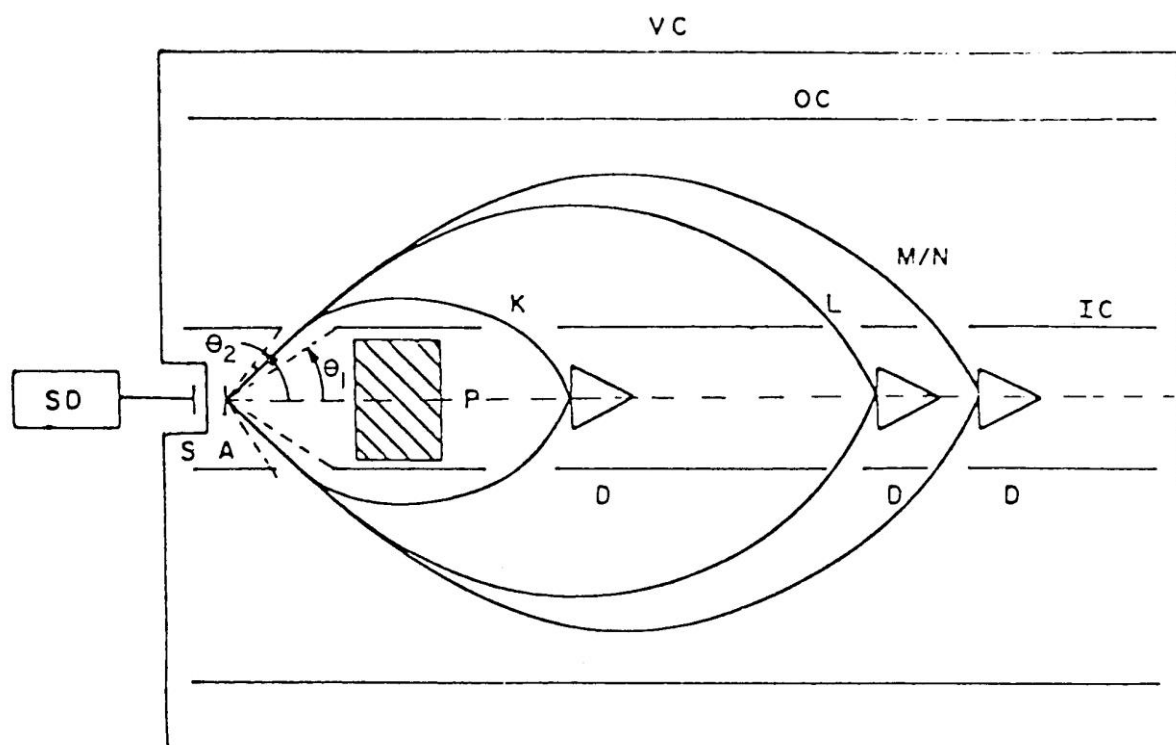
$$T = \chi/4 ; \qquad R = T^2 .$$

Fig.3.23 Schematic diagram of a DCEM spectrometer (from[3.60]) based on the electrostatic cylindrical mirror analyzer. Forwards - scattering geometry is used. S - source, SD - driver, A - sample, θ_1 and θ_2 - minimal and maximal angles for the input slit edge positions, P - lead shielding, D - detectors, IC and OC - inner and outer cylinders, VC -vacuum chamber.

It follows that if the angle χ is reduced, the resolution improves as χ^2 whereas the transmission reduces linearly with χ (R = 2 %, T = 13 %). For most magnetic spectrometers $R \geq 25$ T^2. Hence none of the magnetic spectrometers and only the "orange- type" spectrometer can achieve the same luminosity (at the same energy resolution) as this spectrometer.

The inner aluminium sphere is filled with lead and ground. The negative high voltage is applied to the rods of the outer sphere. A sample under investigation (1 cm diameter) is placed 6 mm above the inner sphere (Fig.3.24c) to reduce electron scattering. The distance between the collimator of Mössbauer radiation and the sample is not less than 1 cm, and the ratio of the high voltage on the collimator to the voltage on the sphere is 0.4. If the collimator is "floating", the count rate is unstable, therefore a suitable high voltage is necessary to compensate for the disturbance in the electric field.

An important feature of the spectrometer is that it detects electrons leaving the surface layer of the absorber at nearly the glancing angle. It improves the surface-selectivity of the spectrometer but not the depth resolution. To achieve a good depth selectivity the spectrometer should detect electrons which leave the sample surface in a small solid angle.
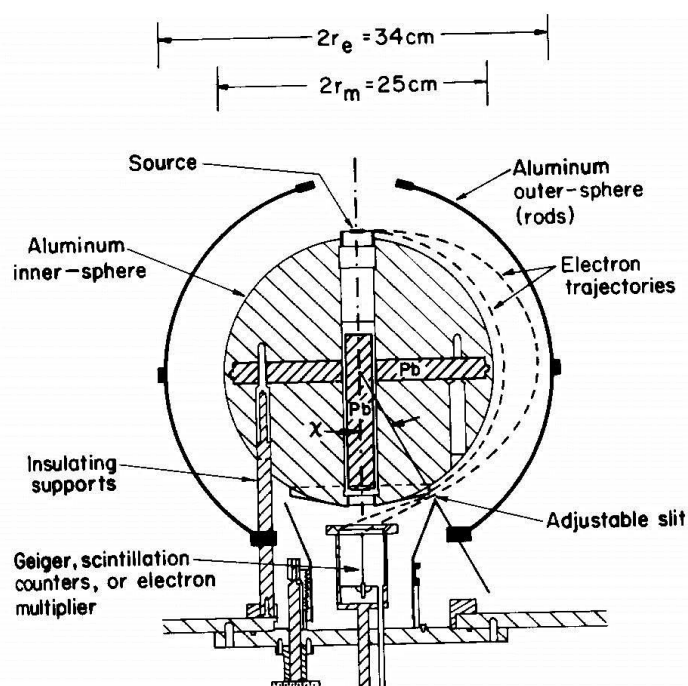
Fig.3.24 a - Schematic diagram of a DCEM spectrometer ($\theta = 7.5^{o}$, R = 2 %) (from [3.58]) based on the spheric electrostatic β-spectrometer.
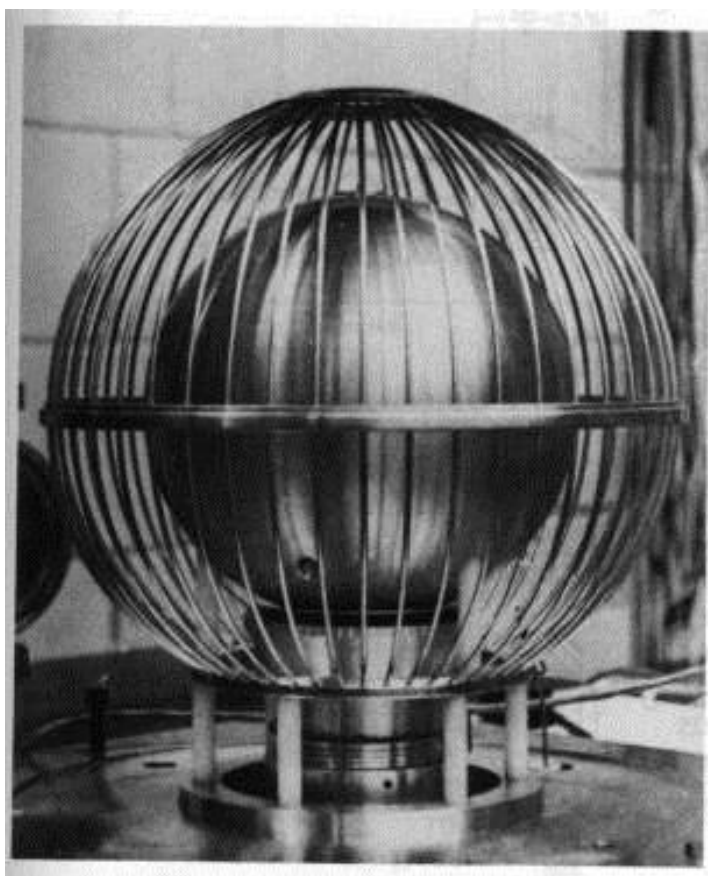

Fig.3.24 b - A photograph of the electrostatic spherical electron analyzer; the outer cover of the vacuum system is removed.
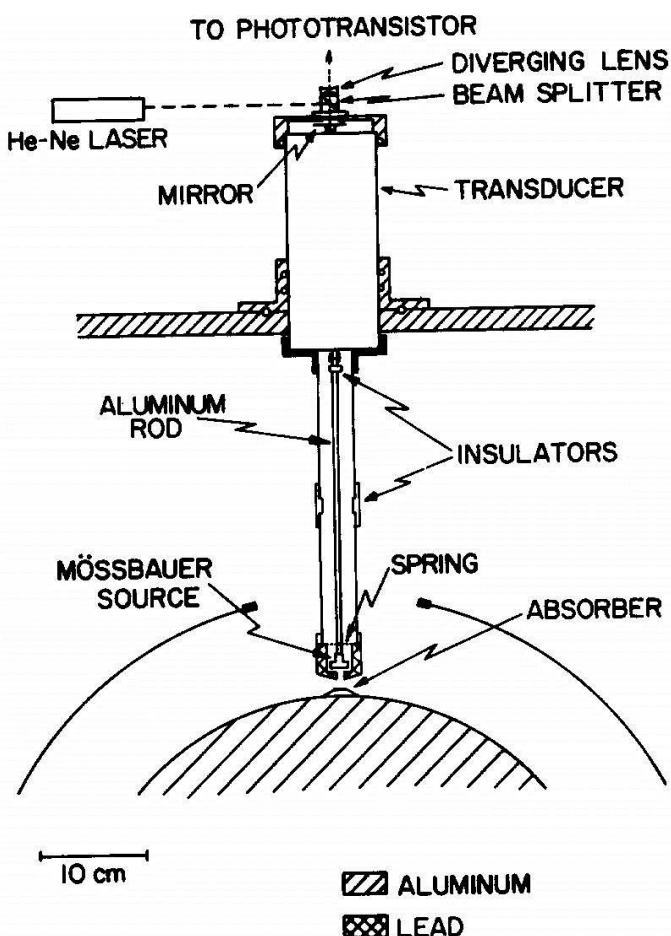
Fig.3.24 c - A schematic diagram of the experimental set up for studies of resonant γ-quanta scattering in the sample placed above the inner sphere of the spectrometer.

A magnetic β-spectrometer of this type is described in [3.44], and an electrostatic one in [3.61]. The latter is an electrostatic electron analyzer (150° spherical sector) as commonly used in photoelectron spectroscopy and appropriately modified for Mőssbauer spectroscopy [3.61]. The solid angle of only 0.27 % of 4π results in a low luminosity. However, the low geometric transmission as compared with the transmission of the spectrometer in Fig.3.24a, is partly compensated by the energy distribution of electrons emitted by the surface which has a maximum in the direction of the surface normal (see Fig.3.5).

An analysis of the known types of magnetic spectrometers shows that this type of instrument has not exhausted its resources. For example, it has been shown [3.62] that a DCEM spectrometer based on the β-spectrometer described in [3.63] allows high-quality α-^{57}Fe Mőssbauer spectra to be recorded in 3 - 4 hours, i.e. comparable with the DCEM spectrometers based on the electrostatic analyzer.

It is known that magnetic β-spectrometers have a focal plane. By placing a position-sensitive microchannel-plate detector in this plane, the simultaneous recording over 3 - 4 hours of a series of DCEM spectra at a fairly high energy resolution has been achieved [3.62]. Even the perfect position- sensitive detectors used with spectrometers based on the electrostatic analyzer are less efficient since these analyzers have a focal surface.

There are many of electrostatic and magnetic electron spectrometers designed and developed for Conversion Electron Mőssbauer Spectroscopy [3.26,36,44-48,51,54-73]. A comparison of performance of these spectrometers was made in [3.63] and is updated in Table 3.3. The energy resolution depends on how monochromatic the electron source is. The best resolution was achieved for electrons emitted from a hot filament set at the source position of the spectrometer. By setting a ^{57}Co source in place of the filament a lower energy resolution is obtained and the result depends on the specific activity and dimension of the source. The same problems arise if a β-spectrum of the absorber (scatterer) under study is recorded.

Table 3.3
Comparison of electron spectrometers for Mőssbauer spectroscopy

Type	Energy resolution at 7 keV, [%]	Accept- ance angle, [degr.]	Detection efficiency (transmis sion[*]),[%]	Sample dimen- sion, Ø mm	S/N ratio for α-^{57}Fe	Refe- ren- ces
cylindrical mirror	2.5	38-48	6[*]	5	9	[3.56]
cylindrical mirror	4		7			[3.64]
cylindrical mirror	0.67	56-60	2[*]	1	3.6	[3.60,65]
cylindrical mirror	3.0		6.4		7.3	[3.51]
second order						
focusing cylindr-						
ical mirror	0.2-0.5	41±3		7		[3.54]
a double cylindrical mirror-ana lyser	0.1			3		[3.55]
retarding field	6	6-30	10	10	[3.48]	
analyser	4		7			[3.66]
cylindrical						
retarding						
grid	1.5		1.0			[3.36]
semi-sphe rical	2	30-90	5.5	4	3	
retarding	1	30-60	2.1	4	1	
grid	0.3	30-60	1.2[*]	3		[3.63]

spherical condenser	2.0	75-90	13[*]	10	8	[3.58]
spheric elec-trostatic	2	75	13	4		[3.67]
spheric electrostatic	2.7	72-86 / 47-63		8	[3.68]	
iron free[**] orange type	1		20			[3.25,69]
mini-orange[**] magnetic filter	8		2			[3.70]
150°spherical sector	2.0	9-11	0.27	10×4	3	[3.61,71]
ellipsoidal mirror retard.						
grid	9	10-90	35	5	1	[3.72]
π|2 air core magnetic	2	_15	1.2[*]	5	10	[3.44]
magnetic sector β-spectro-meter[**]	0.7		0.6	1x15		[3.62]

[**] Simultaneous recording is possible

Acceptance angles are not always given, but for a particular type of the spectrometer the differences in the acceptance angles are not high.

Comparing the detection efficiency given in the Table it should be kept in mind that this value depends on several parameters of the spectrometer. Sometimes the detection efficiencies for various resolutions are obtained using a ^{57}Co β-source and different apertures, acceptance angles or negative voltages applied to grids in retarding-grid electron spectrometers, e.g. [3.36,63]. The detection efficiency of course depends on the efficiency of the detector of electrons used in the β-spectrometer. For example, if the channeltron is changed this may result in a change of the detection efficiency of the spectrometer. The transmission of a spectrometer depends sharply on its acceptance angle. As a rule, the large transmission is connected with a good surface-selectivity but poor depth-selectivity.

Scatterer's (absorber's) dimensions is a very important parameter. An electron emitter of large area (diameter) is desirable for Mőssbauer spectroscopy but both the energy resolution and detection efficiency decrease when the source is moved in radial direction.

The signal to noise ratio is given for an enriched α-Fe foil and depends on the spectrometer design, especially on the background due to scattering in grids and other parts, and on the source intensity. Apart from it, the S/N ratio depends on the scatterer thickness and surface quality.

3.5 β-Spectra and Weight Functions for DCEMS

It is also necessary when considering β-spectrometers to discuss the β-spectra. In Mőssbauer spectroscopy two types of β-spectra should be distinguished: spectra of Mőssbauer sources and spectra from samples under investigation (scatterers). The former are used to calibrate DCEM spectrometers and also for experimental studies on the penetration of electrons in solids. These studies serve to obtain experimental weight functions and to test various models of electron interactions in the energy interval of interest. The β-spectra from samples provide the same information and are used under optimal experimental conditions.

The shape of a β-spectrum depends on the β-spectrometer design, the energy resolution, the specific activity and composition of the substrate, and the type of electron detector. The low specific activity or high absolute activity of the source results in the conversion- and Auger-electron lines smearing out and being displaced in the lower energy direction. Deposition of the activity onto a substrate containing heavy elements may lead to a deformation of the spectra due to strong backscattering.

Geiger-Müller (GM) counters, scintillation detectors, channel electron multiplier detectors(channeltrons), open electron multipliers and microchannel plates are used to detect electrons < 20 keV in β-spectrometers. A serious disadvantage of the channeltron is that the maximum efficiency is at the electron energy of about 500 eV. The efficiency for the 3 - 15 keV electrons is nearly 20 %, but in practice is often only 10 %. Detectors used in the DCEM spectrometer of Fig.3.24 are shown in Fig.3.25. Electrons are produced in the upper conical part of the channeltron (Fig.3.25b) and then multiplied. The channeltron window is covered with a nickel mesh of 90 % transmission at a small negative potential to cut off the secondary electrons. This reduces the background count rate of the spectrometer to about 1 count/s.

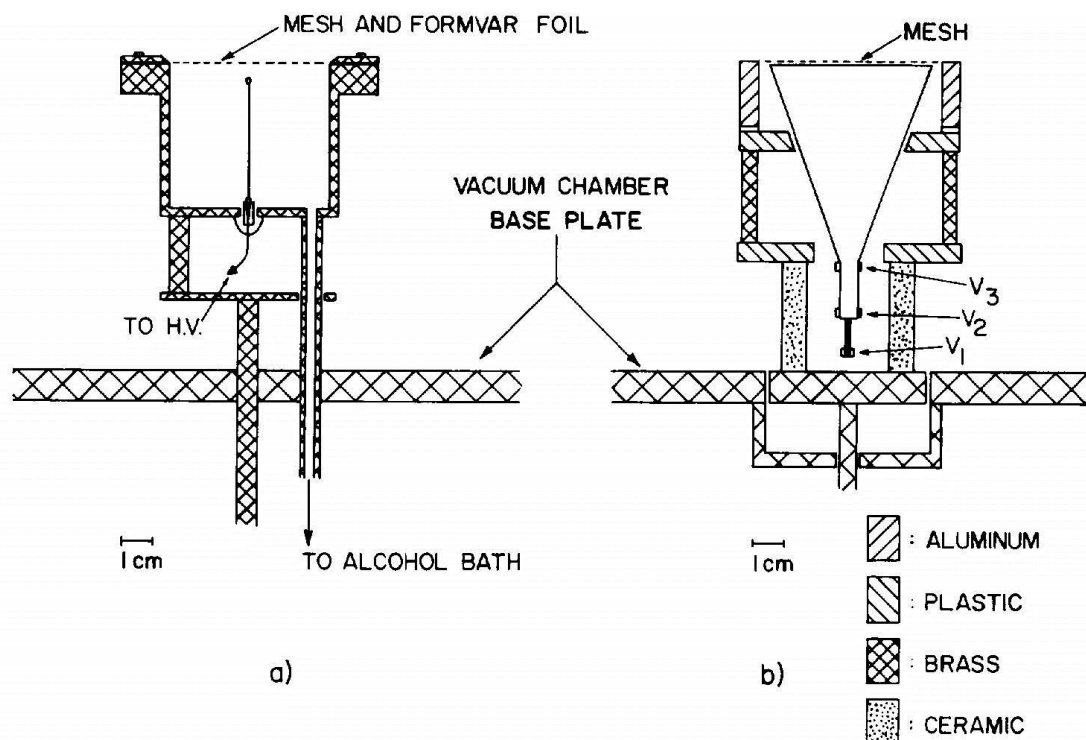Spectra are given of electrons from a source of ^{57}Co,

Fig.3.25 Schematic drawings of detectors used in the spectrometer of Fig 3.24 (from [3.58]); a - GM counter, b - the channeltron.

electrodeposited onto aluminized formvar in Fig.3.26. The efficiency of gas-filled counters for the electrons of interest is nearly energy-independent, unlike the channeltron, if the source of electrons is inside the counter and $\in = 1$ is easy to reach. The low count rate in DCEM spectrometers allows the Geiger region mode to be used. The necessity to keep the filling gas pressure above 1 Torr together with the relatively large diameter of the detector entrance window requires the use of reinforced windows. The end-window GM counter (see Fig.3.25a) operates at a filling gas pressure of 1.5 Torr and has a formvar window 40-50 $\mu g/cm^2$ thick. The 7.3 keV electrons are more efficiently detected than with the channeltron. However, less than 6 keV electrons are absorbed by such a thick formvar film and the Auger-electron lines appear to be suppressed (see Fig.3.26a). Spectra of high-energy conversion electrons obtained with this GM counter are given in Fig.3.26c and d.

Scintillation detectors are used in some DCEM spectrometers with an efficiency for slow electrons of nearly 100 %. These detectors can be made of any shape and size; they are fast, rugged, electrically stable and reliable. However, the low quantum yield for low energy electrons, the necessity to cool photomultipliers and to use light reflectors which also absorb electrons, restricts the use of scintillation detectors in DCEMS. Furthermore, the scintillators are light-sensitive and affected by electromagnetic radiations.
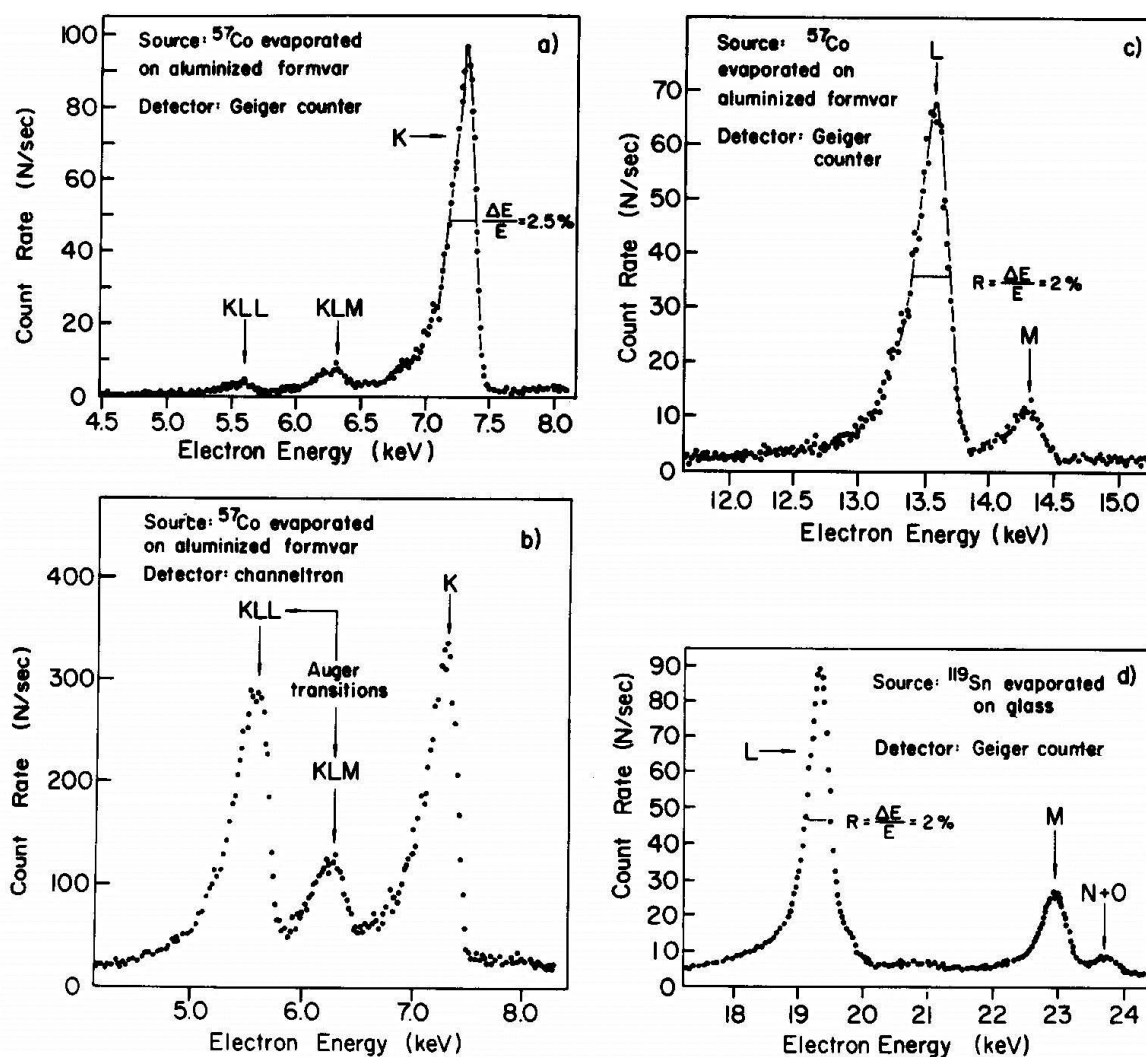
Fig.3.26 Spectra of electrons (from[3.58]) with the energy of: less than 8 keV (a and b), between 12 keV and 15 keV (c), between 17 and 24 keV (d).

To summarize, the experimentalist in DCEMS should try to use a detector with an efficiency close to 100 % and which is energy-independent in the energy region of interest. There should be no window in the path of the electrons. The entrance window, if any, should be less than 10 $\mu g/cm^2$ thick of formvar for ^{57}Fe.

Electrostatic β-spectrometers enable the energy resolution to be enhanced in an unusual way. Indeed, the R and T - parameters depend on the spectrometer design. If at a constant energy resolution R = 3 % a retarding voltage is applied to the source, say 6.3 kV, the 1 keV energy K-conversion electrons are detected. The instrumental line width might be expected to be about 30 eV, and at voltages close to 7.3 kV the line width could be expected to reach zero. In practice, it remains at ca. 70 eV due to scattering in the source material and back reflection. The energy resolution enhancement may prove substantial as has been shown by experiments on spin density studies of 2s- and 3s-electrons in Fe by CEMS [3.60,74].

Complex and time-consuming precision measurements of electron passage through matter should be carried out for correct interpretations of experimental spectra. For these measurements it is desirable to have a β-spectrometer with a good energy resolution and a large luminosity, and a source material wherein there is no absorption or scattering. To minimize backscattering the backing should consist of light elements (e.g. formvar). However, the backing should be conductive and this requires the deposition of aluminium or heavier metals. Layers in which the electron absorption is to be studied should have a thickness x from several tens to several thousand Дngstroms and be uniformly thick.

In these experiments the β-spectra are recorded and are described by the $F(x,E)$ function. From the experimental data $(F(x,E))$ the functions $L(x,E,\theta)$ can be calculated. These describe the energy loss distribution of electrons which are isotropically emitted by the source and have penetrated through a layer x and left the surface at angle θ relative to the surface normal with an energy in the interval $E_{min} < E < E_0$, where $E_0 - E_{min} << E_0$. Usually the values of E are in the APK interval. Radionuclides are normally used as a source of electrons in these experiments. The specific activity of ^{57}Co is _ 5 mCi/µg. Hence, for a source area of 1 cm and an activity of 1 mCi, the equivalent ^{57}Co thickness will be ≈ 2.5 Å.

If the monolayer thickness $d_s \to 0$, the experimental β-spectrum of the source will be described by the function $F(0,E)$. The problem is to evaluate the weight functions and parameters of the electron interaction with matter from the experimentally obtained $F(x,E)$ and $F(0,E)$ functions.

This can be approached by considering a simplified hypothetical case. Suppose that we have a monolayer source isotropically emitting electrons with a spectrum described by the $F(0,E)$ function. The following relation may be written:

$$F(x,E,\theta) = \int_{E_{min}}^{E_0} F(0, E')L(x, E-E', \theta) \, dE' = F(0,E) * L(x,E,\theta) \ .$$

The operation * means convolution. Any real spectrometer detects electrons emerging within a certain angular interval $\theta_{min} < \theta < \theta_{max}$. Hence, the electron energy distribution $F(x,E,\theta)$ is deformed depending on the instrumental line profile and the energy resolution of the spectrometer. A simple rearrangement gives

F(x,E) = F(0,E) * L(x,E)

$$F(x,E) = \int_{\theta_{min}}^{\theta_{max}} F(x, E, \theta)\,d\theta, \quad L(x,E) = \int_{\theta_{min}}^{\theta_{max}} L(x, E, \theta)\,d\theta,$$

.

A similar relation is also satisfied for experimental spectra and means that by the Fourier transform the L(x,E) function may be obtained from the experimental spectra.

Such studies have been carried out by BÄVERSTAM et al. [3.42]. ^{57}Co was electrodeposited onto a copper backing. Thin iron films 150 Å| to 2570 Å| thick were evaporated onto the sources. Electrons were detected with a magnetic spectrometer by recording the momentum loss of electrons with a momentum resolution of about 6 %. The F(0,p) and F(x,p) spectra obtained as a function of the evaporated layer thickness and of the electron momenta can be easily transformed into functions F(0,p) and F(x,p) which are energy- and thickness-dependent. The F(O,p) and F(x,p) functions are connected by the above relation and it is possible by the Fourier transform to obtain a function L'(x,p) which is analogous to the L(x,E) function. An analytical expression for the L'(x,p) function has been given in [3.42]. If the electron energy is detected in the APK interval then by interpolation the L'(x,p) function corresponding to a layer which is N times thicker can be obtained. The validity of this approximation depends on the energy resolution of the spectrometer. However, this approximation is physically motivated. It allows the evaluation of L(x,E) and then L(Nx,E) from L'(x,p) and eventually T(x,E). It must be noted that the technique is not generally applicable, if another spectrometer is used then new experiments must be performed.

Spectra obtained by Bдverstam et al. are shown in Fig.3.27. The upper and lower curves correspond to the experimentally observed dependences F(0,p) and F(2570 Å, p), the dashed curves give the interpolated dependences corresponding to layers n135 Å thick. Although the F(0,p) and F(2570 Å, p) dependences are quite different, the interpolation is fairly good and this is confirmed by the experimental data F(650 Å ,p). The weight functions obtained from these dependences, were used for the quantitative interpretation of DCEM spectra.

For a direct determination of the weight functions and the quantitative characterisation of electron interaction with matter it is necessary to considerably enhance the energy resolution of the spectrometer and the quality of the source and the absorbing layers. This has been demonstrated in [3.52]. The radionuclide was purified on a chromatography column and was electrodeposited on a thin nickel foil to give a 30 mCi ^{57}Co source 3 mm diameter.

By a simple evaluation (5 mCi/μg) the layer thickness was found to be 36 Å , although it should be noted that in practice it is extremely difficult to obtain such a layer of a uniform thickness. A spectrum of this source is given in Fig.3.28. The source was then covered by vacuum evaporation with thin uniform iron layers with a thickness measured with an accuracy of ±4 Å. The deposition of the first layer 63 Å thick (curve b in Fig.3.28) results in a complete disappearance of the LXY Auger electron line. This means that it is an entire layer. Four layers more were successively deposited onto the source.
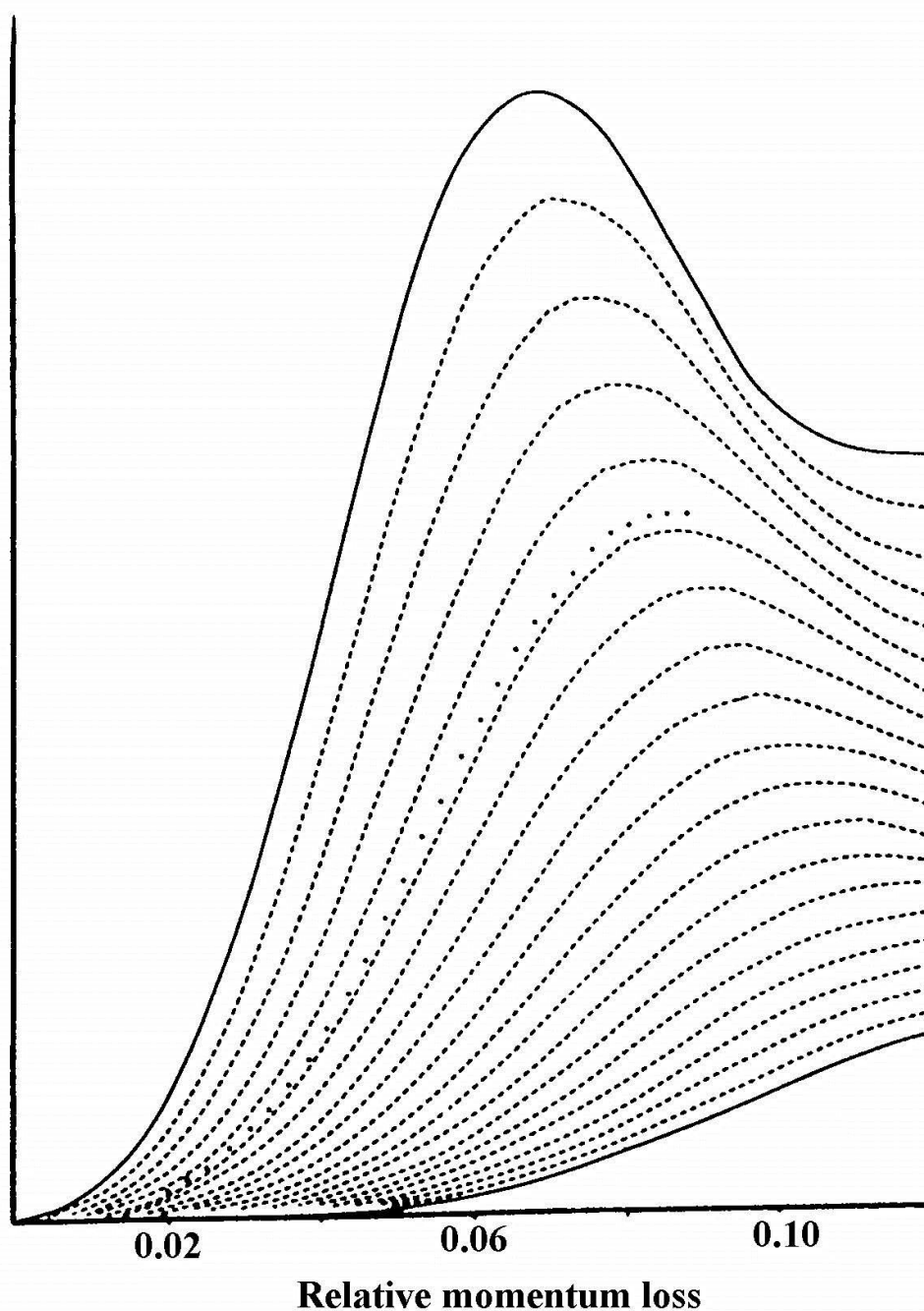
Fig.3.27 Experimental and computed electron spectra (from [3.42]) from a [57]Co source: lower solid line - electrons are scattered by an iron film 2570 Å thick evaporated onto the source, upper solid line - the unscattered electrons. The dashed lines are computed by means of the interpolation technique. The dots are the experimental data (see text). The ordinate is the relative intensity $F(x,p)$.

β-Spectra recorded after each deposition are presented in Fig.3.28. It is seen from the Figure that the deposition of each
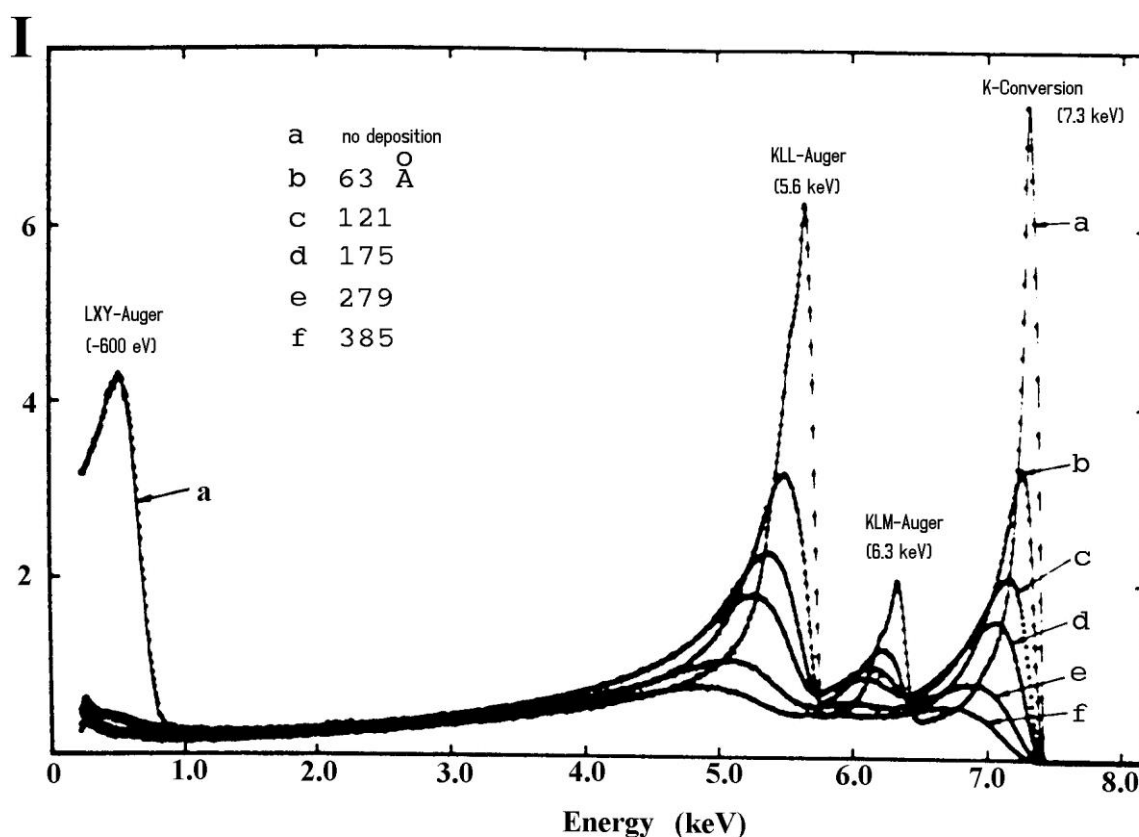
Fig.3.28 Electron spectra from a 30 mCi ^{57}Co source. The source was covered successively by iron layers b - f. θ = 45°; R = 1.3 % at 7.3 keV (from [3.52]).

new layer causes the centroid of the K-conversion electron line to shift towards lower energy and the line itself to broaden significantly. The analysis of these experimental spectra have shown that the theoretical calculations are in agreement with the experimental data (F(0,E) versus E), if d_s = (100 ± 5) Å. In accordance with the evaluation given above, d_s should be about 36 Å , and it follows that either the radionuclide has not been uniformly deposited or that there was a large amount of other nuclides present in the preparation. The weight functions $T_{E,45°}(x)$ are given in Fig.3.29. The calculations assumed that E values are accurate within 8 eV. These data show that the study of a near surface layer less than 50 Å thick requires a β-spectrometer with the energy resolution of about 0.5 %. This was demonstrated [3.52] using the L(x,E) function and assuming d_s = 100 Å and calculating the F(x,E) functions to obtain $T_{E,45°}(x)$, and comparing them with the experimental data. The results which are presented in Fig.3.30 illustrate a good agreement with the experiment.
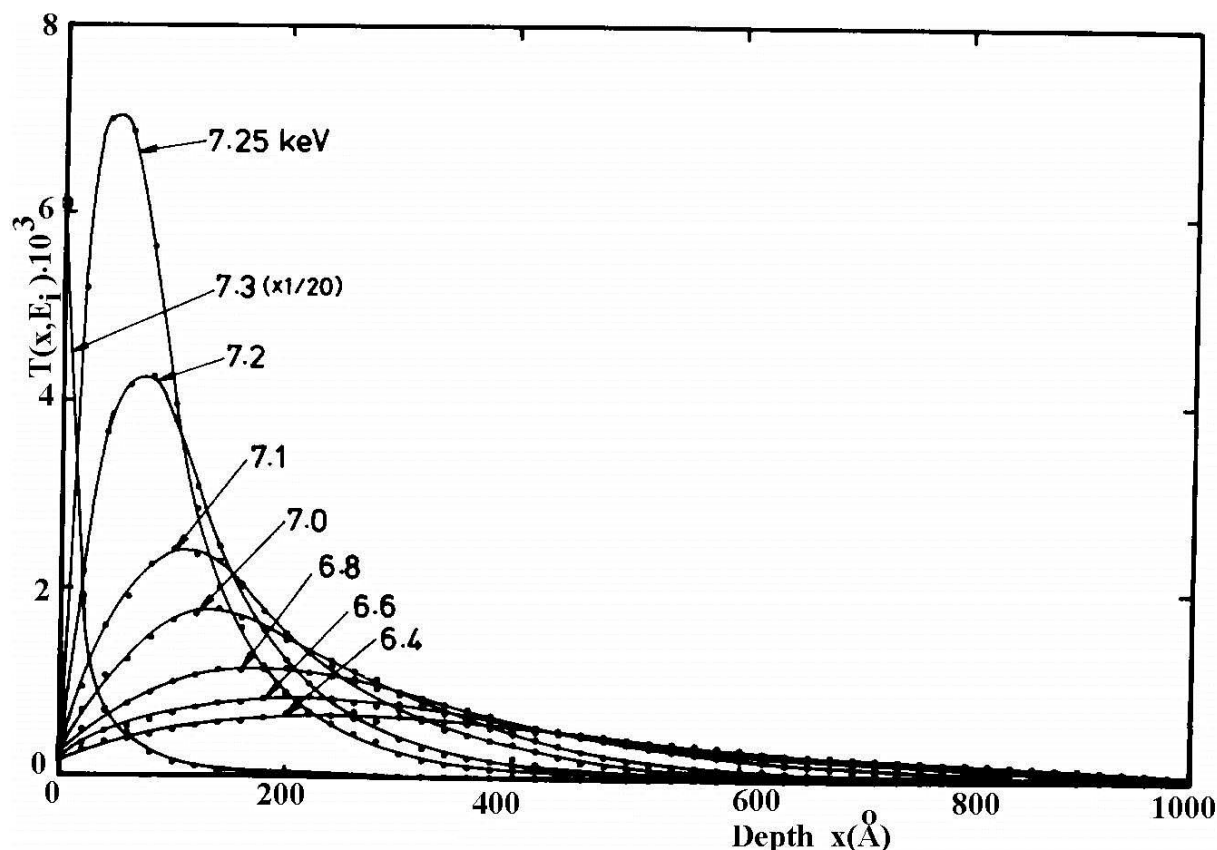
Fig.3.29 The weight function, obtained from experimental energy distributions by the convolution interpolation and extrapolation [3.52].

The results obtained are valid only for a particular DCEM spectrometer. For example, the electron spectra, presented in Fig.3.28 and the weight functions of Fig.3.29 were obtained with the spectrometer described in [3.63] with an energy resolution R = 1.3 % for the 7.3 keV line and detecting electrons at angles 30° to 60° relative to the surface.

Similar investigations with a spectrometer having R = 2 % for the 7.3 keV line and detecting electrons in the angular interval 0° - 15° have also been performed [3.75]. ^{57}Co was deposited onto two backings: aluminized formvar and a sapphire disk covered with a copper layer. For the second source the K- conversion electron line was broader due to stronger backscattering. Successive covering of the first source with two carbon layers of 9.6 g/cm^2 (approximately 120 Fe Å) resulted in a sharper decrease of the line intensities and their shift to a lower energy region (Fig.3.31) relative to the equivalent iron coating thickness (cf. Fig.3.28). This difference between the spectra may reflect that in different spectrometers the detected electrons escape at different angles from the surface of the sample.

The weight functions and energy distributions for the electrons of interest can also be obtained from the direct detection of electrons produced by resonant scattering. The obstacles to this procedure: first, the necessity to prepare a thin Mössbauer scatterer with the factor f' being independent of the distance from the surface; second, non-resonant scattering should not substantially reduce the signal-to-background ratio in comparison with the experiments using the Mössbauer source.
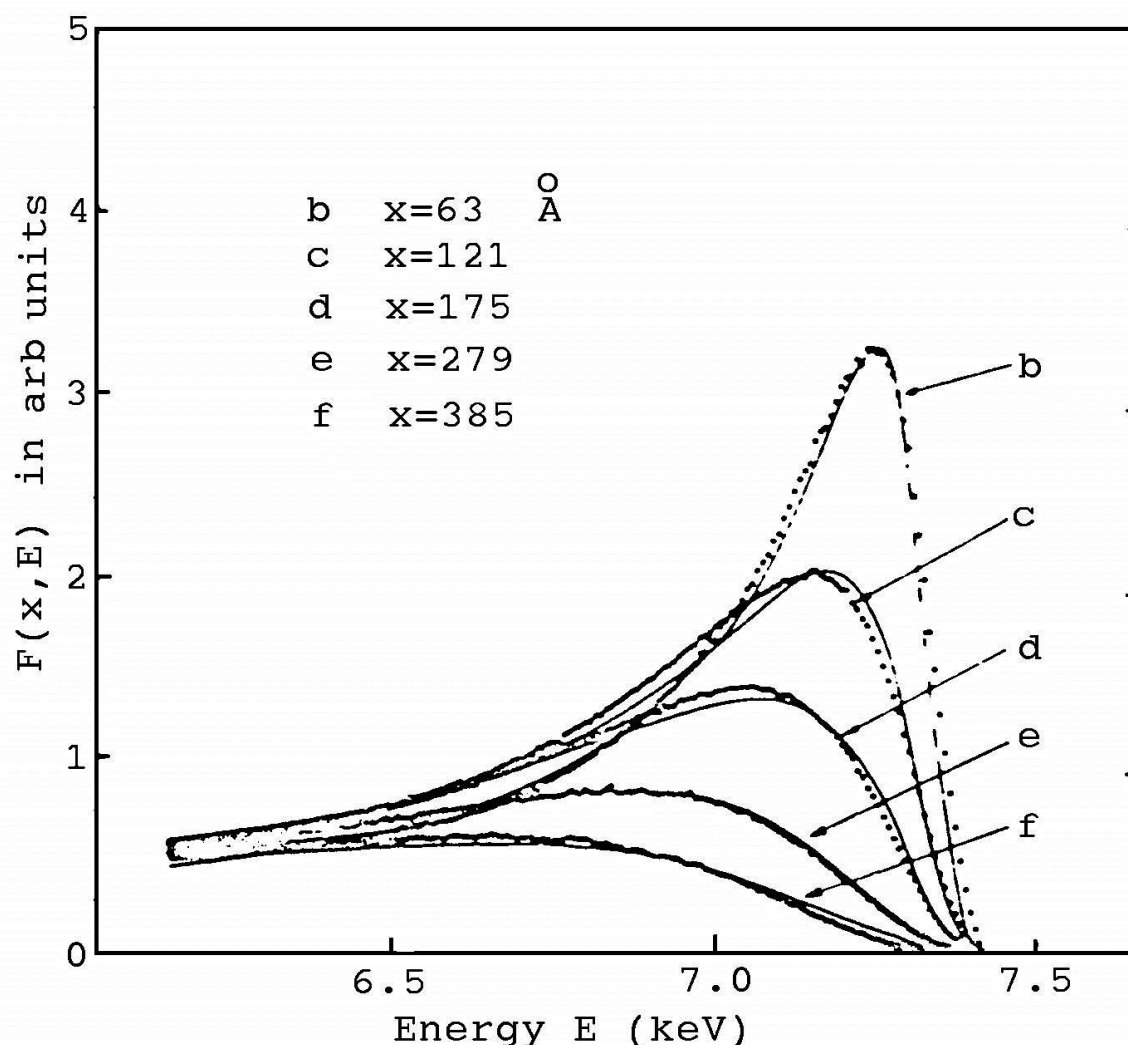
Fig.3.30 Comparison of the computed spectra (solid lines) with the spectra experimentally obtained in the APK interval (dotted lines) (cf. Fig.3.28).

Experiments of this type are especially useful when Mőssbauer sources have a low specific activity. The experimental difficulties involving [119]Sn have been overcome by BONCHEV et al. [3.11,76,77]. In these experiments SnO_2 layers 200 and 500 A| thick (a = 85 % [119]Sn) were used as electron sources and were irradiated by a source of [119m]$SnBaO_3$ (1 mCi). The passage of the 19.6 keV conversion electrons through layers of Be, Cu, Ag, Sn, Au and Pb was investigated. Deformations of the electron spectra as a function of layer thickness were found to be the same as shown in Fig.3.27 for [57]Fe.

Similar experiments with [57]Fe have been made possible by the development of β-spectrometers with a high luminosity in addition to the good energy resolution [3.75,78]. Layers of [57]Fe of only 15 Å thickness have been used as a thinner source of

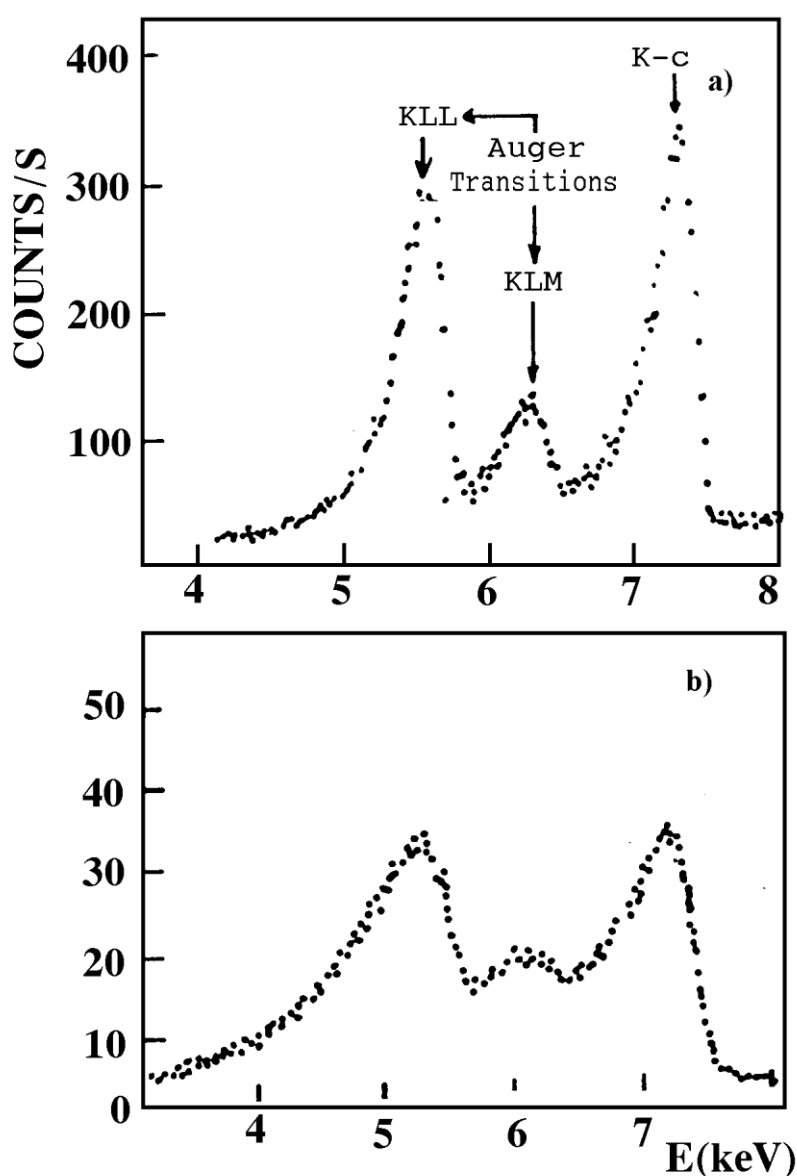Fig.3.31 Electron spectra (R = 2 %, θ = 7.5°) from a ^{57}Co source (from [3.84]): a - on an aluminized formvar backing, b - on a copper covered sapphire disk.

electrons than the ^{57}Co source (d$_s$ = 100 A|) used in [3.52]. The ^{57}Fe layers were deposited onto 100 Å - 200 | - thick backings of ^{56}Fe. The γ-quanta from a ^{57}Co(Rh) Mőssbauer source (100 mCi) were resonantly scattered by the ^{57}Fe nuclei, and the passage of electrons through layers of ^{56}Fe evaporated on the ^{57}Fe layers was studied. The thicknesses of the coating layers ranged from 12 Å to 170 Å. The electron spectra from such sandwiched iron layers of a total thickness of 275 A| are shown in Fig.3.32 together with the order of the layers. The thicknesses of the emitting layers were 15 A| and 11 A|, and those of the absorbing layers were _ 50 Å and 170 Å. Electron spectra were recorded either at resonance (the first line of the sextet v$_1$), or off resonance. A spectrum is presented in Fig.3.32 corresponding to
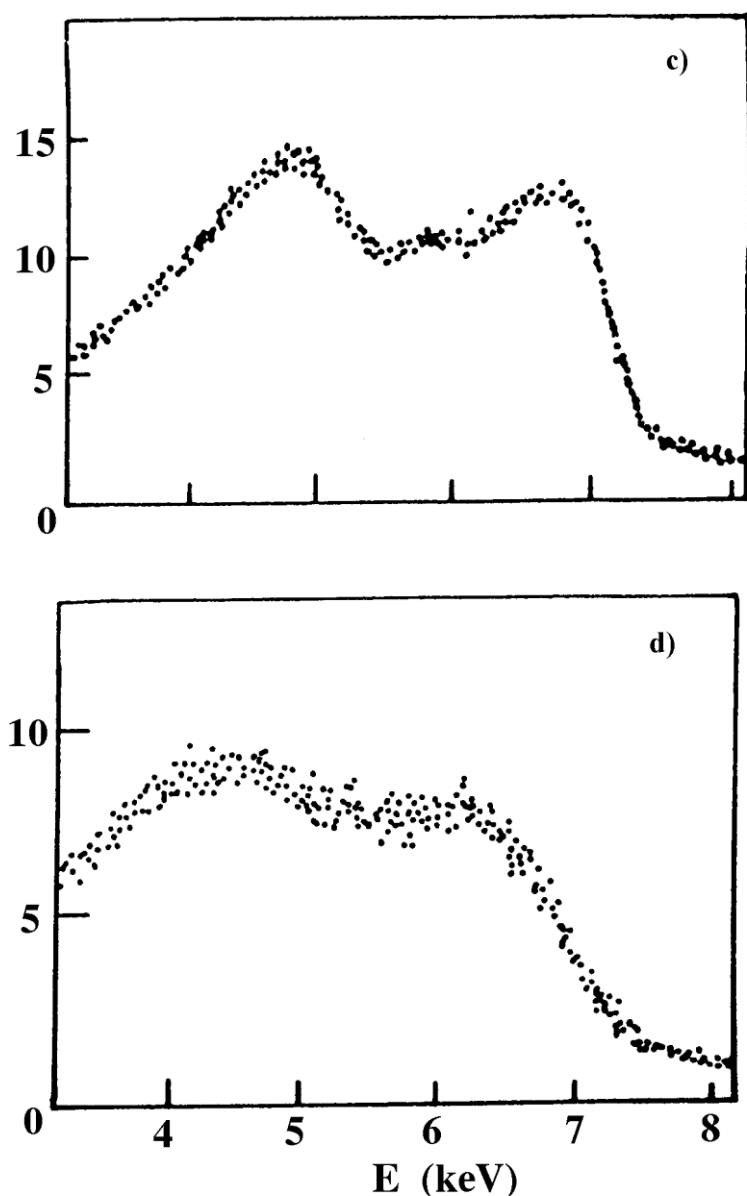
Fig.3.31 Electron spectra (R = 2 %, θ = 7.5°) from a ^{57}Co source on an aluminized formvar backing: c - the source covered with one carbon layer (9.6 g/cm^2), d - the same source covered with two such carbon layers (from [3.84]).

the velocity v_1. The spectra of Fig.3.32c and d, are from electrons following de-excitations of the resonantly excited nuclei. These spectra were obtained after normalization followed by subtraction of an off resonance spectrum from a corresponding on resonance (v_1) spectrum. The K-conversion electron lines appear to be sufficiently narrow. Using the approach of KRAKOWSKI and MILLER [3.30] the authors [3.78] calculated the $T_x(E)$ dependence and obtained good agreement with the experimental result.

A certain amount of experimental data related to studies with β-spectrometers including the spectral shapes of electrons emitted by thin Mössbauer sources or a thin resonant scatterer has been accumulated. Transformations of these spectra as a result of the passage of electrons through absorbing layers
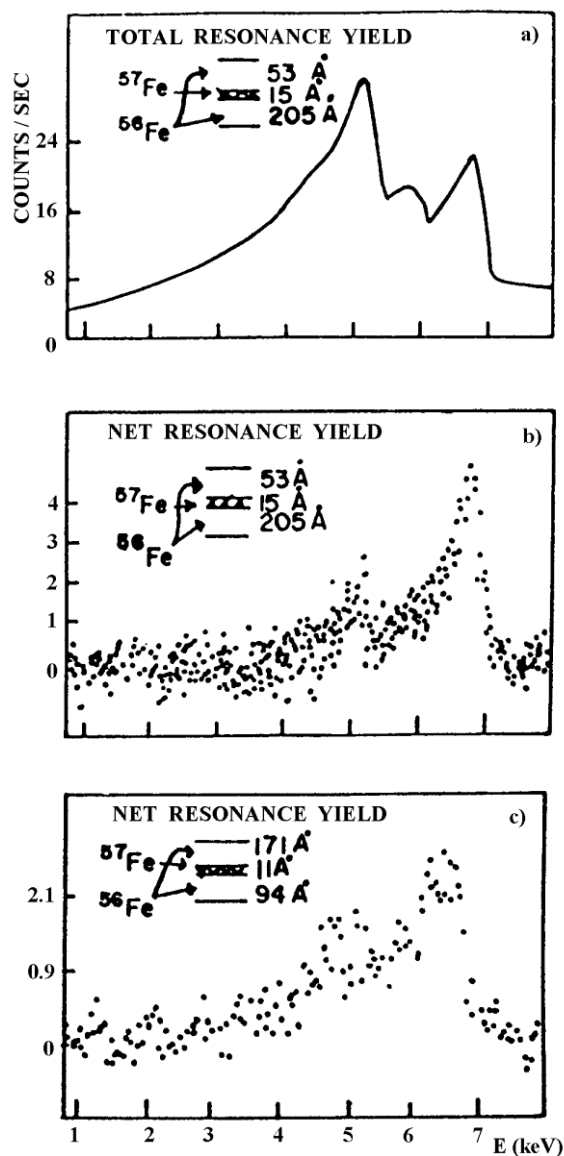
Fig.3.32 Electron spectra from iron layers 275 Å thick (from [3.52]): a - the source velocity is v_1, b and c - difference spectra (spectra corresponding to $v(\infty)$ have been subtracted from those corresponding to v_1).

deposited onto the sources have also been recorded and the weight functions have been obtained experimentally for several DCEM spectrometers. Nevertheless it remains desirable to use Monte Carlo calculations of the weight functions in order that DCEMS can be used as an analytical technique.

Before discussing these calculations the trajectories of electrons used in DCEMS must also be considered. LILJEQUIST et al. [3.79] have computed the K-conversion electron trajectories in α-Fe originating from 50 Å or 500 Å depth. The electron trajectories were terminated when the electron reached the surface or when the electron energy was below 6.3 keV (i.e. outside the APK energy interval). Simulated K-conversion electron trajectories in iron in which the electrons have lost not more than 1 keV of their energy are given in Fig.3.33.

A correlation exists between the starting direction of the electron and the direction of its emergence from the sample surface. It follows that the study of surface layers at a depth of less than 10 nm requires a consideration of the high energy resolution and also the angular selection.

The concept of the weight functions was presented in Sect.3.3 where the difficulties of computation of the weight functions when electrons were detected in a definite energy interval were discussed. The main contribution to the development of the weight function theory has been made by two groups: D. Liljequist et al. for [57]Fe and PROJKOVA et al. [3.77,80] for [119]Sn. It has been shown that straggling should be accounted for and nuclear elastic electron scattering should be described by a corrected screened Rutherford cross section in DCEMS studies. By this the mean free path λ_e relative to elastic scattering can be evaluated. For the 7.3 keV electrons λ_e= 2.5 nm. The λ_i parameter, defined as the path length on which the electron loses energy I in the substance with the stopping power S (see eq.(3.4)) is important in these calculations.   Liljequist showed that λ_i is of the order of 7 nm. Energy losses   are accounted for by different processes and have been described by Liljequist and by Proykova. Due to Proykova binary collisions, whose cross section is described by the relativistic Molier formula, produce ionization. Energy losses on excitation   are considered to be a continuous process not affecting electron trajectories and described by formula (3.2) from which the ionization energy loss has been subtracted. The influence of different electron orbits is differentiated. Liljequist envisaged that the energy is lost only in discrete inelastic collisions. The energy losses are proportional to the squared electron energy and are spread from E_{min} to E_{max}, where E_{min} is about 10 eV, and E_{max} may be taken to be $E_0/2$. Both models give close results. We can consider the β-spectrometer to be characterized by a triangular line profile such that all the electrons with a   selected energy E are independently detected of the angle of emergence relative to the surface normal [3.79]. At first, let us compare spectrometers with the energy resolution R = 3 % and 8 %. The weight functions $T_V(E,x)$ for these spectrometers are given in Fig.3.34. The weight function may be viewed as a surface. Cuts through this surface perpendicular to the energy axis with the interception at E give the weight function corresponding to the spectrometer setting V = cE. Cuts parallel to the energy axis give the electron energy loss distribution for different depths of origin and are determined by the interception points on the depth axis. The instrumental profile is given by the cut through the point x = 0. A comparison of   the surfaces on Fig.3.34a and b, shows the influence of resolution R of the β-spectrometer on the sharpness (the minimum overlap between) of the $T_V(E,x)$ functions and thereby on the depth-selectivity of the DCEM spectrometer.
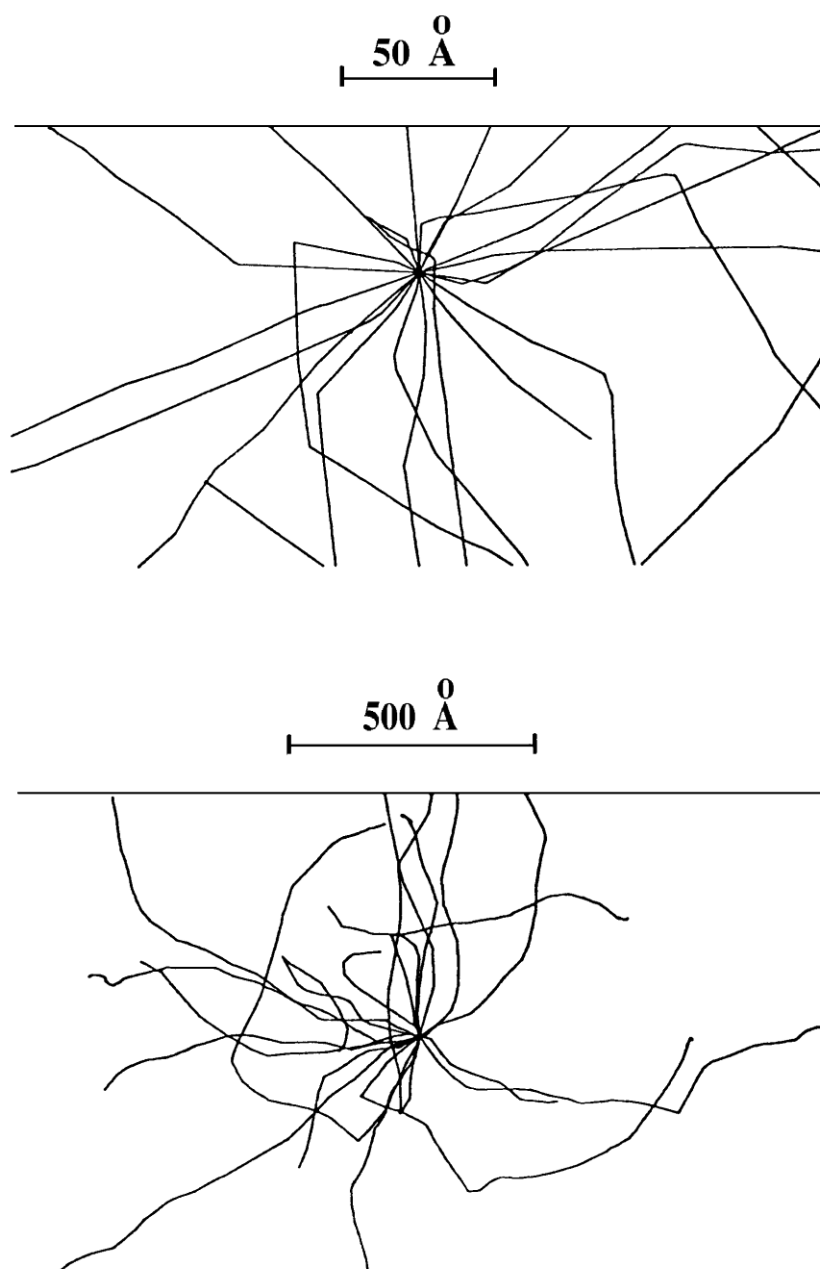
Fig.3.33 Simulated 7.3 keV K-conversion electron trajectories in iron (from [3.79]). The depth of origin is a) 50 Å , b) 500 Å .

Every β-spectrometer is characterized by an average angle θ relative to the surface normal and by an angular interval Δcosθ within which electrons are focused by the spectrometer. For practical applications the weight functions should be known for a particular instrument. All β-spectrometers may be divided into   three groups. Spectrometers of the first group can detect electrons which are emitted at angles close to the surface   normal, i.e. θ ≈ 0°, 0.98 ≤ cosθ ≤ 1.00. For the second group of spectrometers θ ≈ 45°, 0.5 ≤ cosθ ≤ 0.8; for the third group   θ ≈ 80°, 0 ≤ cosθ ≤ 0.3. The weight functions are presented for DCEM spectrometers based on the above three types of spectrometers in Fig.3.35 on the assumption of the triangular
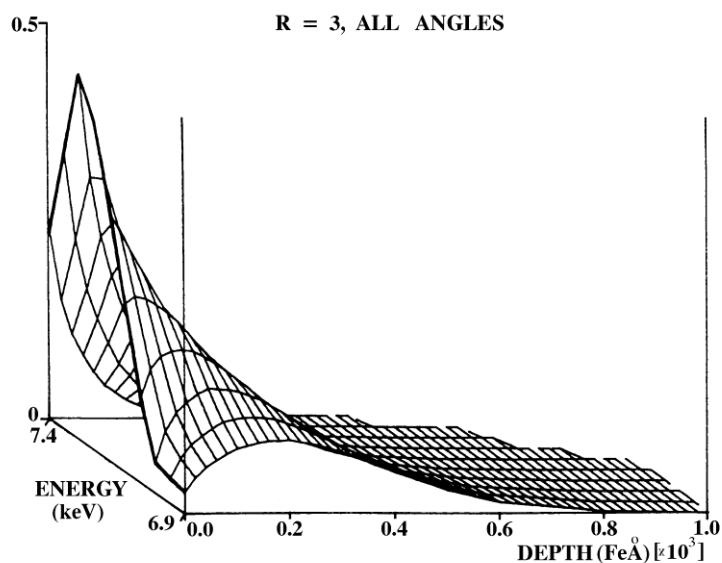
Fig 3.34 a) A Monte-Carlo computed surface of the weight function for [57]Fe DCEMS; the energy resolution R = 3 % .The scatterer is of α-Fe. (Detection at all angles). (from [3.79]).
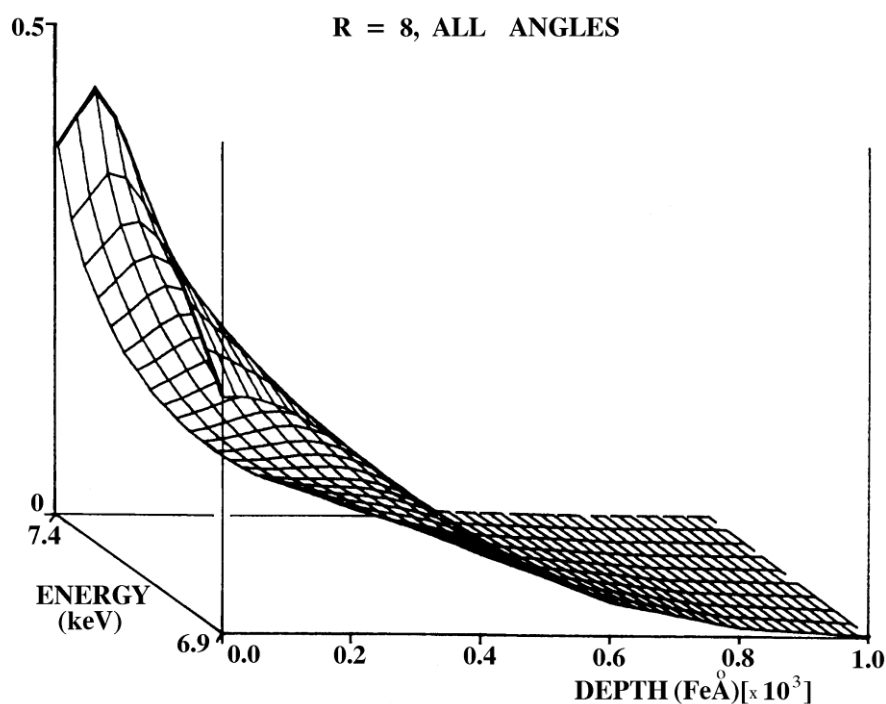

Fig 3.34 b) A Monte-Carlo computed surface of the weight function for [57]Fe DCEMS; the energy resolution R = 8 % .The scatterer is of α-Fe. (Detection at all angles). (from [3.79]).
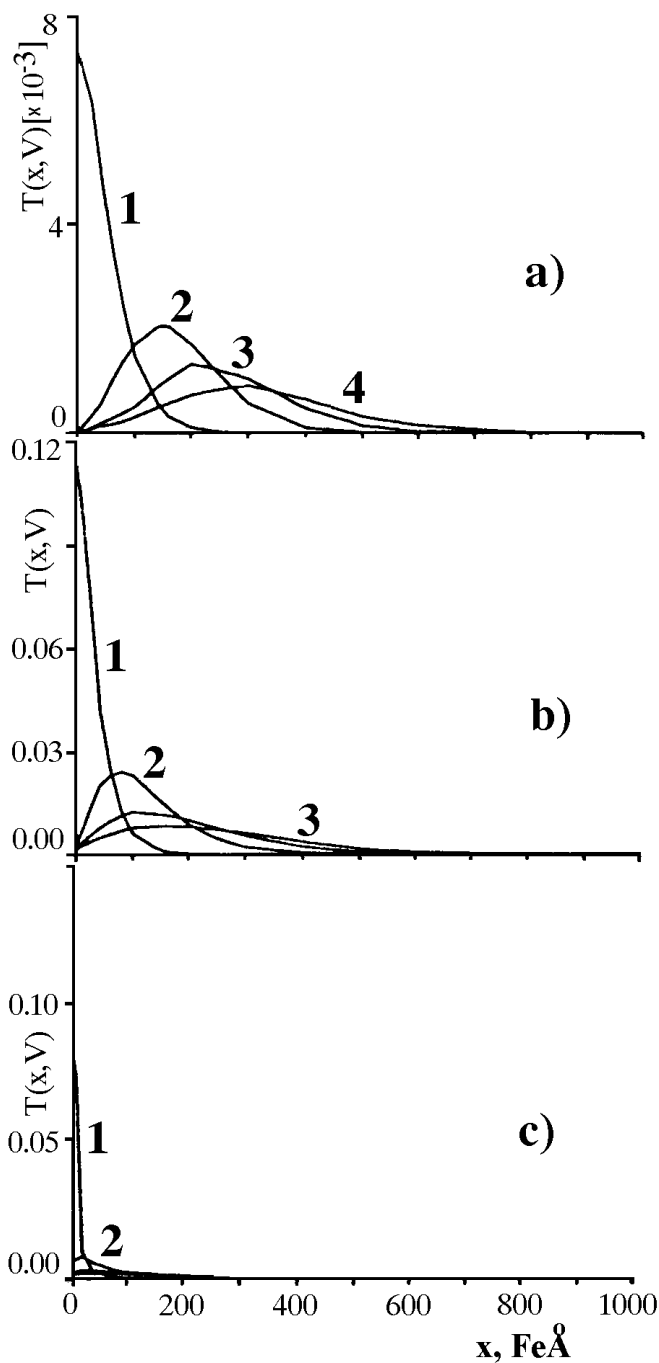
Fig.3.35 Weight functions assuming a triangular spectrometer profile, R = 0.5 %. The weight functions are shown at energies 7.3, 7.2, 7.1 and 7.0 keV and numbered 1 to 4 , respectively. a) electrons are detected emitted at nearly perpendicular angles relative to the surface (0.98 < cos θ < 1), b) intermediate angles of detection (0.5 < cos θ < 0.8, c) glancing angles of detection (0.0 < cos θ < 0.3) (from [3.79]).

spectrometer profile and R = 0.5 %. The $T_{V,\theta}(x)$ functions correspond to the following energy settings of the spectrometer: 7.3, 7.2, 7.1 and 7.0 keV (numbers 1 up to 4, respectively). The ordinate axis numerical values are obtained from a simple evaluation which is based on the fact that at the energy setting 7.3 keV all the electrons which are detected emerge within the selected angular interval. Since half of the electrons start from the surface, the maximum $T_{V,\theta}(x)$ function value is Δ cosθ/2.

These dependences together with those given in Figs.3.29 and 2.34 illustrate the situation of interest for DCEMS. In order to perform a depth-selective analysis it is desirable that the weight functions corresponding to a different parameter V, are as "orthogonal" to each other as possible, i.e. the overlap between two functions should be minimal. At low resolutions of the β-spectrometer the orthogonality is bad. A better surface- selectivity can be achieved (at the expense of the intensity) by using energy settings which are appreciably higher than 7.3 keV. However, the energy resolution should be high, since for $R \geq 8$ % there can be no gain in the surface-selectivity.

Comparison of the weight functions for the detected electrons emerging at different angles for the same energy resolution shows that the best depth resolution is achieved by detecting electrons emerging perpendicular to the surface. At glancing angles the surface layers make a substantial contribution into all weight functions, i.e. the surface selectivity is maximized, although the depth resolution is impaired.

The selectivity problem must be considered in more detail. It follows from Figs. 3.34-35 that the maximal depth of ^{57}Fe analyzed by DCEMS is less than 700 Å. From Fig.3.33 it is seen that electrons whose depth of origin is less than 700 Fe Å will still retain the starting direction on reaching the surface. This means that electrons having started at the same depth d, but which are detected by different spectrometers, will have travelled different distances (d/cosθ). It is obvious that electrons emerging at glancing angles to the surface should travel larger distances and both their energy loss distributions and the weight functions would appear to be strongly smeared out and hence the depth resolution lost. Thus, for example, if a spheric electrostatic β-spectrometer [3.58] is used in DCEMS, then for the detection of electrons with a depth of origin of 100 Å, they should travel a distance of about 760 A| and, hence their energy (loss) distribution will be smeared out.

The detection of electrons with a good β-spectrometer when the electron energy is approximately equal to their initial energy and at different angles of their emergence from the surface has made it possible to create a new variety of DCEMS - the glancing-angle method, GA DCEMS [3.33,79-83]. Suppose that electrons having travelled the distance $d/\cos\theta \leq \lambda_i$ emerge from the surface with an average energy loss I and the β-spectrometer is able to resolve the electron energies E_0 and E_0 - I. For iron $\lambda_i \approx 7$ nm. At a spectrometer setting $V = cE_0$ and $\theta \approx 85°$, a surface layer can be analyzed which is approximately 0.6 nm thick.

The necessity to take into account the roughness of real surfaces in DCEMS requires the introduction of the topographic weight functions instead of the $T_{E,\cos\theta}(x)$ functions which are presented in Fig.3.35. Similar to (3.31) this may be written as

$$T_{E,\cos\theta} (Z_T) = \quad 5 \quad 6T(E, Z_T, \cos\theta)\, dE\, d\cos\theta \ .$$
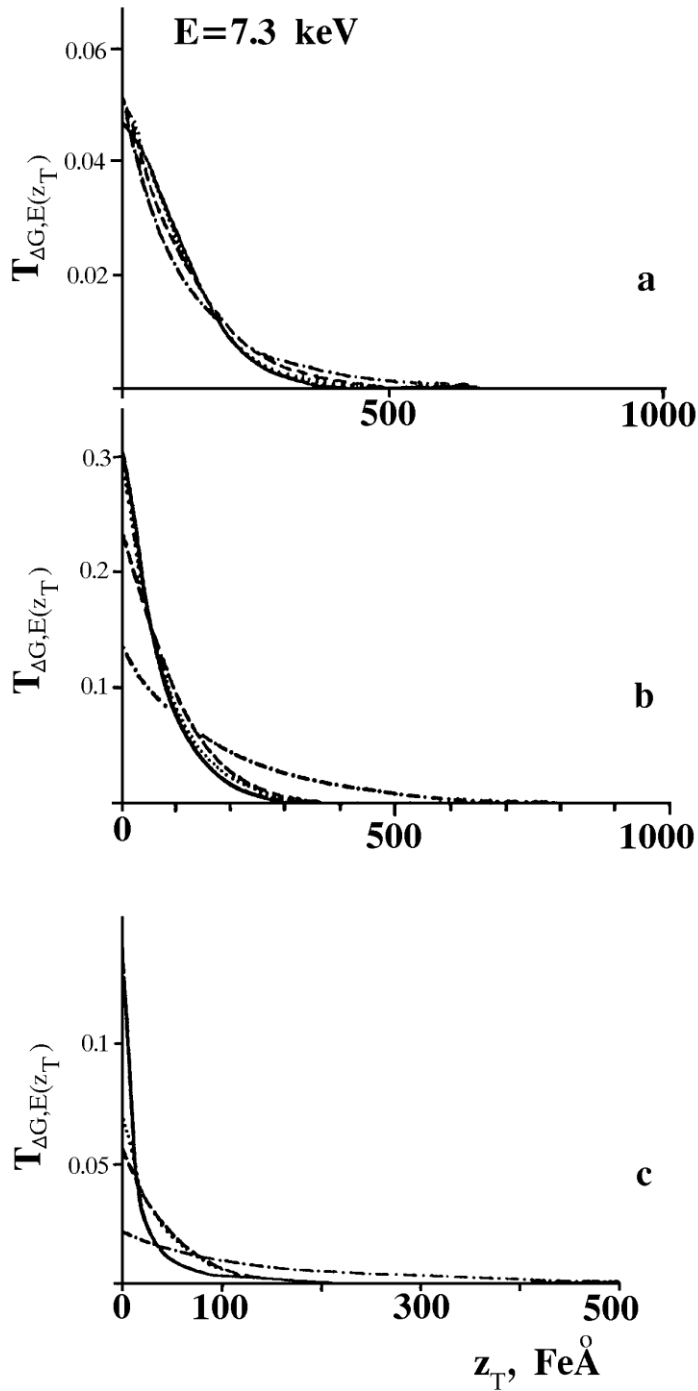
Computed topographic weight functions are given in Fig.3.36

Fig.3.36 Topographic weight functions at energy setting 7.3 keV, R = 2 %: a) at normal angles ($0^o < \theta < 26^o$), b) at intermediate angles ($26^o < \theta < 73^o$), c) at glancing angles ($73^o < \theta < 90^o$). Solid lines - plane surface; dashed lines - the wavy surface which is

characterized by the amplitude Å = 100 and the wavelength W = 2000; dotted lines - Å = 100, W=1000; dot and dash lines - Å = 1000, W = 1000 (from [3.18])

[3.18] for the above mentioned three groups of β-spectrometers at V = cE$_0$ and R = 2 %. It should be noted that the calculations require that the energy resolution and the angular intervals be somewhat different from those used in the calculations presented in Fig.3.35. This produces difference in the absolute intensities. The topographic weight functions corresponding to the detection of electrons emitted perpendicular to the sample surface are different from the T(x) functions only when the spectrometer is set to detect electrons with energy E < 7.2 keV. For electron detection at intermediate angles, it is only a very rough surfaces (1000, 2000) [cf.p.234] that appreciably affects the shape of the T$_{E,cosθ}$(Z$_T$) function. Since the detection of electrons at glancing angles means that the surface layers make the largest contribution to the Mőssbauer spectrum the presence of surface roughness has an especially strong effect. Fig.3.36c demonstrates this. The potentially high surface selectivity of GA DCEMS is practically lost in the presence of such surface roughness.

In order to use the weight functions computed for a plane surface in GA DCEMS the condition of the form Å^2/W < 1 Å or (90° - θ) > φ, where φ = arc tg 4 Å/W must be fulfilled. It may be said that the surface roughness will have no effect on the surface selectivity if the angle (90° - θ) is larger than the average value of the inclination angle relative to the surface.

An illustration of the effect of the surface roughness on the depth resolution and surface selectivity is provided by the evaluation of the relative contribution of the topographic layer to the beam of detected electrons. Monte Carlo simulations have enabled the position to be found of the nuclei emitting the electrons which are detected in the spectrometer. Despite the resonant scattering probability being the same at any location of the scatterer the conversion electrons are emitted isotropically and the contributions from different microvolumes of the layer to the total intensity are different. The Monte Carlo simulation results are given in Fig.3.37 and are shown as a cut through the (100,1000) surface defined by eq.(3.38) on which the locations of electron emission are represented as crosses.

More detailed calculations have shown that the surface selectivity is gradually lost as the surface roughness increases, and this has been explained by "a concentration of the selected electron source volume to the interior of the protrusions on the surface" [3.18].

3.6. Structure Determination of Near Surface Layers by DCEMS

The application of DCEMS requires the use of scatterers whose properties are well known and stable. These requirements are met by the iron and stainless steel system which is widely used in CEMS. A feature of DCEMS is its capacity to study layers which are thinner than in CEMS. This results in a low count rate